UNIVERSITA’ DEGLI STUDI DI CATANIA

UNIVERSITE’ DE RENNES 1

Ph.D. in Materials Science and Nanotechnology

XXXV CICLO

Ph.D. Thesis

LUMINESCENT NANOSTRUCTURES FOR BIOSENSING AND BIOIMAGING

Regina Maria Chiechio

A.A. 2019/2022

Supervisors	**Coordinator**
Dr. Maria José Lo Faro (University of Catania)	*Prof. Giuseppe Compagnini*
Prof. Paolo Musumeci (University of Catania)	
Dr. Valerie Marchi (University of Rennes 1)	

CONTENTS

1 Introduction *5*

1.1 Thesis Outline **5**

1.2 Lanthanide doped Yttrium Oxide Nanoparticles **7**
1.2.1 Background 7
1.2.2 Rare-earth properties 9
1.2.3 Rare-Earth Doped Ceramic NanoPhosphors (RED-CNPs) 10
1.2.4 RED-CNPs Applications in different fields 12
1.2.5 Bioimaging application of RED-CNPs 13
1.2.6 Cathodoluminescence of RED-CNPs 14
1.2.7 RED-CNPs interaction with living systems 16
1.2.8 Synthetic approaches and pegylation techniques 18
1.2.9 Aim and perspectives 20

1.3 Luminescent Gold Nanoclusters **22**
1.3.1 Background 22
1.3.2 Medical applications of Nanoclusters 24
1.3.3 Toxicity Studies on Nanoclusters 25
1.3.4 Nanoclusters formation mechanism 28
1.3.5 Fluorescence properties of Nanoclusters 30
1.3.6 Nanoclusters synthetics approaches 31
1.3.7 Role of Surface ligands 31
1.3.8 Nanocluster Interaction with lipid membranes 32

2 Synthesis and Characterisation of Nanoparticles *35*

2.1 Erbium and Neodymium doped Yttrium Oxide Nanoparticles **35**
2.1.1 Presentation of three synthetic approaches 35
2.1.2 MORPHOLOGICAL CHARACTERIZATION 36
2.1.3 Compositional characterization 39
2.1.4 Optical characterisation 42
2.1.5 Pegylation process after synthesis 45
2.1.6 Ultrafiltration purification process 46
2.1.7 Characterization of pegylated and purified Nanoparticles 48
2.1.8 Comparison between ultracentrifugation and ultrafiltration 52
2.1.9 Conclusions and perspectives 53
2.1.10 Experimental section 53

2.2 Gold Nanoclusters with different emission wavelength **57**
2.2.1 Red emissive Nanoclusters (Red GSH NCs) 57
2.2.2 Infrared emissive Nanoclusters (IR GSH NCs) 62
2.2.3 Blue emissive Nanoclusters (C_3E_6D NCs) 66
2.2.4 Different emissive Nanoclusters comparison 71
2.2.5 Synthetic peptides functionalization of Nanoclusters 74
2.2.6 Microwave assisted Nanoclusters synthesis 78
2.2.7 Experimental section 80

3 Biological applications 83

3.1 Nanoclusters Interaction with Synthetic and Biological Membranes 83
3.1.1 Synthesis of positively and negatively charged Nanoclusters 84
3.1.2 Synthesis of synthetic vesicles with different dimensions 87
3.1.3 Electrostatic interaction between NCs and vesicles (synthetic and biological) 89
3.1.4 Nanocluster positioning over the vesicles membranes 95
3.1.5 Conclusions and perspectives 98
3.1.6 Experimental section 98

3.2 Nanoclusters Encapsulation inside Liposomes 103
3.2.1 Synthesis Nanoclusters and encapsulation method 103
3.2.2 Estimation of encapsulation efficiency 105
3.2.3 Optical and morphological characterisation of the fluorescent liposomes 109
3.2.4 Conclusions and perspectives 115
3.2.5 Experimental section 116

3.3 Extracellular Vesicles from Follicular Fluids: Characterisation and Nanoclusters Interaction 121
3.3.1 Size separation 124
3.3.2 Pathologies 136
3.3.3 miRNA 147
3.3.4 Antibody exosomes labelling 159

3.4 Nanoclusters Targeting of Pancreatic Tumor Cells 162
3.4.1 Synthesis of functionalized $C_3E_6U_{11}$ NCs 163
3.4.2 Quantity of recognition segment optimization for labelling 164
3.4.3 Functionalized Nanoclusters positioning inside the cells 167
3.4.4 Conclusions and perspectives 169
3.4.5 Experimental Section 170

3.5 Biocompatibility study of Nanoclusters with Zebrafish 173
3.5.1 Nanoclusters incubation with Zebrafish eggs 173
3.5.2 Nanoclusters incubation with Zebrafish Embryo 174
3.5.3 Conclusions and perspectives 176
3.5.4 Experimental Section 176

4 Conclusions 177

5 List of publications 179

6 Annexes 180

6.1 Ligands chemical structure 180

6.2 Preparation of phospholipidic vesicles 183
6.2.1 Protocol SUVs synthesis (Small Unilamellar Vesicles) 184
6.2.2 Protocol LUVs synthesis (Large Unilamellar Vesicles) 184
6.2.3 Protocol GUVs synthesis (Giant Unilamellar Vesicles) 185

6.3 Post synthesis techniques 187
6.3.1 Size exclusion chromatography 187
6.3.2 Ultrafiltration 187
6.3.3 Freeze-drying 188

6.4 Characterization techniques 189
6.4.1 UV -VIS spectroscopy 189
6.4.2 Fluorimetry 189
6.4.3 Electrophorese 190
6.4.4 Dynamic Light Scattering (DLS) 190
6.4.5 Zetametry 192
6.4.6 Optical microscope 193
6.4.7 Transmission Electron Microscopy (TEM) 193
6.4.8 Small-angle X-ray scattering (SAXS) 195
6.4.9 Mass spectroscopy (ICP-MS) 196
6.4.10 Fourier Transform Infrared Spectroscopy (FTIR) 196
6.4.11 Fluorescence macroscope 198
6.4.12 Transmission Electron CryoMicroscopy (CryoTEM) 198
6.4.13 Energy Dispersive X-ray Analysis (EDX) 200
6.4.14 Rutherford Back Scattering (RBS) 201
6.4.15 Nanoparticle Tracking Analysis (NTA) 202
6.4.16 RAMAN Spectroscopy 203
6.4.17 Scanning Electron Microscope (SEM) 204

7 References 206

8 Acknowledgments 222

1 INTRODUCTION

1.1 THESIS OUTLINE

The objective of my PhD work is focused on the in vitro and in vivo labeling of biological material using fluorescent nanoparticles for theragnostic (therapy and diagnosis) and biosensing purposes. In particular, among the different types of existing fluorescent nanoparticles, I focused on Au NCs and lanthanide doped Y2O3 NPs.

- Lanthanide doped Y2O3 NPs, thanks to their optical properties of fluorescence emission in the near infrared region (NIR) and up conversion (UPC), are excellent candidates for biological applications and for bioimaging. Unlike classical organic fluorophores, these lanthanide NPs do not exhibit photobleaching and a long luminescence lifetime that can be exploited for many applications. In addition, they have a low phototoxicity and light scattering if they are enough small. Finally they are excellent probes for cathodoluminescence since their luminescence is not extinguished by electron beams[1–3].
- Au NCs, unlike other types of Au NPs with dimensions above 2 nm, are luminescent and can overcome the biological barriers (particularly the kidney), so they are easily eliminated by the body. Their biocompatibility, high electron density and ultra-small dimensions that generate unique photoelectrochemical and luminescence properties, make them particularly suitable for biological applications such as diagnosis, bio-imaging and theragnostic[4–7].

Before being able to proceed with the applications, preliminary studies were made to focus on the interaction between biological membranes and nanoparticles, in particular Au NCs. The goal was to study the positioning of AuNCs on the membranes surface and the possible perturbation they could cause. To do this, a rudimentary model of biological membranes, synthetic vesicles of different sizes (SUV, LUV, GUV), were initially used, to simulate the lipid bilayer and simplify the system, neglecting the role of membrane proteins and extracellular matrix. These synthetic membranes were also exploited to encapsulate NCs for drug delivery purposes.

In view of diagnostic applications, the interaction between AuNCs and extracellular vesicles (EVs) was studied, which can be considered as a model of cell, including membrane phospholipids, proteins and biological contents but without the presence of extracellular matrix and nucleus.

For all these studies, the NCs were functionalized with negatively or positively charged peptides to study electrostatic interactions with membranes. Subsequently, the NCs were functionalized with a U_{11} recognition peptide, capable of binding to the membrane Upar receptor overexpressed by pancreatic cancer cells to test the selective bioimaging of these cells and to study the toxicity and internalization capacity of the NCs[8].

Finally, to study the toxicity of NCs in vivo, it was decided to test them on living beings such as zebrafish.

1.2 LANTHANIDE DOPED YTTRIUM OXIDE NANOPARTICLES

1.2.1 BACKGROUND

Organic dyes are the most commonly used materials for bioimaging.[1-4] However, these fluorescent probes present a series of problems, such as photobleaching, short stokes shift and wide absorption and emission bands, for which very short observation times and reduced sensitivity of the tests are available[13].

The photobleaching problem has been solved through the introduction of quantum dots whose emission wavelength can be varied through the quantum effect and consequently the dimensions of the NPs. However, these materials, in addition to having a high toxicity, require ultraviolet (UV) excitation which can cause serious damage to the biological material. Furthermore, biomolecules often generate self-fluorescence upon UV excitation which, by creating a high background signal, reduce the sensitivity of the test. Another serious drawback is that UV light cannot deeply penetrate in the biological systems as it is absorbed by the surface layers. For example, the limit of penetration of the blue excitation light is the intradermal blood vessels and that of the red excitation light is the subcutaneous tissues.[11]

To solve these problems, fluorescent bioimaging using rare earth doped ceramic nanophosphors (RED-CNP) has been reported as a promising alternative material to overcome the problems of photobleaching, phototoxicity, self-fluorescence and depth of penetration. Furthermore, it is known that RED-CNPs having low phonon energy exhibit an upconversion (UC) luminescence in which rare earth ions emit visible light under near infrared (NIR) excitation.[14–18] These characteristics are generated by the electronic states of the 4f electrons and by the weak electron-phonon coupling, as a result of the shielding effect of the 5s and 5p shells filled with RE ions. Among the various RED-CNP Y_2O_3 is a promising candidate thanks to its chemical and physical durability and its phonon energy which is low enough to give rise to the phenomenon of UC and to the emission of NIR fluorescence if it is doped with a trivalent RE ion.[19–23]

RED-CNPs have several advantages such as narrow absorption and emission lines, long average lifetimes and high photostability. Furthermore, being able to excite them with NIR radiation, the biomolecules are not excited, eliminating the background noise of auto fluorescence, and not causing damage to the system, unlike excitation by UV light. In addition, NIR radiation is able to penetrate more deeply into biological tissues, since its wavelength range between 0.8 and 2 mm is the so-called "biological window" and thus attracts great interest for biomedical fluorescence imaging.[11]

Another characteristic of RED-CNPs is their stability of fluorescence even under electron beam excitation which allows their use in Correlated light and electron microscopy (CLEM). This imaging technique allows to acquire the signal emitted by the sample under electronic excitation (cathodoluminescence, CL) in addition to the SEM (or TEM) image, with the possibility of correlating the morphological image to that of luminescence. Using CL microscopy, it is possible to study the details of biological systems with higher spatial resolution than conventional optical microscopies by overcoming the limitations of individual microscopic techniques and by combining luminescence imaging and high spatial resolution imaging in the same region of a sample[24].

On the other hand, the RED-CNPs, for the most part, are oxides Y_2O_3:Ln^{3+} or $NaYF_4$:Ln^{3+} , i. e. ceramic systems and consequently insoluble and highly inert. For these reasons, one of the challenges is to be able to obtain stable suspensions of these nanoparticles in aqueous solutions, an essential requirement for targeting biological material and for biomedical research in general.[25] Furthermore, when introduced into biological fluids, NPs are recognized as a foreign body, and therefore are promptly cleared from the systemic circulation by the mononuclear phagocyte system (MPS), preventing their accumulation in target cells and tissues[26]. Around each NPs present in biological fluids the “corona effect” is created due to the interactions with plasma proteins which leads to a new biological state of the nanoparticle that could influence the effect in the organism in terms of bioaffinity, biodistribution and excretion. This effect would cause a more rapid recognition of NPs by the immune system, considerably reducing the circulation time and making it difficult to reach the proposed target. The quantity and type of proteins that bind on the surface of the NPs depend on the physicochemical properties of the particle itself[27].

For this reason, it is necessary to confer “stealth” properties to the nanoparticles through ad hoc approaches to increase their circulation time. One of these approaches is to coat their surface with an inert polymer that resists interactions with the components of biological fluids, precisely conferring these invisibility properties. Polyethylene glycol (PEG) coatings on NPs protect the surface from clumping, opsonization and phagocytosis, thus extending circulation time. Pegylation also renders soluble and biocompatible materials that otherwise could not be used. Furthermore, pegylated nanoparticles can be easily functionalized by different selected biomolecules capable of selective recognition of vesicles and / or target tissues.

1.2.2 RARE-EARTH PROPERTIES

The term "rare earths" designates a group of 17 chemical elements of the periodic table, which includes the lanthanides, Scandium and Yttrium. Specifically, they are divided into (**Figure 1**):

- Light rare earths: Scandium (Sc), Yttrium (Y) and elements ranging from Lanthanum (La) to Samarium (Sm);
- Heavy rare earths: from Europium (Eu) to Lutetium (Lu).

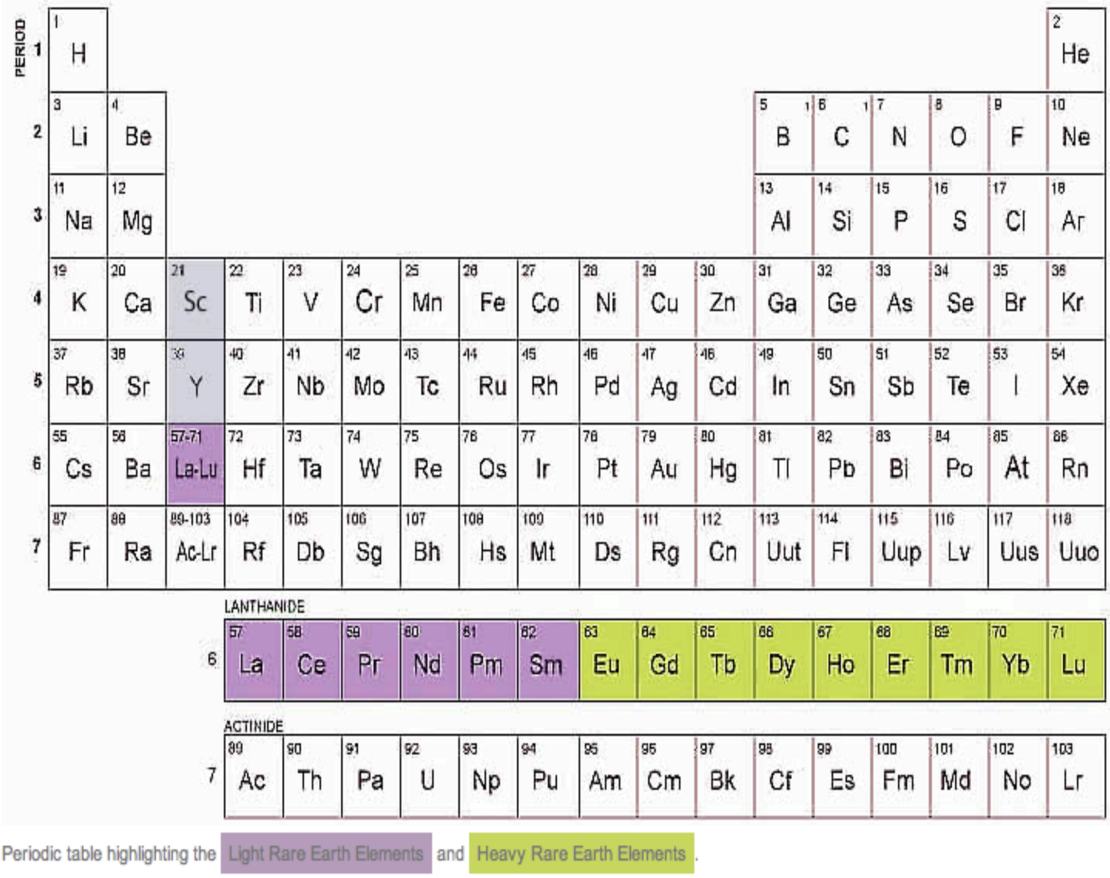

Figure 1. In purple the “light” rare earths, in green the heavier ones.

Such metals only differ in the size of their atomic radii that show a smooth decrease across the series. Rare earths elements have an electronic configuration [Xe] 6s25d14fn while the trivalent ions have a configuration [Xe] 4fn due to the removal of the 3 electrons occupying the 6s and 5d shells. The 4f orbitals are more or less filled, depending on the atomic number of the element which causes the number of electrons in the 4f orbitals to vary from 0 (La^{3+} or Ce^{4+}) to 14 (Lu^{3+}). It is precisely the partially filled 4f orbitals that generate the particular electronic and magnetic properties of these elements. In fact, the 4f-4f optical transitions are almost independent from the chemical neighborhood due to the shielding from the 5s and 5d orbitals, which have a greater radial expansion; for this reason, the 4f orbitals are called "internal" in the ion. According to Laporte's rule, such transitions should be prohibited but, thanks to the shielding of 5s and 5d orbitals on the 4f orbitals and the Stark Effect of splitting, the energy levels inside the crystalline matrix and very efficient luminescence phenomena can be obtained despite the low coefficient of absorption of these materials. These fluorescence properties can be varied by varying the type of trivalent ions present in the crystalline matrix, their concentration as well as the quality of the matrix crystal itself. In fact, by varying the synthesis methodology or the parameters, it is possible to obtain emissions adapted to the chosen objective[28].

Furthermore, the unique thermal, electrical and magnetic properties of rare earths allow their use for various application purposes. They can be used in various forms, such as core-shell fluorides (eg. $NaGdF_4$) or the more common oxide form (e. g. CeO_2, MoO_3 and Y_2O_3) subject of this thesis.

1.2.3 RARE-EARTH DOPED CERAMIC NANOPHOSPHORS (RED-CNPS)

The trivalent ions of rare earths inside suitable crystalline matrices generate very efficient mechanisms of light emission with peculiar characteristics. These materials called rare-earth doped ceramic nanophosphors (RED-CNP) find application in many fields ranging from the creation of light emitting diodes (LEDs), the realization of panels with plasma displays (PDP), as well as the detection of infrared radiation and bioimaging.

In the field of bioimaging, among the various RED-CNP, Y_2O_3 doped with lanthanides is the most promising candidate; in fact the Y_2O_3 matrix has good characteristics as a host material having a remarkable physicochemical inertia and low phononic energy which limits non-radiative phenomena to favor usually not very favored radiative phenomena, such as upconversion.

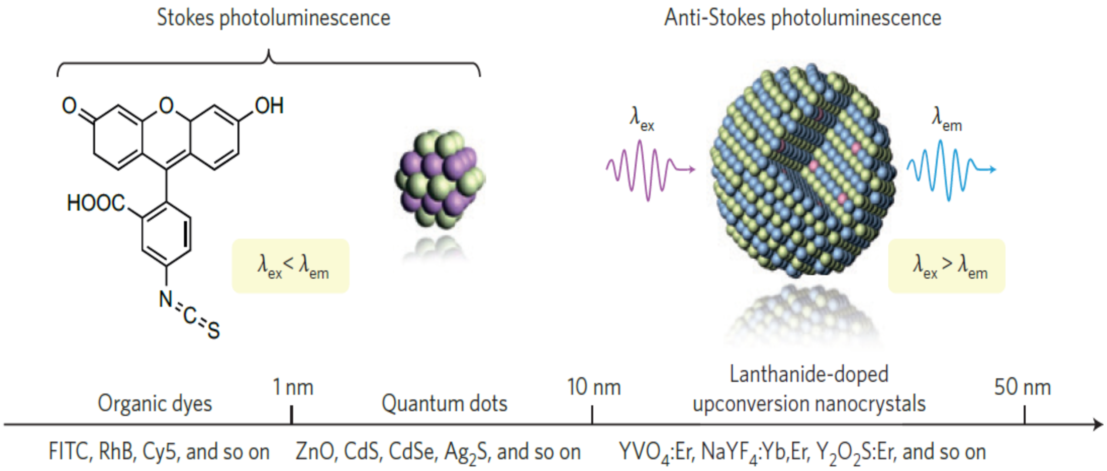

Figure 2. Comparison between nanoscale species. (Chen et al. 2007)

Unlike organic dyes and quantum dots which show only Stokes-type luminescence phenomena ($\lambda_{ex}<\lambda_{em}$), RED-CNP show upcoversion phenomena, i.e. anti-Stokes luminescence ($\lambda_{ex}>\lambda_{em}$) with very sharp peaks (**Figure 2**)[29].

Upconversion (UC) is a non-linear optical process that consists of the sequential absorption of two (or more) low-energy photons leading to the emission of a higher-energy photon (anti-Stokes emission), i.e. the conversion of electromagnetic radiation with a wavelength in the range between 1 mm and 780 nm (IR) in radiation with a wavelength in a range between 780 nm and 380 nm (VIS).

UC, unlike two photon absorption (TPA), does not occur through a simultaneous absorption of incident photons, but following a sequential absorption. For this reason, many intermediate levels are needed between the ground state and the excited state that can act as a reservoir of energy; thus Lanthanides, having available 4f orbitals, rich in energy levels, are the optimal candidates. Furthermore, UC is favored if the crystal lattice has a low phonon energy, which allows to suppress the non-radiative emission by multiphonon relaxation and to generate a fluorescence emission with very narrow peaks[30]. Theoretically, most of the lanthanides can cause upconversion phenomena, but not all of them give rise to the same efficiency. For this reason, in recent years, to optimize the efficiency of UC the choice has been reduced to a few trivalent lanthanides in specific matrices such as Terbium (Tb), Erbium (Er) and Neodymium (Nd) in a Y_2O_3 matrix. In this work, in particular, we focused our attention on Er:Y_2O_3 and on Nd:Y_2O_3. In the case of Erbium, when it is excited at 980 nm, there is an emission of UC in the green and in the red (around 550 nm and 650 nm) corresponding to $^2H_{11/2} \rightarrow {}^4I_{15/2}$ and $^4F_{9/2} \rightarrow {}^4I_{15/2}$ respectively[31]. In the case of Neodymium, when it is excited at 808 nm, emission bands of UC are observed at 750 nm and 680 nm, corresponding respectively to the transitions $^4G_{9/2} \rightarrow {}^4I_{15/2}$ and $^4G_{7/2} \rightarrow {}^4I_{7/2}$[32]. Both types of nanoparticles emit radiation with wavelengths falling in the "biological window", in which there is the maximum depth of penetration of the radiation into biological tissues. Furthermore, these systems low values of cytotoxicity, and thus they are excellent candidates for applications in bioimaging. and in theragnostic.

1.2.4 RED-CNPs APPLICATIONS IN DIFFERENT FIELDS

To date, RED-CNPs have been successfully applied to the bioimaging of various biological samples, including living cells and small animals (**Figure 3a**)[33]; in particular, they seem to be very promising e in biological applications, such as imaging, sensing and cancer therapy[30].

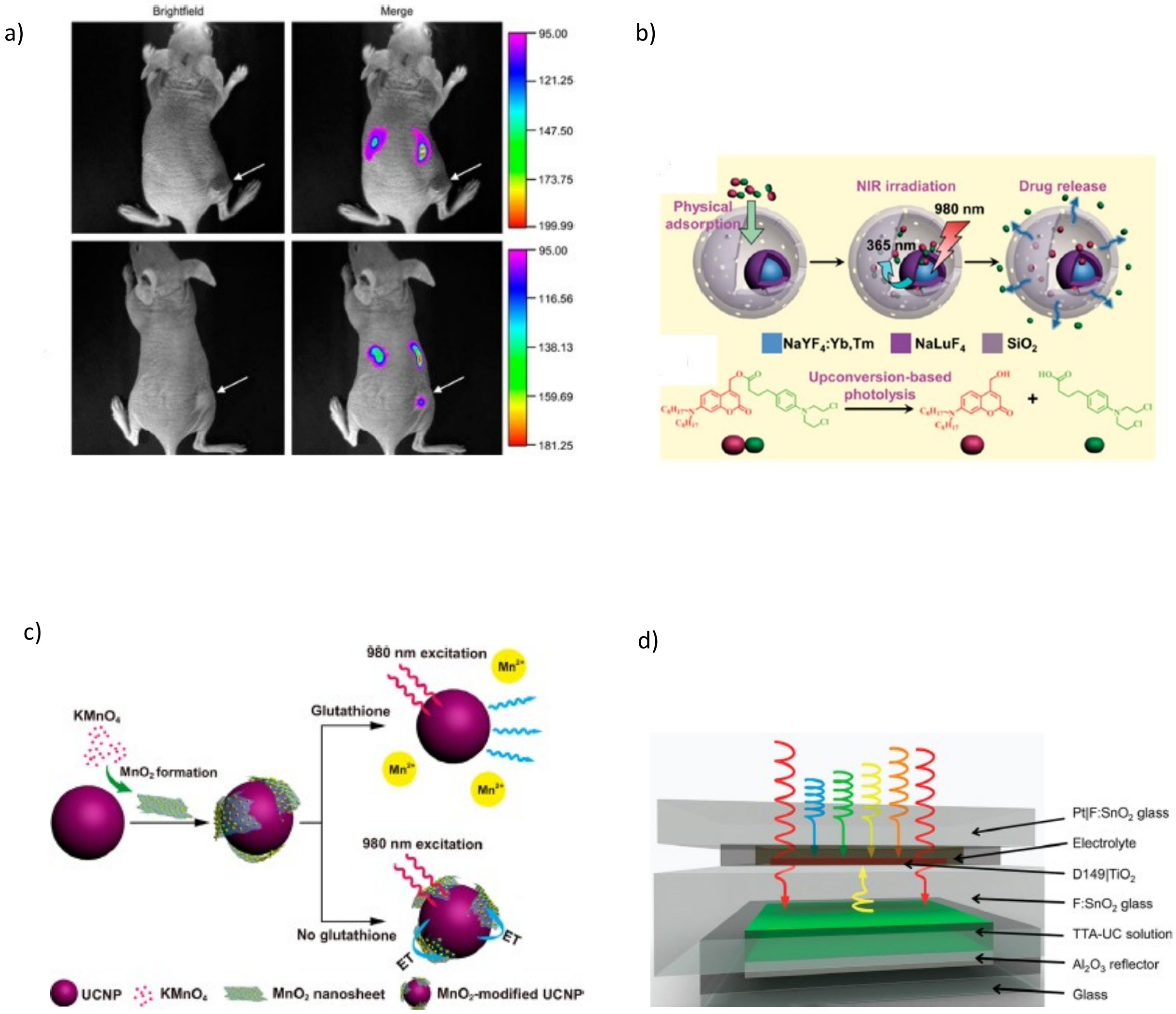

Figure 3. (a) in vivo upconversion imaging of a tumor in a nude mice after intravenous injection of functionalized NaYF$_4$: Yb, Er NPs. (b) therapy process and photolysis of the drug under upconversion emission triggered by a NIR excitation. (c) NaYF$_4$:Yb, Tm NPs modified with a MnO$_2$-nanosheet for glutathione (GSH) detection. (d) structure of an integrated device for photocurrent generation with an upconversion layer. (Zhou et al. 2015)

Some types of RED-CNPs have also found therapeutic applications such as in photodynamic, photothermal and controlled drug release therapy. These applications have been possible thanks to the possibility of such NPs to operate in the NIR range in vivo[34]. In these cases, if there is an effective energy transfer between the NPs and the therapeutic drug molecules, the emission of UC can be used to monitor the quantity of drug released (**Figure 3b**). By appropriately functionalizing the RED-CNPs it is also possible to use them for the specific targeting of metal ions, anions, neutral molecules, DNA and proteins[35]. The interaction between the target and the NPs can be detected through the variation of the intensity of the UC signal of one or more bands, following the physico-chemical variation of the surroundings (**Figure 3c**).

Finally, RED-CNPs were used inside solar cells, electronic devices, for the generation of photocurrent, reaction catalysts and data storage[36]. For example, introducing materials with UC properties into the active layer of a solar cell allows the conversion of photons of lower energy (sub-band gap) into photons of higher energy, which can then be absorbed by the solar cell thus improving the efficiency of the device (**Figure 3d**); due to the low efficiency of upconvesion, however, the actual benefit is still limited.

1.2.5 BIOIMAGING APPLICATION OF RED-CNPS

Bioimaging is a set of methods that allows to view biological material in a non-invasive way contextually limiting interferences with the vital processes. One example is the photoluminescence (PL) imaging, which has revolutionized medical diagnostics by becoming an indispensable method for monitoring changes in biochemical markers and the appearance and development of biomarkers in living systems[37].

This technique generally employs contrast agents such as organic dyes, organically modified silica, fluorescent proteins, metal complexes, and quantum dots (QD)[38,39]. Most of these agents use ultraviolet (UV) l as excitation wavelength, but it has a number of limitations:

- low depth of penetration of UV rays into the biological tissues;
- low signal-to-noise ratio (SNR) caused by strong light scattering and unwanted autofluorescence from biological tissues when excited at low wavelengths;
- potential DNA damage and cell death due to prolonged exposure to energetic radiation, particularly if excited by UV radiation[28].

Furthermore, QDs contain toxic elements (e. g. cadmium, mercury and lead), which severely limit their use in this type of applications. On the other hand, biological tissues exhibit an "optical transparency window" in the NIR range of 700-1100 nm and, therefore, the use of NIR excitation light not only allows reduced photo-damaging effects and penetration deeper[28,29] , but it also offers reduced phototoxicity, lower light scattering and with high spatial resolution given a good signal-to-noise ratio[30] . Indeed, rare earth doped yttrium oxide nanoparticles exhibit upconversion in a wavelength range that falls within the spectral range of the biological window, resulting in promising agents for bioimaging [31–34] .

Numerous studies have recently been conducted to improve the optical properties of these nanostructures and of their upconversion properties. Furthermore, in order to be used in medicine, it is possible to functionalize its surface, through the use of special ligands, in order to allow the specific recognition of metabolites, biomarkers and vesicles[47].

To be useful in the field of bio-applications, RED-CNPs also known as Upconversion Nanoparticles (UCNP) must meet the following requirements:

- small and monodisperse particles;
- high luminescence efficiency;
- precise stoichiometric composition, obtained through a rigorous control of the dopant concentration, in order to finely modulate the optical properties;
- surface engineering of UCNPs to improve the stability of the suspension in the aqueous phase and for specific functionalization according to the desired applications.

UC imaging of UCNPs can be combined with other imaging modalities, such as computed tomography (CT), positron emission tomography (PET), magnetic resonance imaging (MRI) and ad tomography. single photon emission (SPECT) in order to significantly improve early diagnosis for certain types of diseases[36].

1.2.6 CATHODOLUMINESCENCE OF RED-CNPS

Conventional cell imaging methods, such as light microscopy (LM) and electron microscopy (EM), have some limitations. LM reveals protein distributions with fluorescent probes, but their exact location is difficult to obtain due to the diffraction limit of light. On the contrary, the EM allows a higher spatial resolution than the LM. For example, through properly functionalized Au NPs, EM allows to individuate the proteins position with resolution on the nanometer scale, being able to discriminate even two types of Au NPs with different sizes, but the discrimination becomes more difficult if three or more types of AuNPs are used. For this reason, multilabelling, easier to achieve with the LM, becomes difficult to achieve with the EM[37].

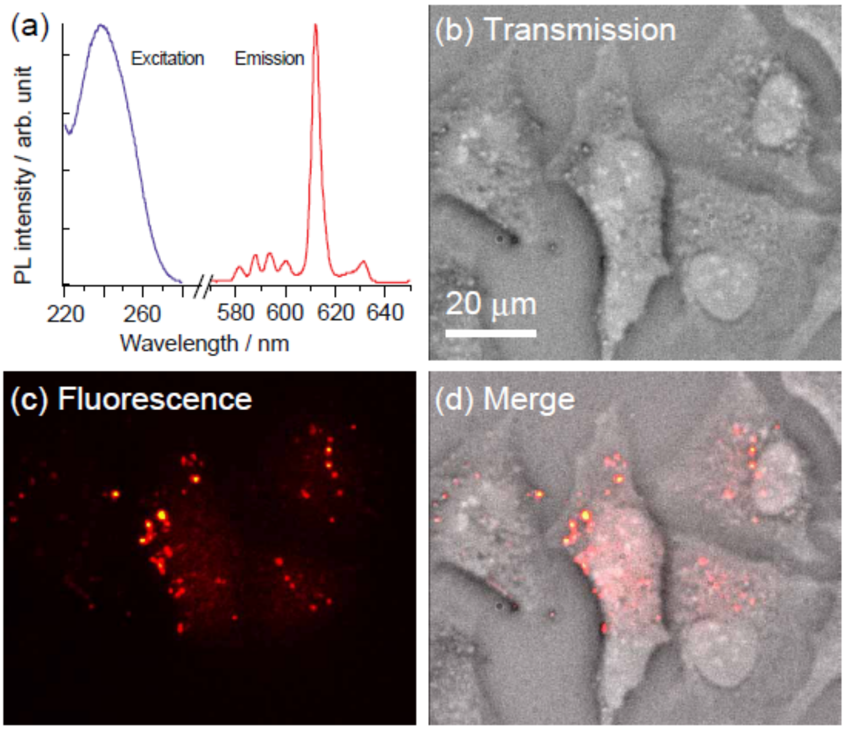

Figure 4. (a) excitation and emission spectra of laser-ablated Y_2O_3:Eu, Zn. (b) transmission, (c) fluorescence, and (d) combined images of Y_2O_3:Eu, Zn nanophosphors contained in a hela cells. (Taichi Furukawa et Al. 2013)

Recently, an innovative technique has been developed that brings together the best characteristics of both LM and EM allowing to overcome their respective limits. This technique, the Correlated Light and Electron Microscopy (CLEM) allows to obtain an accurate superimposition of fluorescence and electron microscopy images using the electron beam of the SEM (or TEM) to excite the sample and then detecting the cathodoluminescence signal results. The excitation of the luminescence by an electron beam allows for sub diffraction imaging allowing luminescence images with much higher resolution than that which could be obtained with any optical microscopy. Cathodoluminescence (CL) provides unique and complementary information to other SEM-based techniques. This technique also allows to observe an emission energy range (from 0.5 to 6 eV) in which it is possible to obtain information on the composition, the crystal structure and the electron band gap. Then, combined with other SEM-based techniques, it can be used to produce the most comprehensive materials analysis. In addition, the depth of electron penetration is adjustable, which allows for depth-resolved studies[38,16].

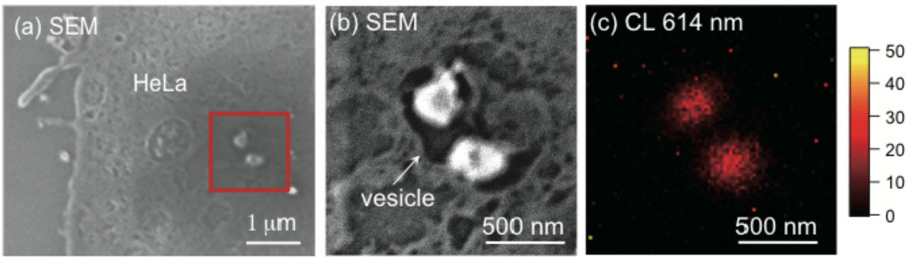

Figure 5. SEM (a, b) and cl (c) images of 100 nm sliced section of a hela cell.
(Taichi Furukawa et Al. 2013)

Several probes have been studied for CL imaging of biological tissues and cells, such as organic molecules, fluorescent proteins, quantum dots, and rare earth doped nanophosphors (RED-CNPs). Among the various types of NPs, RED-CNPs are very promising probes for cathodoluminescence bioimaging (**Figure 4** and **Figure 5**) Unlike organic fluorophores and semiconductor quantum dots, which suffer from a significant loss of intensity of emission subjected to electron beam, the nanoparticles doped with rare earths have a very high and stable luminescence even when irradiated by the electron beam (**Figure 6**); moreover, their small dimensions allow to obtain a resolution on the scale of a single protein (tens of nanometers)[37].

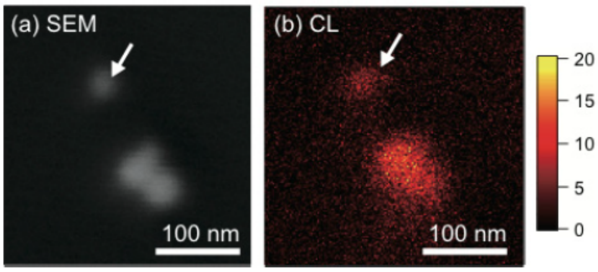

Figure 6. SEM (a) and cl (b) images of Y_2O_3:Eu, Zn.
(Taichi Furukawa et Al. 2013)

1.2.7 RED-CNPS INTERACTION WITH LIVING SYSTEMS

Before being able to use nanomaterials in the medical field, it is important to test their biofunctionality and biocompatibility: biofunctionality refers to the ability of a material to perform a specific biological function, while biocompatibility refers to the ability to be well tolerated by the organism that continues to perform its functions without interferences.

Nanoparticles are very promising materials in the biomedical field as they can be used for drug delivery and theragnostic (diagnosis and therapy). However, to keep these functions it is also important to evaluate their biodistribution within the organism which depends on their size and on the ability not to be recognized by macrophages and the endothelial reticulum system in general.

The size and shape of the nanoparticles influences the ability to penetrate into the tissues; smaller particles are able to enter the capillaries, cross the epithelial lining, penetrate inside the cells[40] , and only in very particular cases even enter the nucleus. In addition to the dimensions, the surface properties are essential because through a surface coating with a hydrophilic, non-ionic polymer, such as polyethylene glycol (PEG), it is possible to avoid recognition as a foreign body by the reticulo-endothelial system[52], thus increasing the circulation time inside the body. PEG therefore avoids the rapid removal of NPs by opsonization, a reaction by opsonins (proteins contained in blood serum) which make phagocytosis by monocytes-macrophages possible[53].

Another essential parameter to be evaluated before using NPs in vivo is cytotoxicity. It mainly depends on two factors: the chemical composition and the size. It is evident that cadmium or silver particles are more toxic than gold which is inert; consequently it is essential to preferably use materials with low toxicity[54]. Furthermore, smaller particles decompose faster than larger particles thanks to a high area-volume ratio[55], avoiding prolonged retention by the reticulo-endothelial system which is unable to digest them with consequent inflammations that increase their toxicity. In addition to the toxicity of the core of NPs, it is also important to evaluate that of the surface ligands[56].

Through various studies[57–59] it has been shown which interactions between NPs and cellular systems can induce cytotoxicity:

- the interaction with biomolecules (such as proteins and lipids) which can lead to different types of biological effects following the absorption on the surface of the NPs (protein-corona);
- the interaction with the plasma membrane which can destabilize ion transport, signal transduction, and even lead to cell death;
- interaction with the cytoskeleton which can prevent vesicular trafficking and cause mechanical instability and cell death;
- interaction with mitochondria which can alter metabolism or interfere with antioxidant defenses and ROS production;
- DNA binding which can be damaged by interfering with protein synthesis and cell division[60].

Since nanomaterials have different physico-chemical properties from the same bulk or atomic-sized materials, it is important to specifically test and regulate them (SCENIHR, 2007). Given the complexity of the system and the number of factors to be evaluated, preliminary studies on cell cultures are necessary before toxicity can be predicted, using protocols suitable for nanomaterials in particular (EPA, 2007).

1.2.8 SYNTHETIC APPROACHES AND PEGYLATION TECHNIQUES

One of the biggest challenges faced in the preparation of nanomaterials is to maintain reproducibility of the processes[61]. RED - CNPs, for biological applications in particular, should exhibit a narrow size distribution and be highly stable in aqueous solutions. The main techniques present in the literature to synthesize such NPs will be examined below.

Chemical precipitation consists in the formation of a solid substance starting from a liquid supersaturated solution or making the substance insoluble through chemical reactions. Once formed, the NPs are removed by filtration and / or decantation processes. This technique is the simplest and the lowest cost of the solution techniques for the production of NPs on a large scale[62]. The precursors are usually inorganic metal salts such as nitrates and chlorides, dissolved in water. The quality of the final product depends on many parameters such as pH, synthesis temperature, solvent and any post synthesis treatments (**Figure 7a**). Due to the presence of all these variables the synthesis of NPs by chemical precipitation is not always easily controllable and reproducible, as the obtained nanoparticles often present a wide size distribution.

The sol – gel technique is quite popular despite being more expensive than the previous one. It consists in the creation of an initial colloidal suspension (sol) of nanometric nanoparticles which is then transformed into a gel through various condensation processes; this gel is then dried to obtain a precipitate which can then be calcined (**Figure 7b**). Also in this case the final product depends on various parameters such as pH, temperature, reaction time and agitation. This technique brings different advantages as it has a more precise morphological control, a high purity and a lower working temperature[63].

Microwave synthesis (MW) uses microwaves to induce and accelerate the process of precipitation and generation of NPs (**Figure 7c**). Through this technique it is possible to produce most types of NPs, including inorganic, polymeric, metallic and nanocomposites. It is a very convenient technique since it allows to obtain NPs in a few minutes, in an economical way, with high purity and ultra-fine control on the dimensions. It has yet to be adapted to mass production and one of the few limitations concerns the choice of solvents which is limited[64].

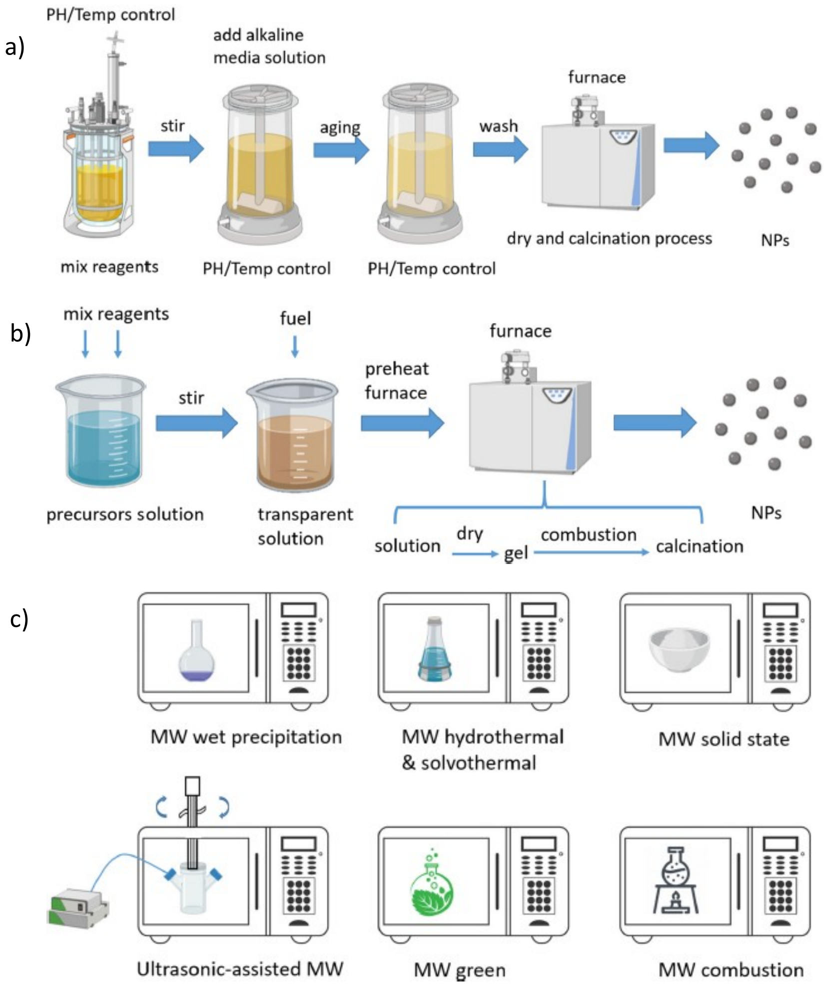

Figure 7. A standard chemical precipitation synthesis method, (b) a mixed sol-gel combustion synthesis method, (c) a standard mw-assisted synthesis method. (Wang et al. 2021)

Most of the RED-CNPs produced by these methods are not soluble in water, and therefore an additional treatment is necessary to cover the surface and create stable aqueous suspensions[65].

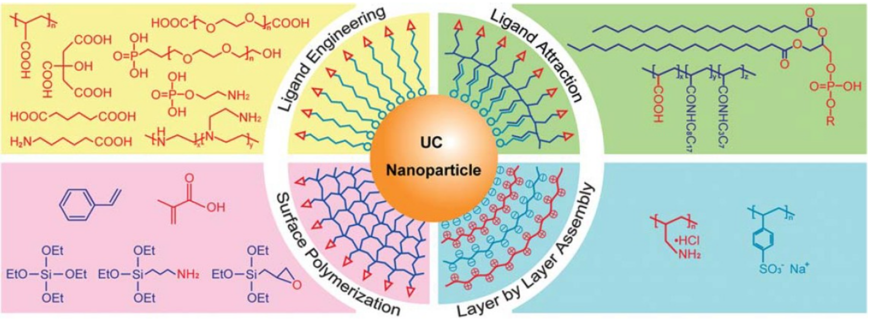

Figure 8. Typical strategies for making hydrophilic UCNPs, from the top to the left, going clockwise: ligand engineering, ligand attraction, layer-by-layer assembly, surface polymerization (Wang et al. 2010)

Figure 8 provides a summary of the most common strategies for surface modification of RED-CNPs, also called Upconversion NPs (UCNPs):

- ligand Engineering is a technique that consists in replacing the surface hydrophobic bonds with hydrophilic bonds through an engineering of the surface binders;
- ligand Attraction involves the adsorption of an additional polymer on the surface of the nanoparticles, if one is already present after synthesis, through the attraction of Van Der Waals;
- layer by Layer Assembly and related to the electrostatic absorption of charged ions alternately on the surface of the NPs;
- surface Polymerization generates the growth of a polymer shell on the NPs core by condensation of small monomers.

1.2.9 AIM AND PERSPECTIVES

The obtainment of naked and pegylated Er: Y_2O_3 and Nd: Y_2O_3 nanoparticles, through the optimization of the procedures reported in the literature with the aim of obtaining ceramic nanophosphors with dimensions in the range of a few nanometers with good crystallinity characteristics and with good upconversion properties that are maintained even after their functionalization, which is the goal more challenging in this research field. This step, in fact, constitutes the starting point for further functionalization with specific antibodies capable of recognizing the proteins present on the surface of the EVs.

In fact, in addition to bioimaging, the use of upconversion nanoparticles could be strategic for the early diagnosis of various diseases, for example through the targeting and quantification of exosomes, a class of small membrane-bound extracellular vesicles (EVs) that are produced. in the endosomal compartment of most eukaryotic cells[66]. Extracellular vesicles have the ability to exchange biological material (e.g. nucleic acids, lipids, proteins, etc.) between cells and to act as signaling vehicles in normal cellular physiological processes or as a consequence of pathological developments. The number and burden of EVs may vary according to physiological or pathological conditions; for example, in the presence of oncological pathologies, the number of EVs present in biological fluids increases and their content appears altered with the presence of differentially expressed molecules (DE) (mainly RNA and proteins) which could be diagnostic or prognostic biomarkers of disease[67–69]. Obviously, to obtain the selective targeting of small extracellular vesicles, such as exosomes, whose dimensions are typically 30-150 nm in diameter, obtaining small rare earth doped yttrium oxide nanoparticles is strategic.

1.3 LUMINESCENT GOLD NANOCLUSTERS

1.3.1 BACKGROUND

Cancer remains one of the most devastating diseases in the world with more than 10 million new cases every year. The rate of growth of the tumor masses is impressive, as tumor cells replicate much faster than healthy cells; hence the need for therapies effective enough to be able to counteract the speed of development of cancer cells, limiting the destruction of healthy tissues as much as possible. The therapies currently used to treat it are usually intrusive processes with many side effects: chemotherapy to shrink the tumor, followed by surgery to remove it when possible, and further sessions of chemotherapy and radiotherapy.

Over the past 25 years, a lot of research has been conducted that has allowed for greater efficacy of therapies, but these improvements are still not enough. Current research focuses on creating vectors to deliver the drug directly to the place of interest (drug delivery), looking for new targets to attack (for example the blood vessels that feed tumor growth) and trying to improve current therapies by making them more targeted and selective. The aim of these studies is to increase the quality and life expectancy of patients[70].

In recent years, the possibility of using nanoparticles (NPs) to improve existing therapies has been explored. Thanks to the possibility of choosing the surface ligands of these particles, it is possible to use recognition ligands that bind to tumor cells in a preferential way, and at the same time add fluorophores that make imaging and diagnostics possible.
In application to drug delivery, this method allows to transport chemopharmaceuticals or radiopharmaceuticals on the surface of the NPs and allowing their delivery directly to the tumor area in a preferential way.

One of the methods conventionally used for the treatment of cancer is chemotherapy.
Conventional chemotherapeutic agents are distributed in a non-specific way in the body, and therefore damage both cancer cells and healthy ones: this on the one hand limits the dose received by cancer cells and on the other makes the treatment excessively toxic for the body.
Through the nanoparticles it is therefore possible to increase the specificity of the treatments and allow the drug to enter directly into the cell to increase efficacy: the NPs, by binding to the cell through specific receptors, are able to bypass the recognition of the P-glycoprotein (one of the main defense mechanisms) and usually enter the cell via endocytosis[71].

The other widely used method of cancer therapy is radiotherapy, which is used on about 50% of patients. Similarly to chemotherapy, one of the main problems of this technique is non-specificity, as the beams are able to kill cancer cells but also healthy ones. It is therefore extremely important, through an improved imaging technique, to precisely delineate the volume of the tumor mass and adjust the radiation dose administered to the patient.

A cutting-edge technique concerns the use of radiosensitizers which is able to increase the effectiveness of radiotherapy by increasing the damage to the cell. The most common radiosensitizers are of the chemotherapeutic type and have the purpose of reducing the resistance of cancer cells, preventing, for example, the formation of the blood phases that nourish them.
An innovative role of radiosensitizers has been played in recent years by NPs, even if still only at an experimental level. The principle of operation is based on the ability of the metal to absorb, diffuse and re-emit the incident radiation through X-rays, photoelectrons, Compton electrons and Auger electrons, causing radiochemical damage (free radicals and ionization). Thanks to the recognition ligands, the NPs are located mainly on the surface or inside the tumor cells, thus allowing the exaltation of the radiation (even by 200%) precisely in correspondence with the place of accumulation of these NPs and therefore in the tumor so preferential. This is due to the fact that elements with a high atomic number (Z) have a higher energy absorption coefficient than soft tissues. Among these emerging radiosensitizers, gold nanoparticles (Au NPs) are particularly attractive due to their strong interaction with radiation ($Z_{Au} = 79$), good biocompatibility of gold and excellent chemical stability.

However, most Au NPs are typically larger than 50 nm, which causes them to be absorbed and trapped by the reticulo-endothelial system (RES) and accumulate in the liver and spleen. Reducing the size of Au NPs (<20nm) would avoid this problem as they could easily escape from the RES. However, to be expelled from the renal system, the size must be even smaller (<5.5nm). If the particles cannot be disposed of via the kidneys, they build up in the body, which makes them toxic in the long term.

The solution to solve this accumulation problem could therefore be the use of Au NP with nucleus dimensions lower than 2 nm (Au Nanoclusters, Au NCs) in combination with ligands such as glutathione (GSH) which guarantees excellent biocompatibility and a small hydrodynamic diameter (HD). Furthermore, it has also been shown that by decreasing the size, the effectiveness of radiosensitization increases[3,73].

1.3.2 MEDICAL APPLICATIONS OF NANOCLUSTERS

In recent years there has been a growing interest in the synthesis and application of fluorescent gold nanoclusters (AuNCs) with nucleus dimensions <2 nm: these are small aggregates of gold atoms that represent a middle ground between molecules and nanoparticles. Due to their excellent biocompatibility, fluorescence properties with good photostability, and very small size, AuNCs have found significant applications in biosensing, bioimaging and cancer therapy. The efficacy of GSH-AuNCs as radiosensitizers has already been demonstrated [3] : they are able to enhance the effect of radiotherapy, escape the endoplasmic reticulum and subsequently be expelled from the body via the kidneys.

As can be seen in **Figure 9a**, the NCs are able to increase the efficiency of the radiation by decreasing the tumor volume by 66% compared to the group treated with radiation alone[72].

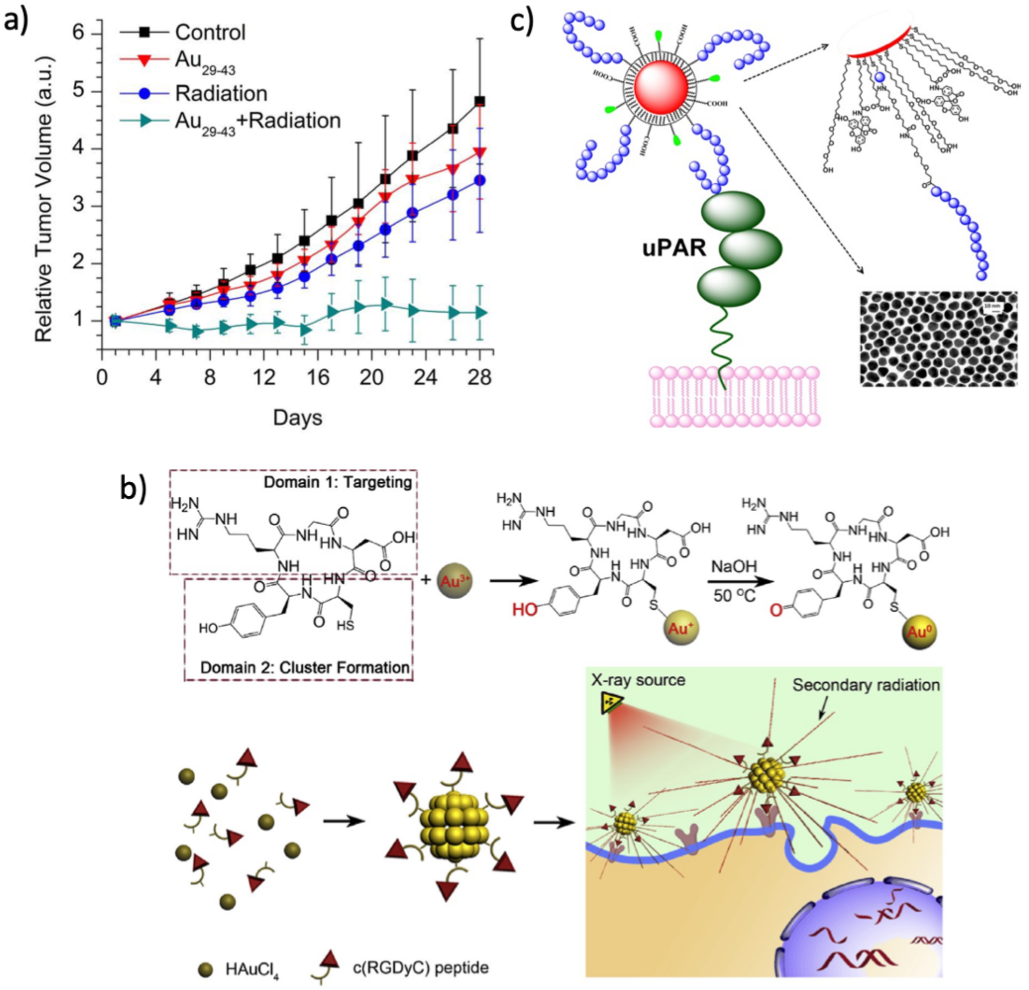

FIGURE 9. a) Tumor volume as a function of time following various radiotherapy treatments in the presence and absence of Au$_{29-43}$ GSH$_{27-37}$ NCs at a concentration of 5.9 mg-Au / kg body weight. (Zhang et al. - 2015) b) Schematic illustration of c (RGDyC) -AuNCs formation and application for advanced radiotherapy. (Liang et al. - 2017) c) Schematic representation of fluorescent NPs functionalized with U$_{11}$ peptide. (Avvakumova et al. - 2014)

However, these NCs do not have a recognition system for cancer cells, and therefore a ligand is needed that allows specific targeting of cancer cells. A number of peptide-based ligands have been described in the literature for targeting cancer cells. Since the uPAR receptor was found to be over-expressed on a variety of cancer cells and tissues (including breast, lung, pancreas, liver, and stomach), it was thought to use ligands that would recognize it for targeting. One of the most important examples of the peptide family concerns arginine glycine-aspartate (RGD): the peptide has only five amino acid residues (**Figure 9b**), but simultaneously plays the role of reducing agent in synthesis, stabilizing and targeting since it binds to the uPAR receptor[73].

Another uPAR targeting ligand used is the U_{11} peptide (**Figure 9c**). The efficiency of its targeting role has already been tested on NPs [5] and in this report its use as a recognition ligand on AuNCs synthesized during the stage will be presented.

1.3.3 TOXICITY STUDIES ON NANOCLUSTERS

Gold nanoparticles (NPs) have given excellent results in the diagnosis and therapy of cancer, but due to their large size they cannot be disposed of by the body and this makes them toxic in the long term; on the contrary, gold nanoclusters (NCs), thanks to their very small size (<2nm), are able to be disposed of much more easily. To evaluate more precisely the toxicity of NCs, in vivo studies have been made for renal disposal, biodistribution and damage to the organism (through blood tests).

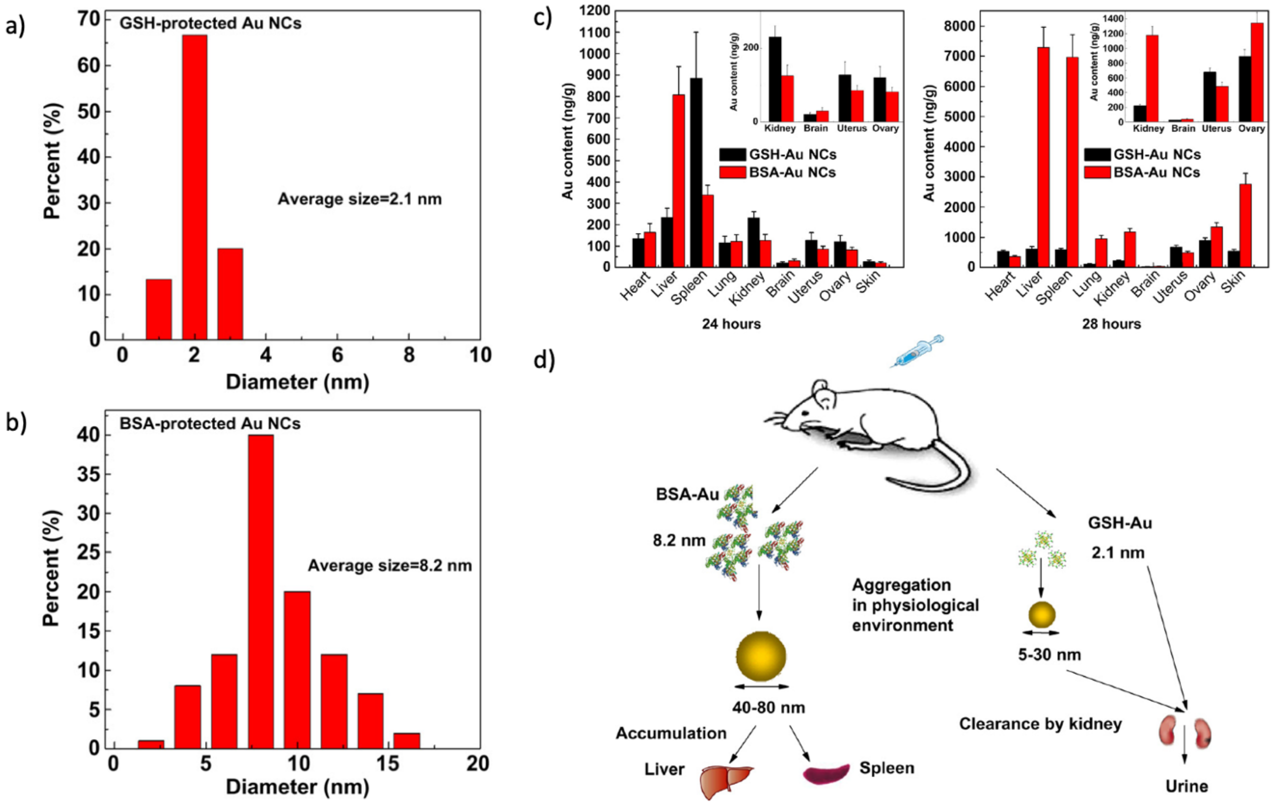

FIGURE 10. Histogram on Au$_{25}$NCs sizes protected by a) GSH and b) BSA. c) Biodistribution on treated mice of Au$_{25}$ NCs protected by GSH and BSA after 24 hours and 48 hours. d) Scheme of the biodistribution and renal evacuation of Au$_{25}$ NCs protected by GSH and BSA. (Zhang et al. - 2012)

The toxicity of NCs protected by BSA and GSH was studied and compared by measuring after 24 hours and 28 days. In **Figure 10 a,b** the size distribution of the two types of NCs is compared before coming into contact with the blood plasma. The results show that the NCs, once in contact with the blood, aggregate forming larger particles, which are more difficult to dispose of. This process is visible by studying the absorbance spectrum of the NCs which, having come into contact with the blood, show the absorption of surface plasmon, typical of NPs but absent in NCs. This aggregation process is visible in both types of NCs. After 24 hours, the GSH NCs reach sizes between 5 and 30 nm, while the dimensions of the BSA-NCs are around 40-80 nm. After 24 hours, 36% of GSH NCs are excreted from the body via urine, as opposed to 1% of BSA NCs. After 28 days 94 % of the GSH NCs and only 5% of the BSA-NCs are expelled. Both types of NCs cause acute infection, inflammation and damage to the renal system after 24 hours, but all normal functions are recovered after 28 days for GSH NCs, as opposed to BSA NCs which show irreparable signs of toxicity. This conclusion was also verified by standard hematological marker analyzes. The difference in biodistribution (**Figure 10c**) between mice treated with GSH NCs and BSA NCs demonstrates that the surface chemistry of AuNCs plays a very important role in biodistribution and toxicity. The results obtained respect the expectations related to the size of the NCs: the GSH NCs have reduced dimensions and can therefore be disposed more easily via the kidney and significantly reducing their toxicity (**Figure 10c**) [6] .

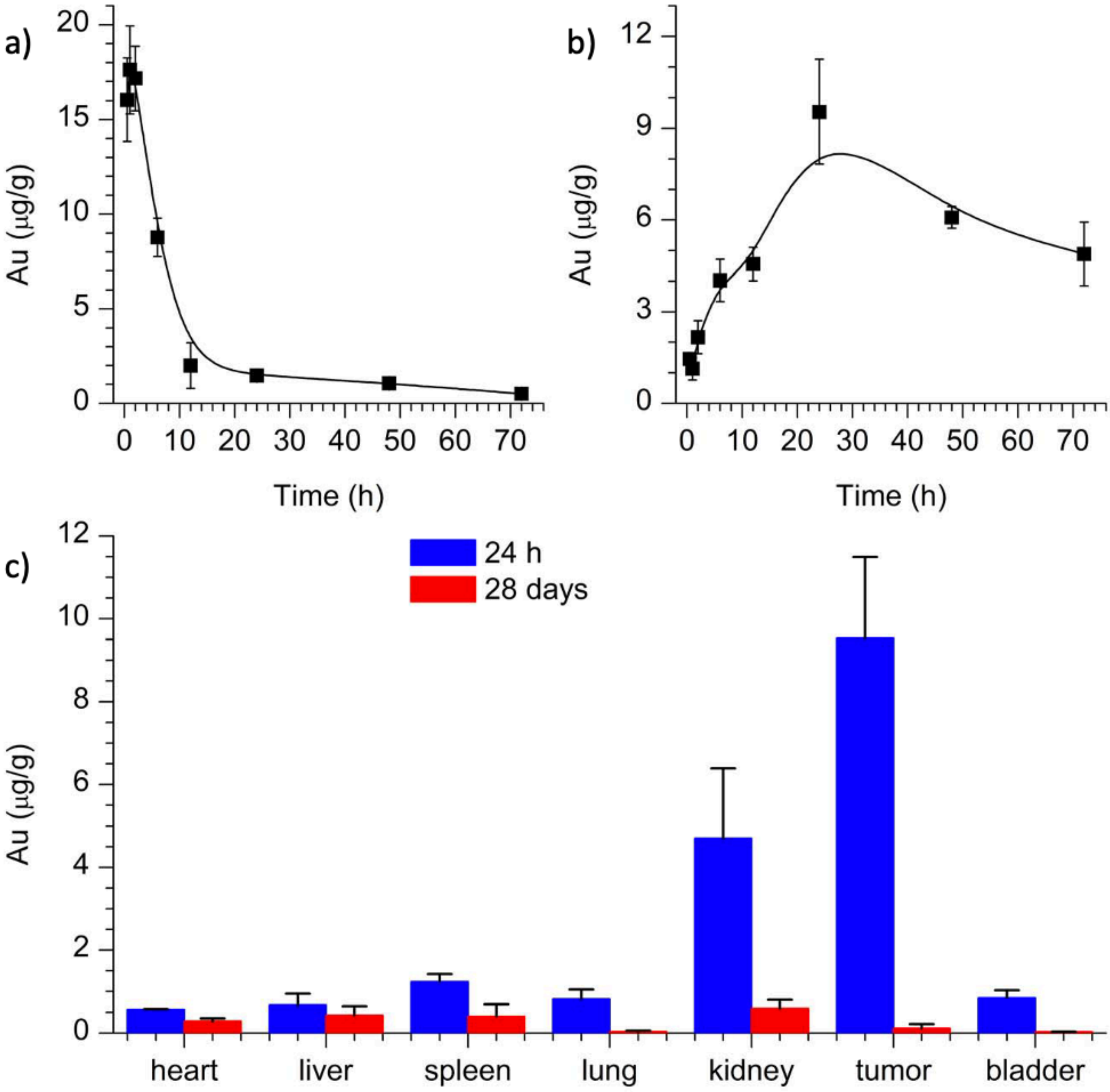

FIGURE 11. a) Concentration versus time of GSH-NCs Au_{29-43} in blood after injection in vivo. (b) Tumor uptake of GSH-NCs Au_{29-43} at different time after injection. (c) Biodistribution of GSH-NCs Au_{29-43} after 24 h and 28 days from the injection (Zhang et al. - 2015).

Focusing on the GSH NCs that seem to give the best results, studies have been done on the residence time of the NCs in the blood and on their biodistribution in the presence of a tumor. After about 12 hours from the injection, the concentration in the blood drastically decreases, stabilizing (**Figure 11a**) and after 24 hours the maximum concentration of NCs inside the tumor is observed (**Figure 11b**). After 24 hours, in fact, most of the NCs are no longer found in the blood but inside the tumor or in the kidneys from where they are then expelled; after 28 days the concentration of NCs in the blood is almost zero (**Figure 11c**)[72] .

It is therefore important to conduct further studies on the surface chemistry and the ligands choice, to obtain more stable NCs within the blood plasma (preventing their aggregation and decreasing their toxicity), luminescent enough to allow imaging, and equipped with of recognition ligand for specific targeting of tumor cells. All these measures would make NCs ideal candidates for in vivo imaging and cancer therapy.

1.3.4 NANOCLUSTERS FORMATION MECHANISM

Nanoclusters (NCs) are an aggregate of atoms with dimensions <2nm. The very small size (comparable to the wavelength of electrons at the Fermi level) gives rise to a quantum confinement effect that generates electronic levels with discretized energy and new optical properties.

NCs, following quantum confinement, do not have the collective plasmon excitation typical of NPs and exhibit composition and size-dependent fluorescence properties. These new optical properties mean that NCs can compete with QDs and fluorescent proteins in use as fluorescent imaging probes. The small size gives the NCs properties very similar to those of a molecule: in fact, there are characteristic molecular electronic bands HOMO and LUMO with quantized optical absorption reminiscent of semiconductors[7,76].

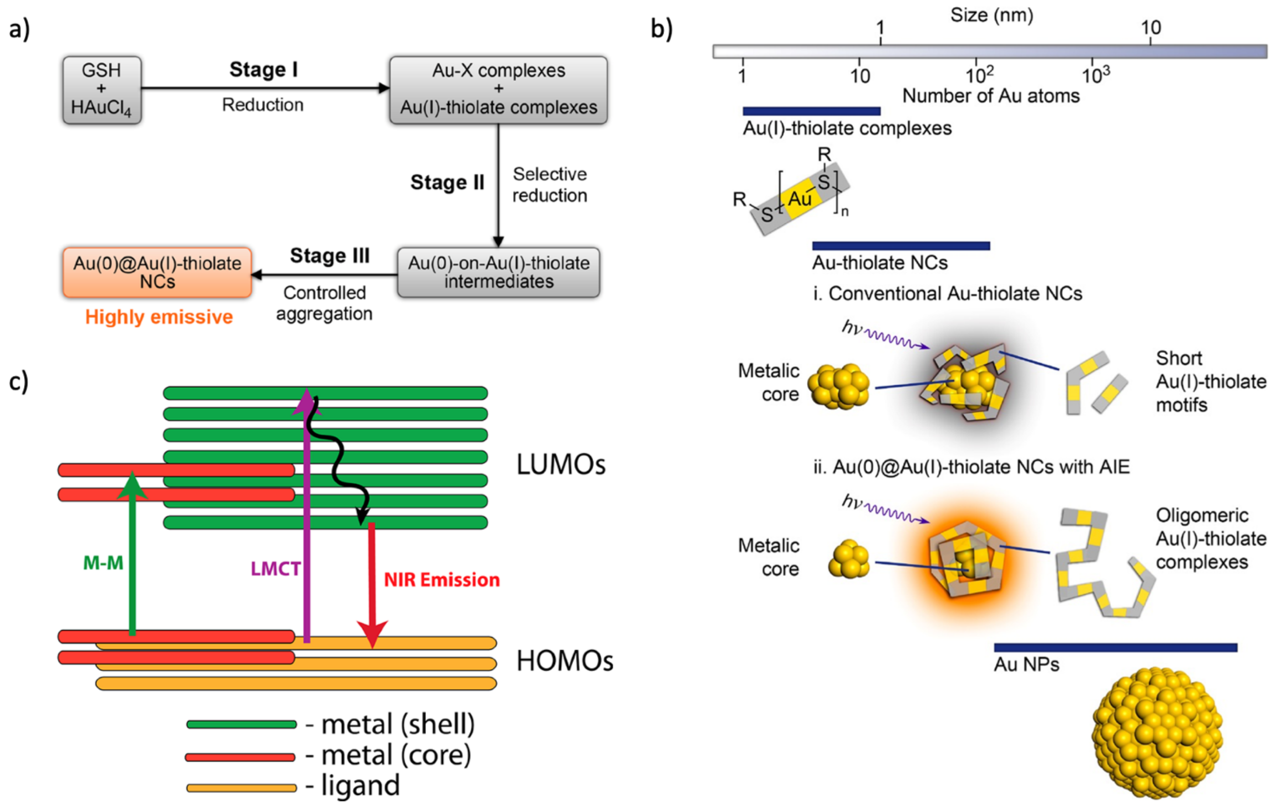

FIGURE 12. a) Synthesis scheme of high luminescence Au (0) @Au (I) NCs. (Luo et al. - 2012) b) Schematic illustration of luminescent AuNCs structures. (Luo et al. - 2012) c) Energy level diagram of AuGSH NCs. (Stamplecoskie et Kamat - 2014)

The chemical formula of NCs with metal core protected by ligands can be described as $M_n L_m$, where M and L refer to the type of metal and protective ligand, while n and m are the number of metal atoms and protective ligands respectively (e.g.$Au_{25}(SG)_{18}$). The most commonly used ligands include molecules, peptides, dendrimers, proteins, DNA and polymers. Each ligand has different structures and affinities with the metal, and this affects the final size, optical properties and solution stability of the NCs. Among the various ligands, the most similar to metals are those that have thiol groups[75]. At the moment the most used ligand for the production of NCs is the GSH peptide which gives the NCs a good stability and solubility in water thanks to the electrostatic and steric stabilization effects.

The aim of the synthesis is to produce highly fluorescent NCs by condensing Au(I)-thiolate complexes on an Au (0) nucleus to form a compact shell.

The process of aggregation of Au(I)-thiolate complexes is important since the oligomeric complexes of Au (I) are not luminescent, but following the aggregation a strong luminescence (aggregation induced emission, AIE) is generated. The first step in the synthesis of GSH-NCs concerns the reduction of Au (III) to Au (I) by the thiol group of GSH which at the same time binds to A (I), to form Au (I) -thiolate complexes: the thiol group performs the function of reducer and ligand at the same time. Similarly, other Au (I) –X complexes are also formed, where X represents any non-thiolated ligand, such as the carboxyl group of GSH. The second stage concerns the selective reduction of these Au (I) -X complexes into Au (0) atoms. The third stage involves the aggregation of Au (0) atoms into an Au (0) nucleus covered by a shell of Au (I) -thiolate complexes (**Figure 12 a,b**)[77].

1.3.5 FLUORESCENCE PROPERTIES OF NANOCLUSTERS

Valence electrons in AuNCs cannot move freely on the surface and, consequently, the continuous energy band typical of large nanoparticles is not present. However, AuNCs have visible (VIS) to near-infrared (NIR) fluorescence that can be adjusted simply by changing the number of Au atoms.

Various mechanisms have been proposed to explain the luminescence mechanism of Au nanoclusters. Fluorescence could arise from the metallic nucleus (as it manifests quantization effects due to the confinement of atoms in the nucleus) and from the surface of the particle (following the interaction between the metallic nucleus and surface ligands). Various studies have shown that the role of electronic transitions between HOMO-LUMO energy levels (**Figure 12c**), following the electron transfer between the shell and the nucleus, could be the predominant mechanism that gives rise to fluorescence in NCs[10,11,79].

Different strategies can be employed to enhance the fluorescence of NCs. Since the electron transfer between the ligands and the nucleus is probably the main mechanism that generates the fluorescence, one strategy is to improve this transfer, for example by using good ligands with high affinity for the metal (such as the S-Au bond of the thiol group). Furthermore, it has been shown that using ligands with atoms (eg. N, O) and groups (eg. COOH, NH2) rich in electrons, further increases this electron transfer and consequently increases the fluorescence of the NCs[79].

Another strategy is to minimize non-radiative emissions which can decrease fluorescence emission. Aggregation and stiffening limit the freedom of movement of the complexes (intramolecular vibrations and rotations) thus decreasing the possibility of non-radiative relaxation in favor of radiative emission (luminescence emission). This explains the appearance of luminescence following the aggregation of the non-fluorescent Au (I) -thiolate oligomeric complexes. [77]

Experiments in the laboratory have also shown that by stiffening the ligand shell around the nucleus (by adding an additional rigid polymeric shell or by freezing the solution), the fluorescence is enhanced[80].

1.3.6 NANOCLUSTERS SYNTHETICS APPROACHES

The NCs of noble metals are prepared with proteins, peptides or small organic molecules that increase their biocompatibility and allow to easily modify their surface properties for specific applications.

The most common chemical approach for the synthesis of NCs involves the use of protein templates: examples of proteins are bovine serum albumin[10] (BSA) and pepsin. With regard to pepsin, it has also been shown that by varying the pH of the solution it is possible to create NCs of different sizes with fluorescence in blue (Au$_5$ and Au$_8$), green (Au$_{13}$) and red (Au$_{25}$) (Figure 13)[81].

Another method for the synthesis of AuNCs is the use of peptides[11,10]. The length and type of peptide influences the physicochemical properties of the synthesized NCs. Glutathione (GSH) is the most used peptide for the synthesis of AuNCs.

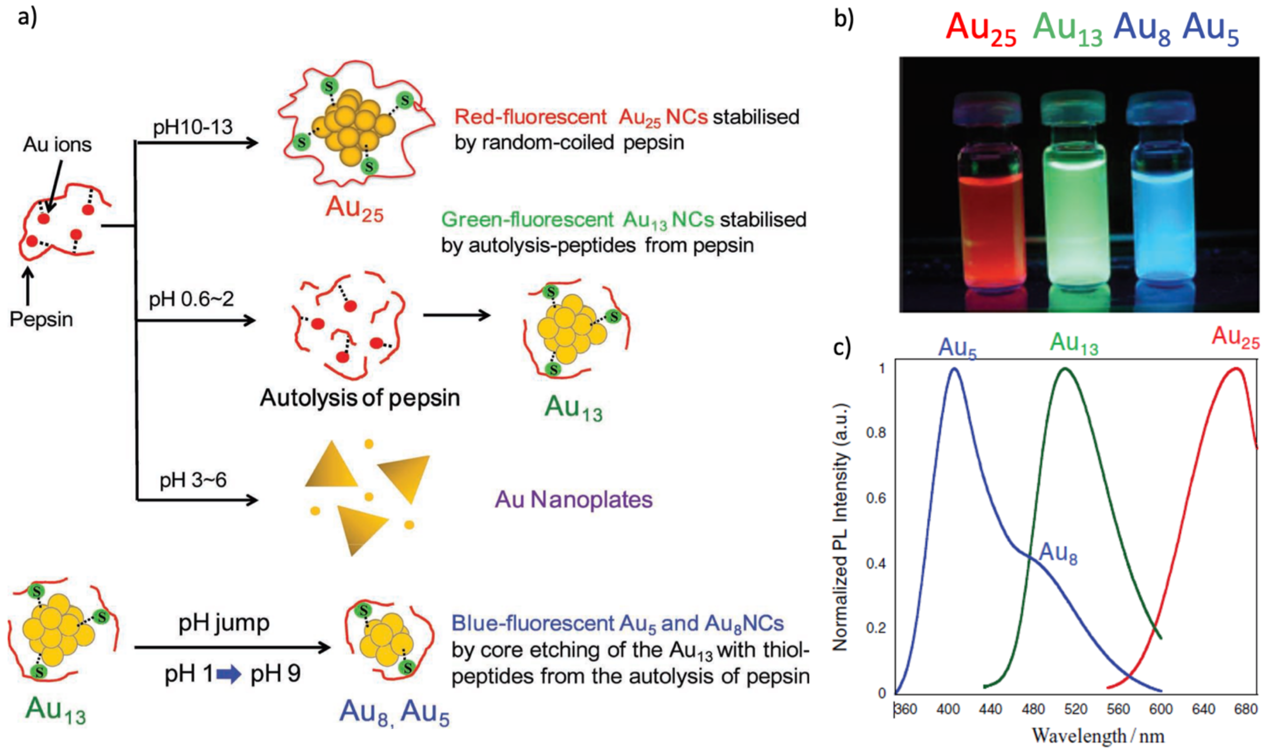

FIGURE 13. a) Schematic illustration of PH-dependent synthesis of pepsin-mediated AuNCs with fluorescent blue, green and red emission. b) Pepsin-coated AuNCs samples with red, green and blue emission and corresponding normalized luminescence emission spectra under UV excitation. (Kawasaki et al. - 2011)

1.3.7 ROLE OF SURFACE LIGANDS

The surface chemical structure of the NCs and therefore the ligands found on its surface, are of fundamental importance because they influence the synthesis, the physicochemical properties and any catalytic applications (**Figure 14**).

During synthesis the type of ligand influences the speed of the formation process and the size of the NC. It is possible to change the surface ligand even at finished synthesis through a ligand exchange, so as to be able to control the fluorescent properties and stability in solutions of the NCs or for any applications, such as biological interactions for the search for specific active sites.

Recently we are beginning to explore the possibility of combining different types of ligands on the same cluster in order to exploit their different functionalities at the same time[82].

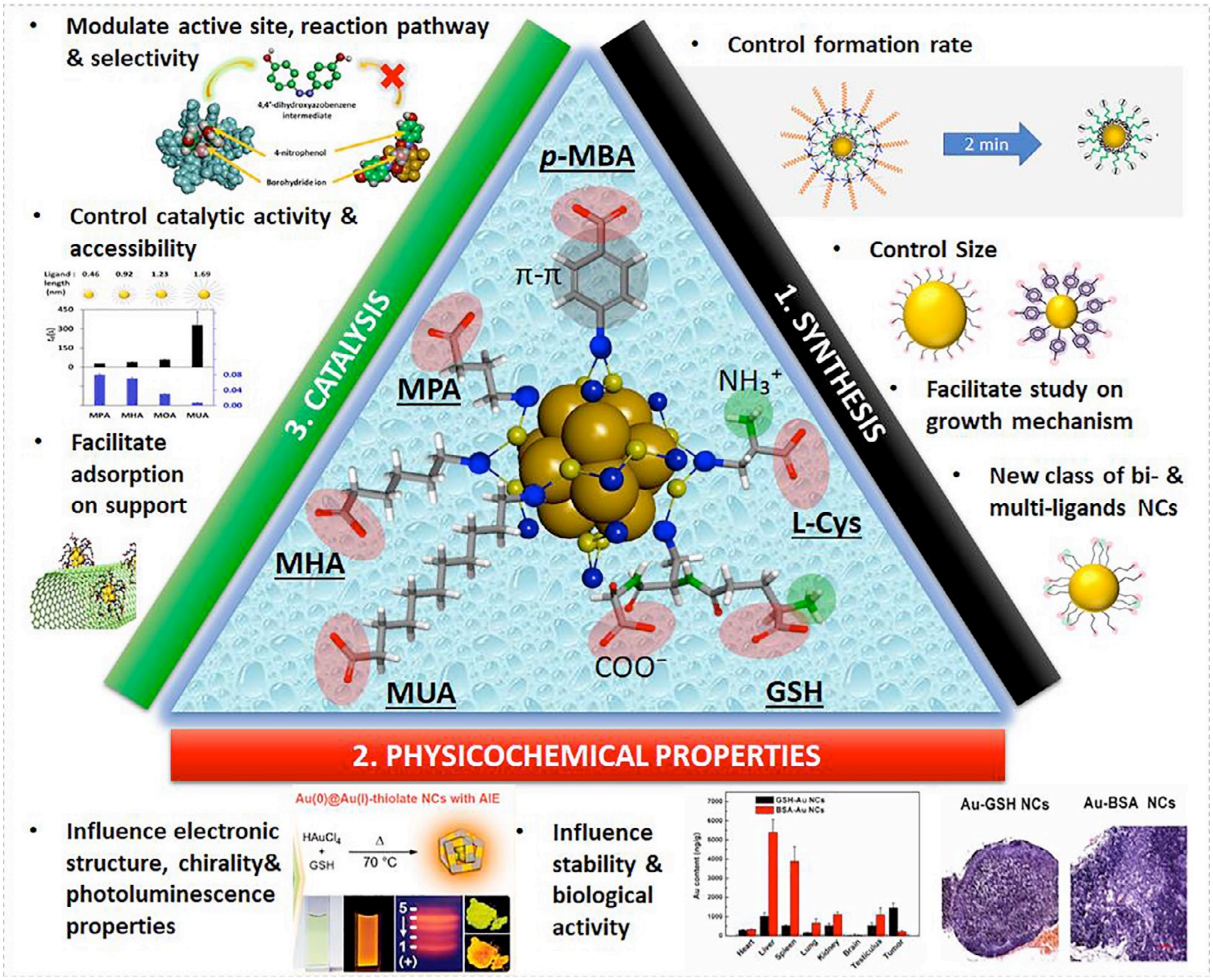

FIGURE 14. Ligands Roles on the synthesis, physicochemical and catalytic properties of water-soluble AuNCs protected by hydrophilic thiolate ligands. (Nasaruddin et al. - 2018)

1.3.8 NANOCLUSTER INTERACTION WITH LIPID MEMBRANES

An essential aspect to be explored for the diagnostic and therapeutic use of NCs is their interaction with biological membranes. Two important parameters to be taken into consideration during the interactions are the surface charge and the dimensions in the NCs: as these parameters vary, the interactions will give rise to different scenarios. Most of the information we have on these mechanisms refers to NPs, while further studies must be conducted to elucidate the mechanism of interaction with NCs.

The influence of the surface charge of NPs has been studied and summarized in **Figure 15**. NPs with a negative surface charge have a lot of difficulty in reaching the cell membrane, since it too has a negative potential. If the charge is slightly positive, the NPs are able to reach the membrane and be internalized by endocytosis. The increase in the surface charge density means that internalization can take place by diffusion without involving the endocytosis mechanism, but too high densities can lead to rupture of the membrane causing serious damage to the cell (high cytotoxicity).
For the therapies, the internalization of NPs is a very important process, it is therefore necessary to find the right surface charge value to favor this process without reaching high cytotoxicity values[83].

The size of the NPs plays a key role in the internalization process. NPs with dimensions greater than 70 nm cannot penetrate inside the cell. When the dimensions are between 20 and 50 nm, the cell has the ability to bend its lipid bilayer in order to incorporate the NPs through the process of endocytosis and let them enter the cell. If the dimensions of the NPs were smaller than 20 nm, the cell wall would spend too much energy in creating areas with high curvature, and consequently the generation of pores is favored that allow the passage of NPs in a passive way, without involving endocytosis[83].

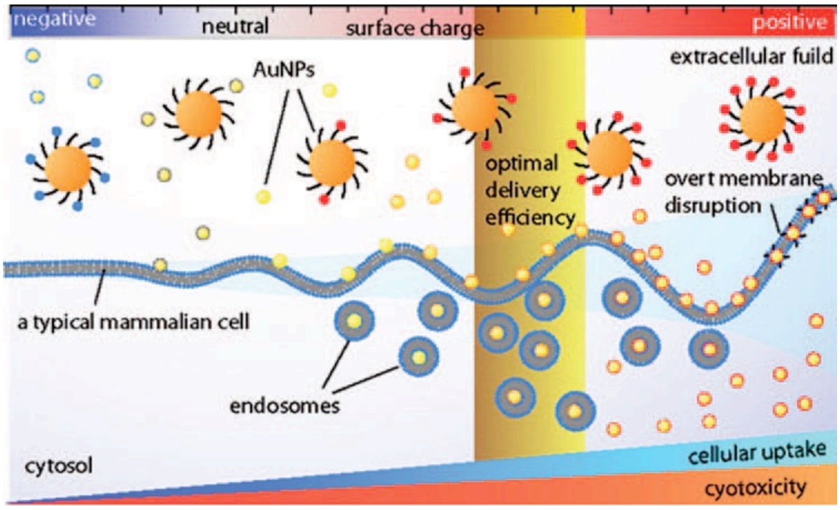

FIGURE 15. Schematic illustration of the internalization and cytotoxicity of AuNPs with different surface charge on mammalian cells. (Riveros et al. - 2013)

NCs would fall into the latter category, but there is still little information about the interaction mechanisms of NCs. Recent studies have investigated the behavior of commercial NCs (Aurora ™) in iterations with membranes[17] . Cryo-TEM observations demonstrate the incorporation of Aurora™ gold NCs into lipid membranes via an increase in contrast due to the positioning of the NCs between the two lipid layers.

We will see later in this manuscript the studies made by our group on the interaction between NCs and biological membranes, still not very detailed in the literature.

2 SYNTHESIS AND CHARACTERISATION OF NANOPARTICLES

2.1 ERBIUM AND NEODYMIUM DOPED YTTRIUM OXIDE NANOPARTICLES

2.1.1 PRESENTATION OF THREE SYNTHETIC APPROACHES

To synthesize Erbium or Neodymium doped Yttrium oxide nanoparticles a basic environment is required:

$Y^{3+} + 3\ OH^{-} \leftrightarrows Y(OH)_3$

Subsequently, through a calcination treatment, the hydroxides give rise to the corresponding oxides:

$2\ Y(OH)_3 \rightarrow Y_2O_3 + 3\ H_2O$

The high temperature treatment of the calcination not only causes the oxides to form, but also improves the crystallinity of the nanoparticles, thereby also improving the luminescence properties.

The most common way to obtain a basic environment for the synthesis of Er or Nd:Y_2O_3 is the addition, in the appropriate ratio, of urea to a solution containing the nitrates of the metal ions.

$$CO(NH_2)_2 + 3H_2O \xrightarrow{\Delta} 2NH_4^+ + HCO_3^- + OH^-$$

Then, the solution is heated above 60°C, in order to decompose the urea for the reaction:

To obtain nanoparticles of inorganic oxides the simplest thing would be to keep the temperature close to 100 ° C during the synthesis, since, despite the formation of precursor hydroxides is very favored due to their high insolubility, their kinetics are rather slow and the simplest way to speed up the process is to turn up the temperature. However, this causes the formation of NPs with dimensions between 30-150 nm, too large for our aim, that is the selective targeting of extracellular vesicles, such as exosomes, of comparable size. For this reason, it was decided to use two types of syntheses at room temperature, to limit the phenomenon of NPs growth due to the high temperatures. In the first procedure used (sample E1), reported in literature,[85] the presence of the urease enzyme causes the urea to decompose without the need of increasing temperature; this synthesis was used in the literature to have a uniform ammonia release in the reaction solution, in order to have a narrow size distribution; for this reason this method is also called homogeneous precipitation method. The second synthesis (sample E2), instead, does not foresee the presence of Urea, but NH_3 concentrated in the reaction solution is added directly at room temperature in this case the ammonia is already available without the need for external energy input. The creation of a supersaturated solution of NH_3 was used to have a high nucleation and small growth of the nuclei, since at room temperature the diffusion process at the base of the growth of NPs nuclei is strongly limited. This would have led to the formation of many small diameter NPs (**Figure 16**). In the opposite case in which it is decided to use a solution in conditions of modest supersaturation, the number of nuclei formed would be small; moreover, by heating, the supersaturation conditions would further decrease, following the increase in solubility, and the growth processes of the nuclei would be favored, thus forming few and large NPs, with results opposite to those desired.

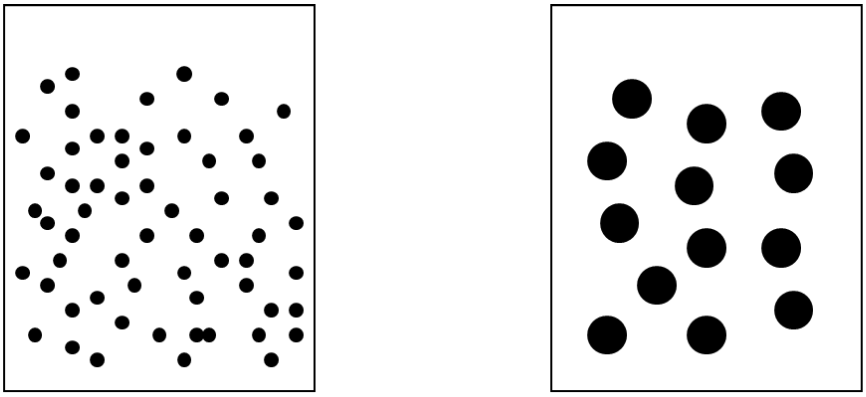

Figure 16. Representation of a) highly and b) mild oversaturated solution giving rise to a precipitate.

Besides Synthesis 1 (sample E1) and Synthesis 2 (sample E2) carried out at room temperature, a third method carried out at 80 °C in the presence of polyacrylic acid (PAAc) was used (Synthesis 3, sample E3) to synthesize Er:Y_2O_3 NPs.

2.1.2 MORPHOLOGICAL CHARACTERIZATION

The concerning yields of reaction for the three synthesis and the SEM images are reported in **Table 1** and in **Figure 17**, respectively. The images clearly show that all the syntheses generate NPs with dimensions of the order of a few tens of nanometers, therefore of the expected dimensions. However, neither Synthesis 1) nor Synthesis 2) gave satisfactory results. In fact, despite having obtained precipitates with small particles, in the first case the yield was very low (**Table 1**) and in both cases the reaction times were extremely long (1-2 weeks). Probably, the experimental precipitation times actually observed could be due to the fact that in Synthesis 1 the decomposition rate of the enzyme is different from that expected, generating a concentration of ammonia in solution much lower than that expected. In Synthesis 2, probably, the observed times are due to the fact that, since ammonia is a gas, it moves away from the solution, failing to guarantee the necessary supersaturation.

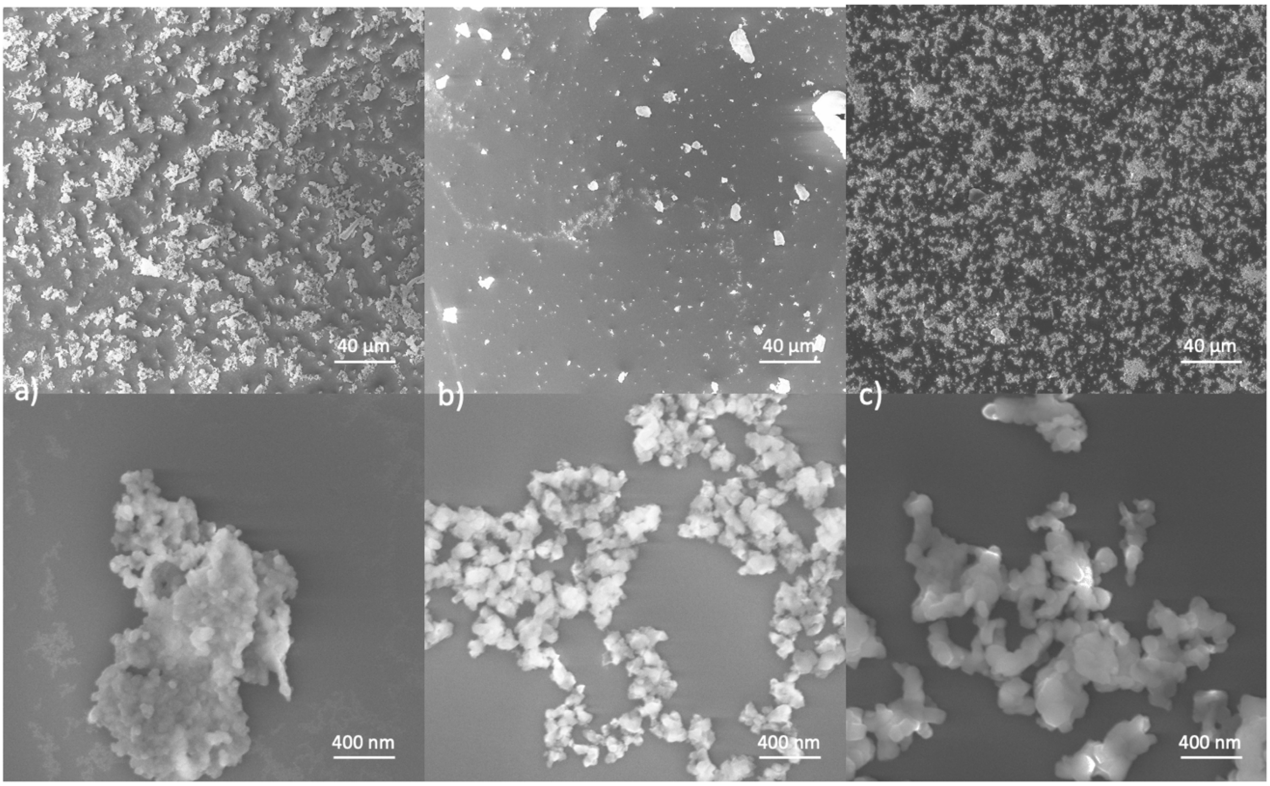

Figure 17. SEM images at different magnification of Er:Y_2O_3 NPs a) sample E1, b) sample E2 and c) sample E3

On the other hand, Synthesis 3), carried out using the PAAc as a template, as reported in literature[86], gave rise to a good yield in a very short time. The use of both natural and synthetic polymers to direct a synthetic path is a well-recognized procedure for obtaining nanoparticles[87–93]. In our case in particular, the presence of poly (acrylic acid) influences both the nucleation process and the subsequent growth phase of the nanoparticles, allowing to obtain particles of regular and monodisperse shape. The reason is due to the COOH side chain which deprotonates (COO-) at pH>5. Therefore, in aqueous media of appropriate pH and ionic strength, the carboxyl groups ionize and develop fixed charges on the polymeric network that, surrounding the nanoparticles, acts as a capping agent, generating electrostatic repulsive forces that limit the uncontrolled growth of the nanoparticles themselves. Furthermore, PAAc is a biodegradable polymer and is effectively removed through subsequent heat treatments. Since this synthesis gave excellent results for the obtainment of Er-doped nanoparticles, it was decided to carry out in the same way the synthesis of the analogous system doped with Nd, obtaining the N1 sample. Also in this case, the SEM images show very small NPs of the order of tens of nm (**Figure 18**).

	Calculated	Obtained	Yield
E1	0.2703 g	0.0157 g	5.6%
E2	0.2703 g	0.1006 g	37.0%
E3	0.2703 g	0.0637 g	23.6%
N1	0.2703 g	0.1152 g	42.6%

Table 1. Obtained yields for the different synthetic procedures.

Since in all cases the NPs are highly aggregated, to better evaluate their size, shape and degree of crystallinity, the samples obtained with procedure 3 (E3 and N1), the ones that gave the best results, were analyzed by a High Resolution Transmission Electron Microscopy (HR TEM) and the concerning images are reported in **Figure 19a-d**. Through the TEM images it is also possible to notice that the particles of erbium (E3) and those of neodymium (N1) appear crystalline and of similar dimensions, since there is the presence of bright spots on the diffraction pattern (**Figure 19b,d**), which correspond to precise distances of the crystalline lattice. Furthermore, the presence of many bright spots on the same circumference indicates either the presence of a polycrystalline sample or a high quantity of crystalline NPs differently oriented. Through the HR-TEM images it is also possible to see the crystallographic structure inside the nanoparticle and it will be shown that these are crystalline particles oriented in a different way.

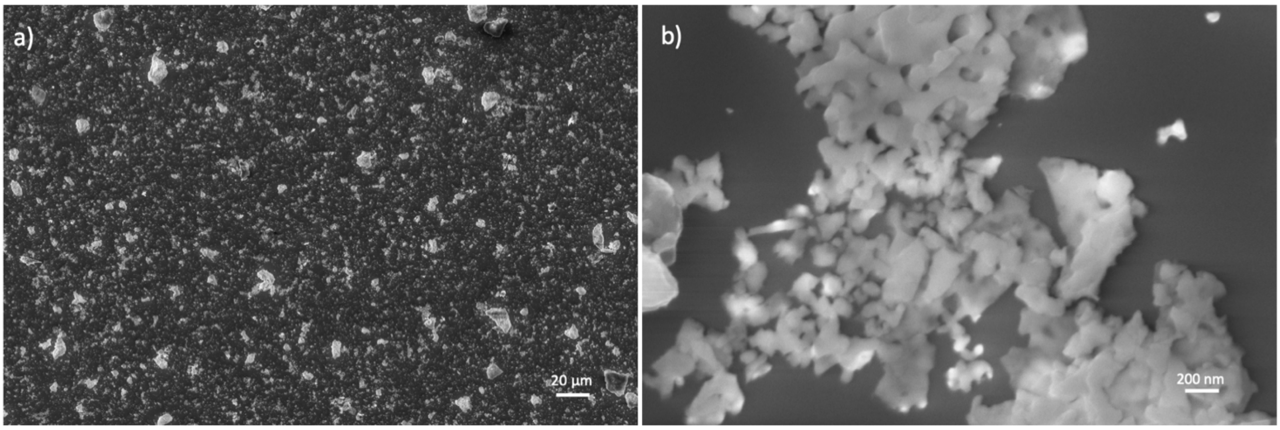

Figure 18. SEM images at different magnification, of Nd:Y_2O_3 NPs sample N1.

To evaluate the crystalline quality, in addition to the diffraction image obtained at HR-TEM, Raman spectroscopy was used which, in addition to offering a fingerprint linked to the elements present and to the crystallographic structure, gives a further insight of the sample crystallinity. **Figure 19**e shows the normalized Raman spectra carried out on samples E1, E2 and E3. All spectra were normalized to the highest peak, which is the one at 682 cm^{-1}. The peaks are almost coincident for all the samples indicating that the composition and crystallographic structure of the matrix (host) is similar whatever it is the synthetic procedure used; however, the peaks of the E2 and E3 samples are quite narrow while the peaks of the E1 sample are wider, indicating that the crystalline quality of the matrix for this last sample is worse than the other two. Furthermore, comparing the experimental spectra with those reported in the literature by Osimov et al.[94], the peak present at 400 cm^{-1} can be associated with the internal vibrations of cubic elementary cells, YO_6 , thus demonstrating that the crystalline phase of the three samples is cubic (**Figure 19f)**.

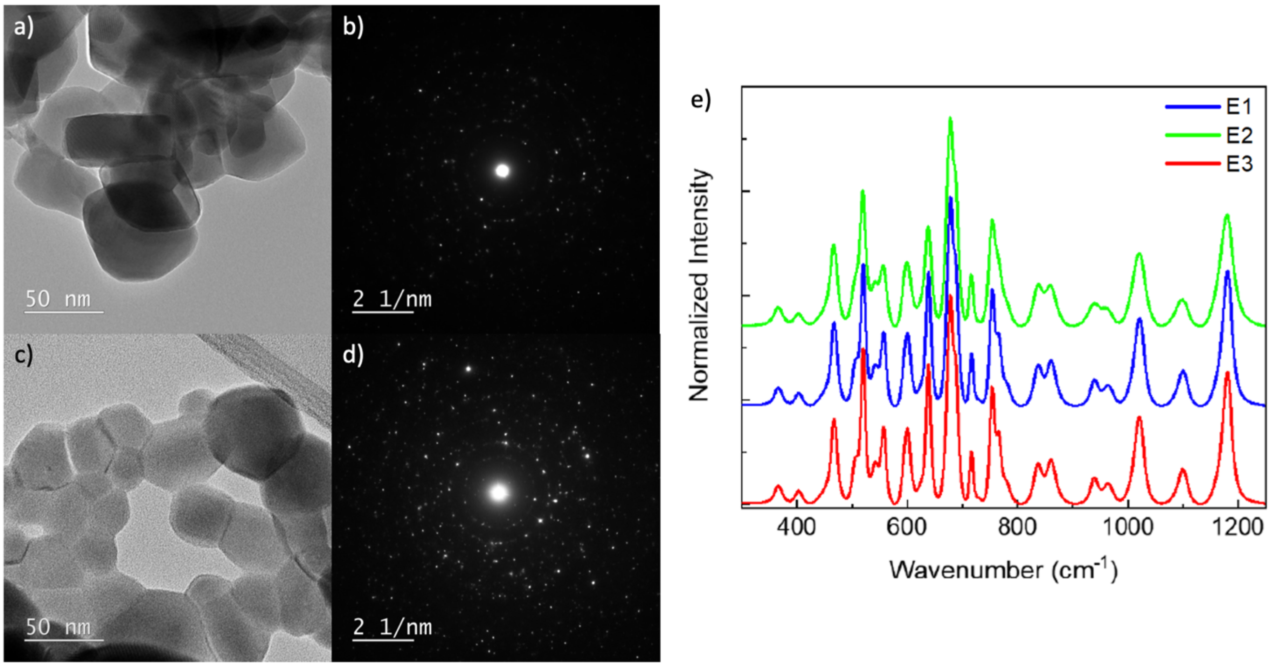

Figure 19. TEM micrographs and related diffraction patterns for a) and b) sample E3, and c) and d) sample N1; e) normalized Raman spectra of Er:Y_2O_3 NPs samples E1, E2, E3.

2.1.3 COMPOSITIONAL CHARACTERIZATION

The compositional analysis of the E3 and N1 samples was performed by RBS and EDX techniques. RBS spectra for the NPs doped with erbium and neodymium are reported in **Figure 20a** and **Figure 20b**, respectively. Yttrium, erbium and neodymium peaks have been identified, while the oxygen peak cannot be resolved as the backscatter yield is rather poor for light elements. The background signal at lower energies is related to the silicon wafer on which the samples are deposited to make the measurements.

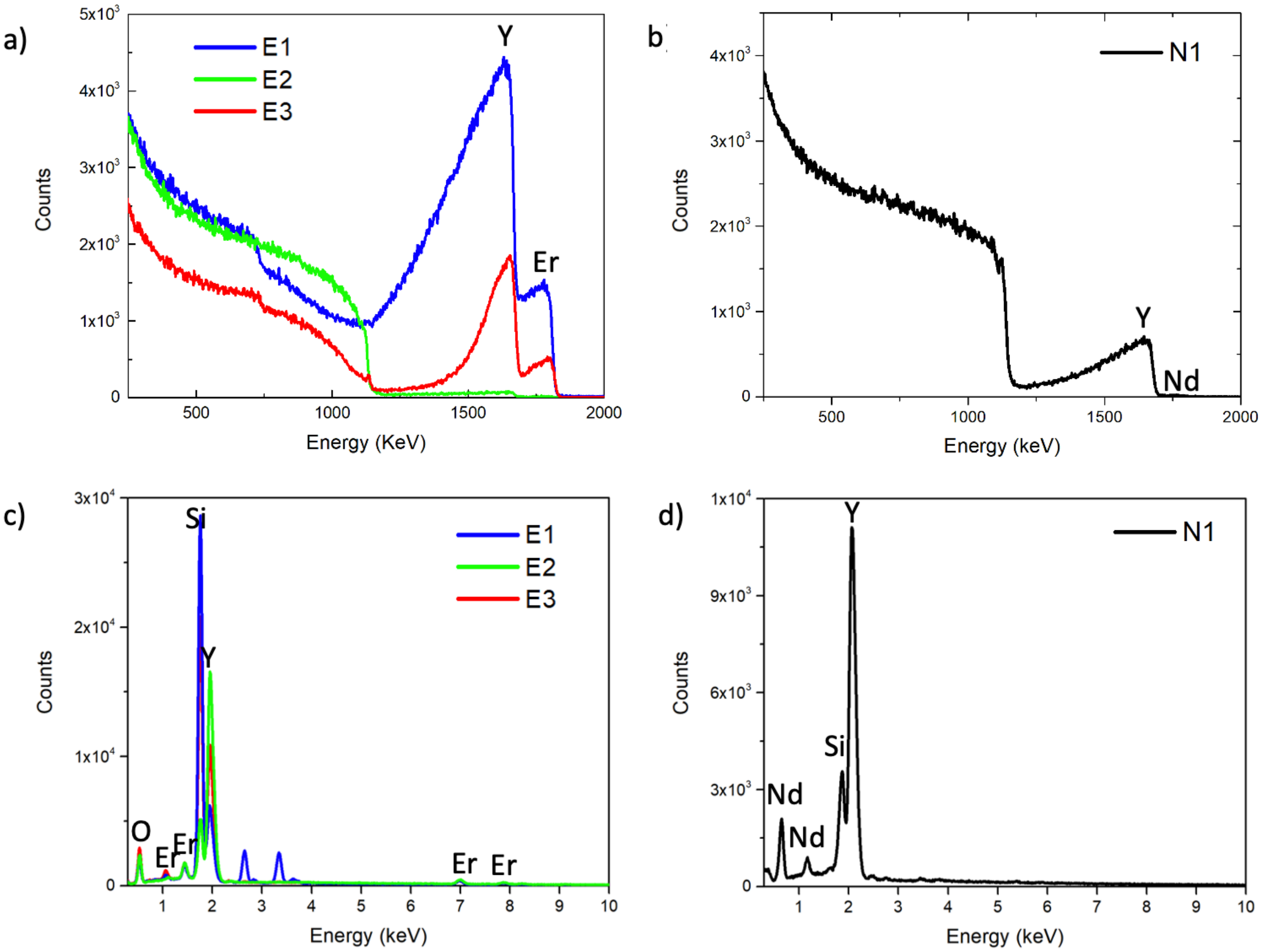

Figure 20. RBS spectra of a) Er:Y_2O_3 NPs samples E1, E2, E3 and b) Nd:Y_2O_3 NPs sample N1. EDX spectra of c) Er:Y_2O_3 NPs samples e1, e2, e3 and d) Nd:Y_2O_3 NPs sample N1.

Since RBS is a technique created for the analysis of thin films, its application to NPs is still largely unexplored, since the presence of NPs aggregation and the consequent formation of non-homogeneous porosity generates density gradients that make difficult the simulation and calculation of the elemental concentration.[95] This non-uniform sample density is easily visible in the spectrum since each peak (in the case of Y, Er or Nd) is not represented by a rectangular shape, as in the case of thin films, but by a triangle. In the case of rectangular shapes, the length of the base is related to the thickness, while the constant height designates a constant density of the film. In the case of NPs, on the other hand, the triangular shape indicates a surface roughness that generates a non-uniform density along the thickness of the NPs film. Therefore, in order to simulate the inhomogeneity of the NPs distributed on the silicon surface, the simulations of the spectra were performed by the simNRA software, modeling the sample as three different layers of Er:Y_2O_3 with decreasing concentrations of yttrium and erbium and where silicon is also present both as a surface element and as a substrate.

The surface concentration values of yttrium and erbium were calculated from this simulation. Since the oxygen peak cannot be detected because it is a too light element, its areal density has been theoretically predicted, considering the stoichiometric ratios of the elements within the sample. The same procedure was also performed with neodymium-doped NPs. Through this technique it is possible to obtain an accuracy of 1% and the values obtained are reported in **Table 2.**

The data in **Table 2** show that, excluding sample E1 which has an Er/Y value approximately double the expected one, samples E2 and E3 have an Er/Y ratio slightly higher than the theoretical one (Er/Y = 0.07); such deviations can therefore fall within the experimental error. In the case of the particles doped with Neodymium, the RBS spectra (**Figure 20b**) simulated with the simNRA program showed a Nd/Y value slightly higher than the expected value (Nd/Y = 0.0075). However, the overall value of the Nd turned out to be slightly lower than expected (0.5%).

RBS				
	Y 10^{15} at/cm^2	Er 10^{15} at/cm^2	Er / (Er+Y)	Er % in NPs
E1	535± 27	70 ± 4	0.12 ± 0.01	4.6 ± 0.3 %
E2	8.0 ± 0.4	0.75 ± 0,04	0.09 ± 0,01	3.4 ± 0.2 %
E3	229 ± 11	22 ± 1	0.09 ± 0.01	3.5 ± 0.2 %
	Y 10^{15} at/cm^2	Nd 10^{15} at/cm^2	Nd/ (Nd+Y)	Nd % in NPs
N1	63 ± 3,14	0.84 ± 0.04	0.010 ± 0.001	0.5 % ± 0.1%
EDX				
	Y (At %)	Er (At %)	Er / (Er+Y)	Er % in NPs
E1	89.50 ± 0.11	10.50 ± 0.71	0.110 ± 0.008	4.2 ± 0.3 %
E2	93.50 ± 0.03	6.50 ± 0.39	0.060 ± 0.003	2.6 ± 0.2%
E3	92.40 ± 0.05	7.60 ± 0.46	0.080 ± 0.005	3.2 ± 0.2%
	Y (At %)	Nd (At %)	Nd / (Nd +Y)	Nd % in NPs
N1	98.60 ± 0.46	1.4 ± 31.28	0.01 ± 0.22	0.6 % ± 13.4 %

Table 2. Elemental concentrations of and Er:Y_2O_3 NPs samples E1, E2, E3 and Nd:Y_2O_3 NPs sample N1 as determined by RBS analysis and EDX analysis.

To further verify the results of the elemental analysis obtained through RBS, it was decided to also conduct an EDX analysis on the same samples. **Figure 20c** and **Figure 20d** show the EDX spectra of the erbium-doped NPs obtained from the three different syntheses and the EDX spectrum of those doped with neodymium, respectively, while the values obtained are reported in **Table 2**.

In the quantitative analysis, performed for the EDX measurements, the spectra were processed to remove the background (Bremsstrahlung radiation) and spectral artifacts; then, the characteristic X-rays were compared with data from the standards libraries. Through this type of analysis, it is possible to identify the elements corresponding to the energy of the peaks and to obtain the atomic and weight percentages. Also in this case, the values obtained differ from those expected with a discrepancy comparable to the values obtained with RBS. In the EDX spectra, unlike the spectra in RBS, the signals of Silicon and Oxygen are present (which includes both the one associated with Y_2O_3 and the silicon oxide used as support).

EDX measurements did not allow to make an accurate estimate for the N1 sample, as the dopant percentage was close to the detection limit of the technique (1% LOD). However, the technique and associated computational algorithms managed to detect a small concentration, which appears to be close to that obtained by RBS. The small discrepancies found between the stoichiometric ratios present in the starting solutions and the results obtained from the compositional analyzes for samples E2 and E3 fall within the experimental error. For sample E1, which has a higher content of Erbium than expected, the discrepancy found could probably be due to the presence of precipitation phenomena stabilized from the kinetic point of view, so that the precipitate obtained show a higher percentage of dopant than the initially stoichiometric ratio.

2.1.4 Optical characterisation

To study the luminescence properties and find the excitation wavelength for which the maximum emission is obtained, a spectrofluorometer was used in order to obtain 2D excitation-emission maps. In the case of the $Er:Y_2O_3$ NPs (**Figure 21a**) there is the maximum emission by exciting at 378 nm while for the $Nd:Y_2O_3$ NPs (**Figure 21b**) by exciting at 358 nm.

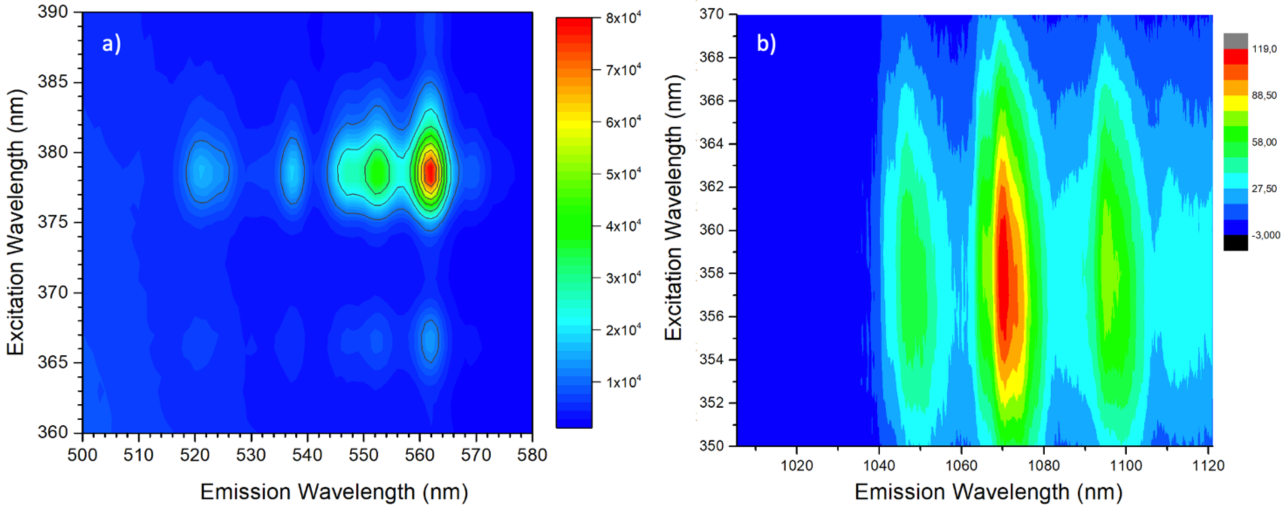

Figure 21. Photoexcitation 2D maps of a) Er:Y_2O_3 NPs and b) Nd:Y_2O_3 NPs.

Using these excitation wavelengths, photoluminescence spectra relating to the various types of synthesized particles were obtained (**Figure 22**).

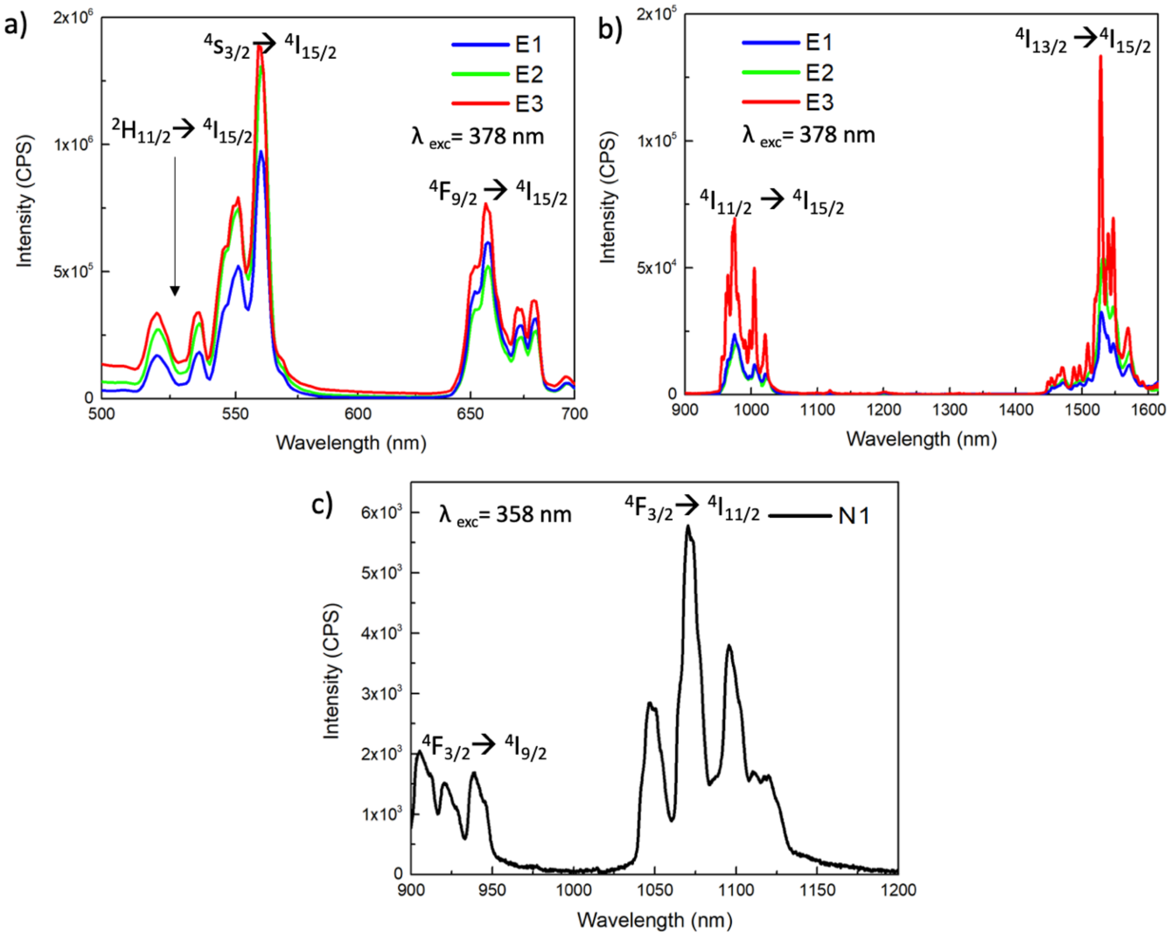

Figure 22. PL emission spectra of Er:Y_2O_3 NPs samples E1, E2, E3 in the visible a) and IR b) range (λ_{exc}=378 nm). (c) PL emission spectrum of Nd:Y_2O_3 NPs sample N1 (λ_{exc} =358nm).

All Er:Y_2O_3 nanoparticles (E1, E2 and E3) show the typical peaks of erbium present in the visible region at about 550 nm and 660 nm, deriving from electronic transitions $^4S_{3/2} \rightarrow {}^4I_{15/2}$ and $^4F_{9/2} \rightarrow {}^4I_{15/2}$ respectively, and in the infrared region at 980 nm and 1522 nm, resulting from the electronic transitions $^4I_{11/2} \rightarrow {}^4I_{15/2}$ and $^4I_{13/2} \rightarrow {}^4I_{15/2}$, respectively. Since each spectrum was obtained from an average of 3 measurements on the same sample and all measurements were performed under the same conditions and on the same day, it is also possible to compare their intensities. It is possible to note how the NPs synthesized with procedure 3) show a greater intensity of fluorescence especially in the IR range.

Figure 22c shows the PL spectrum for Nd:Y_2O_3. The most intense emission band was observed at 1064 nm, due to the transition $^4F_{3/2} \rightarrow {}^4I_{13/2}$. Furthermore, a manifold was observed at about 946 nm, due to the transition $^4F_{3/2} \rightarrow {}^4I_{9/2}$. Thus, the PL spectra clearly show that Er:Y_2O_3 and Nd:Y_2O_3 have the required luminescence properties. In addition, upconversion measures were also conducted on Er:Y_2O_3 NPs obtaining the spectrum shown in **Figure 23**.

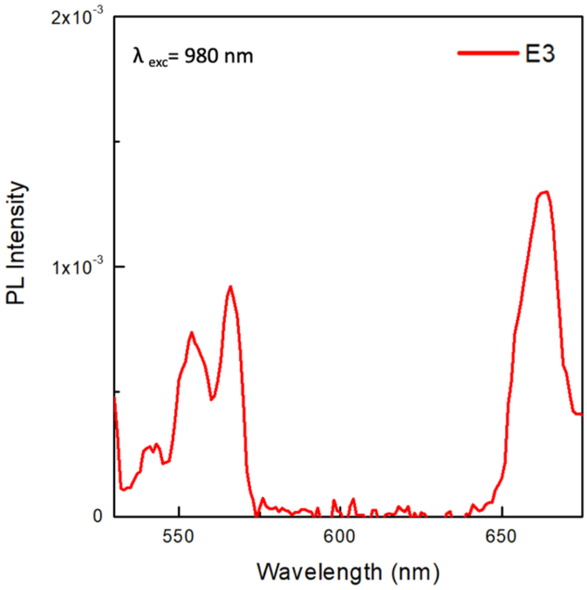

Figure 23. Upconversion spectrum of Er:Y_2O_3 NPs sample E3 (λ_{exc}=980nm).

Furthermore, to test the ability of NPs to emit a stable luminescence signal by electron beam excitation, Cathodoluminescence (CL) spectra of Er:Y2O3 NPs were acquired simulataneously with the SEM micrographs; the images obtained from secondary electrons (SE) and cathodoluminescence (CL) are shown **Figure 24a** and **Figure 24b** respectively. The two images are morphologically very similar indicating that the luminescence signal coincides with the position of the NPs and consequently it seems that all the NPs emit a signal strong enough to be detected.

Furthermore, through the SEM it is also possible to measure the emitted CL spectra (**Figure 24c**) which is very similar to that obtained by photoexcitation (**Figure 24d**, λ_{exc} = 378 nm), indicating that the CL signal comes from the NPs, even if the CL spectrum shows a better spectral resolution with more and thinner peaks.

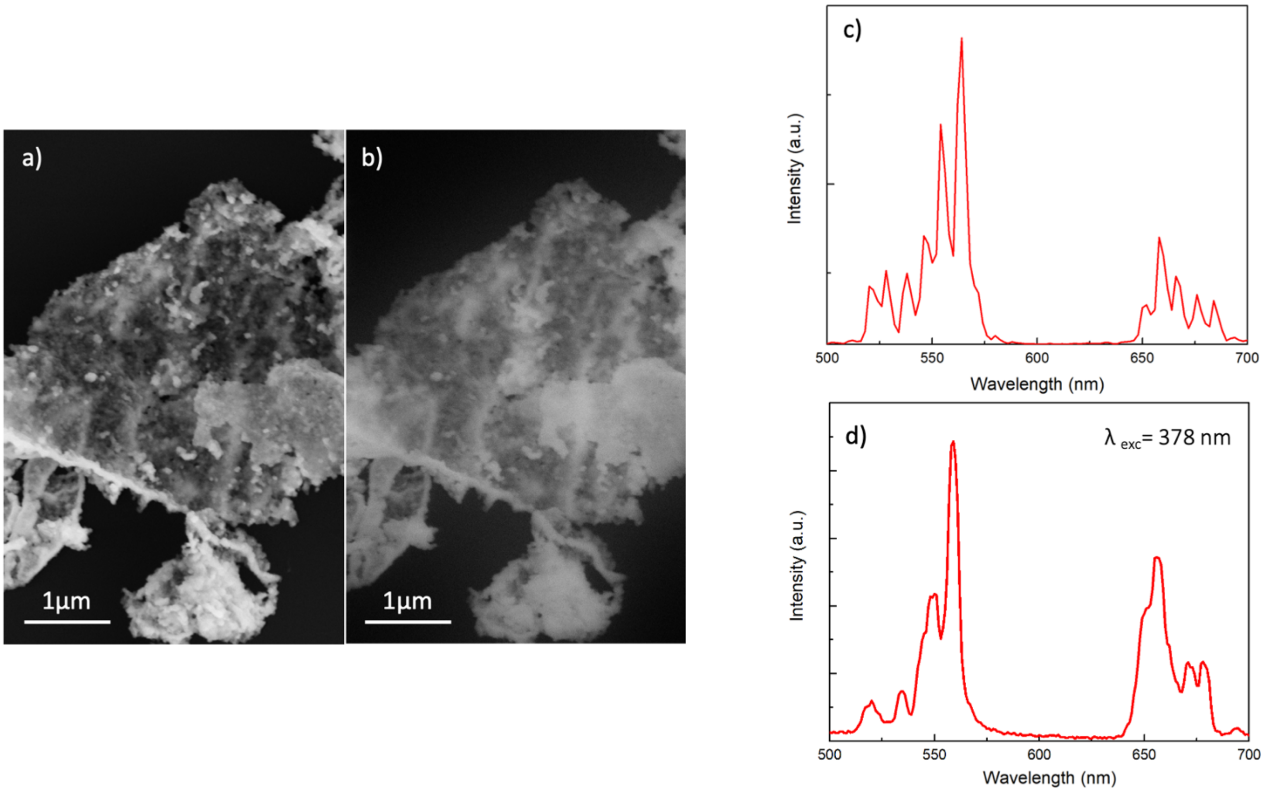

Figure 24. a) SEM image of Er:Y_2O_3 NPs obtained by a) secondary electrons and b) cathodoluminescence. Related emission spectra obtained by c) electron beam excitation and d) photoexcitation (λ_{exc} = 378 nm).

2.1.5 PEGYLATION PROCESS AFTER SYNTHESIS

However, the most challenging goal in this research field is to obtain ceramic nanophosphors with good luminescence and upconversion properties that are maintained even after their functionalization. In fact, a functionalization process through PEG is necessary forall kinds of NPs since once inside biological fluids, each type of NP is recognized as a foreign body, and therefore is promptly eliminated from the systemic circulation by the cells of the mononuclear phagocyte system (MPS), precluding accumulation in target cells and tissues[26]. Moreover, Er: Y_2O_3 and Nd:Y_2O_3 are ceramic systems, insoluble and highly inert, and therefore, without proper pegylation, their use in biological fluids to label specific targets is practically not possible.

The pegylation procedure is a well-known process for the functionalization of proteins and peptides used in drug delivery which are usually rapidly degraded and eliminated from the bloodstream and therefore require ad hoc approaches to increase their circulation time. The approach is to coat the surface of the therapeutic with an inert polymer that resists interactions with bloodstream components, giving it invisibility. The PEG coatings on the NPs protect the surface from aggregation, opsonization and phagocytosis, thus prolonging the circulation time. In this specific case, pegylation also renders soluble and biocompatible materials that, otherwise, could not be used. This functionalization allows the creation of stable NPs suspensions in water, thus decreasing the phenomena of aggregation and precipitation. In fact, as reported in **Figure 25**, before pegylation a whitish and turbid solution is observed due to the formation of precipitates and to the presence of aggregated particles (**Figure 25a**); on the other hand, through the pegylation process, transparent and non-precipitating solutions are obtained, containing well-separated particles (**Figure 25b**).

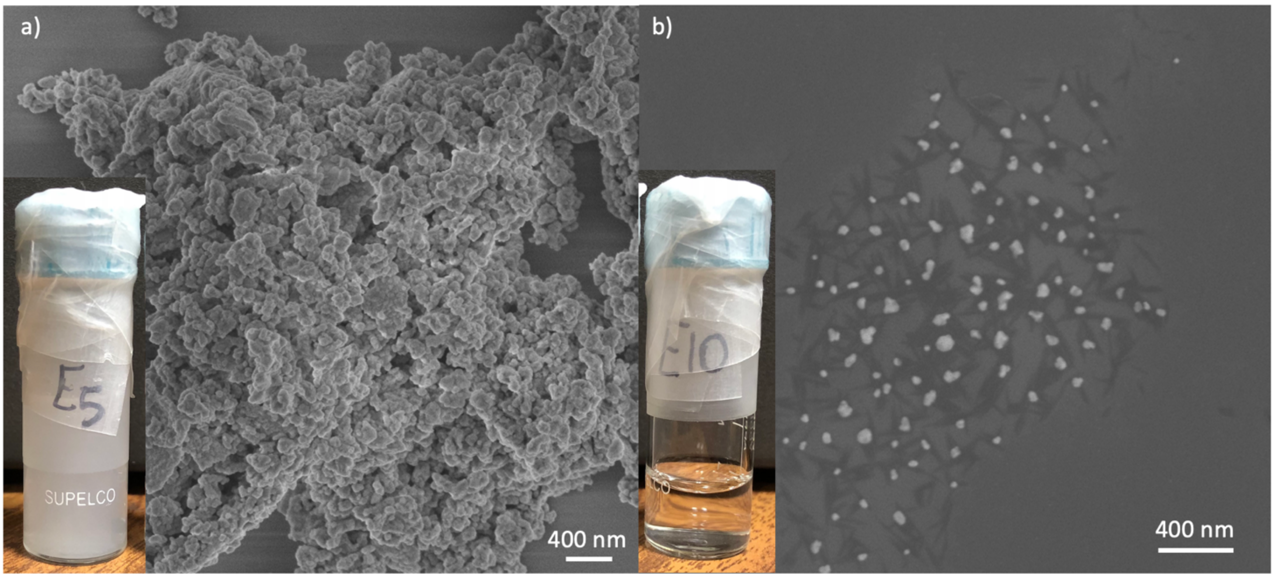

Figure 25. SEM images of Er:Y_2O_3 NPs a) before and after pegylation with corresponding solutions in the insets.

The pegylation reaction is quite simple; it is sufficient to put together a buffered solution of the polymer with the nanoparticles and let the synthesis go until the end, as described in literature.[96]

2.1.6 ULTRAFILTRATION PURIFICATION PROCESS

The critical step is to carefully remove excess PEG as it exhibits a broad emission spectrum in the visible region and it covers the acute lanthanides emission peaks. For this purpose, the solution containing the nanoparticles and the unreacted PEG was ultrafiltered using benchtop centrifuge filters, easily accessible in any laboratory. It was decided to use this alternative approach to the ultracentrifugation procedure, which is reported in most of the articles dealing with the purification of these NPs, in order to make the process more accessible even in laboratories not extremely advanced.

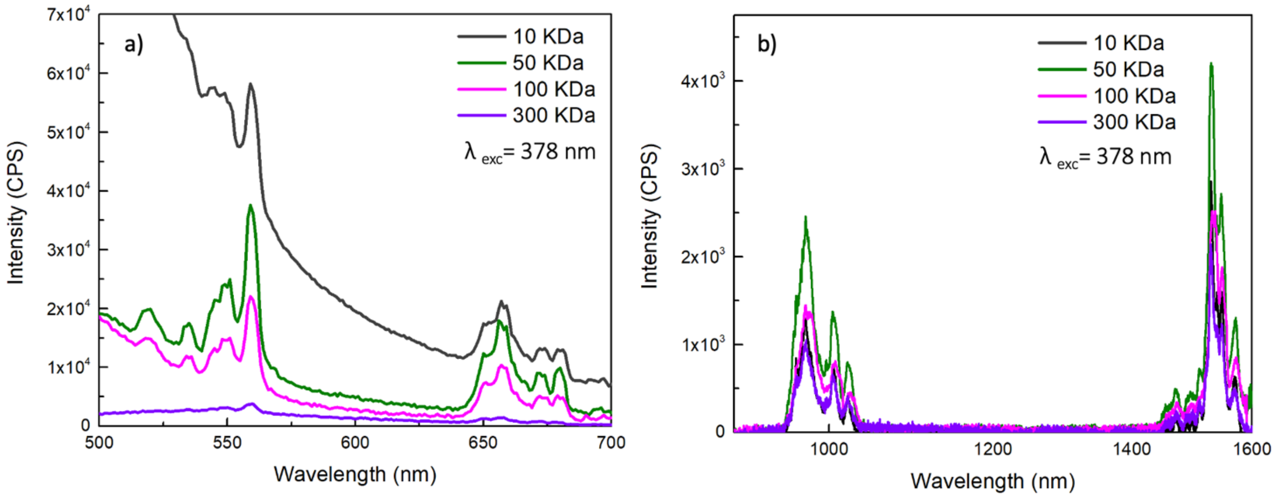

Figure 26. PL emission spectra comparison in a) visible and b) IR range of pegylated Er:Y_2O_3 NPS sample E3 after ultrafiltration using Amicon with different pore sizes (λ_{exc} =378 nm).

Ultracentrifugation is a technique that allows, by applying the right degree of acceleration, to settle the pegylated NPs and remove the supernatant containing the unreacted polymer. However, a result quite similar can be obtained through ultrafiltration, a filtration process in which centrifugation and concentration gradients lead to a separation through a semipermeable membrane. In this case the force driving the separation is still provided by the centrifuge, even if a lower acceleration is needed compared to ultracentrifugation process. Furthermore, the membranes of the filters have pores with a precise cut-off that can be opportunely chosen to optimize the separation between NPs and unbound polymer.

To purify the Er:Y_2O_3 NPs filters with different cut-offs (10, 50, 100, 300 kDa) were used and, to select the best ultrafiltration device, PL spectra were performed on pegylated nanoparticles purified with the different filters (**Figure 26**). The PL spectra obtained show that the filter having a cut-off of 10 kDa has too small pore sizes which also retain the PEG and, for this reason, its parasitic background fluorescence is present in the spectrum. On the other hand, 300 kDa cut-off filters have too large pore sizes and thus the NPs pass through the filter together with the PEG in excess, as testified by the PL spectra in which the peaks due to the Er luminescence in the visible seem to disappear.

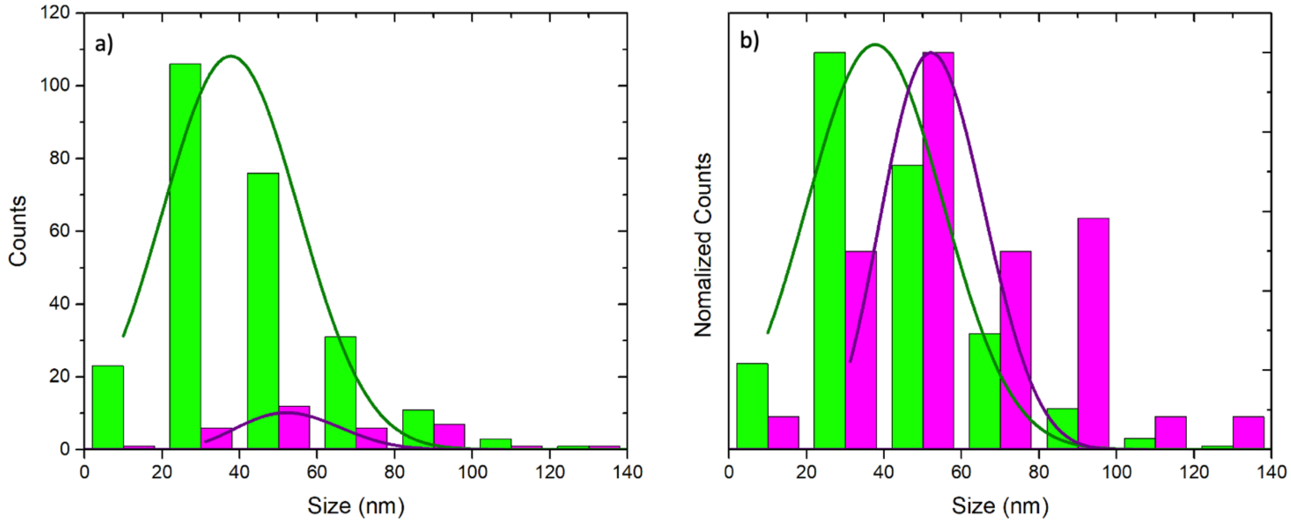

Figure 27. a) Particles size distribution histogram and gaussian fit obtained by TEM images of Er:Y_2O_3 NPs after ultrafiltration using (green) 50 kDa and (pink) 100 kDa amicon. b) normalized histograms.

	Diameter (nm)
Er 50 kDa	37.7 ± 17.5
Er 100 kDa	57.8 ± 27

Table 3. Average dimensions obtained by TEM images of Er:Y_2O_3 NPs after ultrafiltration using 50 and 100 kDa amicon.

Based on the PL spectra, the filters that seemed to give results were the 50 and 100 kDa cut-off filter, and thus the so filtered NPs were analyzed by TEM in order to evaluate the NPs sizes in the two cases. The histograms showing the dimensions of the two NPs measured by the TEM images are presented in **Figure 27a.** Although more TEM images for 100 kDa filtered NPs have been analyzed, the number of NPs is higer in the case of filtration with 50 kDa, indicating that with the 100kDa filter there is a considerable loss of NPs. Furthermore, normalizing the two histograms (**Figure 27b**) we obtain a smaller average NPs size (**Table 3**) in the case of the particles filtered with the 50 kDa filter (d = 37.7 ± 17.50), indicating that with the 100 kDa filter (d = 57.8 ± 27) the loss of most of NPs with diameters smaller than 40 nm occurs.

2.1.7 CHARACTERIZATION OF PEGYLATED AND PURIFIED NANOPARTICLES

Therefore, once the ultrafiltration process was optimized, the Er:Y_2O_3 NPs and the Nd:Y_2O_3 NPs filtered with 50 kDa filters were both analyzed, using the same techniques used for naked NPs. It is interesting to note that pegylation makes the particles well dispersed and therefore it was easier to carry out the task of studying their morphologies.

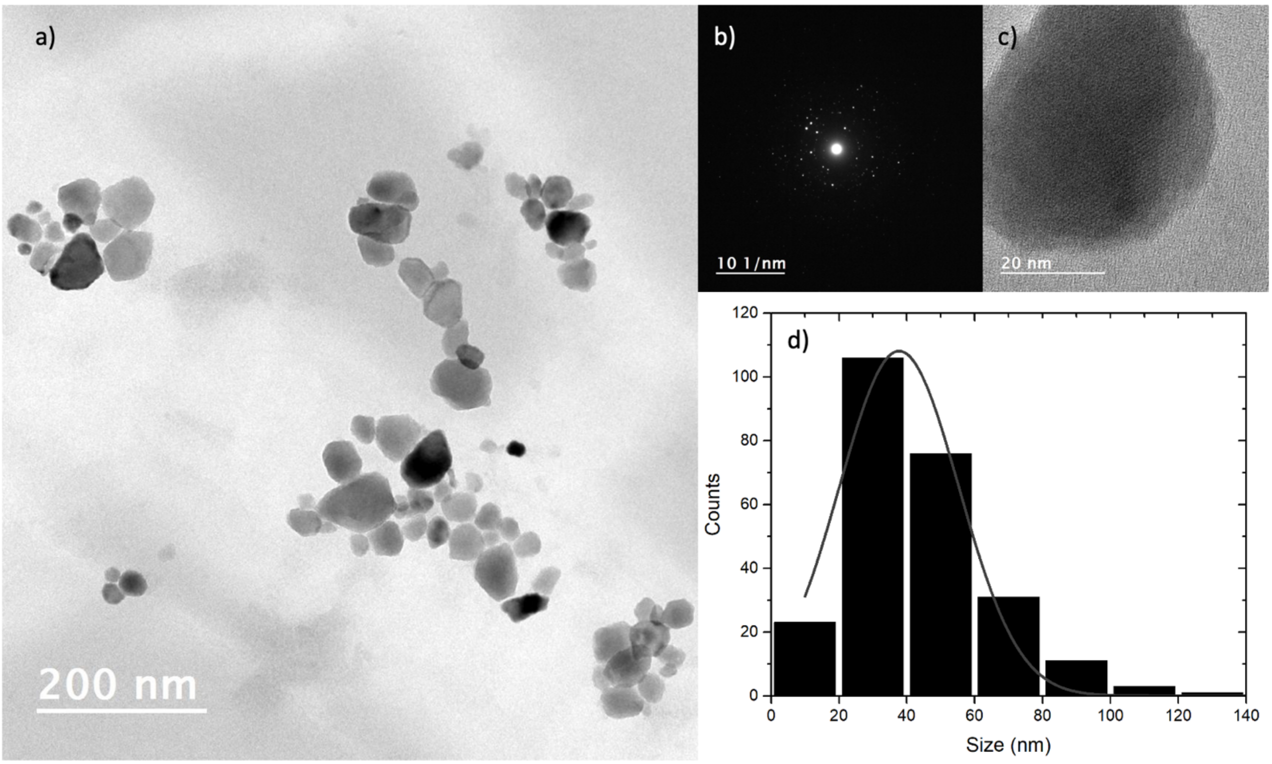

Figure 28. a) TEM image, b) HR-TEM detail and c) related diffraction pattern of pegylated Er:Y_2O_3 NPS sample E3. d) Particles size distribution histogram and gaussian fit obtained by TEM images.

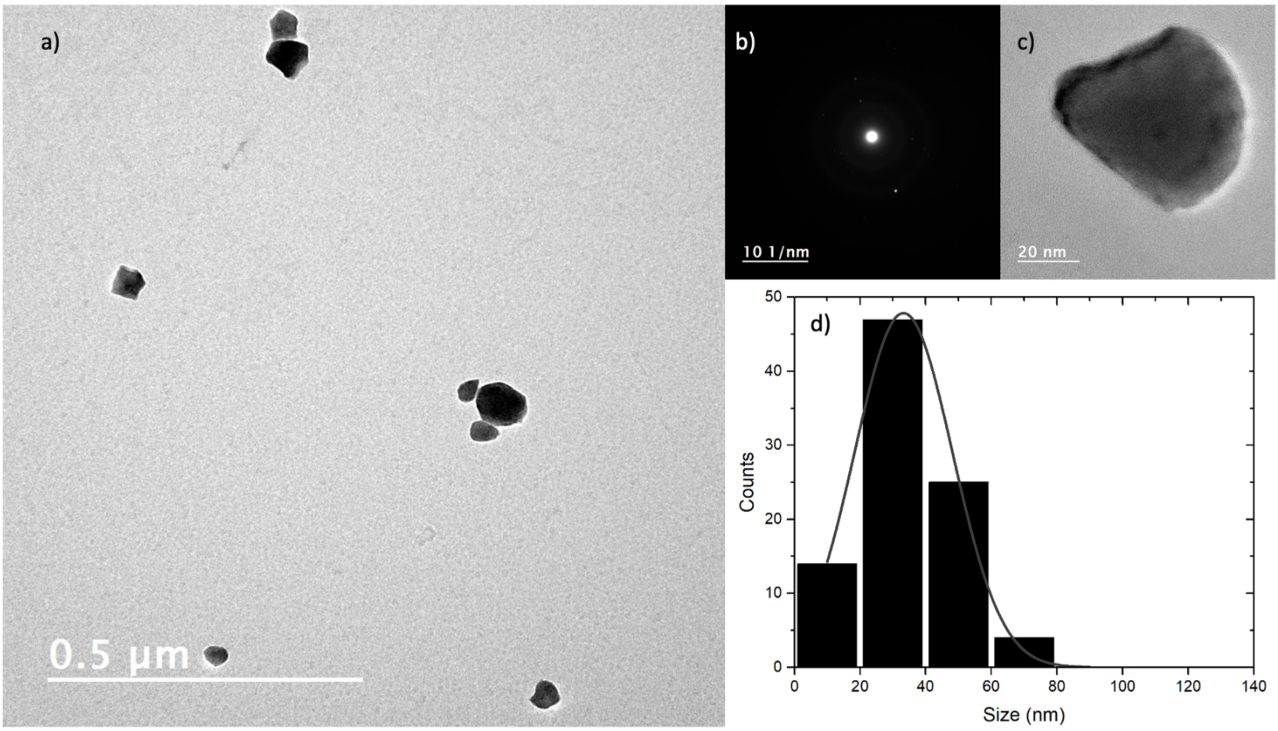

Figure 29. a) TEM image, b) HR-TEM detail and c) related diffraction pattern of pegylated Nd:Y_2O_3 NPs sample N1. d) Particles size distribution histogram and gaussian fit obtained by TEM images.

The TEM image, the HR-TEM detail and the relative size distribution for the pegylated NPs E3 and N1 are shown in **Figure 28** and **Figure 29**, respectively. Through the HR-TEM details it is possible to see the NPs crystallographic planes showing that both erbium and neodymium NPs are almost monocrystalline (**Figure 28**b and **Figure 29**b respectively). The size distribution for the two types of NPs has been compared and reported in **Figure 30**. Although analyzing the same number of images, a smaller number of neodymium NPs are obtained compared to those of erbium (**Figure 30**a). Furthermore, by normalizing the histograms and the relative Gaussian fits, we obtain an average dimension for Nd NPs which are smaller (d = 33.2 ± 14.9) than the Er doped ones (d = 37.7 ± 17.5).

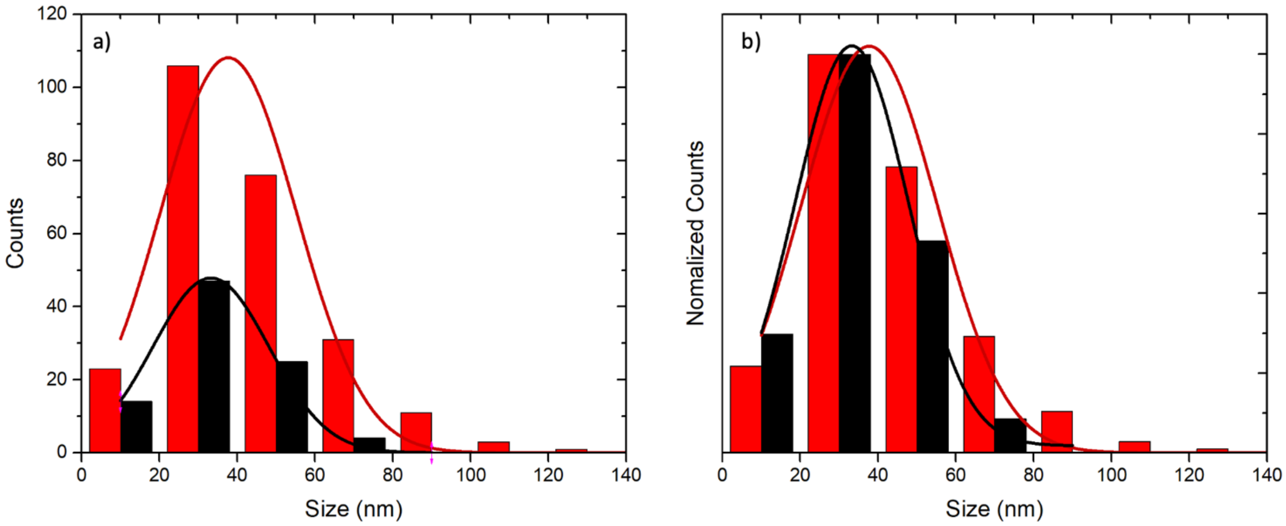

Figure 30. a) particles size distribution histogram and gaussian fit obtained by TEM images of (red) Er:Y_2O_3 NPs and (black) Nd:Y_2O_3 NPs after ultrafiltration using 50 kDa Amicon. b) normalized histograms.

	Diameter (nm)
Er	37.7 ± 17.5
Nd	33.2 ± 14.9

Table 4. Average dimensions obtained by TEM images of Er:Y_2O_3 NPs and Nd:Y_2O_3 NPs after ultrafiltration using 50 kDa Amicon.

To evaluate any changes in the crystallographic and optical properties due to the pegylation process, the Raman (**Figure 31**) and luminescence (**Figure 32**) spectra before and after pegylation were compared. Since the width of the Raman peaks are almost unchanged, it can be deduced that the pegylated nanoparticles maintain the crystallinity of the naked ones.

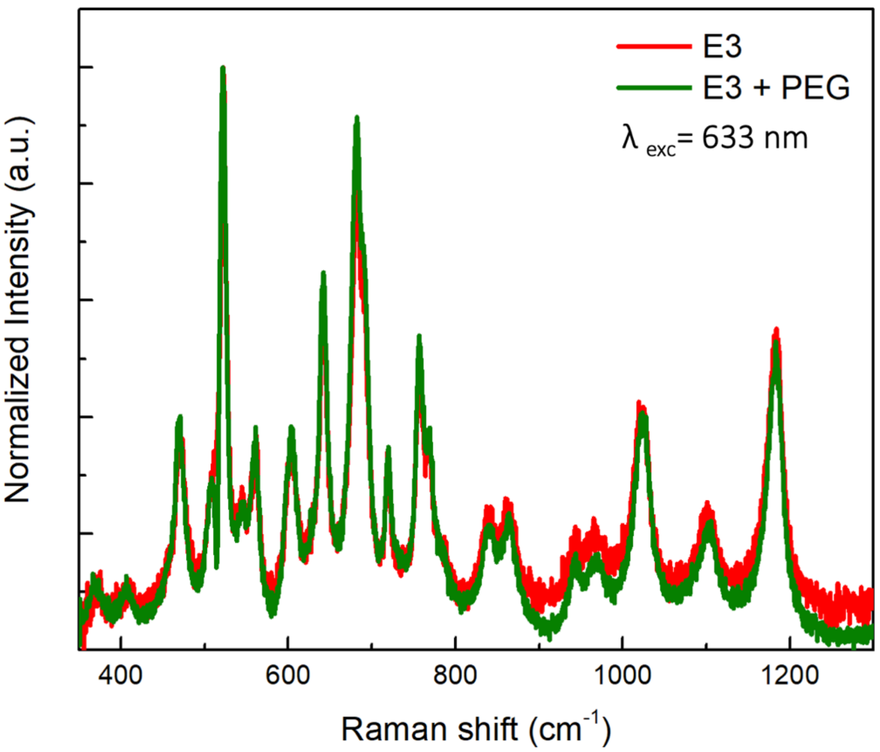

Figure 31. Normalized Raman spectra of naked and pegylated Er:Y_2O_3 NPs sample E3.

On the other hand, for the optical properties, there is a drastic decrease in the luminescence emission intensity following pegylation, with a signal decreasing by about 10 times compared to naked particles. This difference could be explained by the loss of NPs following the PEG filtration process, or by absorption processes due to the presence of the PEG on the surface that limit the effective quantity of photons directly exciting NPs that generate radiative de-excitation.

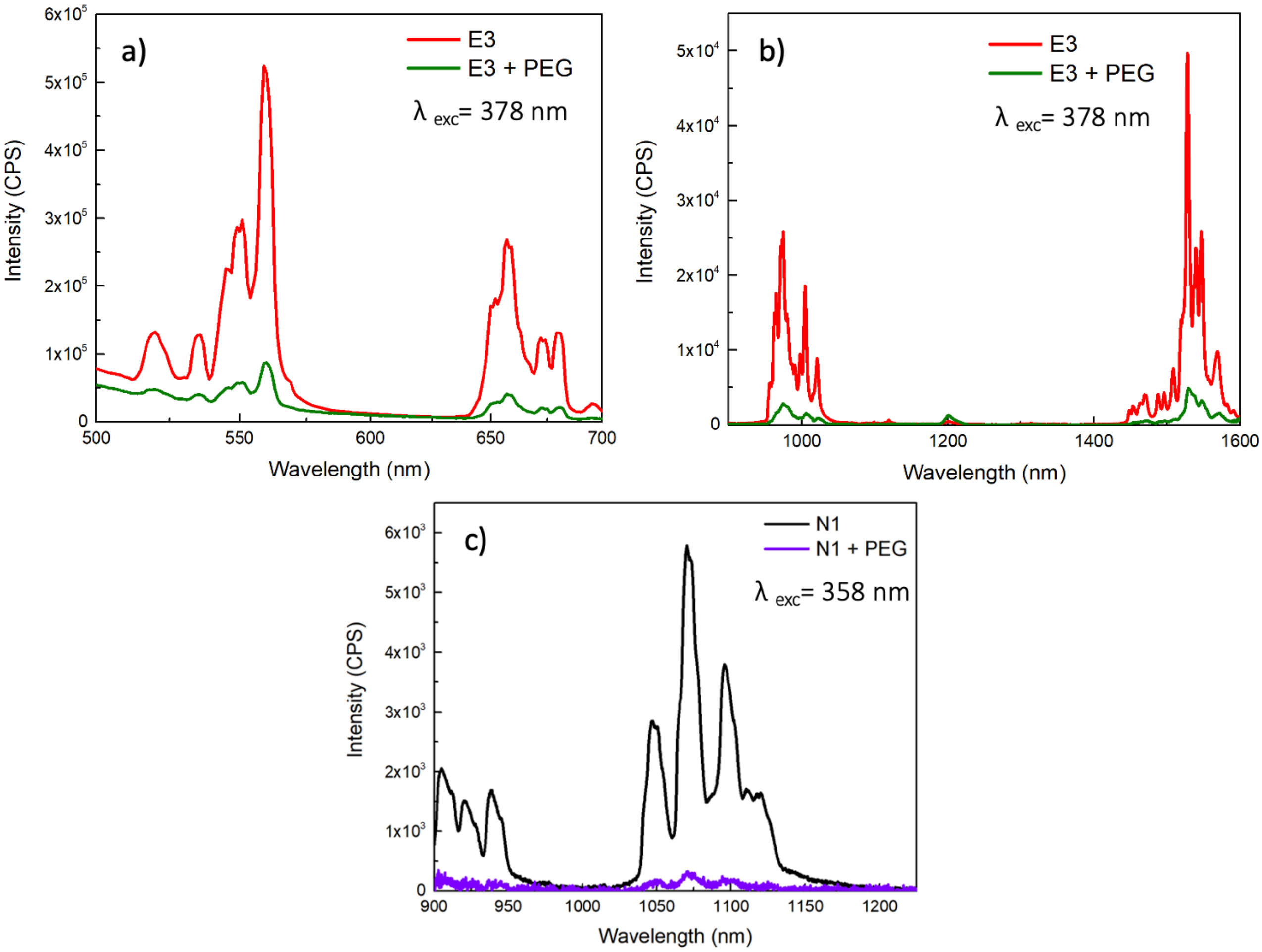

Figure 32. PL emission spectra in the visible range of a) Er:Y_2O_3 NPs and in the IR range of b) Er:Y_2O_3 NPs an c) Nd:Y_2O_3 NPs before and after pegylation.

2.1.8 COMPARISON BETWEEN ULTRACENTRIFUGATION AND ULTRAFILTRATION

The luminescence emission spectra of both ultrafiltered with 50kDa filters or ultracentrifuged Er:Y_2O_3 NPs were compared (**Figure 33**). In both cases lower emission spectra compared to the naked NPs are obtained, but for both purification techniques the intensities are comparable, meaning that the two methods are equivalent, although a better result is obtained in the IR for ultracentrifuged NPs.

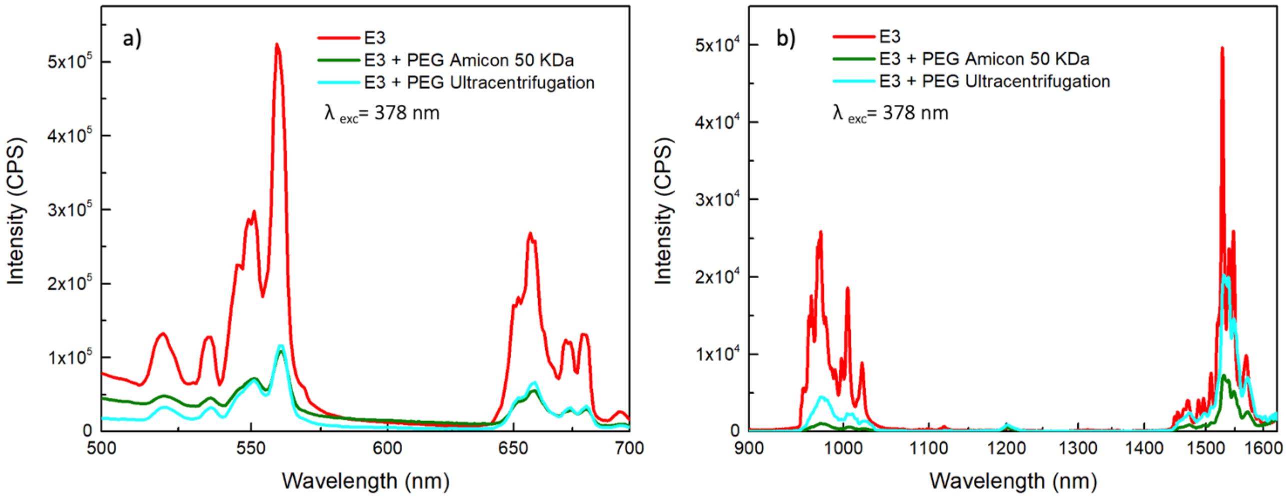

Figure 33. PL emission spectra of Er:Y_2O_3 NPs sample E3 naked and pegylated after purification.

2.1.9 CONCLUSIONS AND PERSPECTIVES

Ultimately, by optimizing the experimental parameters it was possible to obtain small and monodispersed Y_2O_3 nanoparticles doped with Er $^{3+}$ and Nd $^{3+}$. Extensive characterization studies highlighted the unique properties of these systems that exhibit high crystallinity both naked and pegylated. The photoluminescence spectra show the well-known characteristics of the lanthanide ions as well as the upconversion properties.

In the future it is possible to proceed with toxicity studies of these nanostructures on cell cultures, followed by the functionalization of the NPs with an antibody capable of recognizing the exosomes membrane proteins for selective labeling (e. g. antiCD81, CD9, CD63). A protocol for NCs functionalization has already been set up and will be shown subsequently. It is possible to adapt this protocol to lanthanides doped Y_2O_3 NPs, since also in this case the formation of a peptide bond between the carboxyl groups of the PEG-b- PAAc on the surface of the NPs and the antibody amino groups is needed.

2.1.10 EXPERIMENTAL SECTION

Materials. $Y(NO_3)_3 \cdot 6H_2O$, $Er(NO_3)_3 \cdot 5H_2O$ and urea were obtained as commercial reagents by Alfa Aesar (USA); $Nd(NO_3)_3 \cdot 6H_2O$, urease and polyacrylic acid (PAAc) were purchased from Sigma Aldrich (USA), whereas PAAc-b-PEG was purchased from Polymer Source INC. The ultrafiltration devices were Vivaspin Sartorius VS0651, 300,000 MWCO (300 kDa) and Amicon Ultra devices 10,000 MWCO (10 kDa) 50,000 MWCO (50 kDa) and 100,000 MWCO (100 kDa). All solutions were prepared by using Milli Q water.

Synthesis of Er:Y_2O_3 and Nd:Y_2O_3 (in collaboration with Department of Chemical Sciences, University of Catania).Three different synthetic routes have been used to obtain Er:Y_2O_3 nanoparticles. Synthesis 1) (E1) The nanoparticles were synthesized by slightly modifying the procedure previously reported by Venkatachalam et al[85].

Preparation of PEGylated Er:Y_2O_3 and Nd:Y_2O_3 nanoparticles (in collaboration with Department of Chemical Sciences, University of Catania). The pegylation of Er:Y_2O_3 and Nd:Y_2O_3 nanoparticles was carried out by slightly modifying the procedure reported by Kamimura et al.[96] Briefly, to a 20 ml of a buffer solution TRIS/HCl (pH = 7.00), containing 0.5 g/L of PEG-b-PAAC, 2 mg of nanoparticles were added and the resulting mixture was kept at 4° C for 24 h under magnetic stirring. The obtained solution was split in two aliquots that were differently purified. In one case the free excess polymer in the solution was removed by ultracentrifugation (9.0×10^4g, 15 min, 3 times), and the solvent was changed to Milli-Q water, whereas the second aliquot was ultrafiltrated utilizing different ultrafiltration devices: Vivaspin Sartorius VS0651, 300,000 MWCO (300 kDa) and Amicon Ultra device, 10,000 MWCO (10 kDa), 50,000 MWCO (50 kDa) and 100,000 MWCO (100 kDa). In all cases the ultrafiltration was carried out by centrifuging the sample at 3500 rpm for 5 minutes for three times and the solvent was changed to Milli-Q water.

Scanning Electron Microscopy *(SEM).* Morphology and chemical mapping of the samples were obtained using a field emission scanning electron microscope (Gemini Field Emission SEM SUPRA 25) equipped with an energy dispersive X-ray (EDX) microanalysis system (X-MAX, 80 mm^2 by Oxford Instruments, Abingdon, UK). The analyses were performed at an acceleration voltage of 20 kV, with an aperture size of 30 µm, a working distance of 4–5 mm, and using an In-lens detector. Samples for SEM were prepared by placing 1 drop of the colloidal dispersions of Er:Y_2O_3 or Nd:Y_2O_3 both naked and pegylated onto a 1 cm^2 p-doped silicon piece and let dry for 30 minutes.

Transmission Electron Microscopy (TEM) (with the assistance of Dr. Vincent Dorcet, THEMIS platform). Transmission Electron Microscopy analysis was carried out with with JEOL 1400 transmission electron microscope. For the sample preparation, 300 mesh carbon coated nickel grids were placed for 1 min on top of a 40 µL sample droplet (colloidal dispersions of Er:Y_2O_3 or Nd:Y_2O_3 both naked and pegylated) and dried up with paper. A 200 kV acceleration voltage was used. Particle sizes and interparticle distances were determined from TEM micrographs using Fiji Software.

Raman spectroscopy. Raman measurements were performed on erbium and neodymium doped NPs using the HR800 Horiba—Jobin Yvon spectrometer, under a 632 nm excitation produced by a He-

Ne laser. For these measurements the solutions of Er:Y_2O_3 or Nd:Y_2O_3 nanoparticles naked or pegylated were deposited by drop-casting three drops of the NPs solutions (drying each drop on a heating plate at 50°C for 15 minutes, and then depositing the following one) on p-doped silicon pieces of approximately 1 cm^2. An optical microscope was used to select the area of the sample; the scattered light was collected by a CCD detector after passing through a monochromator with a high focal distance (about 0.5 m).

Rutherford Back Scattering. RBS measurements were carried out by using a 3.5 MV Singletron HVEE. A 2 MeV He^+ ion beam incident normally on the sample surface and detected at 165° was used and the current beam was set at 80 nA. In this case, the samples were prepared by drop-casting on silicon one drop of the nanoparticles solution under examination. A standard sample of amorphous silicon was used to get the dead time correction parameters. In order to take into account the roughness of the samples, for quantification of concentrations simulations of RBS-spectra were performed using the SIMNRA simulation package.[97]

Photoluminescence (in collaboration with Prof. Riccardo Reitano, Department of Physics and Astronomy, University of Catania). Photoluminescence measurements were performed on a Horiba Nanolog spectrofluorometer. The measurements were performed at room temperature on samples drop-casted on silicon (three drops). The wavelength resolution of both the excitation and the emission slits was set to 5 nm for measurements in the visible range, and 14 nm for measurements in the IR range. The intrinsic fluorescence of Er:Y_2O_3 and Nd:Y_2O_3 nanoparticles was excited at 378 nm and 358 nm, respectively and the corresponding emission spectra were acquired both in the visible and IR region, by using a photomultiplier Hamamatsu R928 in the UV-Vis-NIR and a Horiba Symphony II InGaAs array in the IR detector, respectively. Two different long-pass filters (400 nm for the visible range and 840 nm for the IR) were used in order to block the lamp excitation wavelength. The acquisition times was of 1 s for measurements in the visible range, and of 60 s for measurements in the IR range.

Luminescence upconversion (in collaboration with Dr. Giorgia Franzo, Department of Physics and Astronomy, University of Catania). Upconversion measurements were realized by an instrumentation made of a tunable Ti:sapphire laser as a light source, a chopper that modulates the frequency of the signal from the source, a sample holder, a photodetector (a classic photomultiplier tube) and a lock-in amplifier. For erbium doped and neodymium doped nanoparticles, the laser excitation was tuned to 980 nm and 808 nm, respectively. The power of the light source was 32 mW and a low-pass filter of 750 nm was used.

Cathodoluminescence. Cathodoluminescence measurements were acquired by a Gemini Field emission scanning electron microscope from ZEISS equipped with a Gatan Mono CL4 setup at 5 kV**.**

2.2 GOLD NANOCLUSTERS WITH DIFFERENT EMISSION WAVELENGTH

For the synthesis of NCs, a synthesis already present in the literature[77] was optimized and, by slightly varying the ratios between ligands and gold salts, different types of NCs were produced. To master the synthesis, the influence of the various synthesis parameters was studied. By increasing the number of thiol groups available, the size of the NCs decreases and consequently there is a blue shift of the emission. Similarly, increasing the pH of the solution also results in a smaller NCs size since the greater quantity of OH groups in the solution causes the thiol group deprotonation (pK_a around 9-10) resulting in the formation of the thiolate that have a strong affinity for gold.
Below we will present the different types of NCs produced, with different emissions.

2.2.1 RED EMISSIVE NANOCLUSTERS (RED GSH NCS)

Referring to an article reported in the literature[77] we have slightly adapted the synthesis based on the reduction of gold (III) salt by the reductant and ligand gluthation (named GSH). The ratios between GSH and gold salts (1 $HauCl_3$: 1.5 GSH) used were identical but the increase in the synthesis temperature results in the formation of GSH NCs with emission in the red region at about 600 nm (Red GSH NCs) with a significant time gain as they are already available after 3 hours instead of 24 hours (**Figure 34a**). The final result is in all similar to that produced in 24 hours. The morphological characteristics were analyzed by HR-TEM (**Figure 34b** and **Figure 35 a,b,c**): the particles appear quite monodisperse (diameter of 2.4nm ± 0.5nm), crystalline and well separated from each other. The inset shows the NCs suspension which appears yellowish transparent. Furthermore, the fluorescence properties of the NCs were investigated by spectrofluorometry, obtaining a 2D map which has the excitation wavelengths on the ordinate and the emission wavelengths on the abscissa (**Figure 34c**). Thanks to this map it is possible to find the maximum of excitation at about 430 nm and that of emission at 620 nm, values that vary slightly from sample to sample. If it is desired to use NCs without any specific functionalization, it is possible to purify them to remove the excess of unbound GSH, keeping the fluorescence properties unaltered (**Figure 35d**). However, it is desirable to keep them in the fridge immediately after synthesis without purifying them, and proceed with purification only just before their use, since removing the excess GSH significantly decreases the stability in suspension to 1-3 days before the GSH Red NCs precipitate. To avoid this instability against aggregation, the NCs are functionalized with PEG or in any case peptides which give them greater stability in suspension (e.g. C_3E_6D) (several weeks to months).

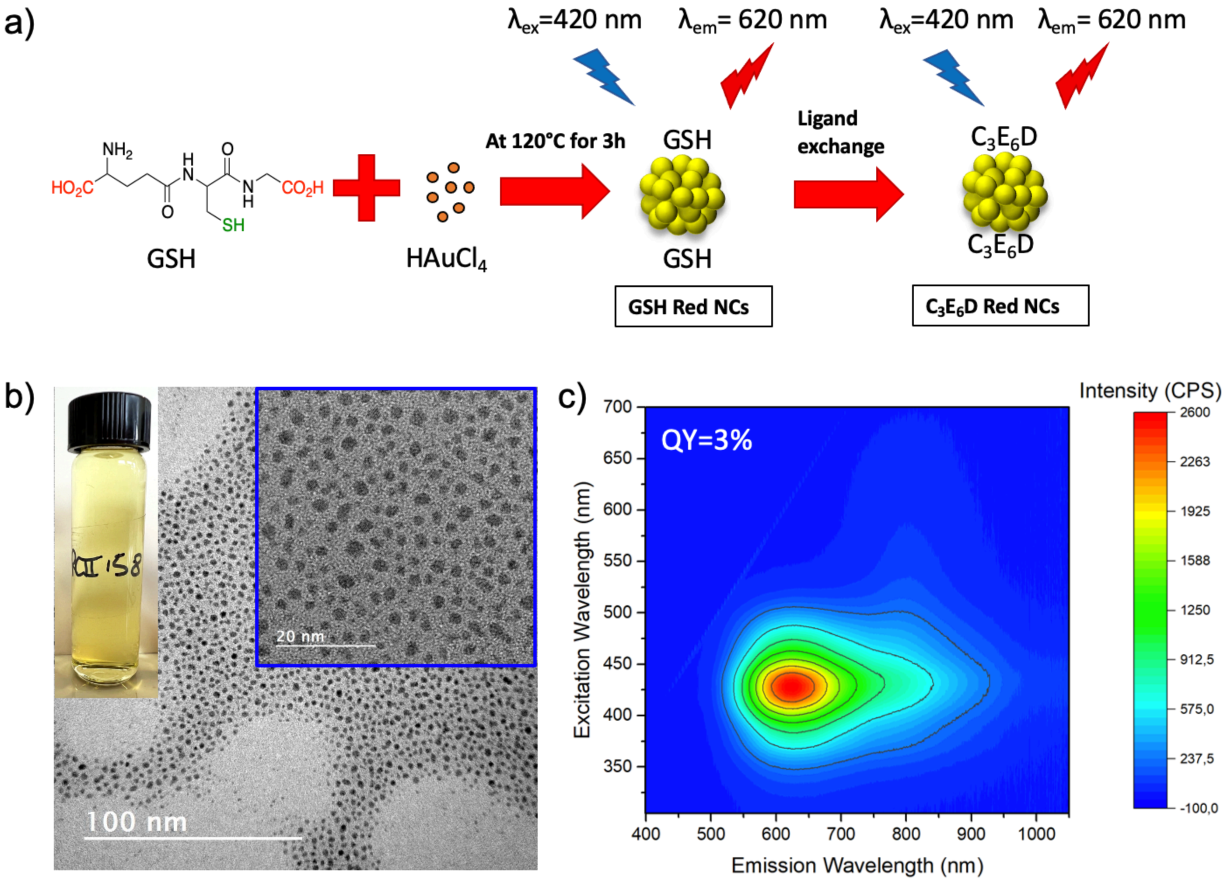

FIGURE 34. (a)Scheme concerning C_3E_6D Red NCs synthesis. (b) HR-TEM images with NCs solution on the left inset and (c) fluorescence 2D map of GSH Red NCs.

To functionalize these NCs with peptides of interest, it was necessary to make ligand exchanges with subsequent purifications. The ligand exchange that we used the most was the one that involved the use of the C_3E_6D peptide. This peptide is of great interest because:

- it increases the stability of the NCs in suspension through a steric stabilization due to the hexa ethylenglycol spacer (short oligoPEG) and electrostatics due to the presence of two carboxylate groups (terminal aspartic acid);
- it has a high affinity to gold thanks to the presence of 3 cysteines and consequently of 3 thiol groups;
- it enhances the fluorescence of the starting NCs thanks to the high affinity and the presence of electron-rich groups;
- it allows to create a multivalent platform by functionalizing the NCs with medicines, antibodies and segments of interest thanks to the presence of the carboxylic groups that react easily with the amines following the formation of a stable peptide bond.

By incubating the NCs in the presence of this peptide and leaving it in the fridge overnight, NCs are obtained with a higher luminescence intensity, with a larger excitation peak but with the same emission wavelength (**Figure 35e**). In addition, there is an increase in fluorescence Quantum Yield (QY) which doubles from 3 to 6.

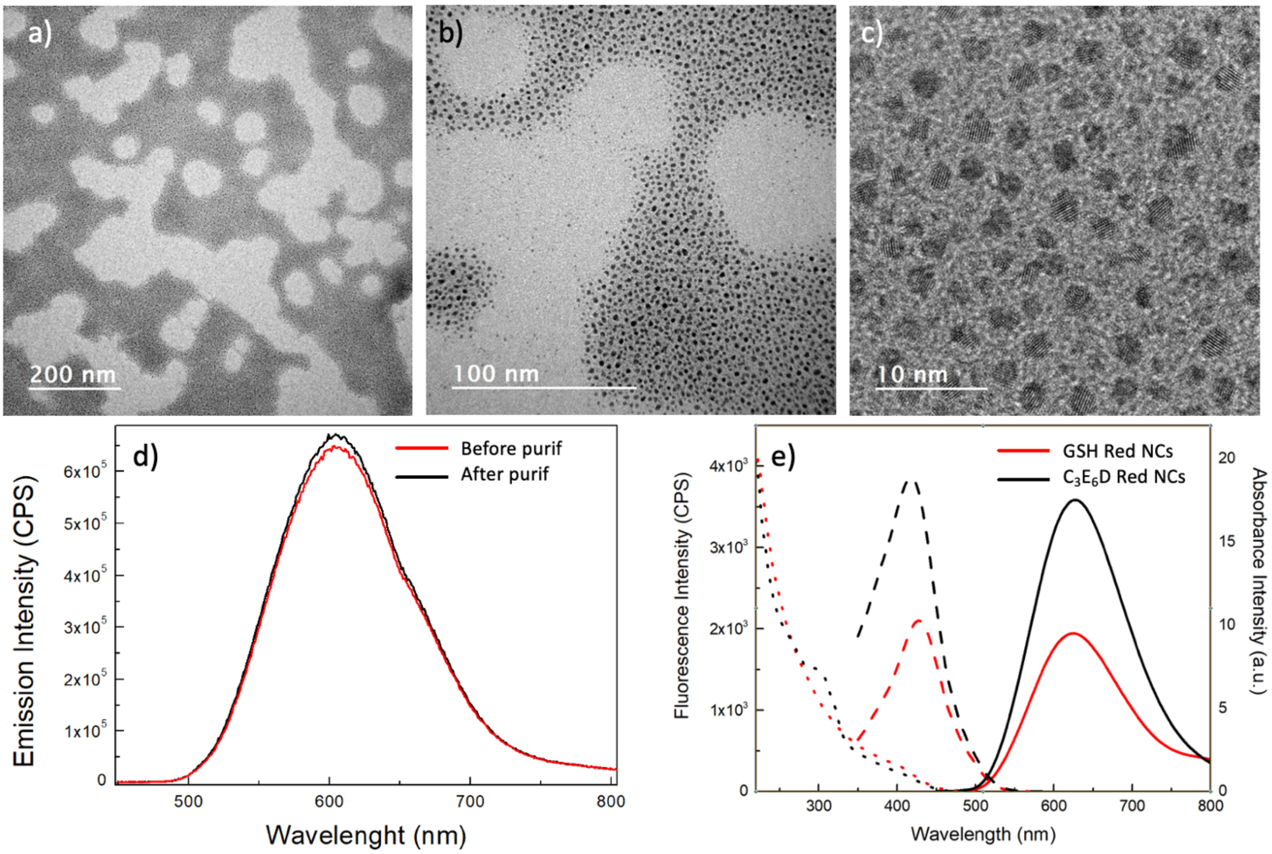

FIGURE 35. (a,b,c) HR-TEM images et different magnification of GSH Red NCs before purification. (d) Fluorescence emission spectra of GSH Red NCs before (red line) and after (black line) purification. (e) Absorance, excitation and emission spectra of GSH Red NCs (red line) and C_3E_6D Red NCs (black line).

To subsequently conduct electrostatic interaction experiments, the NCs were functionalized with peptides of different charges; for example, a negatively charged peptide (C_5PEG_4) and a positively charged one (K_5-C-NH_2) were used for functionalization. To test that ligand exchange took place efficiently, agarose gel electrophoresis was used. The solutions were inserted in the wells created specifically in the gel and subjected to an electric field that allows the migration of the charged species depending on their size and their charge.

Figure 36 shows the migration of the solutions: solutions 1 and 2 are migrated towards the positive electrode, both being negatively charged NCs, on the contrary the solution 3 of positively charged NCs has migrated in the reverse direction and is no longer visible to the inside of the gel. Furthermore, the difference in migration distance of solution 1 and 2 makes it clear that the ligand exchange took place efficiently, since if it had not happened the two solutions would have migrated in the same way. Migration depends on the size, shape and charge of the particles. It is important to take into consideration that the gel is at pH = 8, and under such conditions GSH Red NCs have a negative potential.

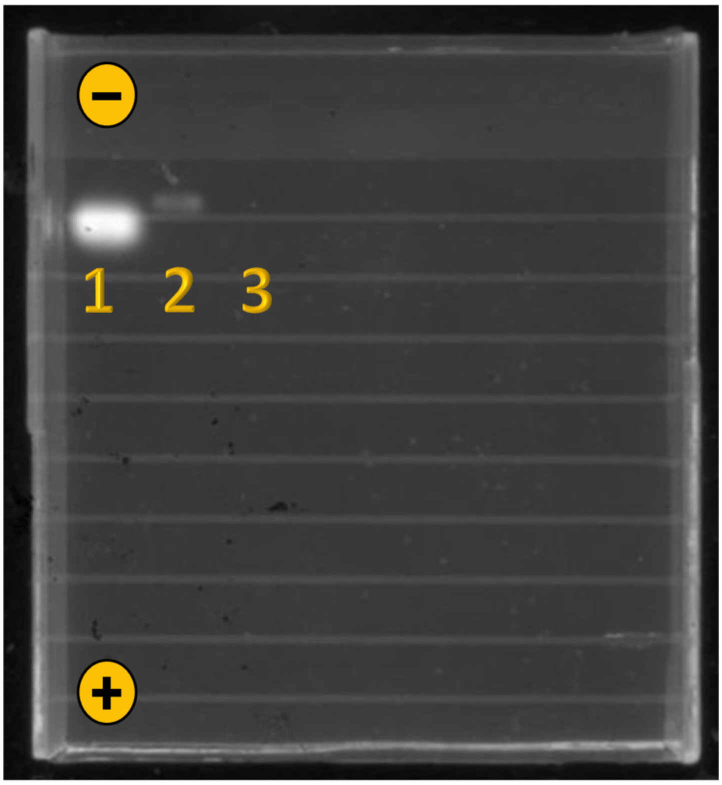

FIGURE 36 Electrophoretic migration of (1) GSH, (2) C5PEG4, (3) K5-C-NH2 Red NCs.

The stability of Red GSH NCs has been tested, both in terms of morphological stability and stability of the fluorescence over time.

Through DLS the size of the NCs was measured: to measure such small particles a protocol (SOP) suitable for measuring the size of the proteins was used, since it performs a fit of the correlation curve that allows for a higher resolution of the peaks. Through this measurement it is possible to see in **Figure 38a** very precise peak at about 3 nm, indicating a slightly larger diameter than that measured in the TEM since the technique does not measure the effective diameter of the metal core (as in the case of the HR-TEM), but the hydrodynamic radius which includes the size of the surface binder and the hydration layer of the nanoparticle. After 12 months, the result remains almost identical, indicating a very high stability of these nanoparticles over time. Only after 30 months does it begin to have a lowering of the main peak and the formation of NCs with a larger diameter. The fluorescence properties are almost unchanged after 4 months as demonstrated by the stability of the fluorescence intensity shown in **Figure 38b**.

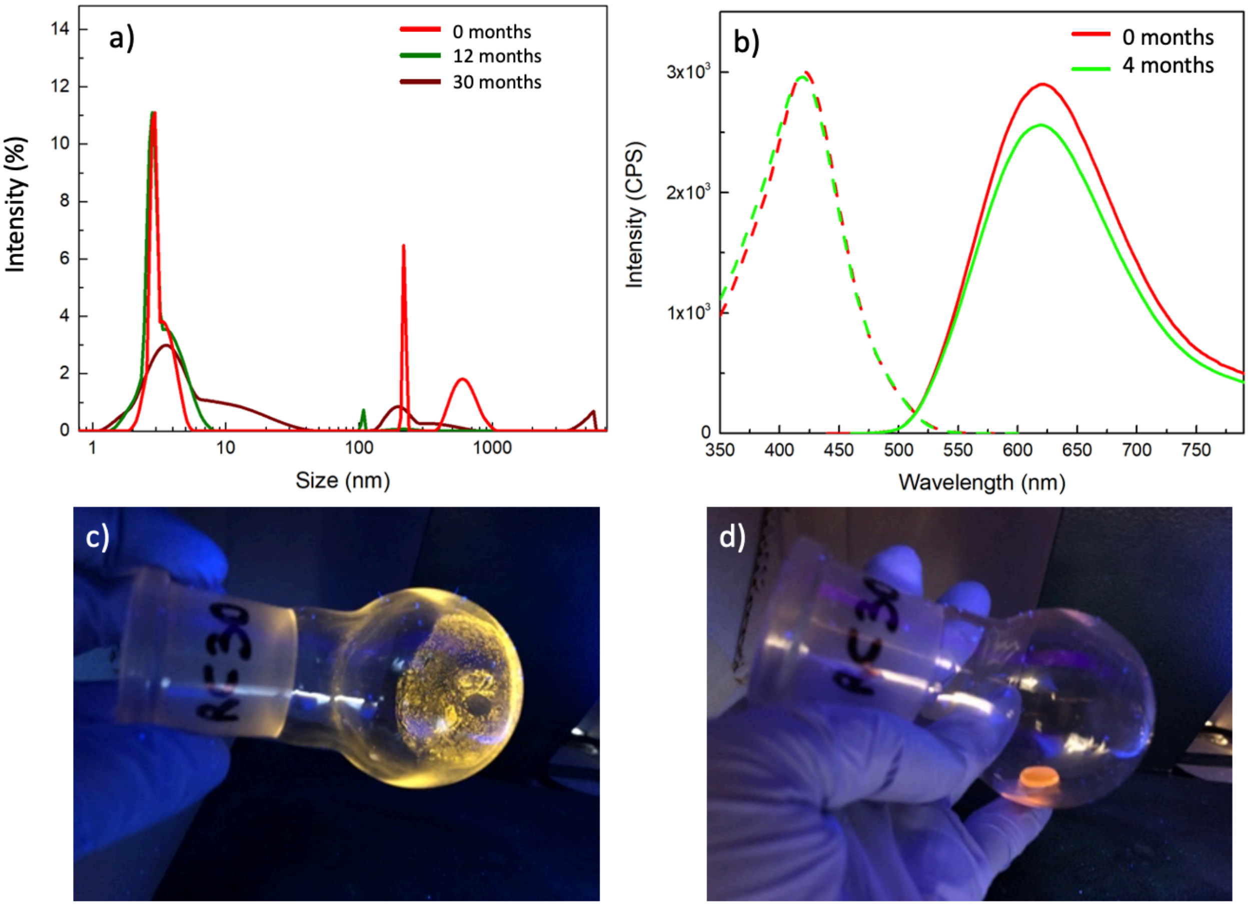

FIGURE 38. DLS (a) and fluorescence (b) stability study of GSH red NCs. Images of lyophilized (c) and redispersed in water(d) GSH Red NCs

To allow the commercialization and transport of these nanoparticles, it is important to be able to have them as a powder by lyophilizing them, without the formation of aggregates following redispersion in water and without changes in fluorescence. For some nanoparticles, eg. quantum dots, obtaining this result is not trivial, as the freeze-drying or freezing process in general turns off the fluorescence phenomena. This does not happen for NCs, which maintain their fluorescence even in lyophilized solid form (**Figure 38c**) and which can be easily redispersed in water without aggregation formation and by keeping the fluorescence properties (**Figure 38d**). Furthermore, in **Figure 38** it is possible to notice a slight variation in the color of the fluorescence once in solid form, which passes from orange to yellow, a reversible process which restores the initial orange fluorescence once brought back into solution.

2.2.2 INFRARED EMISSIVE NANOCLUSTERS (IR GSH NCS)

For our in vivo experiments it was also desirable to have NCs with IR emission, to have an emission in a window that is not coinciding with the autofluorescence of the biological material. To do this, a synthesis already reported in the literature[98] has been optimized in which, by slightly varying the ratios between gold salts and GSH (1 $HauCl_3$: 0.8 GSH) , it was possible to have NCs with emission at 820 nm (IR GSH NCs) in just 2 hours. By decreasing the quantity of GSH with respect to gold salts, NCs are formed with part of the surface not covered by the binder, and this causes infrared emission centers to be created on the surface, not present in the classic Reds. GSH NCs in which the entire surface is saturated with binder (**Figure 39a**).

By imaging the GSH IR NCs with TEM it is possible to see the higher polydispersity compared to the GSH Red NCs, however, underlining in any case crystalline and well dispersed NCs without aggregation phenomena. The solution appears in this case of a slightly darker transparent yellowish, tending to brownish, as shown in the inset of **Figure 39b**.

To probe the optical properties of GSH IR NCs, the 2D mapping of excitation and emission (**Figure 39c**) was obtained by spectrofluorimetry. These NCs have a much wider excitation range ranging from 300 to 700 nm with a peak at about 380 nm; the emission, on the other hand, is narrower with a maximum around 820 nm.

Subsequently, a ligand exchange was carried out with C_3E_6D also for this type of NCs to functionalize it and make it activatable with molecular groups of biological interest. However, this experiment led to different results with respect to the functionalization of the Red NCs, since this time the emission peak does not remain constant. Instead, there is the formation of emission centers at 600 nm that come from the metal core rather than from the surface, following a greater surface coverage of the NCs. Therefore, at the same time we obtain the presence of an emission peak similar to that of GSH Red NCs at 600 nm and another that corresponds to that of GSH IR NCs at 820 nm (**Figure 39d**). Following the ligand exchange there is a reduction in QY which goes from 4% for the post synthesis particles to 2% after the ligand exchange.

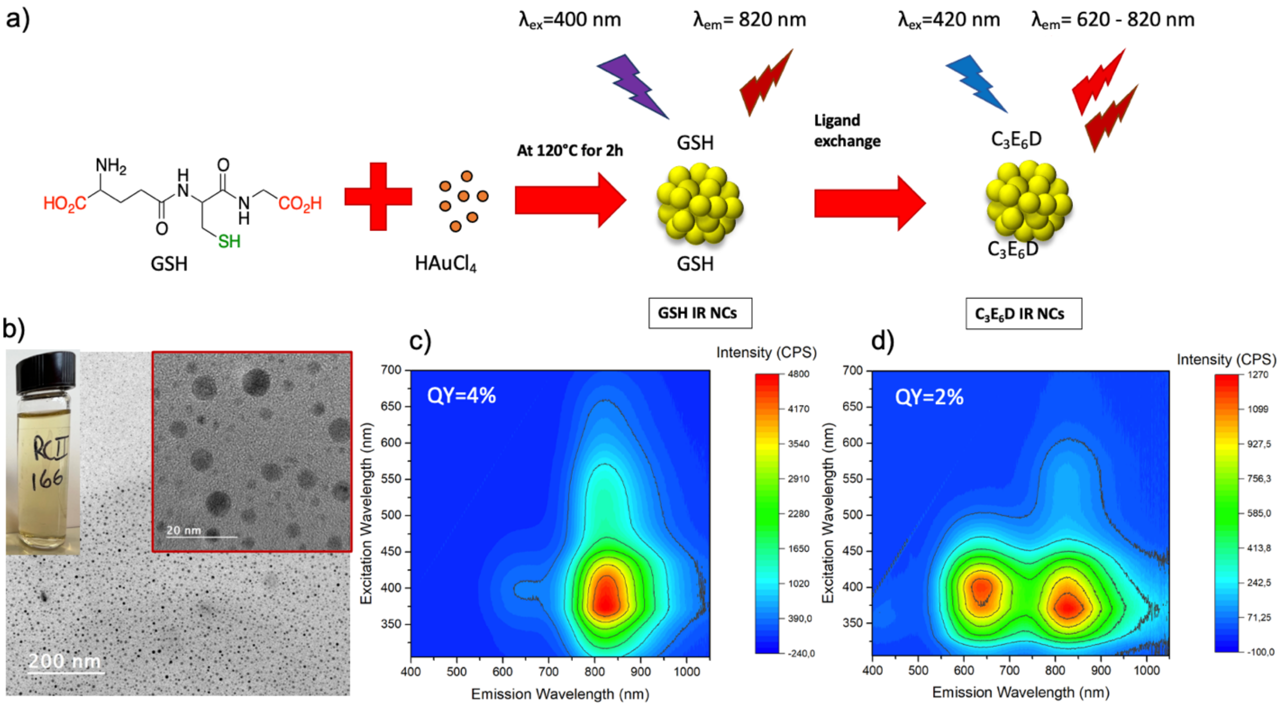

FIGURE 39. (a)Scheme concerning C_3E_6D IR NCs synthesis. (b) HR-TEM images with GSH IR NCs solution on the left inset. Fluorescence 2D map of (c) GSH IR NCs and (d) C_3E_6D IR NCs.

Since a higher synthesis temperature (120°C) was used, it was necessary to follow the fluorescence intensity as the synthesis time changed to optimize it. In **Figure 40 a,b,c** and the 2D excitation-emission mapping respectively after 1, 2 and 3 hours of synthesis time is represented. Comparing the different luminescence intensities (**Figure 40d**) we obtain the highest intensity after 2 hours of synthesis.

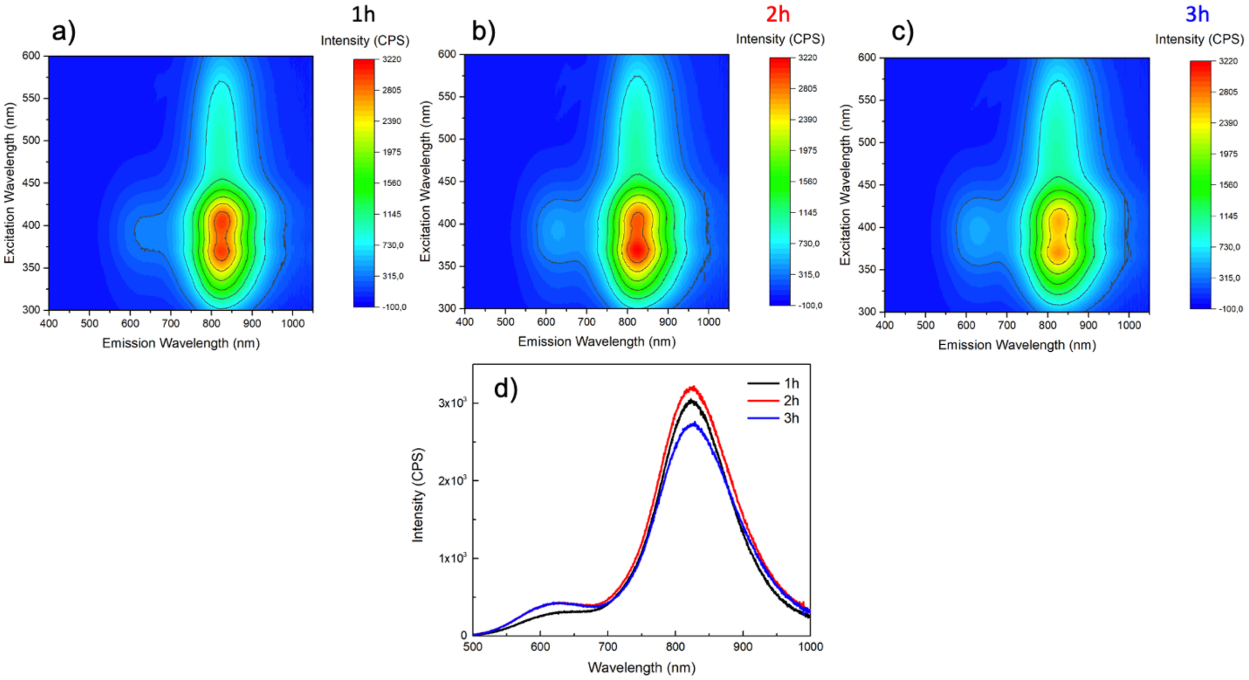

FIGURE 40. Fluorescence 2D maps after (a) 1 hour, (b) 2 hours and (c) 3 hours of GSH IR NCs synthesis. (d) Comparison of luminescence emission spectra at different synthesis times by exciting at 400nm.

The synthesis of IR GSH NCs causes NCs to be created with more polydisperse dimensions than Red GSH NCs. In fact, from the HR-TEM image (**Figure 41a**) it is possible to notice a separation line that shows the presence of different families of NCs within the same sample: in the upper part of the image there are monodisperse NCs of about 2 nm (**Figure 41b**) , while in the lower part in addition to the 2 nm NCs there are crystalline NCs of about 4 nm, which are too large to be fluorescent (**Figure 41 c,d**). Consequently, it would be possible, after synthesis, to remove these non-fluorescent NPs by means of a low-speed centrifugation. Furthermore, even not considering the large NPs of 4 nm, the NCs population of about 2 nm present in the GSH IR NCs sample has a greater polydispersity than the Red GSH NCs, since there is the presence of smaller particles, of about 1 nm, more similar to Blue C_3E_6D NCs which we will talk about later.

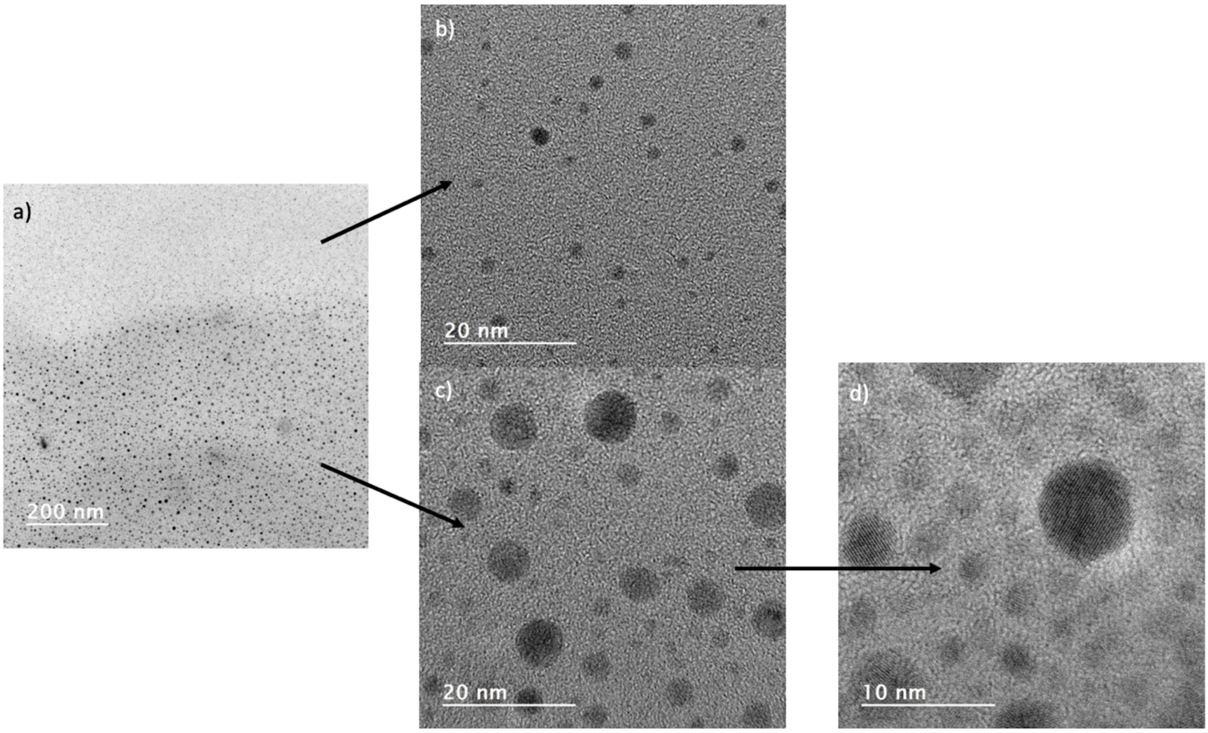

FIGURE 41. (a,b,c,d) HR-TEM images at different magnification of GSH IR NCs.

To measure the dimensions of the NCs, the diameters were measured starting from the HR-TEM images, and a histogram was created by fitting with a single Gaussian and obtaining an average value of 1.9 nm ± 0.7 nm (**Figure 42**). It was realized, however, that fitting the 4 nm peak with only one Gaussian was not considered. Finally, 3 Gaussians were used to make the fit (**Figure 42b**). Thus 3 peaks are obtained, one relating to large non-fluorescent NPs at 4.1 nm ± 1.4 nm, one with dimensions similar to GSH Red NCs at 2 nm ± 0.4 nm and one with even smaller dimensions corresponding to C_3E_6D Blue NCs, which we will present later, at 1.3 nm ± 0.2 nm. As expected from the nucleation process, it is also possible to note that decreasing the size of the NCs also decreases the polydispersity associated with the family.

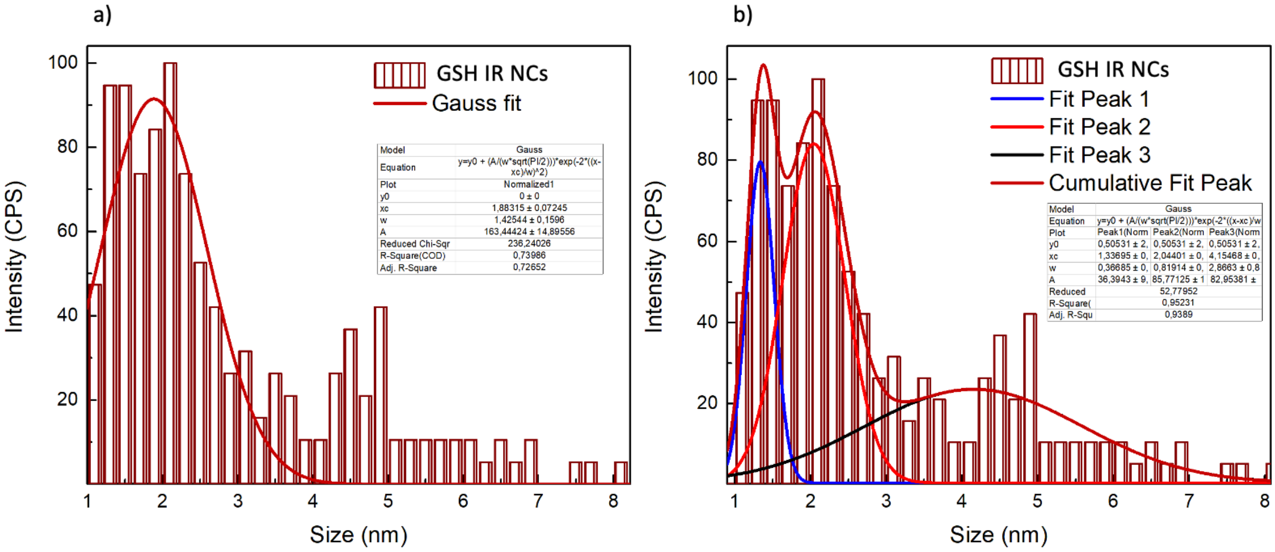

FIGURE 42. HR-TEM size histogram of GSH IR NCs fitted with (a) one or (b) three gaussian.

2.2.3 BLUE EMISSIVE NANOCLUSTERS (C_3E_6D NCS)

To obtain functionalized NCs in a single step, it was decided to proceed with a direct synthesis by placing the gold salts in the presence of C_3E_6D (1 mol eq $HauCl_3$: 1.5 mol eq C_3E_6D) and heating to 120 ° C. After 4 hours the Blue C_3E_6D NCs with emission in the blue region are ready (**Figure 43a**). Analyzing at HR-TEM (**Figure 43b** and **Figure 44 a,b,c**) the NCs appear crystalline, well separated and with very small dimensions (1.7nm ± 0.5nm), even smaller than the GSH Red NCs; This smaller metal core causes a blue shift in the emission wavelength. In the inset of **Figure 43b** is shown the suspension after synthesis; it has a completely transparent color, losing the yellowish color typical of GSH Red NCs. The optical properties have been tested by spectrofluorometry: in the 2D mapping a narrower excitation window was observed in comparison to the other types of NCs ranging from 380 nm to 430 nm. On the contrary, a larger emission window with a peak at 490 nm (**Figure 43c**) was observed. The NCs thus synthesized do not required any ligand exchange and can be directly chemically functionalized thanks to the terminal carboxylic groups.

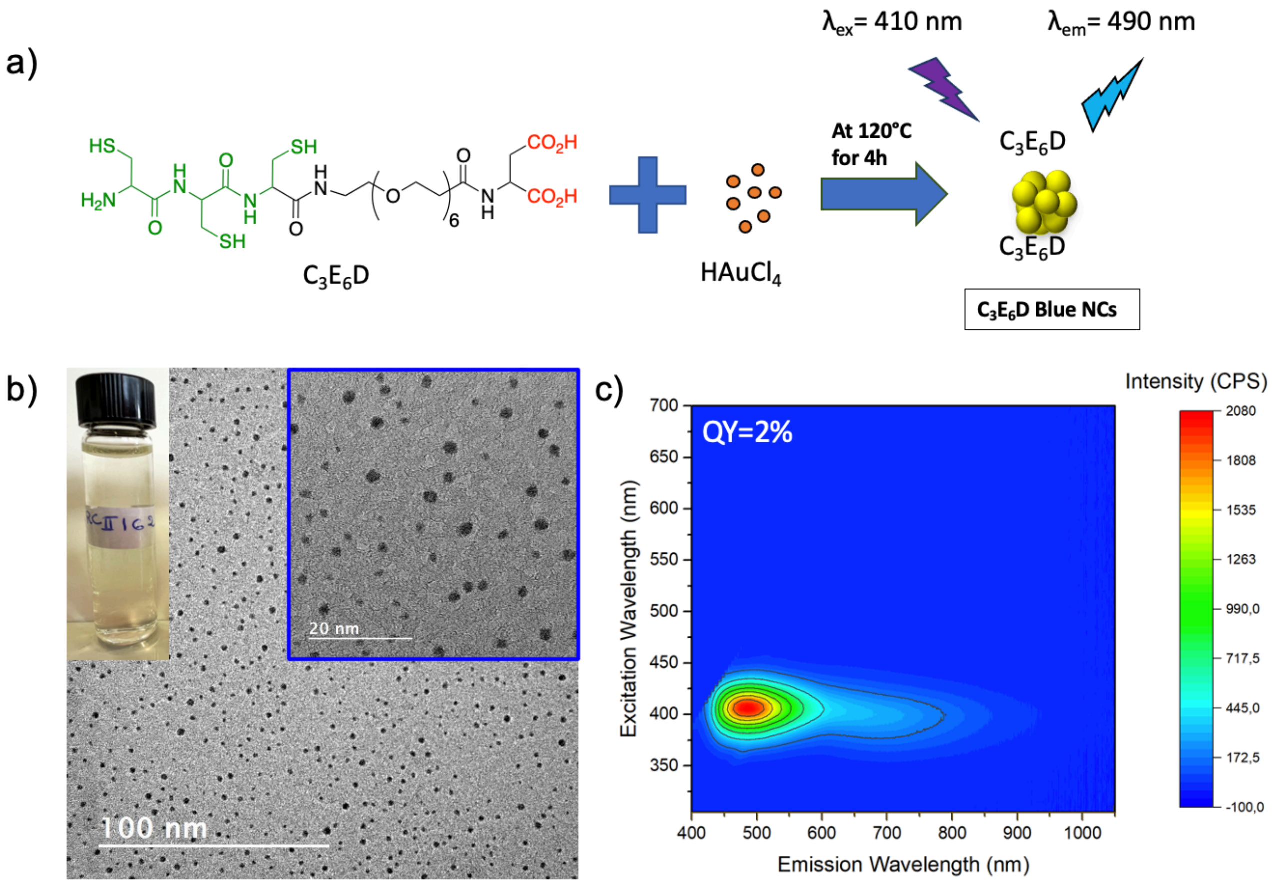

FIGURE 43. (a) Scheme concerning C_3E_6D Blue NCs synthesis. (b) HR-TEM images with NCs solution on the left inset and (c) fluorescence 2D map of GSH Red NCs with

Since it is an innovative synthesis, the kinetics of synthesis have been studied by taking samples every hour or so during the synthesis. In **Figure 44 d,e** it is possible to find the dotted excitation curve and the emission in a continuous line. Initially in the first two hours, there is the presence of NCs emitting at about 700 nm which, during the synthesis, disappear, leading to the progressive increase of the peak at 490 nm, until reaching a maximum intensity and decreasing again if the synthesis is prolonged after, worsening the fluorescence properties. In this way the synthesis times were optimized by finding the maximum fluorescence intensity after 4 hours of synthesis. To understand more clearly what happens to the excitation curve during synthesis, it has been normalized and reported in **Figure 44**; initially the excitation peak is at 390 nm and as the synthesis progresses this peak shifts to the right at longer wavelengths up to 410 nm where it stabilizes.

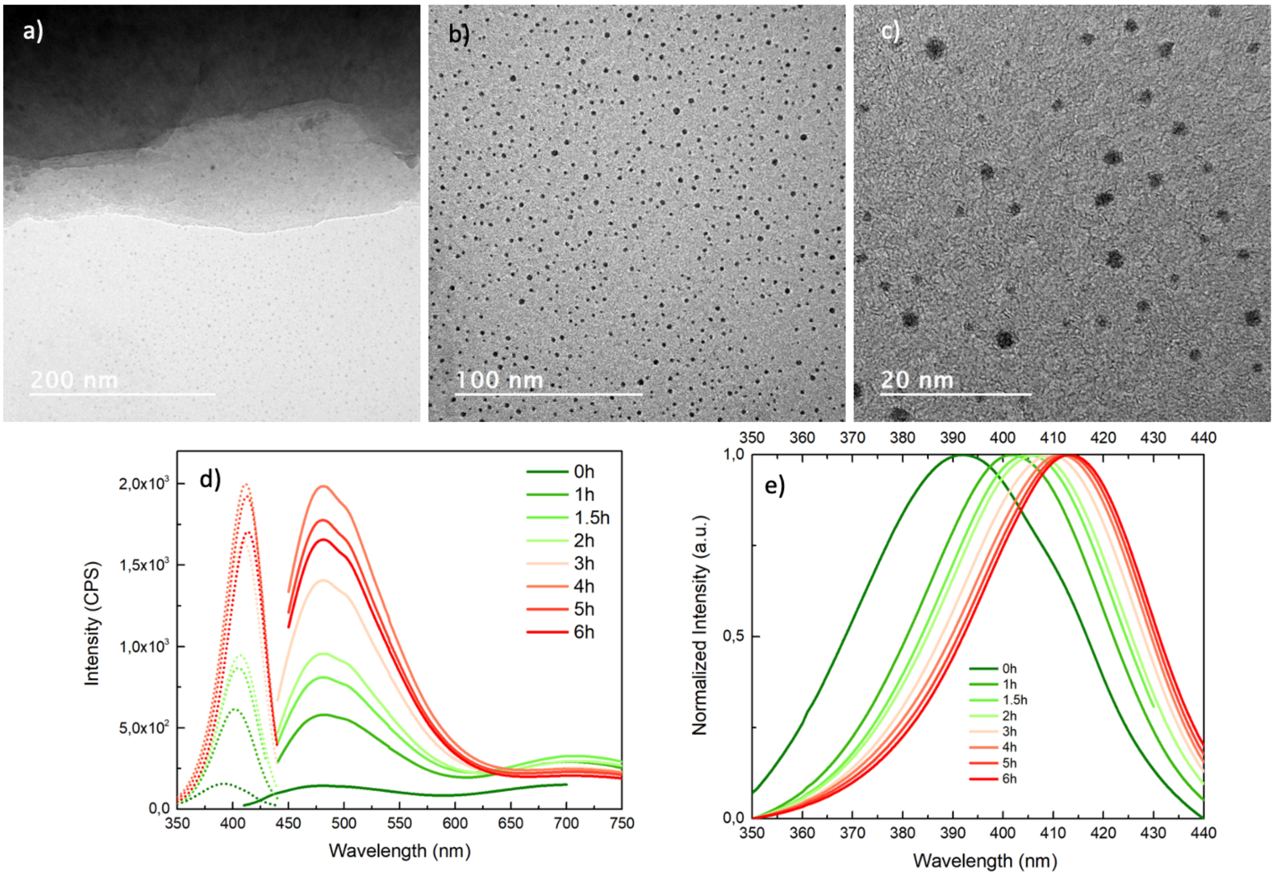

FIGURE 44. (a,b,c) HR-TEM images at different magnification, (d) excitation (dotted line) and emission (solid line) spectra and (e) normalized excitation spectra of C_3E_6D Blue NCs

Similarly to the GSH Red NCs, the evolution of the size of the NCs over time was studied by DLS technique. Analyzing a solution prepared for 8 months, small particles but also of large clusters of hundreds of nm were detected. The situation worsens after 12 months in which most of the sample results in agglomerations of NCs. To visualize what happens in the sample after one year, a measurement was made at HR-TEM (**Figure 45c**) which shows the presence of polymer bubbles with NCs inside, which however continue to be well separated from each other and which consequently do not create precipitates. These processes cause the luminescence intensity to decrease over time faster than for GSH Red NCs, as shown in **Figure 45b**.

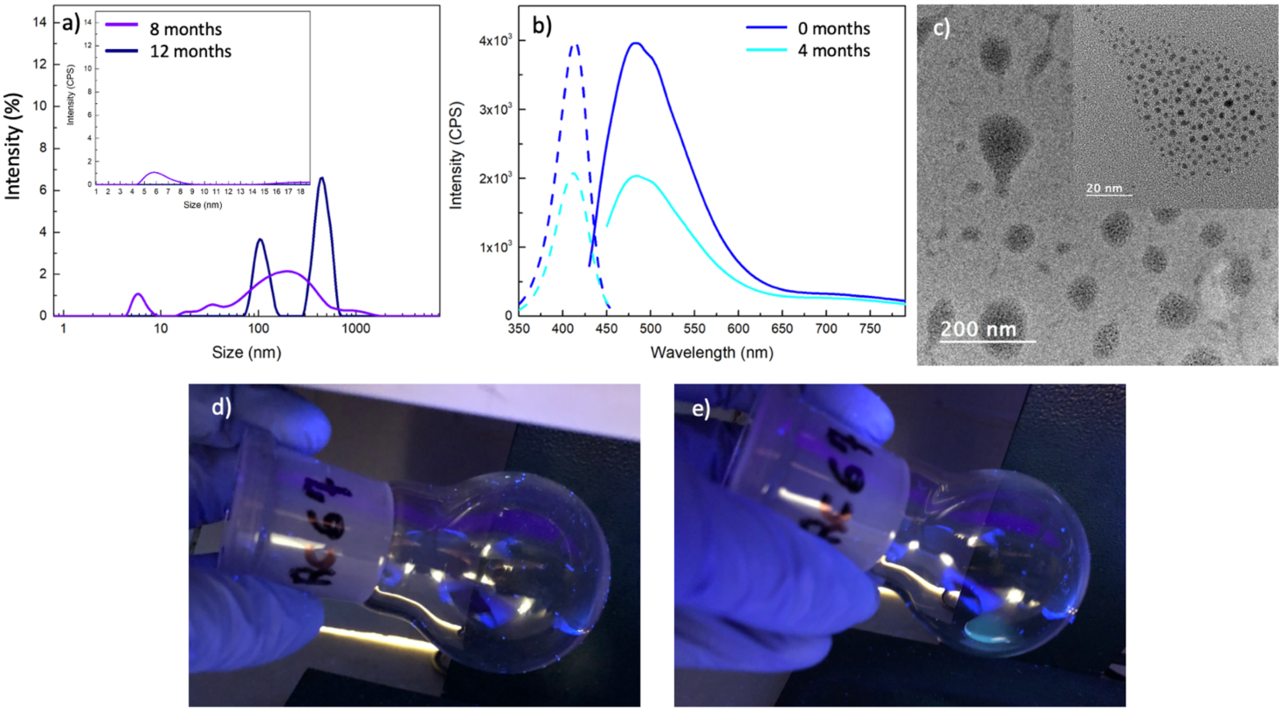

FIGURE 45. DLS (a) and fluorescence (b) stability study of C$_3$E$_6$D Blue NCs. (c) HR-TEM images at different magnification of C$_3$E$_6$D Blue NCs after 12 months from the synthesis. Images of lyophilized (d) and redispersed in water (e) C$_3$E$_6$D Blue NCs.

The Blue NCs were also lyophilized to see if the fluorescence was maintained and if it was possible to easily redisperse them in water after lyophilization. Also in this case the fluorescence is recovered after adding water to the lyophilized powders (**Figure 45e**), but this time the fluorescence of the powder is not visible in the flask (**Figure 45d.)**

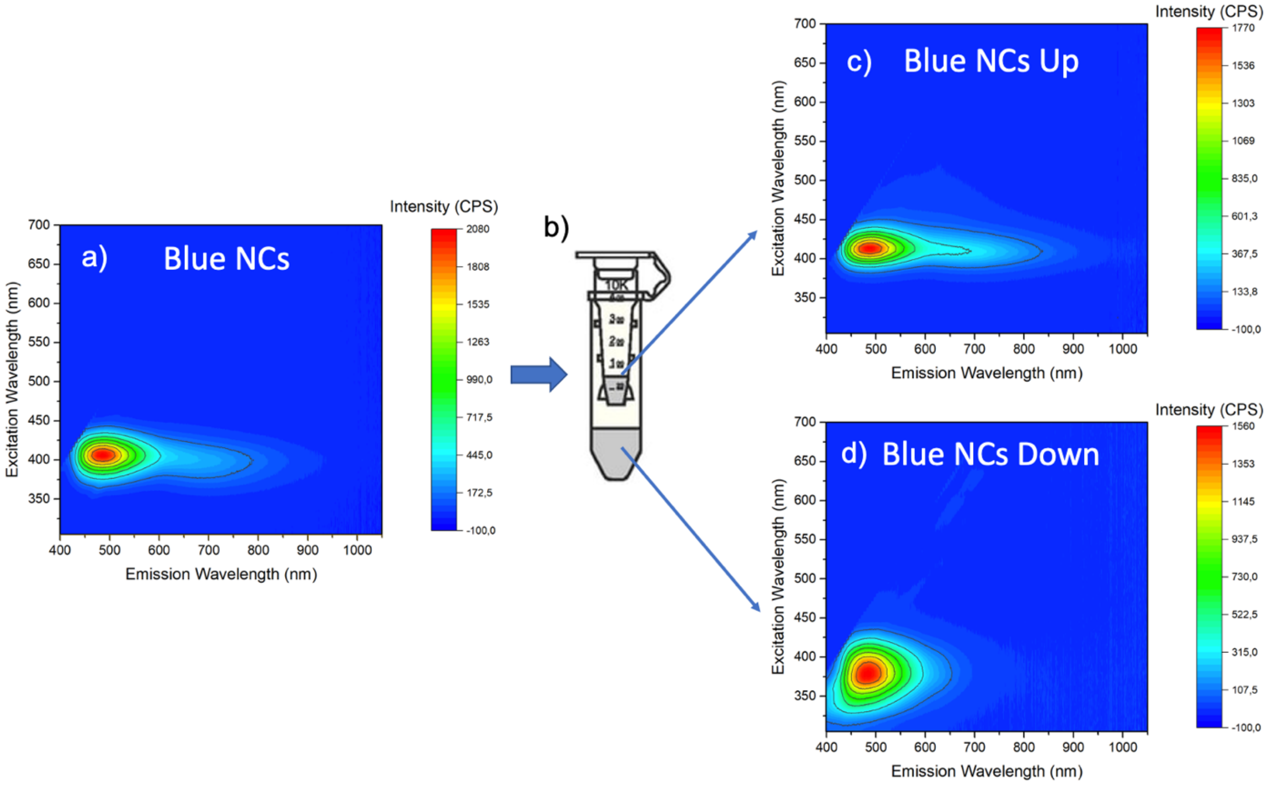

FIGURE 46. C$_3$E$_6$D Blue NCs Fluorescence 2D maps (a) before and (c,d) after Amicon 3KDa Ultrafiltration. (b) Schematic view of Amicon solution separation. Fluorescence 2D maps of (c) filtred NCs solution and (d) excess of free C$_3$E$_6$D overcaming the 3 KDa Amicon filter.

Before using the NCs, purification was carried out by ultrafiltration to remove all the unbound C$_3$E$_6$D. Following this purification, it was realized that what passed the 3 kDa filter was still fluorescent, so we decided to analyze the solution remaining inside the filter (upper solution) and the solution that passes the filter (bottom solution) separately.

In **Figure 46** the 2D fluorescence mapping before (**Figure 46a**) and after (**Figure 46 c,d**) filtration are compared. The upper solution presents a luminescence similar to the unpurified NCs (**Figure 46c**), but the excitation window narrows creating an even more elongated shape. On the contrary the bottom solution exhibits a change in fluorescence since the excitation window starts even from 300 nm (**Figure 46d**). The Au content of both solutions was analyzed by ICP, but no presence of gold was detected in the bottom solution (unlike the upper solution), so the fluorescence found in the bottom solution could be attributed to the ligand heated by the NCs synthesis, even if further experiment as RMN and mass spectroscopy are needed to chemically analyze the sample and understand which is the mechanism that generate the ligand fluorescence. This hypothesis could explain the change in the excitation wavelength during the Blue NCs synthesis (**Figure 44e**), since at the beginning of the synthetic process there is a fluorescence peaked at 390 nm that may be due to fluorescent peptide species (**Figure 46d**), and then with the formation of Au NCs, the peak shifts to 410 nm, the typical excitation wavelength of the purified Blue NCs of the upper solution (**Figure 46c**).

2.2.4 DIFFERENT EMISSIVE NANOCLUSTERS COMPARISON

To get an overview, the three types of NCs have been compared here in their morphological and optical properties. In **Figure 47** are shown the excitation and emission of the 3 types of NCs: the C_3E_6D blue NCs have a smaller excitation band than the emission band; the opposite case is represented by the GSH IR NCs which have a much wider excitation band than the emission one; GSH Red NCs are instead in a middle condition where the size of the two windows is comparable.

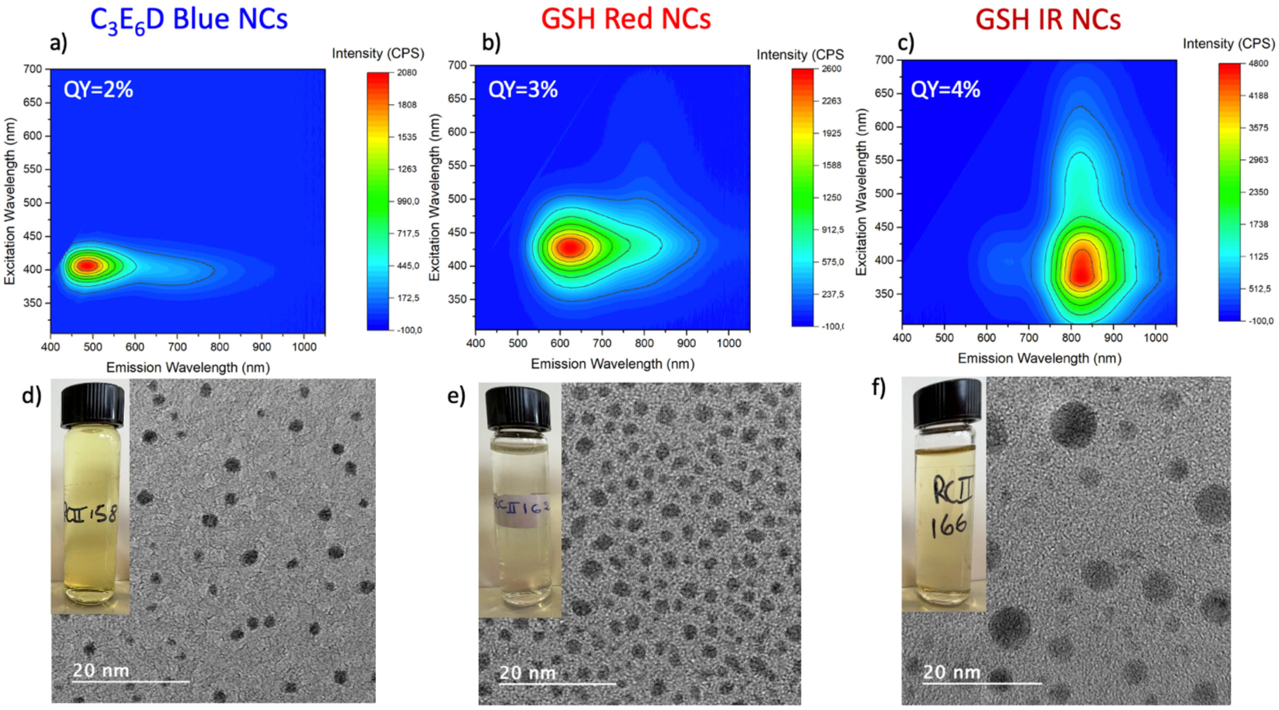

FIGURE 47. (a,b,c) Fluorescence 2D maps, (d,e,f) HR-TEM images and NCs solutions photos in the inset of (a,d) C_3E_6D Blue NCs, (b,e) GSH Red NCs and (c,f) GSH IR NCs.

As can be seen in **Figure 48** the peaks of the excitation curves for the three types of NCs are almost coincident, while the emissions are very different and cover almost the entire visible and infrared spectrum. Although the solutions are quite transparent, the absorption spectrum of each NCs type has been measured (**Figure 48a**): in all cases there are no specific absorption peaks since the surface plasmon are not present in the gold NCs on the contrary to gold nanoparticles (AuNPs). Furthermore, the strong absorption below 300 nm is related to the scattering due to the colloidal size of the NCs.

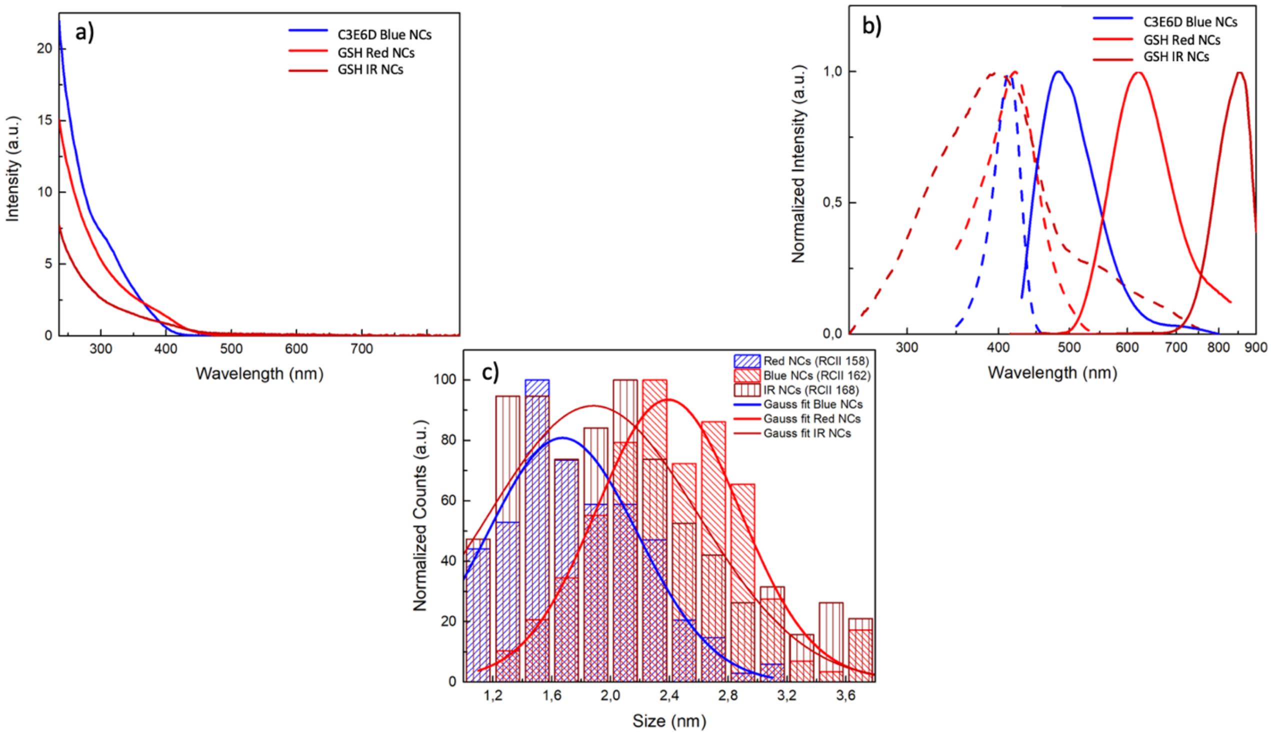

FIGURE 48. (a) Absorbance, (b) excitation and emission luminescence spectra and (c) HR-TEM size histogram of (blue Line) C_3E_6D Blue NCs, (red line) GSH Red NCs and (dark red line) GSH IR NCs.

By analyzing the images at HR-TEM, size histograms were made by measuring the diameters of the NCs. By eliminating the non-fluorescent NCs with dimensions of 4 nm present in the solution of GSH IR NCs after the synthesis, the histogram presented in **Figure 48**c is obtained. The C_3E_6D Blue NCs have an average size of 1.7nm ± 0.5nm and the GSH Red NCs of 2.4nm ± 0.5nm; this increase in size of about 1 nm induces a large red-shift of the position of the emission band, from blue to red. This size effect is attributed to quantum effect as reported in the literature[4,98–100]. In the case of GSH IR NCs they were found to have an intermediate size with an average diameter of 1.9 nm ± 0.7 nm. In this case, although inside the sample there are particles with a diameter similar to the Red and Blue NCs, since there is a greater polydispersity, the fluorescence is different from both. The fluorescence with a maximum at 800 nm belonging to GSH IR NCs is attributed to another process: it doesn't come from the metal core (as for the other types of NCs) but from emission centers on the surface generated by the uncovered metal surface which is not statured by the ligands (initial low ratio ligand/gold). The highest quantum yield (QY) occurs in the case of the GSH IR NCs (4%); it decreases to 3% for GSH Red NCs and even to 2% for C_3E_6D NCs (**Table 5**).

Name	C3E6D Blue NCs	GSH Red NCs	C3E6D Red NCs	MUTAB Red NCs	GSH IR NCs	C3E6D IR NCs
Emission	**500 nm**	**600 nm**	**600 nm**	**600 nm**	**800 nm**	**800 nm**
Ligand	**C3E6D**	**GSH**	**C3E6D**	**MUTAB**	**GSH**	**C3E6D**
QY (%)	2	3	6	3	4	2

TABLE 5. Quantum Yields (QY %) of each type of NCs.

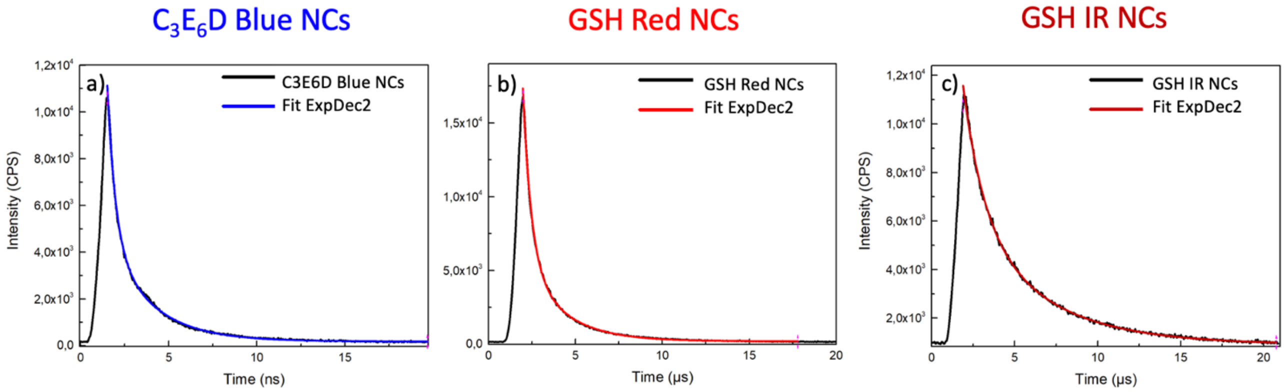

FIGURE 49. Two exponential decay fit of (a) C_3E_6D Blue NCs (blue Line), (b) GSH Red NCs (red line) and (c) GSH IR NCs (dark red line) lifetime measurements.

Lifetime measurements were made to compare the 3 types of NCs (**Figure 49**). In all cases there are two average lifetimes, as can be seen in the corresponding tables also indicating the percentage contribution of each average lifetime (**Table 6**). One can notice that there is a major contribution of one of them, τ_1, in all case Therefore one can compare the values of τ_1. Only the polydisperse IR NCs exhibit a larger contribution of τ_2.

a)

Blue NCs	Value (ns)	Rel (%)
τ_1	0.46 ± 0.01	95.4
τ_2	2.43 ± 0.03	4.6

b)

Red NCs	Value (ns)	Rel (%)
τ_1	484.1 ± 5.8	98.0
τ_2	2197.1 ± 32.3	2.0

c)

IR NCs	Value (ns)	Rel (%)
τ_1	1232.9 ± 36.6	74.4
τ_2	4535.5 ± 115.3	25.6

TABLE 6. Lifetimes values and percentage of (a) C_3E_6D Blue NCs (blue Line), (b) GSH Red NCs (red line) and (c) GSH IR NCs (dark red line) luminescence emissions.

In the case of Blue NCs the lifetime is much lower (in the range of 1 ns) than the ones obtained for the other two types of NCs (Red NCs 500 ns and IR NCs 1230 ns). The Red and IR NCs have a typical lifetime corresponding to a deexcitation process through a triplet state (phosphorescence) whereas the blue NCs appears to have a direct deexcitation process (fluorescence). These data were collected on the CAPHTER platform with the assistance of Dr. Gregory Taupier.

2.2.5 SYNTHETIC PEPTIDES FUNCTIONALIZATION OF NANOCLUSTERS

Through various experiments conducted in the laboratory we were not able to synthesize NCs with red emission through direct synthesis with C_3E_6D, not even by decreasing the amount of C_3E_6D, and consequently the amount of thiol function in the ligand, in order to have a red shift. Consequently, by starting from the chemical structure of GSH, it was decided to design and synthesize new peptides to generate NCs with an emission wavelength that can be modulated based on the number of cysteines in the ligand or on the ratios between ligand and gold.

The objective was to generate NCs directly functionalizable with an emission in the blue, red or IR region without any ligand exchange as for the case of GSH. To do so we decided to synthetize innovative ligands, with a higher affinity to gold and with a longer chain that makes them more stable in aqueous solution and functionalizable through the carboxylic group at the end. To increase the gold affinity a polycystein $(Gly\text{-}Cys)_n$ sequence was added (instead of the single cysteine of GSH). A Gly as a spacer without steric hindrance was introduced between two successive cysteines to ensure that the thiol groups are oriented in the same direction so that they can interact together with gold atoms at the surface of the nanoclusters.

4 peptides have been selected as shown in **Figure 50**. They were prepared using classical solid phase supported synthesis by Raffaello Paolini, who is a postdoc in the chemistry group at the University of Rennes 1. The structures were selected according to the criteria previously mentioned. The parameters expected to play an important role are the following: i) the number of (Gly-Cys) repeat units in the cysteine sequence, ii) the length of the hydrophilic spacer (Gly-Ala).

A parallel synthesis was then conducted to test the role of the different peptides in the synthesis of NCs, using the same GSH Red NCs (1: 1.5) and GSH IR NCs (1: 0.8) synthesis ratios of $HAuCl_4$: peptide.

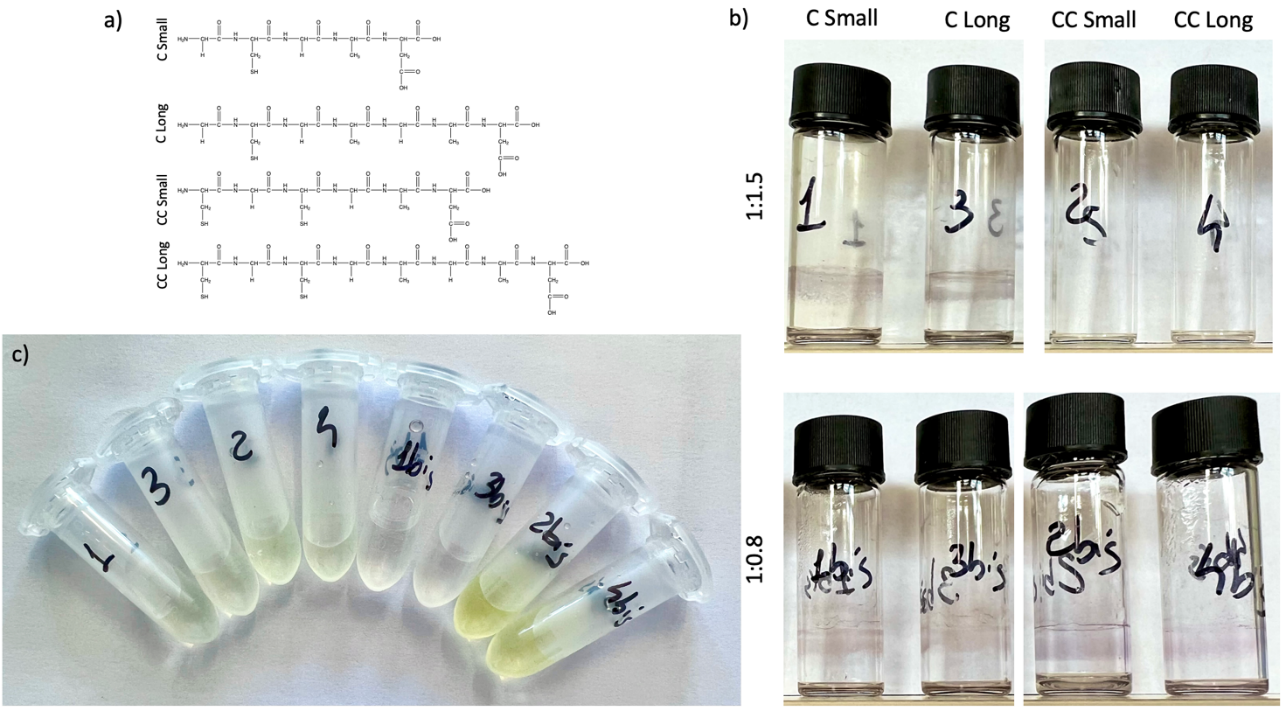

FIGURE 50. (a) Ligands chemical structures used for Peptides NCs synthesis. (b) Gold deposition on vials and (c) NCs solutions obteined after Peptides NCs synthesis.

Almost all the syntheses generated a colored deposition on the walls of the reaction vial, which is attributed to the precipitation of metallic gold sticked to the glass walls. The color of the deposition is different for each type of synthesis. But it is possible to notice similarities when the length of the peptide is the only different parameter (**Figure 50b**). The only case in which there is no deposition on the walls is the peptide with (Gly-Cys)$_2$ with a ratio 1:1.5.

The resulting solutions were taken from the synthesis containers to better see the color (**Figure 50c**). Also in this case, similar colors are obtained for groups of two, when the only difference is the length of the peptide. This indicates that this parameter does not drastically affect the synthesis kinetics. All the syntheses carried out with ratios 1:1.5 have a very transparent yellowish color as a common color, while those with ratios 1:0.8 give very different colors in the case in which the peptide contains one or two cysteines: a completely transparent solution in the case of monocysteine peptides and an intense yellow in the case of two cysteines.

The syntheses were conducted at a lower temperature (80°C) than the temperature used for all other types of NCs presented above (120°C), in order to limit water evaporation as the reaction volumes were very small (2 mL). Because of the lower synthesis temperature, it was necessary to increase the synthesis times. Consequently a preliminary kinetics experiment was carried out by measuring the fluorescence at two different times to optimize the synthesis. As expected, after 8 hours there is an increase in fluorescence compared to the 4 hours of synthesis, indicating that probably by further increasing the synthesis times, more fluorescent NCs can be obtained. In the literature the preparation of NCs at 70°C is described with a synthesis time of about 24 hours; so the reaction time could be further increased to find the best condition.

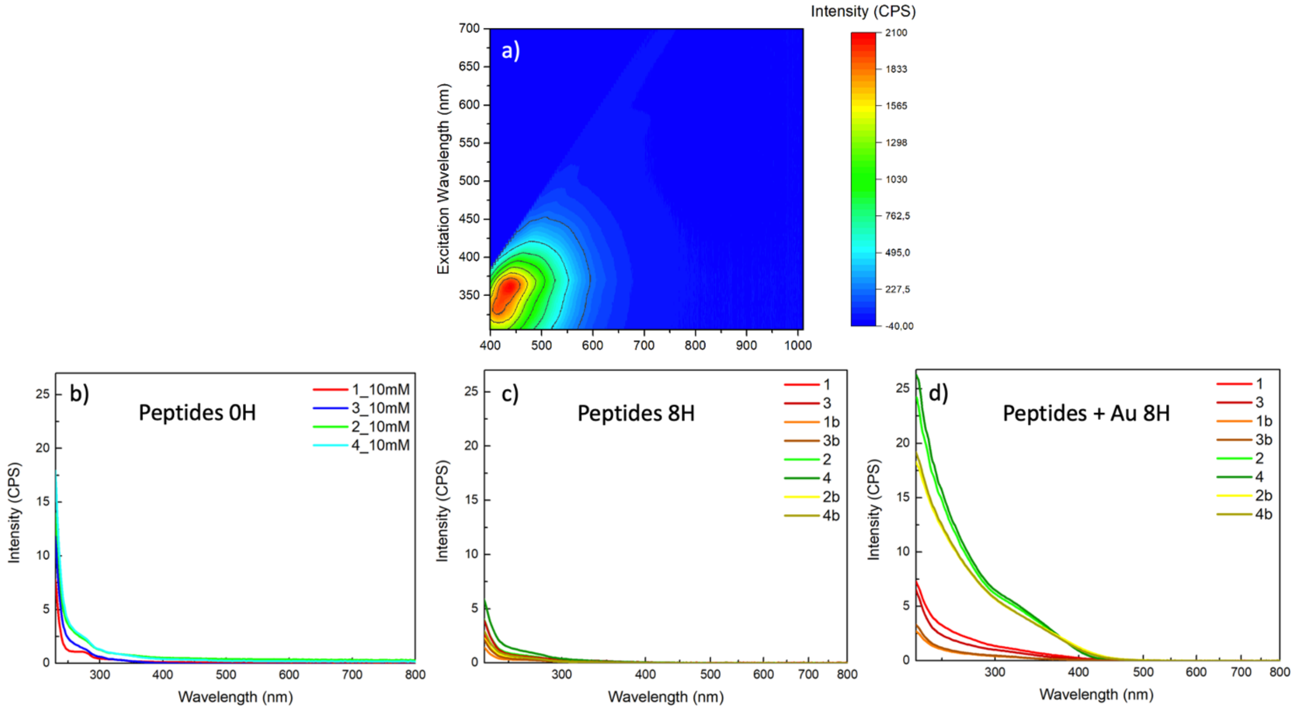

FIGURE 51. (a) Luminescence 2D maps of peptides after heating for 8 hours. Absorbance spectra of peptides (b) before and after heating for 8 hours (b) alones or (d) in presence of gold salts.

The same type of experiment was conducted by heating the peptides under the same conditions but in the absence of gold salts and evaluating the optical properties to consider any fluorescence belonging to the heated peptide, as observed in the case of C_3E_6D. After synthesis, all the solutions showed a blue fluorescence with an elongated diagonal shape that indicates a variation of the emission peak as a function of excitation, a characteristic not related to NCs (**Figure 51a**). In addition, a higher fluorescence signal was noted by increasing the length of the peptide and the number of cysteines in the peptide itself. To go into more detail, the UV-Vis absorption spectra for the initial peptide solutions were measured, and after 8 hours of synthesis in the absence and presence of gold salts. Unlike peptides which maintain an absorbance after 8 hours of synthesis comparable to that before synthesis (**Figure 51 b,c**), in the presence of gold salts, for some samples in particular there is an increase in the intensity of absorption actually due to an increase in scattering processes generated by the presence of NCs inside the solution (**Figure 51d**). It therefore seems that in all cases in which there are two cysteines in the peptide, there is a higher production of NCs, contrary to the cases with a single cysteine and ratio (1:0.8) in which no trace of NCs was detected by absorbance or fluorescence. This hypothesis is also confirmed by the 2D fluorescence map in **Figure 51 a,b,e,f** which shows only a blue fluorescence belonging to the heated peptide; this fluorescence is present in all syntheses with a single cysteine and ratio (1:0.8).

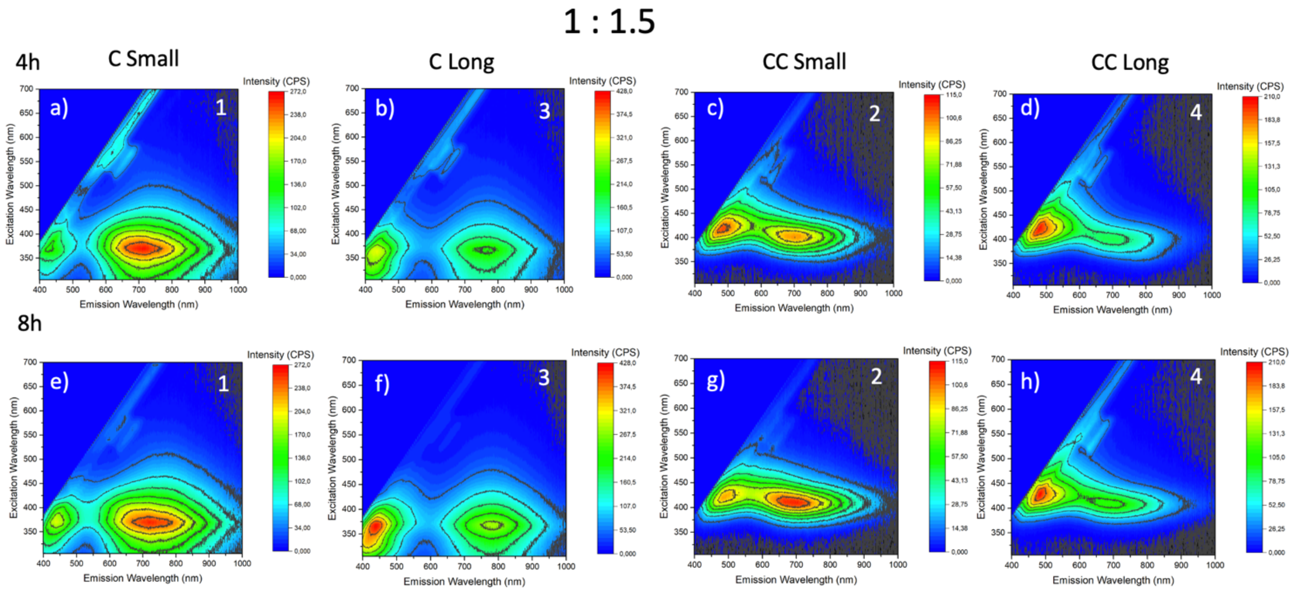

FIGURE 52. Luminescence 2D maps of Peptide NCs obetined using the peptide (a,e) C Small, (b,f) C Long, (c,g) CC Small and (d,h) CC Long after (a,b,c,d) 4 hours and (e,f,g,h) 8 hours of synthesis using the ratio 1 $HAuCl_3$: 1.5 Peptides.

The fluorescence properties of all the syntheses were analyzed in detail, particularly to distinguish the auto-fluorescence of the peptide from that of the NCs in the maps. In the case of syntheses with ratio (1:1.5), NCs are obtained with red emission in the presence of a single cysteine, regardless of the length of the peptide (**Figure 52 a,b,e,f**), while a blue fluorescence begins to appear in the case of peptides with two cysteines (**Figure 52 c,d,g,h**). This could happen because an increase in thiol groups concentration has a similar effect to increasing in peptide equivalents which generate smaller blue emission NCs[4,99,100].Instead, in the case of synthesis ratios (1:0.8) there is the total absence of fluorescence related to NCs in the case of peptides with monocysteine (**Figure 53 a,b,e,f**) and the presence of an IR fluorescence (around 800 nm) in presence of peptides with two cysteines (**Figure 53 c,d,g,h**), as obtained in the case of GSH IR NCs with the same ratio condition (Au : GSH).

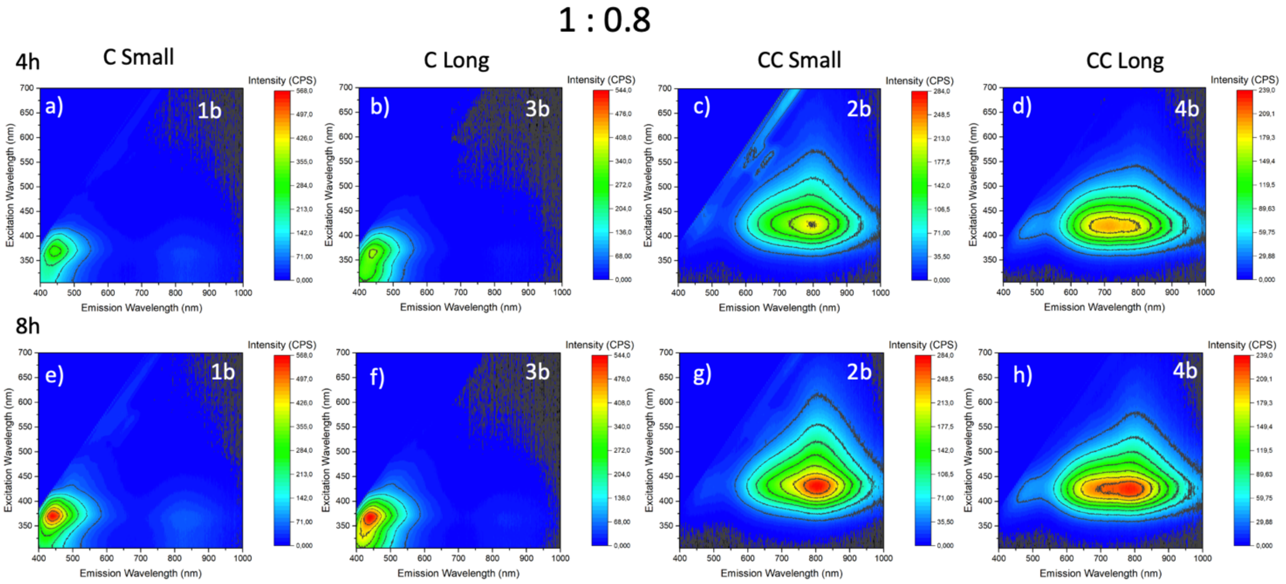

FIGURE 53. Luminescence 2D maps of Peptide NCs obetined using the peptide (a,e) C Small, (b,f) C Long, (c,g) CC Small and (d,h) CC Long after (a,b,c,d) 4 hours and (e,f,g,h) 8 hours of synthesis using the ratio 1 $HAuCl_3$: 0.8 Peptides.

In the future it would be desirable to repeat this synthesis and prolong it for 24 hours, using peptides with even greater purity, since the presence of impurities within the peptides synthesized in our laboratory (above 70% of purity) could have caused the actual ratios between gold and peptide to vary from the calculated one, varying by consequently the results of the synthesis. This could also explain why with (1:0.8) ratio and a single cysteine there are not enough SH groups to form NCs if the actual ratio is lower. In conclusion these preliminary results suggest that the poly cysteine sequence (Gly-Cys) permits to decrease the ratio between gold and peptide to obtain NCs.

2.2.6 MICROWAVE ASSISTED NANOCLUSTERS SYNTHESIS

To further speed up the synthesis process and decrease the formation of parasitic blue fluorescence, it was decided to conduct the synthesis of NCs in the microwave. Different synthesis protocols were used using a classical kitchen microwave and therefore only the power, time and number of cycles have been varied. In all cases fluorescent NCs were obtained with similar emission and excitation wavelengths since it depends more on the type of ligand and on the ratios between the latter and the gold salts. For simplicity, therefore, only the simplest synthesis will be presented which led faster (in less than 2 minutes) to the formation of the NCs and which worked the same way for both the GSH Red NCs and the C_3E_6D Blue NCs (**Figure 54**).

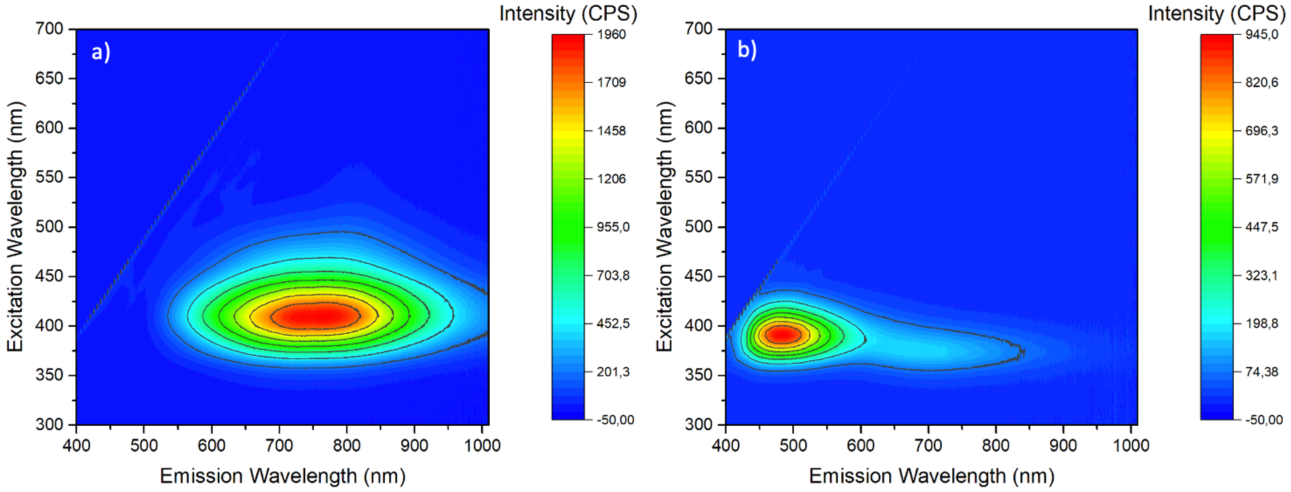

FIGURE 54. Luminescence 2D map of GSH Red NCs and C_3E_6D Blue NCs obteined by microwave synthesis.

To see if the microwave synthesis is able to avoid the formation of residual fluorescence, the same purification experiment of C_3E_6D Blue NCs done previously was reproduced (**Figure 55**) but also in this case the unbound peptide that exceeds the 3KDa membrane turns out to be fluorescent (**Figure 55d**).

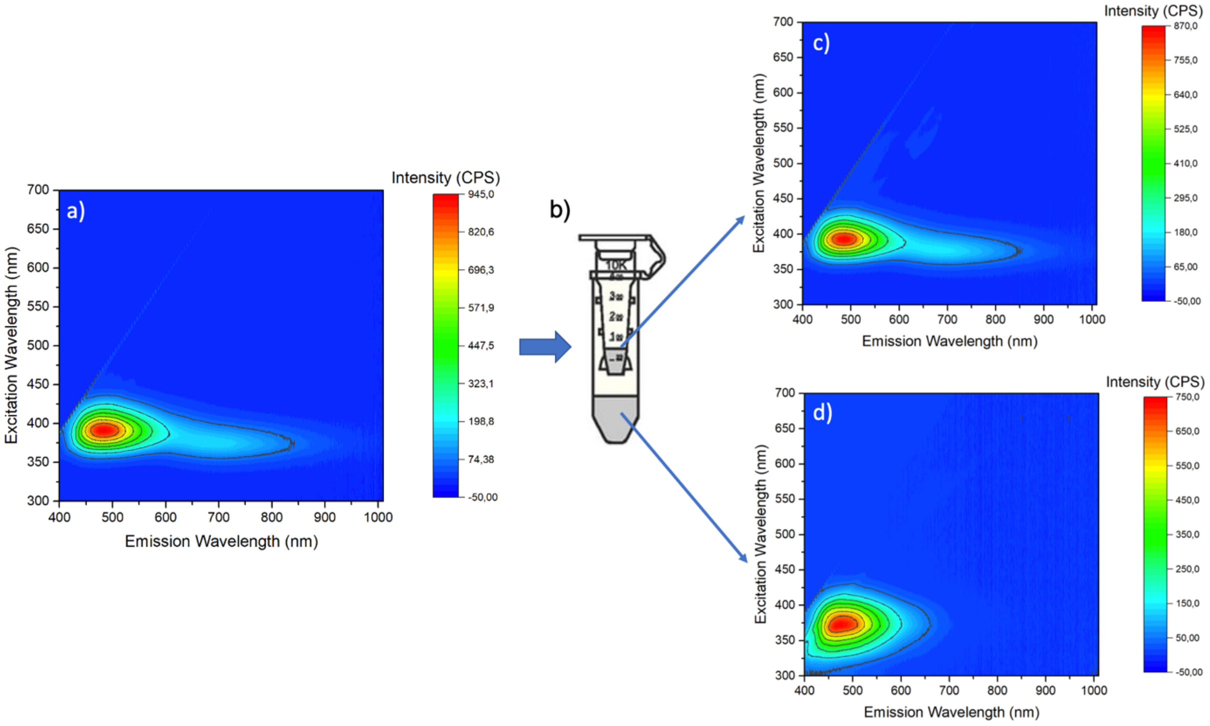

FIGURE 55. Fluorescence 2D maps of C_3E_6D Blue NCs obteined by microwave synthesis (a) before and (c,d) after Amicon 3KDa Ultrafiltration. (b) Schematic view of Amicon solution separation. Fluorescence 2D maps of (c) filtred NCs solution and (d) excess of free C_3E_6D overcaming the 3 KDa Amicon filter.

Although therefore it was not possible to eliminate the undesired peptide fluorescence, this synthesis allowed to produce NCs with different emission wavelengths much faster. These experiments performed in microwave were successful in the formation of both Red and Blue NCs. These syntheses are envisaged in the future to be optimized even on larger volumes and reproduced using the original peptides presented above.

2.2.7 EXPERIMENTAL SECTION

Materials. HAuCl4 * 3H20, 99,99% were obtained as commercial reagents by Alfa Aesar; GSH 98% was purchased by Sigma Aldrich; C_3E_6D was purchased from Agentide (USA); the peptides (C Short, C Long, CC Short, CC Long) used for Peptides NCs synthesis were produced by Dr. Raffaello Paolini, Postdoc in our Team.

NCs Synthesis. All glassware used for these synthesis were cleaned in a bath of freshly prepared aqua regia (HCl:HNO_3, 3:1 by volume) and rinsed in water 10 times before using them. The NCs solution obtained could be stored at 4 ° C for months without significant change in their optical properties.

GSH Red NCs Synthesis. A freshly prepared aqueous solution of glutathione denoted GSH (50 mM, 1,2 mL) was mixed with 16,8 mL of ultrapure water. The solution was heated in oil bath at 120°C and $HAuCl_4$ (20 mM, 2 mL) and was rapidly added to it. The reaction was stopped after stirring for 3h. An aqueous suspension of orange-emitting GSH Red NCs was formed (2.6 µM, obtained by ICP).

GSH IR NCs Synthesis. A freshly prepared aqueous solution of glutathione denoted GSH (50 mM, 1,28 mL) was mixed with 34,72 mL of ultrapure water. The solution was heated in oil bath at 120°C and $HAuCl_4$ (20 mM, 4 mL) and was rapidly added to it. The reaction was stopped after stirring for 2h. An aqueous suspension of IR-emitting GSH IR NCs was formed.

C_3E_6D Blue NCs Synthesis. A freshly prepared aqueous solution of C_3E_6D (20 mM, 0.585 mL) was diluted with distillated and deionized H_2O to reach a final volume of 2.7 mL. After dipping the flask containing the solution in an oil bath at 120 ° C under stirring, a solution of HAuCl4 (20 mM, 0.3 mL) was quickly added to it. The reaction was stopped after 4 h. An aqueous solution of C_3E_6D Blue NCs was obtained which emit in the blue region.

C_3E_6D Red or IR NCs Ligand Exchange. A freshly prepared aqueous solution of C_3E_6D (20 mM, 0.155 mL) was mixed with 1 mL of GSH Red or IR NCs suspension. Afterwards, the mixture was incubated without stirring in dark at room temperature overnight to prepare the final C_3E_6D Red or IR NCs.

NCs Purification. C_3E_6D NCs were purified by ultrafiltration (Amicon Ultra devices 3,000 MWCO (3 kDa)) at 17000 g for 10 min. What remains inside the filter and does not pass the 3 KDa membrane will be the purified C_3E_6D Blue, Red or IR Red NCs.

Peptides NCs synthesis (1 HAuCl4: 1.5 Peptide) (in collaboration with Raffaello Paolini, ISCR Rennes). A freshly prepared aqueous solution of peptides (10 mM, 300 mL) was mixed with 600 µL of ultrapure water. The solution was heated in oil bath at 80°C and $HAuCl_4$ (20 mM, 100 µL) and was rapidly added to it. The reaction was stopped after stirring for 8h. An aqueous suspension of Peptides NCs was formed.

Peptides NCs synthesis (1 HAuCl4:0.8 Peptide) (in collaboration with Raffaello Paolini, ISCR Rennes). A freshly prepared aqueous solution of peptides (10 mM, 160 mL) was mixed with 740 µL of ultrapure water. The solution was heated in oil bath at 80°C and HAuCl4 (20 mM, 100 µL) and was rapidly added to it. The reaction was stopped after stirring for 8h. An aqueous suspension of Peptides NCs was formed.

Microwave synthesis (in collaboration with Dr. Raffaello Paolini, ISCR Rennes). A freshly prepared aqueous solution of GSH (50 mM, 120 µL) or C_3E_6D (20 mM, 390 µL) was mixed with 1,68 mL or 1,41 mL of ultrapure water in a glass vial of 4 mL, in order to obtain a volume of 1,8 mL. Just before putting the solution inside the microwave, $HAuCl_4$ (20 mM, 200 µL) was rapidly added to it. The solution was heated at the microwave for 20s at 400W and for 40s at 200W, than after we cooled the solution with an ice bath and we heat another time for 20s at 400W and for 30s at 200W. At the end an aqueous suspension of GSH Red or C_3E_6D Blue NCs was formed.

Transmission Electron Microscopy (TEM) (with the assistance of Dr. Vincent Dorcet, THEMIS platform). Transmission Electron Microscopy analysis were carried out with with JEOL 2100 transmission electron microscope operated at 200 KV supplied with UltraScan 1000XP CCD Camera. For the sample preparation, 300 mesh carbon coated nickel grids were placed for 1 min on top of a 40 µL sample droplet and dried up with paper. Particle sizes and interparticle distances were determined from TEM micrographs using Fiji Software.

UV-visible Absorbance. The UV-visible Absorbance measurements were performed using a ThermoFisher Scientific NanoDrop with 2 µL of non-diluted sample.

Spectrofluorimetry. Photoluminescence measurements were performed on a Jasco FP-8300 spectrofluorometer. The measurements were performed at room temperature on liquid samples.

The wavelength resolution of both the excitation and the emission slits was set to 5 nm, the response times was 0.5 s, the detector sensitivity was set to medium and the scan speed was 500 nm/min.

Dynamic Light Scattering (DLS). The measurements of the mean hydrodynamic diameters were performed at an angle of 90° using a Nanosizer ZEN3600 (Malvern Instruments, England) and collected at 25 °C.

Absolute Quantum Yield. The absolute quantum yields were measured using a C9920–03 Hamamatsu system by exciting the samples at 410 nm.

Luminescence Lifetime (with the assistance of Dr. Gregory Taupier, CAPHTER platform). Lifetime measurements were realized using a picosecond laser diode (Jobin Yvon deltadiode, 375 nm) and a Hamamatsu C10910-25 streak camera mounted with a slow single sweep unit.

3 BIOLOGICAL APPLICATIONS

3.1 NANOCLUSTERS INTERACTION WITH SYNTHETIC AND BIOLOGICAL MEMBRANES

To design drug nanocarriers or for selective targeting and then evaluation of the toxicity, it is essential to study the interaction between NCs and biological membranes. Already in the literature the AuNCs have been reported as membrane biomarkers[101, 102] and as building blocks for the design of nanocarriers[103, 104]. For example, NCs were used to track and visualize extracellular vesicles arising from mammary cells in their parent cells. Furthermore, NCs self -assemble with extracellular vesicles to form larger paraparticles[105]. Since the lipid membranes possess specific visco-elastic properties, generally when the nanoparticles strongly interact with them, they induce their deformation; this only happens if the attractive interaction is strong enough to balance with the energy cost of bending[12]. For example, nearly spherical quantum dots[106] or nanorods[107] which interact electrostatically they can deform the model membranes into egg-box-shaped structured lamellae or corrugated sheets. It has recently been shown that the smaller the particles, the more they are able to induce a strong deformation of the membrane[108].

In the present study we focused on studying the electrostatic interaction between biocompatible luminescent gold nanoclusters (AuNCs) with a diameter of less than 2 nm and synthetic liposomes of different sizes (with a diameter between 20 nm and 10 μm approximately) or biological human Extracellular Vesicles (EVs). Synthetic liposomes are well known as model membrane to mimic their mechanical, visco-elastic properties and encapsulation capacity. EVs are the particles bounded by a lipid bilayer and without any nucleus released naturally by the cells. They have heterogeneous dimensions and, depending on the secretion mechanism, are defined differently: microvesicles, myelinosomes and exosomes[109,110] They are implicated in cell-to-cell communication mechanisms and are considered biomarkers for early cancer detection[111–115]. Their targeting via nanoparticles could enable the development of a powerful tool for the early detection of specific diseases. To better understand the mechanism of their interaction with AuNCs, a specific human fluid particularly rich in extracellular vesicles was selected: the follicular fluid (FF). The EVs belonging to the FF are useful for communication within the ovarian follicle[116].

3.1.1 SYNTHESIS OF POSITIVELY AND NEGATIVELY CHARGED NANOCLUSTERS

It was decided to make the NCs interact electrostatically with the membranes in order to have a strong and long-range interaction to amplify any possible interaction with the membrane; thus, positively (AuNC +) or negatively charged (AuNC -) AuNCs were synthesized. Two steps were used to obtain them: firstly the synthesis of AuNCs stabilized with glutathione (named GSH) according to literature[77] using a higher temperature to accelerate the nucleation kinetics and secondly an ligands exchange with pegylated peptides that have a stronger chemical affinity to the gold surface [117] than the GSH peptide.

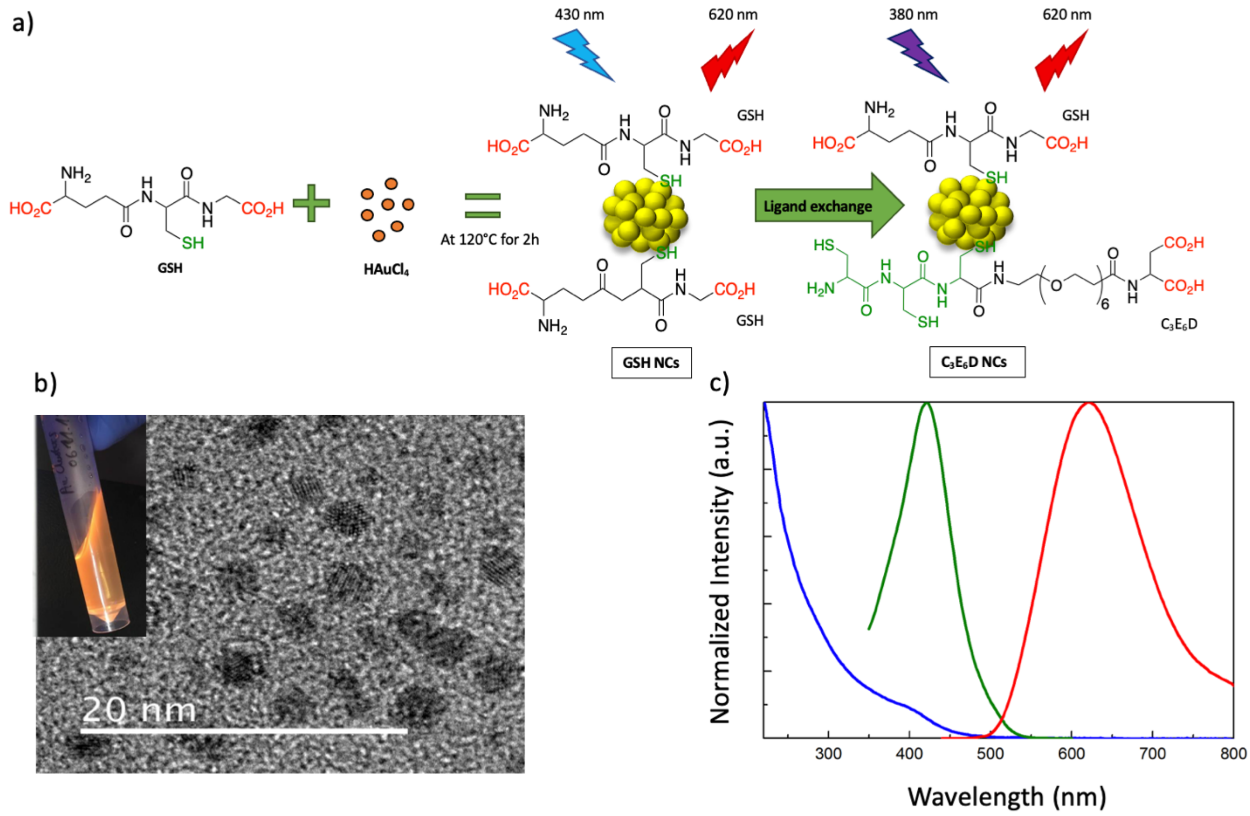

Figure 56. a) Schematic view of the synthesis route to prepare glutathione (GSH) Gold nanoclusters followed by ligand exchange. b) HR-TEM images of GSH Au NCs. Scale bar 20 nm. GSH Au NCs solution under UV lamp in the inset. c) Optical properties of GSH Au NCs: (Blue) UV-Vis spectrum, (Green) Normalized Excitation spectrum (620 nm) and (Red) Normalized fluorescence emission spectrum (430 nm).

The synthesis involves the use of a solution containing the glutathione reducing agent (GSH) and the gold salts (III) which is heated to 120°C for 3 hours to obtain GSH NCs (**Figure 56a**). Analysis of the TEM images (**Figure 56b**) reveals the crystalline structure of the NCs and their ultra-small dimension with a diameter of 1-2 nm. Such small dimension mean that the surface plasmons typical of gold nanoparticles (Au NPs) disappear, and in their place there are fluorescence properties due to surface effects (ligand to metal charge transfer) and quantum confinement[99,100] not present in Au NPs or bulk gold. **Figure 56c** shows the optical properties of GSH NCs with a maximum of luminescence emission at 620 nm and excitation at 410 nm. The absorption spectrum shows a decreasing absorption below 350 nm due to the scattering peak generated by the NCs, which masks the excitation peak of the GSH NCs at 410 nm.

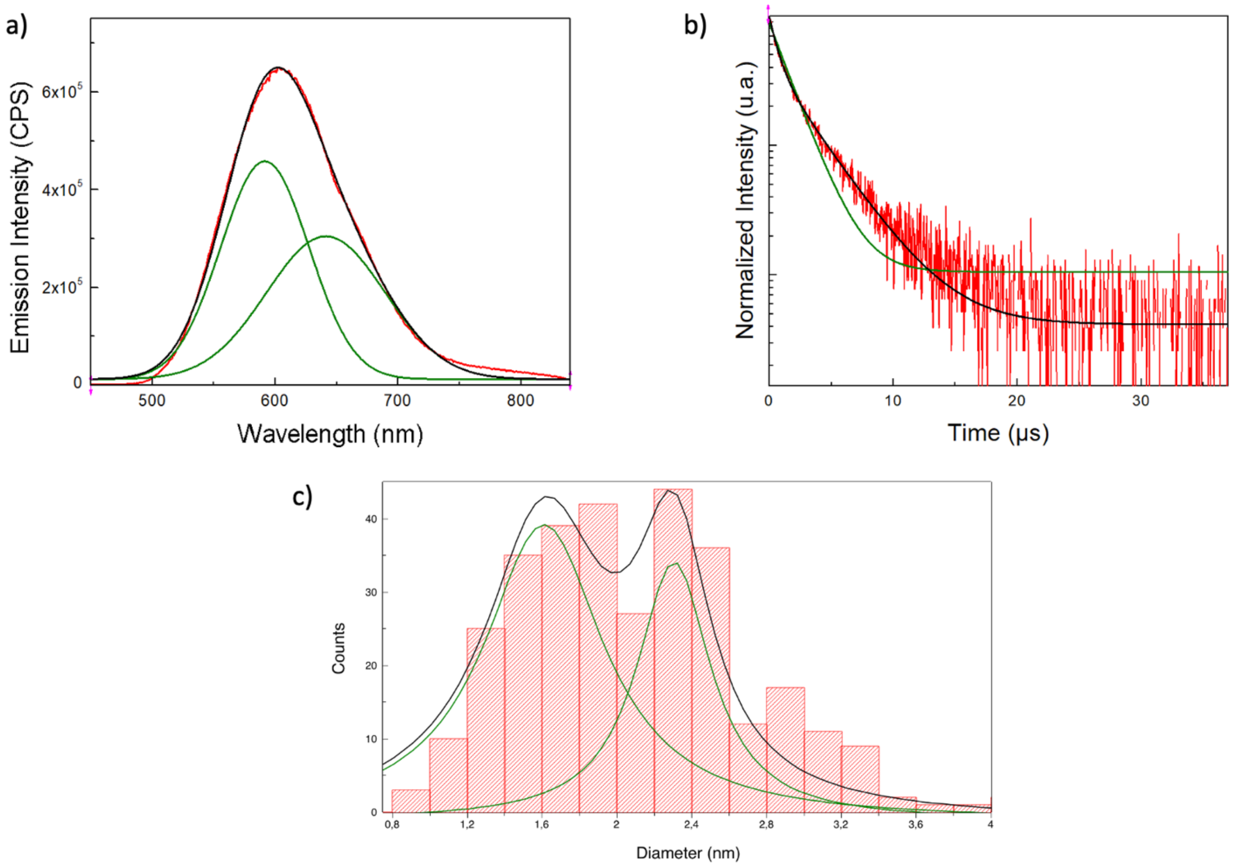

Figure 57. a) Fluorescence Emission spectra (λ_{exc}=432 nm) of GSH NCs (red), multi peak fit (green) representing the population of GSH NCs and the corresponding fit (black). b) Normalized intensity of fluorescence lifetime (red) of GSH NCs (λ_{exc} = 430 nm and λ_{em} = 605 nm) fitted with one (green) ($\boldsymbol{\tau}_1$ = 1.69 ± 0.02 µs) and two (black) exponential decays ($\boldsymbol{\tau}_1$ = 3.1 ± 0.02µs $\boldsymbol{\tau}_2$ = 0.67 ± 0.02µs). c) GSH NCs diameters obtained from HR-TEM images and peak fit (black) resulting from the deconvolution fit (green).

Analyzing more in detail the luminescence emission in **Figure 57a** one can distinguish two peaks (590 nm and 640 nm); furthermore, by fitting the lifetime (**Figure 57b**), we realize that the fit with only one decreasing exponential is not adequate, and consequently it is necessary to fit it with two decreasing exponentials ($\boldsymbol{\tau}_1$ = 3.1 ± 0.02 µs and $\boldsymbol{\tau}_2$ = 0.67 ± 0.02 µ s). This could be due to a dual emission mechanism as often happens for NCs, in which there is an emission that comes from the surface (ligand-metal interaction) and one from the AuNC nucleus[118] corresponding to a quantum effect. The diameter size histogram obtained from the analysis of the TEM images (**Figure 57c**) shows a rather small polydispersity around 2 nm (1.2 - 2.4 nm).

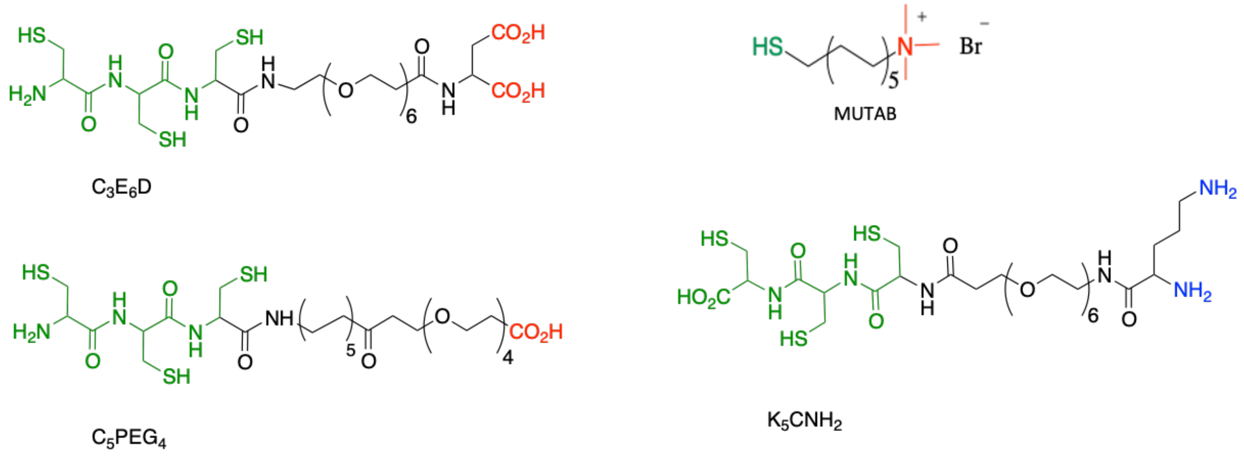

Figure 58. Chemical structures of the ligands used to replace the GSH at the surface of the Au NC.

To increase the stability of Au NCs in solution and limit their aggregation within biological fluids, they have been pegylated using ligands with higher affinity for gold (possessing 3 cysteines) and of different charge (C_3E_6D and C_5PEG_4 negative o K_5CNH_2 positive) selected in the previous, works (**Figure 58**)[119,120]. As an alternative to K_5CNH_2, MUTAB (Mercapto-Undecyl-Trimethyl Ammonium Bromide); this ligand has only one thiol group and can only be used in vitro due to its potential toxicity. Through functionalization with C_3E_6D the NCs become bioactivable by adding a target functional group (antibodies, recognition proteins, drugs, etc.) to the two carboxy groups for further diagnostic and therapeutic applications. To proceed with the ligand exchange, after incubating the GSH NCs overnight in a solution with large excess ligand (C_3E_6D, C_5PEG_4, K_5CNH_2 or MUTAB), the solution was purified by size exclusion ultrafiltration to remove all excess ligand. Following this ligand exchange, the emission remains unchanged at 620 nm while there is a larger excitation peak going from 430 nm to 380 nm[121]. The presence of PEG, in addition to increasing the colloidal stability of the AuNCs, is also able to increase their luminescence intensity, in agreement with previous ratios in the case of the PEGylated thiol ligand[122], increasing the quantum yield of luminescence (3% for GSH AuNCs and 6% after ligand exchange with C_3E_6D). This phenomenon could be attributed to the rigidification of the outer shell which allows to reduce the energy losses due to non-radiative emission due to intramolecular vibrations and rotations[80,79].

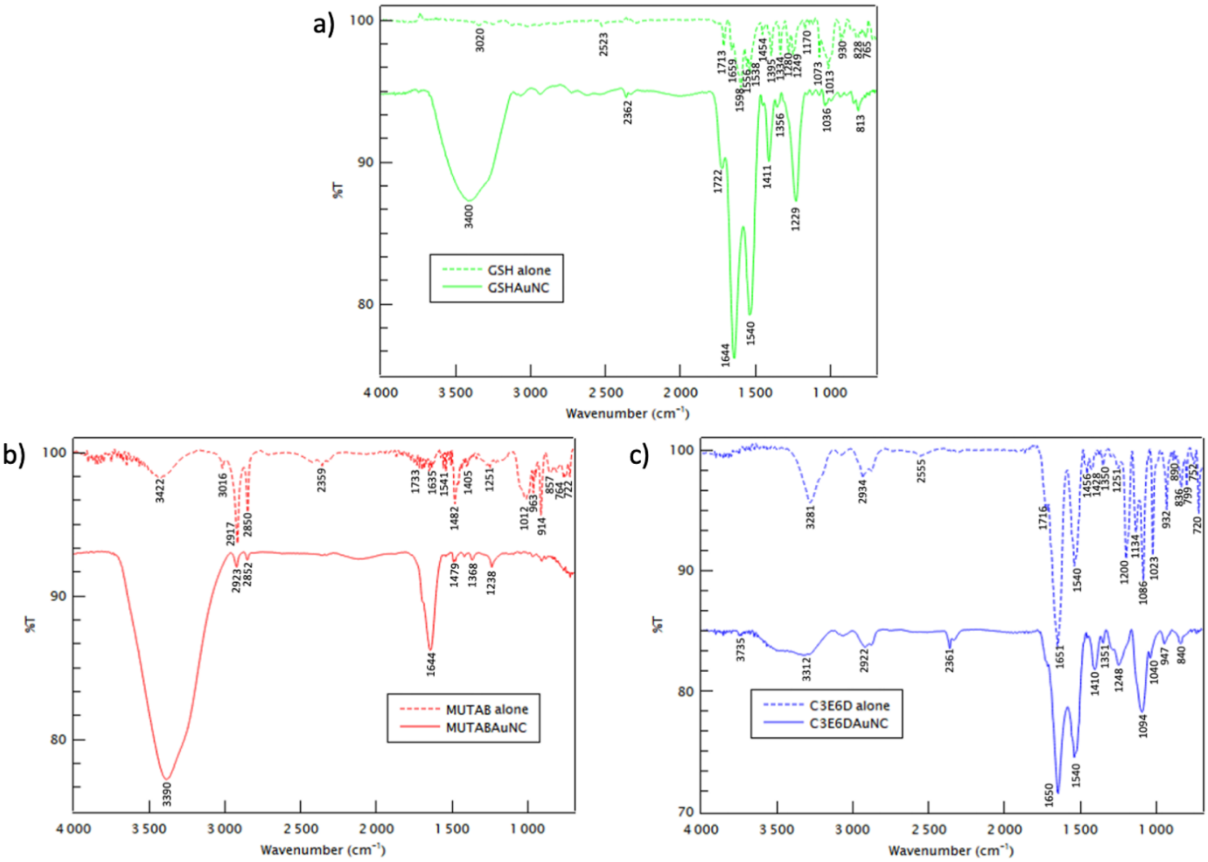

Figure 59. FT-IR spectra of a) GSH, b) MUTAB and c) C_3E_6D ligand (dotted line) and purified AuNCs (straight

To verify that the ligand exchange had occurred correctly, the FT-IR spectra of purified GSH, MUTAB and C_3E_6D AuNCs were recorded, as well as those of GSH, MUTAB and C_3E_6D alone (**Figure 59**). The two ligands have two peaks coming from the amide II and amide I bonds at 1540 cm^{-1} and 1650 cm^{-1}. The presence of C_3E_6D is confirmed by the two peaks coming from the vibration of methylene at 2922 cm^{-1} and 2850 cm^{-1} which are absent only in the case of GSH. As the structures of the other ligands is very similar, we assume that the ligand exchanges with C_5PEG_4, K_5CNH_2 e MUTABs is also efficient.

3.1.2 SYNTHESIS OF SYNTHETIC VESICLES WITH DIFFERENT DIMENSIONS

Thanks to the ultra-small size of Au NCs, such biocompatible nanostructures could label lipid biomembranes. In this perspective we will study the interactions of Au NCs with model and EVs membranes of human follicular fluid and how changing their surface properties affects this interaction.

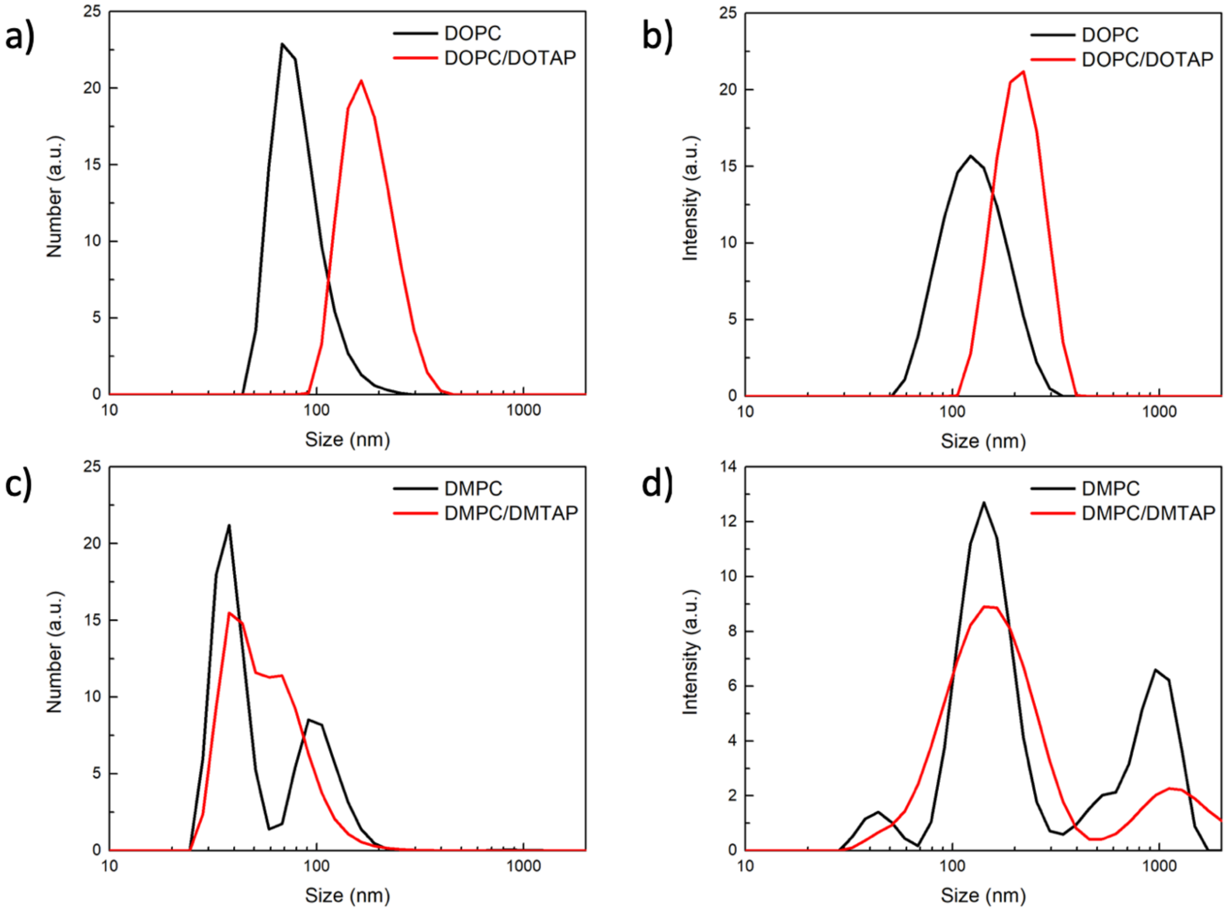

Figure 60. a,c) Number and b,d) Intensity DLS measurements of a,b) LUVs and c,d) SUVs, slightly negatively (DOPC or DMPC) (black line) and positively (DMPC:DMTAP(9:1) or DOPC:DOTAP (9:1) mixtures) (red line) charged. The surprising negatively charged nature of the zwiterrionic DOPC or DMPC vesicles is due to the orientation of the phosphatidylcholine head-groups (Contini et al.2020).

For this reason, the large unilamellar vesicles (LUV, about 100 nm in diameter) were synthesized by the extrusion method and their size distribution measured by DLS is presented in **Figure 60 a,b**. The positively charged vesicles (DOPC / DOTAP 9: 1) were made to interact with the negatively charged NCs (C_3E_6D AuNCs or C_5PEG_4AuNCs) and positively (K_5CNH_2 AuNCs or MUTAB AuNCs). The NCs used were all taken from the batch of GSH NCs prepared as described above; only the ligand exchange was performed with different ligands (**Figure 61 a,b**).

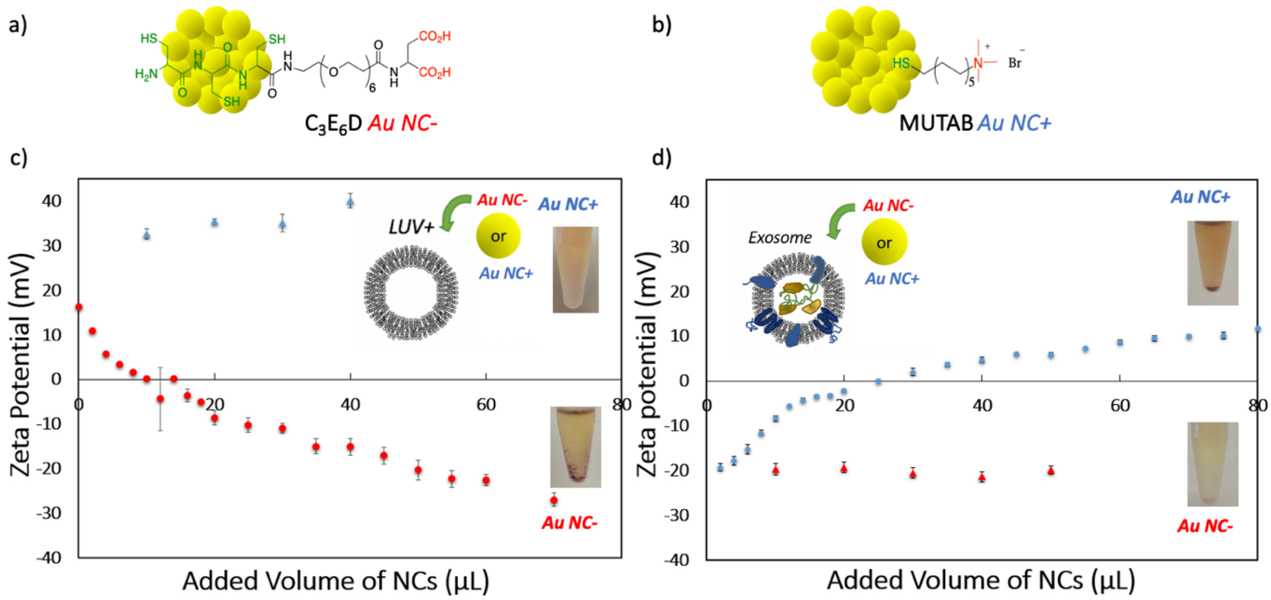

Figure 61. Schematic structure of ligand Exchanged a) negatively charged C_3E_6D AuNC- (red) and b) positively charged MUTAB AuNC+ (blue). c) Evolution of the zeta potential during the titration of positively charged DOPC:DOTAP (9:1) Large Unilamellar Vesicles (LUVs) Liposomes (total lipid concentration 1 mM) with negatively charged C_3E_6D AuNC- (red) or positively charged MUTAB AuNC+ (blue). d) Evolution of the zeta potential during the titration of negatively charged exosomes with negatively charged C_3E_6D AuNC- (red) and positively charged MUTAB AuNC+ (blue).

3.1.3 ELECTROSTATIC INTERACTION BETWEEN NCS AND VESICLES (SYNTHETIC AND BIOLOGICAL)

Titration of the LUVs and EVs with the AuNCs of opposite surface charge was performed, following the evolution of the surface charge by measuring the electrostatic Zeta potential of the vesicles. In the case of AuNCs and LUV with opposite surface charge, the Zeta potential decreases indicating that the negatively charged AuNCs neutralize the positive surface charge of the liposome until charge reversion. This behavior is due to the saturation of the vesicle surface in presence of an excess of negatively charged NCs. Towards the end of the titration experiment a precipitation occurs as the AuNCs-coated vesicles can further interact with each other to form a condensed precipitate stabilized by electrostatic forces as observed in the case of DNA macromolecules or quantum dots and cationic lipids[106]. As a control experiment, in the presence of positively charged AuNCs (MUTAB AuNCs), there is an initial increase in the zeta potential from 15 to 40 mV due to the additional contribution of positively charged AuNCs, which later stabilizes and does not lead to any precipitate formation suggesting that NCs and vesicles retain their surface charge, repulsive electrostatic forces prevent colloidal instability (**Figure 61c**). Similar results were obtained by titration of positively charged liposomes with negatively charged C_5PEG_4 NCs or positively charged K_5CNH_2 NCs (**Figure 62**). The same titrations were performed with EVs extracted from follicular fluid. As previously observed for liposomes, the negative surface charge of the exosomes was neutralized until a charge reversion was obtained by interacting with oppositely charged AuNCs (MUTAB AuNCs) while no variation was observed for the surface charge in the presence. of equally charged nanoclusters (C_3E_6D NCs) (**Figure 61d**). Since a charge inversion was observed during titration of both liposomes and exosomes, a clear interaction between the lipid membranes through electrostatics is demonstrated with consequent precipitation only in the case of charge inversion.

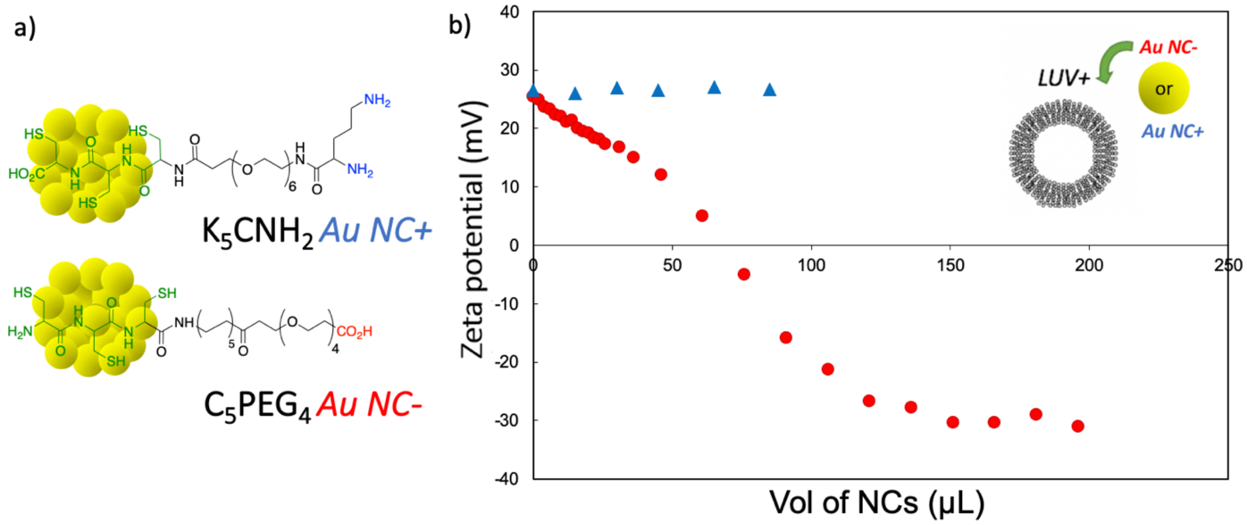

Figure 62. a) Scheme of functionalized Au NCs+ and Au NC- used. b) Evolution of the zeta potential during the titration of positively charged DOPC:DOTAP (9:1) Large Unilamellar Vesicles (LUVs) Liposomes (total lipid concentration 1 mM) with negatively charged C_5PEG_4 AuNC- (red circle) or positively charged K_5CNH_2 AuNCs (blue triangle) (NCs concentration respectively 8,7 µ M and 6,9 µ M).

It was decided to analyze the precipitates using two complementary techniques to study in situ the structuring of mixtures of nanoparticles / lipid membranes[107, 106]: Small Angle X-Ray Scattering (SAXS) and Cryo transmission electron microscopy (CryoTEM). The SAXS experiments were performed in collaboration with Franck Artzner in the physic department at Rennes University. The CryoTEM experiments were performed in collaboration with Aurélien Dupont in the biology department at Rennes University. The SAXS allows us to see if there is a repetition distance inside the sample corresponding to matter organization, as in our case the size of the membrane, and consequently allows us to see if there are any structural variations of the vesicles following the interaction with the NCs. CryoTEM, on the other hand, allows us to visualize biological samples in the form closest to the real one inside the liquid, avoiding the possible artifacts induced by sample preparation. In the case of the interaction between LUVs and NCs of opposite charge, the precipitate formed presents a lamellar structure in the SAXS spectrum (**Figure 63a**) with a narrow peak at 0.14 $Å^{-1}$. Through CryoTEM microscopy it is evident that, compared to LUVs alone (**Figure 63 c,e**), in the presence of NCs of opposite charge the LUVs aggregate forming a precipitate, but without generating a destruction or rearrangement of the membranes (**Figure 63g**) . In the case of EVs , the precipitate shows in the SAXS spectrum the presence of a narrow peak at 0.16 Å $^{-1}$ and a wide peak at 0.281 Å^{-1} (**Figure 63b**), indicating the presence of a multilaminar structure with poorly defined distances between the lamellae due to the presence of NCs between the lamellae. This hypothesis was confirmed by the images obtained by CryoTEM in which it is possible to note the multilamellar structure formed following the destruction of the EVs in **Figure 63 d,f** and the rearrangement of the membrane lipids in the precipitate (**Figure 63h**). Therefore, the interaction with NCs is not the same in the case of liposomes or EVs. Almost all EVs are destroyed to form a condensed lamellar phase while the synthetic vesicles remain only aggregated with each other without rupture of the membrane. In all cases it is not possible to see the NCs by CryoTEM because they are too small, below the resolution limit of the technique; but it is possible to see the aggregates of NCs (black dots scattered on the vesicles).

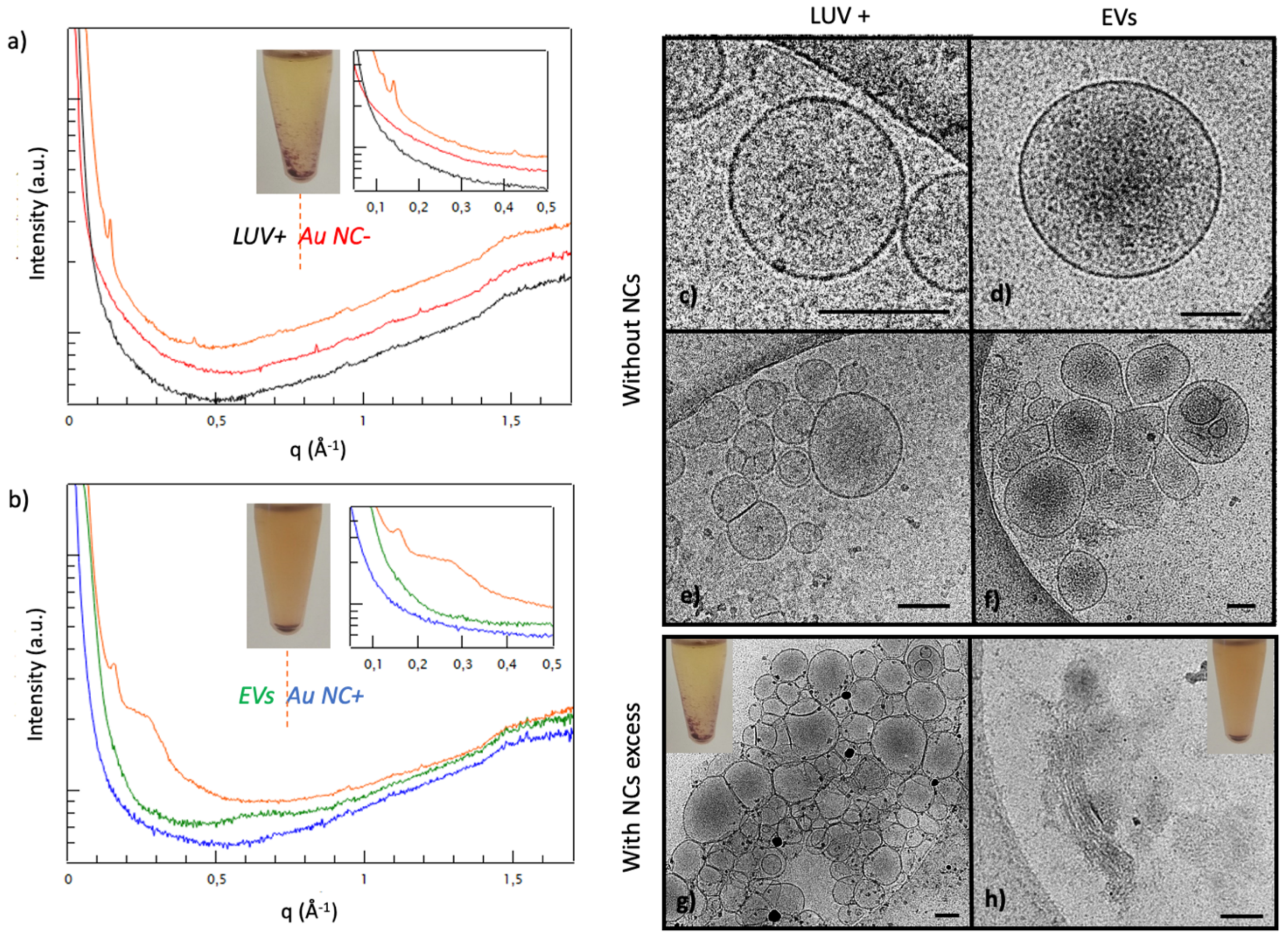

Figure 63. SAXS of the precipitate obtained at the end of the Zetametry titration study of a) LUV+ and AuNC- and b) EVs and AuNC+ after two weeks of incubation time: (orange) precipitate showing the appearance of two peaks, (black) LUV+, (green) EVs, (red) AuNC- and (blue) AuNC+ alone. Cryo-TEM images (scale bar 100 nm) of LUV + (c,e,g) and of EVs (d,f,h) at different magnification without AuNCs (c,e,d,f) and with an excess of C_3E_6D AuNC- (g,h) at the end of the Zetametry titration.

Complementary SAXS analyzes were performed to better characterize the formation of hybrid lamellar phases in the presence of NCs. This time, to obtain a higher lipid concentration and have a higher signal to SAXS, Small Unilamellar Vesicles of approximately 50 nm in diameter (SUVs) have been synthesized (**Figure 60 c,d**) by sonication method from a lipid mixture at a higher concentration (20 mg/mL) following well-known protocols[106]. Capillaries with a diameter of (diameter 1.5 mm) were filled with this solution of DMPC:DMTAP (9:1) SUV by adding on top the suspensions of C_3E_6D AuNCs- or MUTAB AuNCs + without mixing, in order to create a contact surface between the two suspensions. The capillaries were kept at room temperature for 48 hours to allow for self-diffusion of Au NCs and SUV +. Already visually through the insets in **Figure 64** it is possible to see that only in the case of an attractive electrostatic interaction a new intermediate phase is formed in the center, with a diffusion of the initial phases into each other (**Figure 64 a,d**). On the contrary in the case of NCs and vesicles of equal charge, being in the case of electrostatic repulsion, there is no mixing of the two phases and it is possible to notice a clear separation in the center between the phase containing the NCs (transparent) and the one containing the vesicles (turbid).

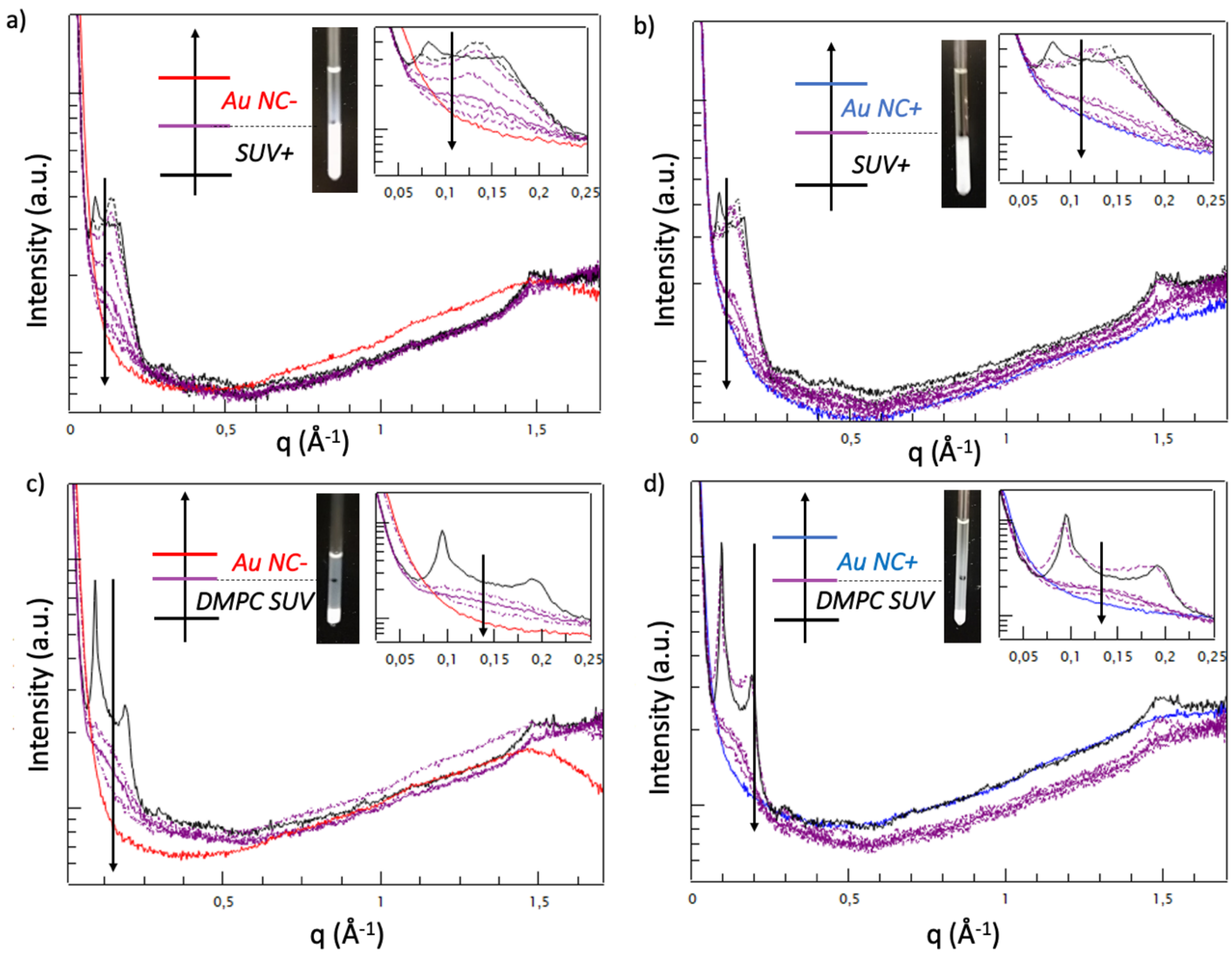

Figure 64. Small Angle X-Ray Scattering (SAXS) spectra of a,b) DMPC:DMTAP (9:1) positively charged Multilamellar SUV+ and c,d) Multilamellar DMPC SUV in contact with a suspension of Au nanoclusters of different charges (violet lines): a,c) negatively charged C_3E_6D Au NC- or b,d) positively charged MUTAB Au NC+. The spectra were recorded at different heights in the capillary where the interface between the two suspensions is marked with a black mark (as shown in the pictures inserted in the figures). The bottoms of the solutions are SUV+ or DMPC SUV alone (black line) and the tops are Au NC-or Au NC+ alone (red and blue lines respectively).

To better understand what happens inside the sample, SAXS spectra were recorded at different heights of the capillary. In the case of electrostatic attraction between SUVs + and AuNCs, there is a lipid phase at the bottom which has two distinct peaks at 0.08 $Å^{-1}$ and 0.16 $Å^{-1}$, a hybrid phase in the center in the presence of Au NCs- with two peaks, slightly shifted compared to the previous ones, at 0.07 $Å^{-1}$ and 0.13 $Å^{-1}$, and an absence of peaks at the top of the phase with only the NCs- (**Figure 64a**); this result indicates that in the hybrid phase the NCs are positioned between the lamellae, inflating them and increasing their size. In the other cases this effect is less evident, with the formation of the intermediate hybrid phase much less pronounced (**Figure 64 c,d,e**). In all the cases presented, through the WAXS analysis it should be noted that the lipid chains remain crystalline even in the presence of NCs, indicating that the latter do not significantly interfere with the arrangement of lipids in the membranes and do not significantly vary their fusion temperature.

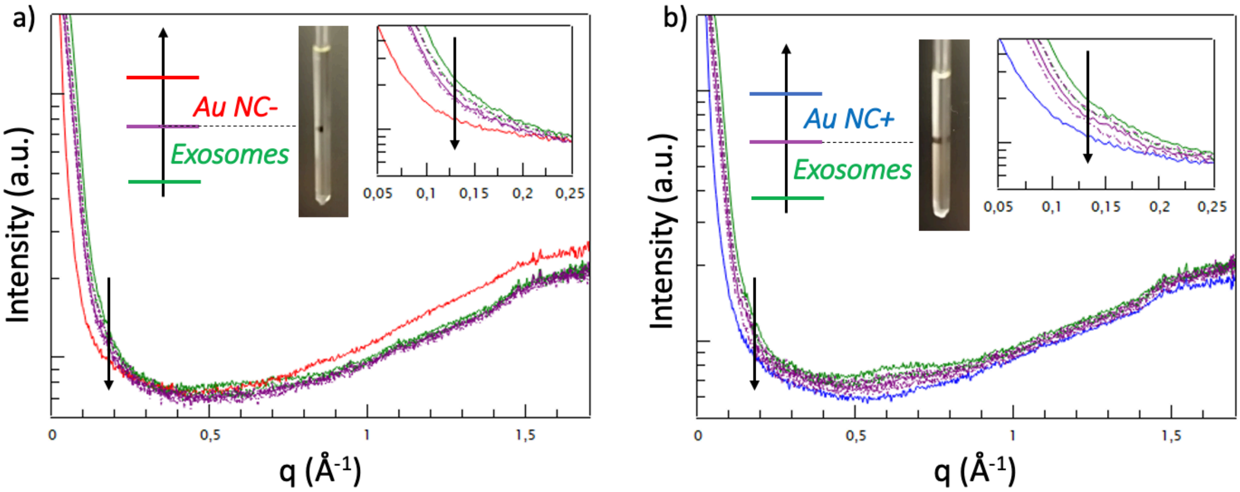

Figure 65. Small Angle X-Ray Scattering (SAXS) spectra of extracellular vesicles (EVs) in contact with a suspension of Au nanoclusters of different charges: a) negatively charged C_3E_6D Au NC- or b) positively charged MUTAB Au NC+ (violet lines). The spectra were recorded at different heights in the capillary where the initial interface between the two suspensions is marked with a black mark (as shown in the pictures inserted in the figures). The bottom of the solutions represents the exosomes alone (green line) and the top are AuNC- and AuNC+ alone (red and blue lines respectively).

The same SAXS experiments were performed on EVs , which however , having a more complex membrane composition including proteins and glycocalix, do not show clear peaks (**Figure 65**) on the SAXS spectra; only a slight increase in intensity in the range of 0.15 Å^{-1} is noted only in the case of AuNCs + which is attributed to the presence of NCs on the surface of the lipid bilayer of the EVs (**Figure 65b**).

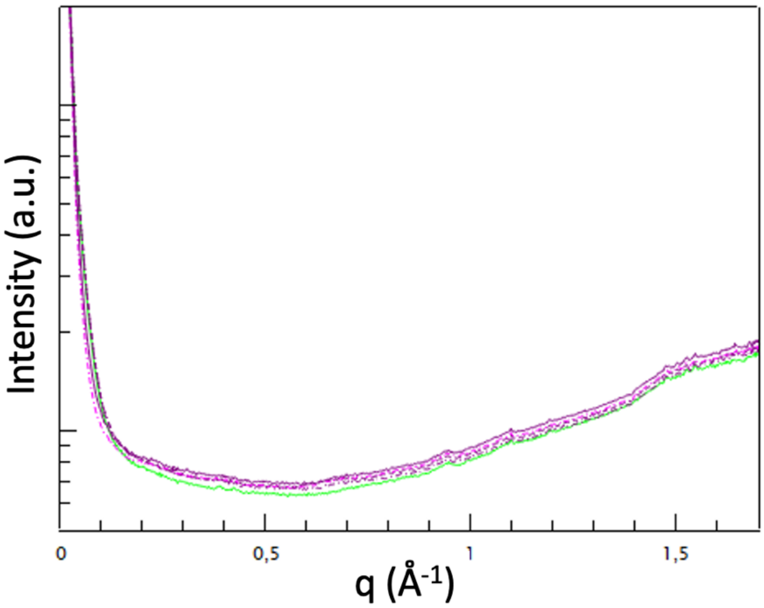

Figure 66. Small Angle X-Ray Scattering (SAXS) spectra of EVs alone (green line), MUTAB at 1.2 mM alone (red line) and EVs in presence of MUTAB at different concentrations 1.2 mM, 120 µM and 12 µM (violet lines).

The spectra corresponding to the control solutions of the exosomes alone, the ligand MUTAB alone and the exosomes in the presence of MUTAB at different concentrations were also analyzed, but in none of these cases there are peaks (**Figure 66**). In conclusion, the CryoTEM images and the SAXS measurements allow us to specify that the strong electrostatic interaction between AuNCs and vesicles determines the formation of a hybrid lamellar phase composed of lipid membranes and AuNCs between the lamellae.

3.1.4 NANOCLUSTER POSITIONING OVER THE VESICLES MEMBRANES

The case of the strongest electrostatic interaction, ie between LUVs + and AuNCs-, was analyzed at CryoTEM to visualize the position of the NCs on the membrane. For this experiment, the solution was prepared with a defect in NCs with respect to the lipids, so as not to generate the strong aggregation and precipitate seen above. In **Figure 67** there are black points of strong electron density near the membranes of the LUV + which could be attributed to the presence of AuNCs (**Figure 67a**). To confirm these hypotheses, Giants Unilamellar Vesicles (GUV), in diameter in the micrometer range, have been prepared by the method of transferring the water-in-oil emulsion[123] which were then incubated in a solution of NCs with opposite charge. Also in this case we placed ourselves in the condition of defect of AuNCs- with respect to the GUVs + which, after an incubation of one hour, were observed under the optical fluorescence microscope to see the position of the fluorescence of the NCs with respect to the GUVs. As can be seen in **Figure 67c**, the fluorescence of the NCs appears to be localized on the surface of the GUVs indicating that the AuNCs have been attracted to the opposite charge of the vesicles, as already observed in the case of the quantum dots in previous reported work of the laboratory[14,106] . Thus, both the CryoTEM and the fluorescence microscope experiments suggest that the NCs adhere to the membranes in agreement with the progressive neutralization of the surface charge observed by Zetametry

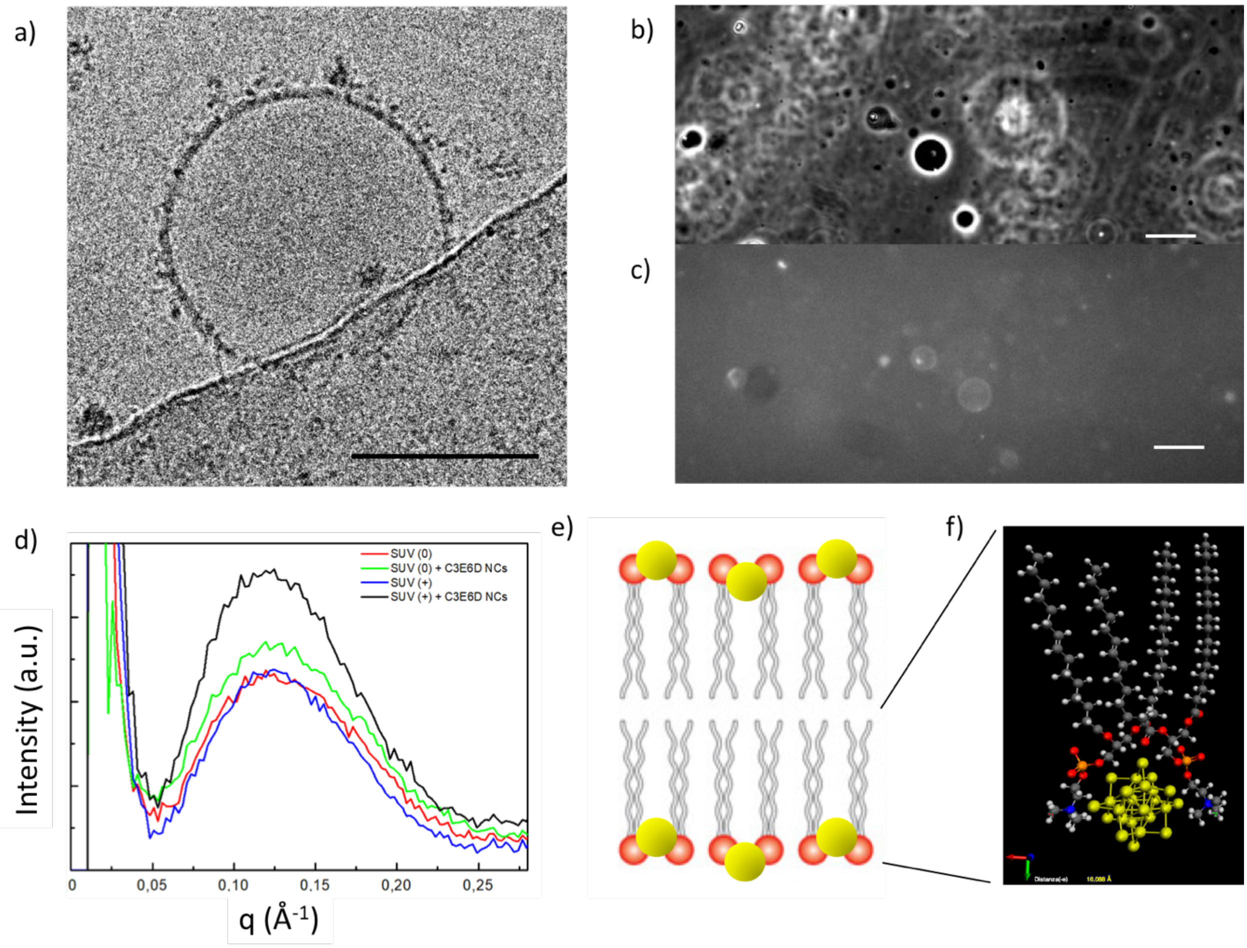

Figure 67. a) Cryo-TEM images (scale bar 100 nm) of LUV+ incubated with of C_3E_6D AuNC-. Optical microscopy Images (scale bar 50 µM) of GUV+ (Giant Unilamellar Vesicles) interacting with C_3E_6D AuNC- obtained b) by phase contrast and c) by fluorescence. d) SAXS spectra of DMPC:DMTAP (9:1) positively charged Unilamellar SUV+ alone (in blue) or in presence of C_3E_6D AuNC- (in black) and SAXS spectra of DMPC Unilamellar SUV alone (in red) or in presence of a suspension of C_3E_6D AuNC- (in green). e) Schematic view and f) Avogadro simulation of AuNCs positioning between the polar heads of membrane phospholipids in the case of electrostatic attraction.

To specify the exact position of the AuNCs on the membrane, solutions of DOPC/DOTAP (9:1) SUVs + and DMPC SUV (0 for neutral charge) in the absence and in the presence of AuNCs- were prepared. The AuNCs were placed in all cases in defect with respect to the lipids and once mixed and allowed to incubate to reach the equilibrium state, SAXS measurements were carried out. In all spectra resulting from these measurements (**Figure 67d**) there is a peak at 0.122 Å $^{-1}$ corresponding to the expected thickness of the SUV membrane (5.1 nm). This peak is enhanced in the presence of the C_3E_6D AuNCs- with opposite charge to the SUV + vesicles, following the electrostatic attraction that causes the NCs to adhere to the membrane; the latter having a high atomic number, increase the scattering and enhance the X-ray signal coming from the membrane and consequently the signal of the corresponding peak on the SAXS spectrum. A final important point is that although the AuNCs are positioned on the membrane, improving the SAXS signal, there is no shift in the peak. This indicates that the NCs, if defective, do not vary the thickness of the membrane and, due to their ultra-small size, are able to fit between the polar heads of the membrane phospholipids (**Figure 67 e,f**) without increasing the thickness of the double layer unlike other larger nanoparticles such as quantum dots[106, 107, 108]. An Avogadro simulation was performed as a rough estimate to assess whether the size of the AuNCs is small enough to fit between the polar head phosphates of the membrane phospholipids. A comparison of the distance between the polar heads with and without AuNCs is also schematized in **Figure 68** which shows that the AuNCs could be positioned at the level of the phosphate groups.

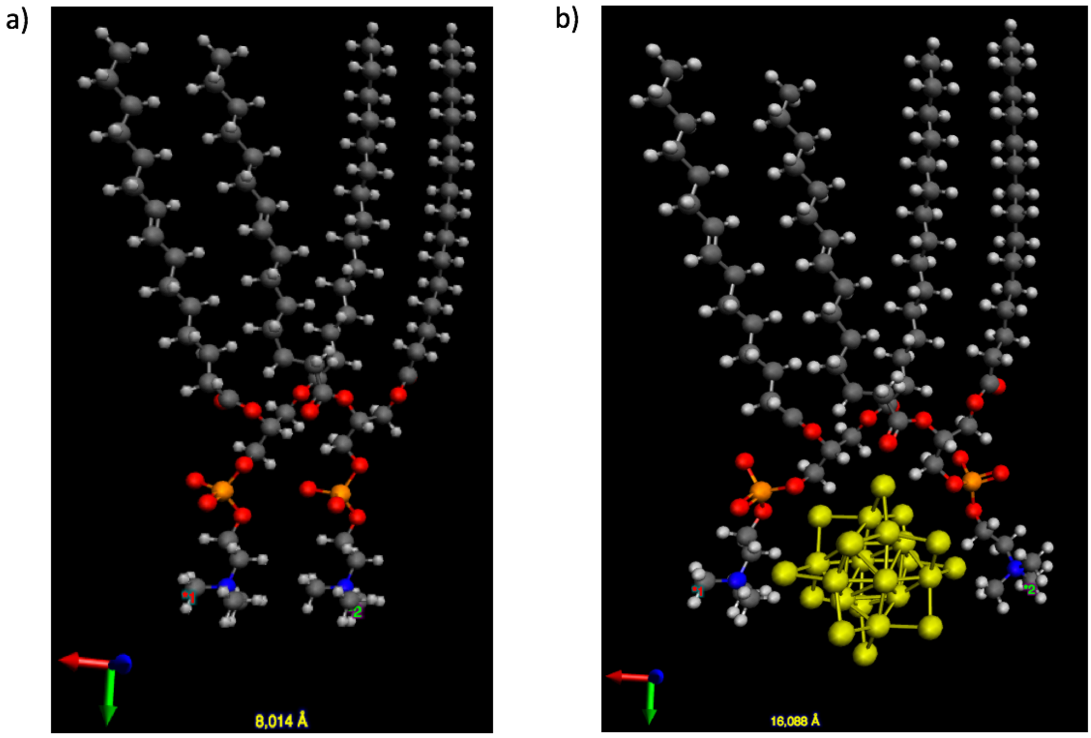

Figure 68. Avogadro DFT Simulation of membrane phospholipids in absence a) and presence of NCs without considering the ligand b). The distance between the membrane phospholipids (point 1 and 2) in both configurations is designed in yellow: 8 Å and 16 Å respectively.

3.1.5 CONCLUSIONS AND PERSPECTIVES

In conclusion, this study offers an overview of the interaction between ultrasmall luminescent gold nanoclusters and lipid membranes through electrostatic attraction, demonstrating that a strong change in membrane structures can be induced or not. In the presence of an excess of oppositely charged AuNCs, the liposomes adhere strongly to each other without disrupting their membrane structure while the EVs extracted from human follicular fluid reorganize into a hybrid lamellar phase. On the other hand, in the presence of an excess membrane surface, the AuNCs do not change the size of the membrane thickness; hence, they are positioned between the polar head groups of the membrane phospholipids unlike the larger gold nanoparticles[108].

By functionalizing the AuNCs with recognition molecular groups, it is possible to have a selective targeting detectable by fluorescence of the AuNCs or by electron microscopy. Furthermore, the possibility of encapsulating AuNCs within synthetic vesicles opens new paths for drug delivery by increasing internalization and decreasing non-specific interactions. In contrast to the larger gold nanoparticles, the smaller size of the AuNCs not only avoids deformation of biological membranes, but also allows targeting with higher spatial resolution. Thus, these ultra-small and stable gold nanoclusters, by controlling their interaction with lipid membranes, can serve as a novel hybrid vector for bioimaging and for in situ biosensing and drug delivery. This work was published in J. Chem. Phys. Letters (Regina M. Chiechio et al. 2022)[124].

3.1.6 EXPERIMENTAL SECTION

Generals. Human ovarian follicular liquid samples were provided by the Biobank GERMETHEQUE. The PEGylated ligands were prepared and purchased from Agentide (purity (HPLC) 85.624%. All the other chemical compounds and solvents were purchased from Sigma aldrich. The measurements of the mean hydrodynamic diameters were performed at an angle of 173° using a Nanosizer ZEN3600 (Malvern Instruments, England) and collected at 25 °C, without dilution or filtration. The absorption spectra were performed on a Thermo Scientific™ NanoDrop™ UV-Vis spectrometer. The absolute fluorescence quantum yields were measured usign a C9920–03 Hamamatsu system by exciting the samples at 410 nm.

Au Nanoclusters Synthesis (AuNCs). All glassware used for these synthesis were cleaned in a bath of freshly prepared aqua regia ($HCl:HNO_3$, 3:1 by volume) and rinsed in water 10 times before use. The AuNCs solution obtained could be stored at 4 °C for months without significant change in their optical properties. A freshly prepared aqueous solution of glutathione denoted GSH (50 mM, 1,2 mL) were mixed with 16,8 mL of ultrapure water. The solution was heated in oil bath at 120°C and $HAuCl_4$ (20 mM, 2mL) and was rapidly added. The reaction was stopped after stirring for 3h. An aqueous suspension of orange-emitting GSH AuNCs was formed (2.6 µM). Then a freshly prepared aqueous solution of the desired ligand (20 mM, 1000 eq / Au) (C_3E_6D, K5CNH2 or MUTAB) was incubated overnight in presence of the GSH AuNCs. The obtained AuNCs were purified on centrifugal filter (Amicon-ultra 0.5 device 3kDa, Merk) to remove the ligand excess. Typically, a freshly prepared aqueous solution of C_3E_6D (20 mM, 0.390 mL) was overnight incubated with GSH Au NCs (2.6 µM, 1 mL) suspension in dark at room temperature to obtain the final C_3E_6D AuNCs (denoted AuNC-).

Small Unilamellar Vesicles (SUVs). a lipid solution is prepared by dissolving 20 mg of DMPC and 1.74 mg of DMTAP in 2 ml of dichloromethane. Using a rotary evaporator (Buchi Heating Bath), the dichloromethane is evaporated (40 ° C, 100 mbar) and an aqueous sucrose solution (2 ml, 50 mM) is added to hydrate the as-formed lipidic film. The solution obtained is sonicated using a titanium ultrasonic probe (Misonix Incorporated) placed at maximum power for 30 minutes. After centrifugation at 7500 g for 10 minutes to eliminate the possible titanium traces, the supernatant is then removed and the SUV solution is ready for use. The SUVs average size estimated by Dynamic Light Scattering was 46± 16 nm (Figure S5c,d).

Large Unilamellar Vesicles (LUVs). Lipidic stock solutions of DOPC (1 mL at 10 mg / mL) and DOTAP (98.5 µL, 10 mg / mL) in dichloromethane were prepared. The appropriated lipidic mixture (total lipid concentration used: 10 mg/mL), either pure DOPC or a molar DOPC:DOTAP (9:1) mixture, was introduced into a 50 mL vial and the organic solvent was evaporated with a rotary evaporator (Büchi Heating Bath) (40 ° C, 100 mbar) to form a lipidic film onto the vial surface during 30 min. Then, an aqueous sucrose solution (1.2 ml, 50 mM) was added, and the suspension was successively placed in a liquid nitrogen bath for 30 s and in a water bath at 40°C for 30 s. The freezing-unfreezing cycle was repeated five times to form the MLV (MultiLamellar Vesicles). This MLV suspension was then extruded 10 times through a 100 nm diameter polycarbonate filter in an extruder (Thermobarrel Extruder Lipex Membrane) under a pressure of 15-10 bar. The mean hydrodynamic diameter of the obtained LUVs was measured to be around 110 ± 20 nm by Dynamic Light Scattering (DLS) (Figure S5a,b).

Giant unilamellar vesicles (GUVs)[123]*.* A lipid solution was prepared dissolving DOPC or DOPC:DOTAP (95:5) molar lipidic mixture lipids in chloroform (10 mg / ml). 20 µL of this solution and 1.8 mL of paraffin oil are mixed and heated at 80 ° C for 30 min in a flask without cap. Then, the suspension is placed in a desiccator for 20 min in order to evaporate the chloroform and to obtain the final lipid organic solution. To prepare the GUV, 50 µL of sucrose (500 mM) are added to 400 µL of lipid solution vortexed for 40 s to form a water-in-oil (w/o) emulsion. Then, this emulsion is gently added on the top of a sucrose solution of high viscosity (200 µL, 500 mM in a second Eppendorf) without mixing. After waiting 10 minutes, the solution is centrifuged for 15 minutes at 18890 g The bottom was transferred into another Eppendorf, redispersed in 300 µl of glucose (500 mM) and centrifuged again at 18890 g for 5 minutes. After centrifugation, the bottom solution is taken up and the GUVs are ready to be stored in the refrigerator.

Small-Angle X-ray Scattering (SAXS) (in collaboration with Dr. Franck Artzner, Institut de Physique, University of Rennes 1). X-ray patterns were collected with a Mar345 Image-Plate detector (Maresearch, Norderstedt, Germany) mounted on a rotating anode X-ray generator FR591 (Bruker, Courtaboeuf, France) operated at 50 kV and 50 mA. The sample to detector distance (422 mm) has been calibrated by using silver behenate. The X-ray patterns were therefore recorded for a range of reciprocal spacing $q = 4\pi \sin\theta/\lambda$ from is 0.04-1.2 $Å^{-1}$ where θ is the diffraction angle. The experiments performed with the present set-up provide accurate measurements of distances between 150 Å and 5.2 Å. The acquisition time was 1 hour. Samples were loaded in thin Lindman glass capillaries (diameter 1 ± 0.1 mm and thickness 10 µm; GLAS, Muller, Berlin, Germany) sealed with paraffin. The lipid-NCs hybrid complexes were prepared by mixture of a micromolar concentration NCs solution (10 µL, 1.70 µM NCs concentration) and millimolar concentration SUV suspension (10 µL, 16 mM total phospholipid concentration) in the glass capillaries. All samples exhibited powder diffraction rings, and the scattering intensities as a function of the radial wave vector were determined by circular integration.

Zeta Potential measurements. The zeta potential measurements were performed using the Zetasizer ZEN3600 (Malvern Instruments, England) equipped with a He-Ne laser source (λ=633 nm). Millimolar concentration solutions of vesicles were loaded into disposable folded capillary cells Zeta Cell (DTS 1060) and data were collected at 25 °C. A 3 mM vesicle solution was diluted 3 times with 25 mM NaCl to give a 1mM vesicle solution. Its zeta potential was measured and then a few µL of NCs (8.7 µM diluted 3 times with 25 mM of NaCl) was added little by little by making a titration and measuring the zeta potential after each addition. The vesicles zeta potential was extracted from the inelastic frequency shift of the laser signal scattered by moving charged colloid under an electric field (applied cell voltage was 15 V).

Spectrofluorimetry. Photoluminescence measurements were performed on a Jasco FP-8300 spectrofluorometer. The measurements were performed at room temperature on liquid samples. The wavelength resolution of both the excitation and the emission slits was set to 5 nm, the response times was 0.5 s, the detector sensitivity was set to medium and the scan speed was 500 nm/min.

Luminescence Lifetime measurements (in collaboration with Dr. Giorgia Franzo, Department of Physics and Astronomy, University of Catania). Luminescence measurements were performed by pumping with the 325 nm line of an HeCd laser. The pump power was 0.6 mW over a circular area with a 1 mm diameter and the laser beam was chopped through an acousto-optic modulator at a frequency of 55 Hz. The luminescence signal was analyzed by a single grating monochromator and detected by a photomultiplier tube. Luminescence lifetime measurements were performed by detecting the luminescence signal at 600 nm after pumping to steady state, switching off the laser beam and analyzing it with a photon counting multichannel scaler having the signal from the modulator as a trigger.

Light Optical Microscopy. The fluorescence optical microscopy observations were performed either under direct bright light and epifluorescence on an inverted microscope IX71 (Olympus, Japan) equipped with both a 20 x, 0.45 (NA) objectives (Olympus, Japan). NCs solutions were excited at 365 nm by a high vacuum mercury lamp (200 W). Images were acquired by a Photometrics CoolSNAP HQ2 camera equipped with a soft imaging system (Olympus, Japan).

Transmission Electron Microscopy (TEM) (with the assistance of Dr. Vincent Dorcet, THEMIS platform). Transmission Electron Microscopy analysis were carried out with with JEOL 2100 transmission electron microscope operated at 200 KV supplied with UltraScan 1000XP CCD Camera. For the sample preparation, 300 mesh carbon coated nickel grids were placed for 1 min on top of a 40 µL sample droplet and dried up with paper. Particle sizes and interparticle distances were determined from TEM micrographs using Fiji Software.

Cryo-Transmission Electron Microscopy (Cryo-TEM) (in collaboration with Dr. Aurélien Dupont, CNRS Inserm). Vitrification of vesicles was performed using an automatic plunge freezer (EM GP, Leica) under controlled humidity and temperature (Dubochet and McDowall, 1981). The samples were deposited to glow-discharged electron microscope grids followed by blotting and vitrification by rapid freezing into liquid ethane. Grids were transferred to a single-axis cryo-holder (model 626, Gatan) and were observed using a 200 kV electron microscope (Tecnai G^2 T20 Sphera, FEI) equipped with a 4k × 4k CCD camera (XF416, TVIPS). Micrographs were acquired under low electron doses using the camera in binning mode 1 and at a nominal magnifications of 25,000x.

3.2 NANOCLUSTERS ENCAPSULATION INSIDE LIPOSOMES

The luminescent NCs are attractive candidates for in vivo biosensing and bioanalysis in cells or in microorganism. In this view it is required to deliver them to the target with a high concentration by keeping their optical properties and their integrity. It is also crucial to avoid undesired interactions with biomolecules within the blood or other fluids during the path of the NCs inside the body to the place of interest. One way is to encapsulate them to deliver them at the target. It was thought to encapsulate them within the same synthetic vesicles as we previously studied to mimic the cell membrane.

3.2.1 SYNTHESIS NANOCLUSTERS AND ENCAPSULATION METHOD

Two types of NCs (C_3E_6D Red and Blue NCs) were synthesized using the two syntheses already described above. The C_3E_6D is of great interest to improve the properties of NCs since, in addition to having a strong adhesion to the particle and increasing its luminescence, it allows to increase the stability in solution thanks to the steric stabilization due to the PEG and to the electrostatic stabilization of the two carboxy groups.

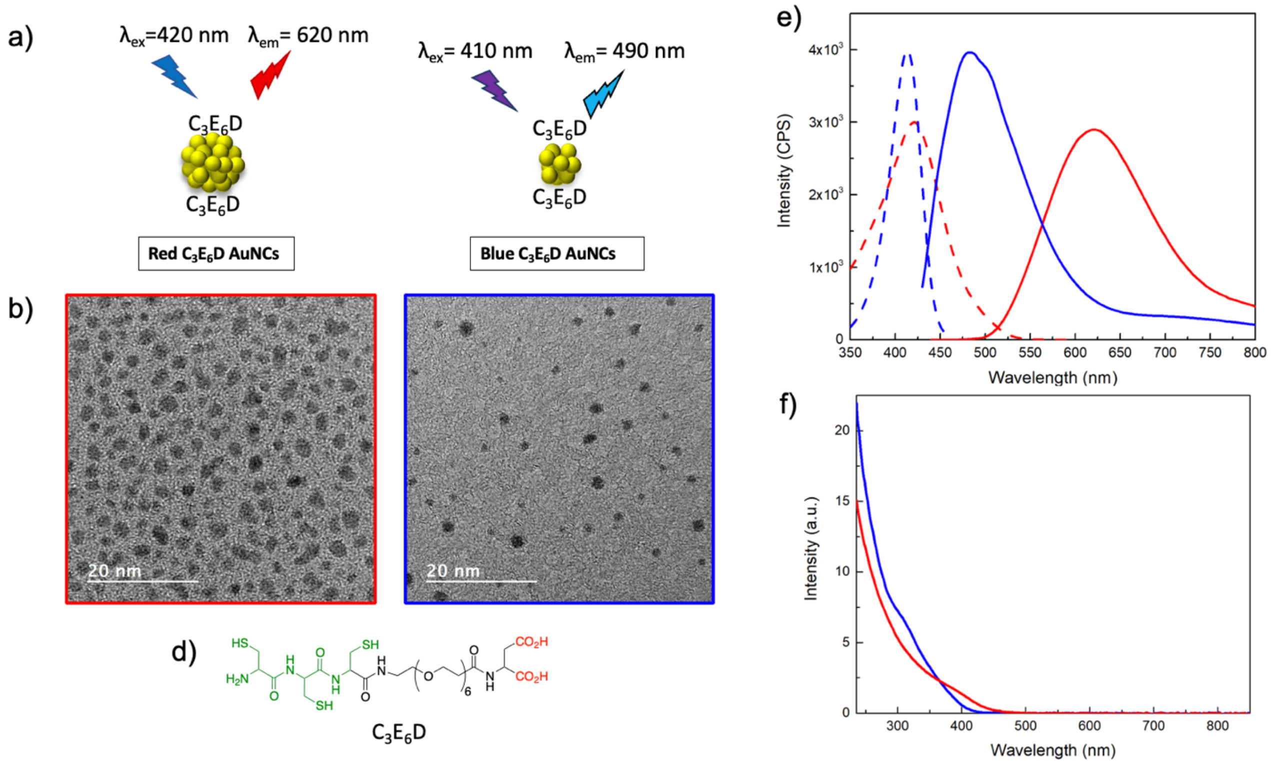

Figure 69. a) Schematic view, b) TEM micrographs, e) luminescence excitation and emission spectra and f) absorbance spectra of C_3E_6D Blue and Red NCs (blue and red line respectively). d) Chemical structure of NCs ligand C_3E_6D.

Furthermore, it also allows to transform the NCs into a multivalent platform by means of the two carboxylic groups that allows to bind drugs, antibodies or other recognition segments for therapy on the surface of the NC.

Once the nanoparticles were synthesized and characterized (**Figure 69**), an innovative encapsulation technique was developed, starting from a protocol described in the literature for the formation of GUVs[123].

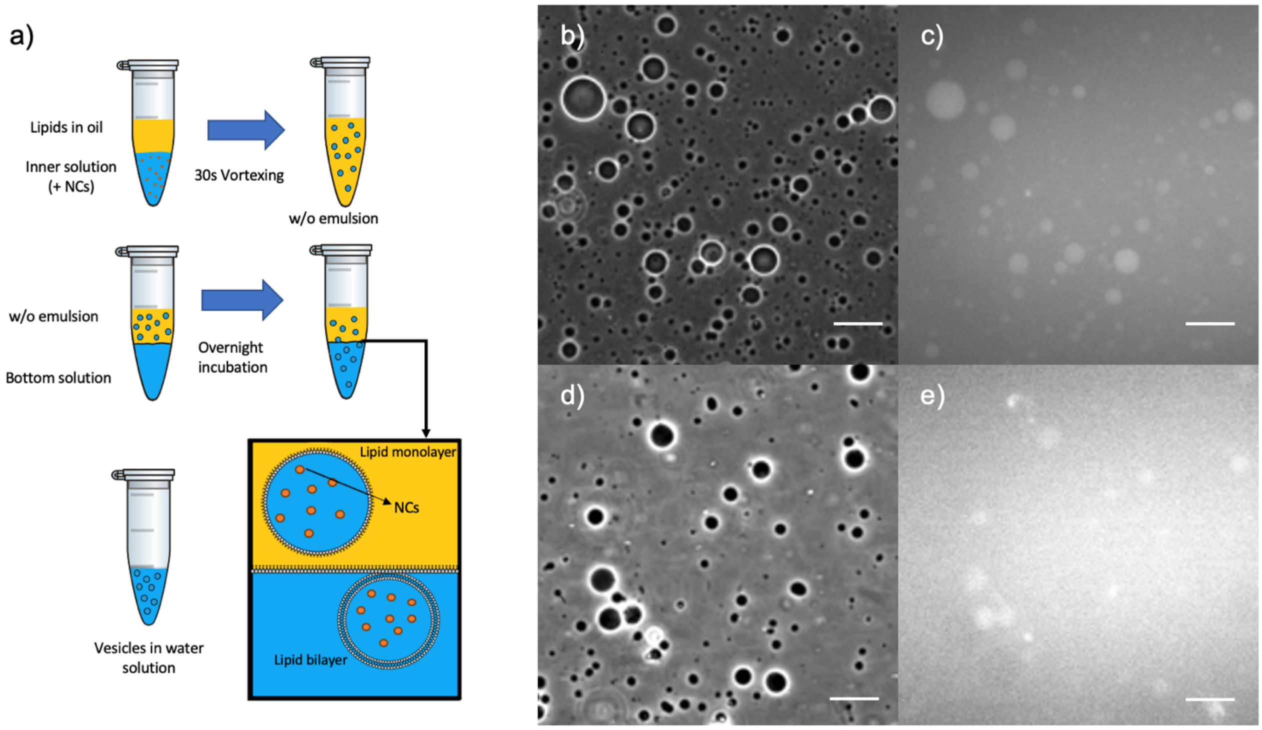

Figure 70. a) Schematic view of Au NCs encapsulation method into GUVs. Optical microscope images b,d) in phase contrast or c,e) luminescence of b,c) C_3E_6D and d,e) GSH Red NCs incapsulated inside DOPC GUVs. Scale bar 50 µM.

A lipid solution was mixed with an aqueous solution containing C_3E_6D Blue or Red NCs (≃2 µM) and a strong concentration of sucrose (500mM) to form a water-in-oil emulsion composed of inverse micelles after vortexing. Then this emulsion was gently poured over the lower aqueous solution containing an isosmolar solution of glucose (500 mM). After the overnight incubation, the reverse micelles of the emulsion cross the lipid interface and pour into the lower solution due to the density discrepancy between glucose and sucrose. By crossing the interface monolayer of the inversed micelles is transformed into a lipid bilayer (GUVs) containing the NCs inside ready for use (**Figure 70a**).

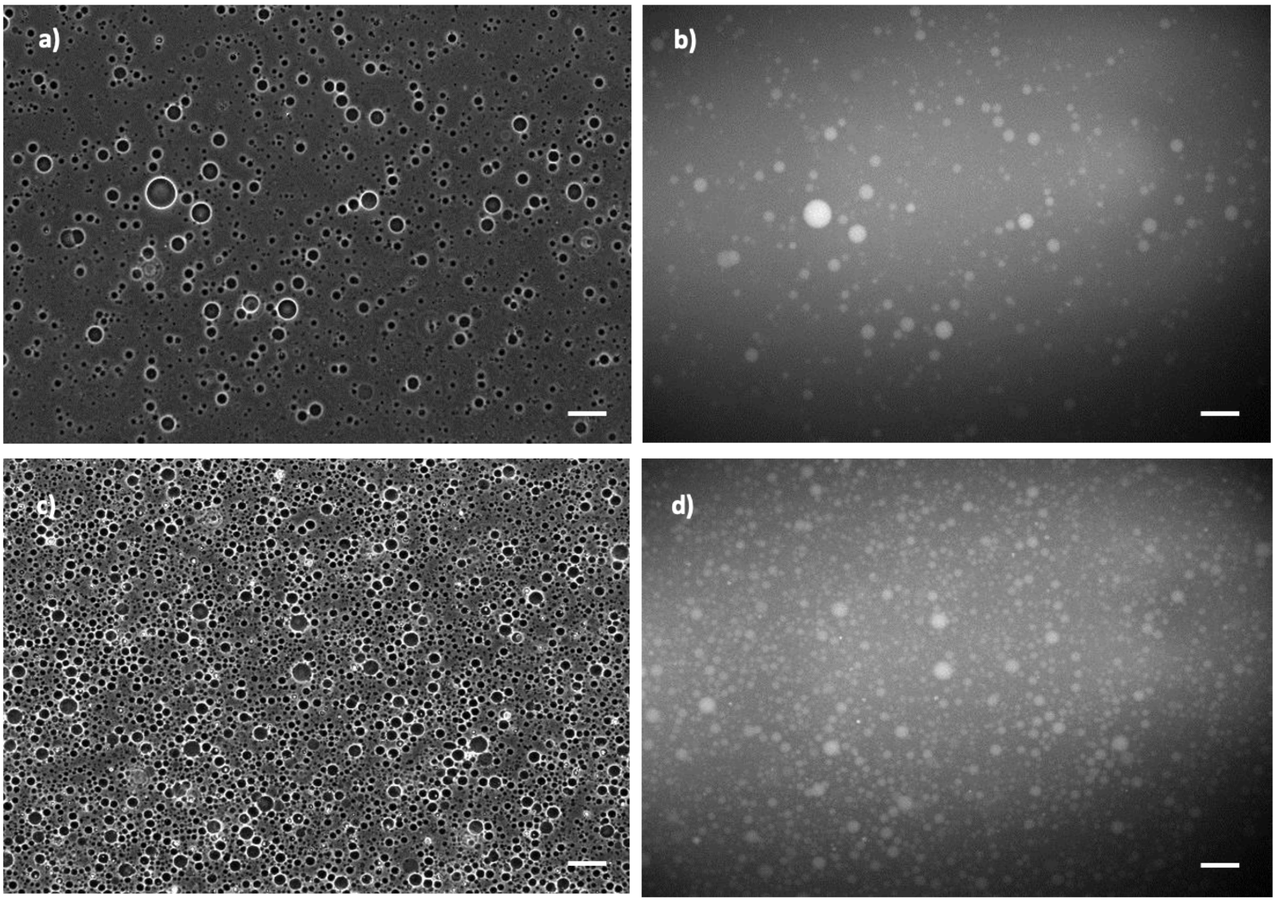

Figure 71. Optical microscope images a,c) in phase contrast or b,d) luminescence of C_3E_6D Red NCs encapsulated inside a,b) DOPC and c,d) DOPC/DOTAP GUVs. Scale bar 20 µM.

Several experiments were performed to better understand how some factors affect the formation of the vesicles containing the NCs. Initially, for simplicity, only the Red NCs were used to optimize the conditions and study the various parameters such as the surface charge of the vesicles, the ligand and the consequent surface charge of the NCs, the concentrations of lipids and NCs involved. For example, negatively charged NCs (C_3E_6D Red NCs) were encapsulated within neutral vesicles or positively charged vesicles, yielding a similar result that led in both cases to efficient encapsulation, regardless of the surface charge of the vesicles (**Figure 71**). Conversely, by varying the type of surface ligand of the NCs, the encapsulation efficiency was not the same. In fact, using GSH instead of C_3E_6D, although also in this case we obtain NCs encapsulated in GUV, the encapsulation efficiency is lower, as can be seen qualitatively from the high background fluorescence in **Figure 70 b-e**. This result is attributed to the lower stability of the GSH NCs which tend to aggregate and destabilize the vesicles or a possible interaction between GSH and the membrane, with consequent rupture and leakage of the NCs. A scheme illustrating the NCs encapsulated within the GUVs is presented in **Figure 72a**.

3.2.2 ESTIMATION OF ENCAPSULATION EFFICIENCY

The GUVs thus formed were observed by confocal fluorescence microscopy (**Figure 72 b-l**) to visualize the luminescence of the NCs inside more accurately. In this experiment, the C_3E_6D Blue (**Figure 72 b-d**) and Red (**Figure 72 e-g**) NCs were used and, in both cases, luminescent discs were observed that coincide with the shape of the vesicles observed by phase contrast.

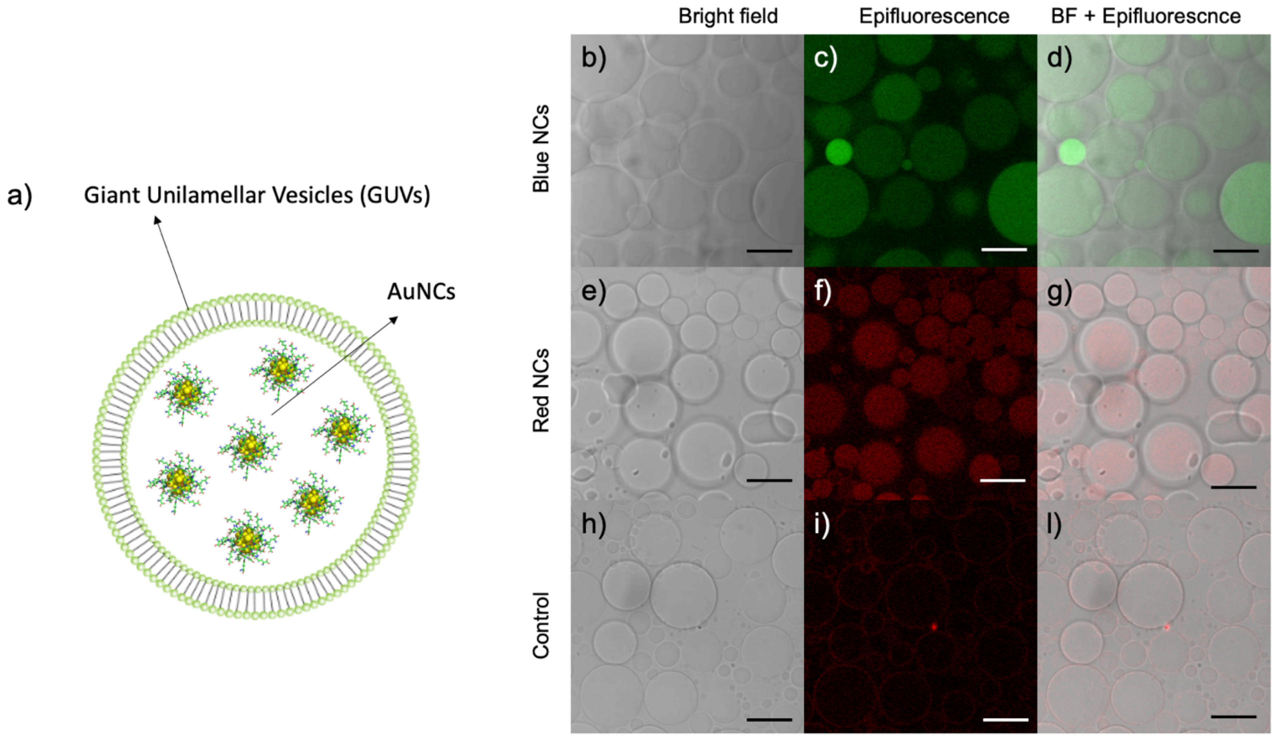

Figure 72. a) Schematic view of AuNCs incapsulated inside GUVs. Confocal microscopy Image of (b,c,d) C_3E_6D Blue Au NCs, (e,f,g) C_3E_6D Red Au NCs encapsulated in DOPC GUVs and **(h,i,l)** DOPC GUVs without Au NCs as a control obtained by **(b,e,h)** bright field, **(c,f,i)** luminescence and **(d,g,l)** merged images. Scale bar 20 µM.

Figure 73 shows images with lower magnification in order to have a more global view. This confocal observation indicates that the NCs were encapsulated within the vesicles without breaking them or altering their integrity. It is noticeable that the fluorescence intensity is not the same in all vesicles. Some of them appear much more fluorescent.

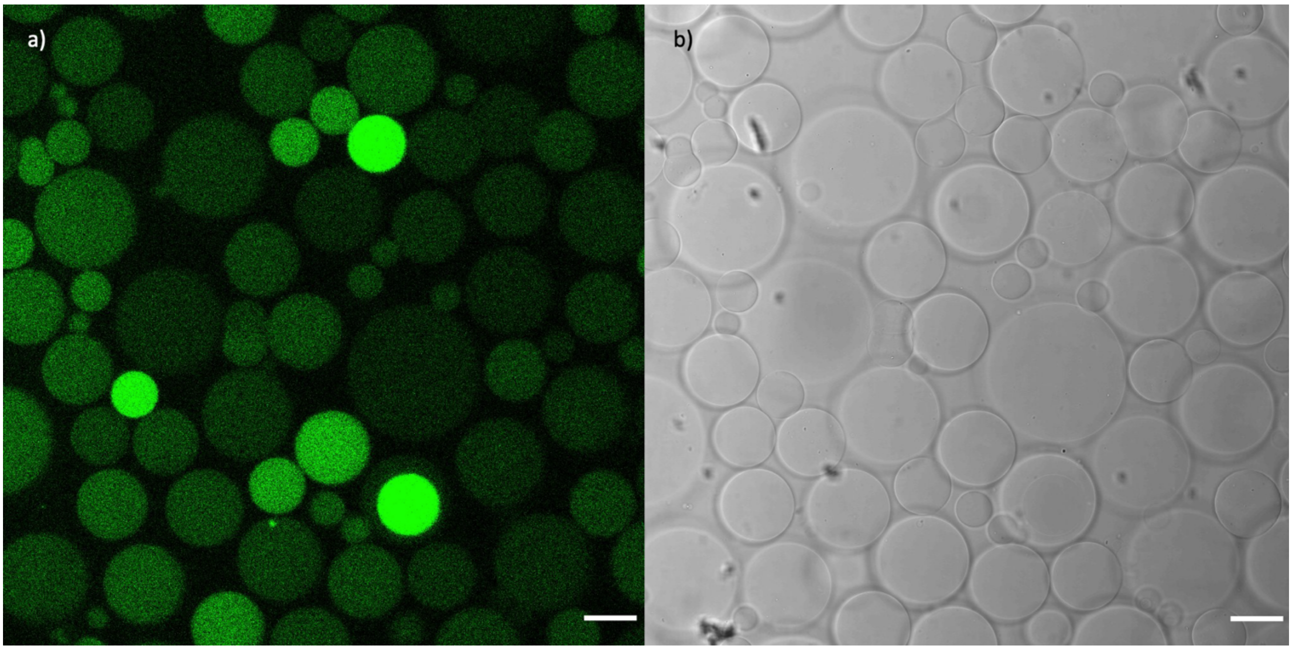

Figure 73. Confocal microscope a) bright field and b) luminescence images of C_3E_6D Blue NCs incapsulated inside DOPC GUVs.

MLVs and LUVs of 100 nm were synthesized in the presence or absence of NCs in aqueous sucrose solution. To quantify the encapsulation efficiency, the concentrations of gold and phosphorus atoms were determined by inductively coupled plasma mass spectroscopy (ICP-MS) in the suspensions before and after extrusion (MLVs or LUVs) and before and after the ultrafiltration process to eliminate excess of non-encapsulated NCs.

	Au Concentration (mg/L)
MLVs + NCs	73.75
MLVs + NCs purified	31.88
LUVs + NCs	53.75
LUVs + NCs purified	30

Table 7. Gold concentration obtained by ICP of C_3E_6D Red NCs solutions incapsulated inside LUVs and MLVs before and after purification.

Regarding the phosphorus concentration, only 18% of the initial amount of phosphorus used to prepare the MLVs was found in the suspension of LUVs with encapsulated NCs, corresponding to a lipid yield of 18% which agrees with the expected bilayer loss during the extrusion process. Furthermore, in **Table 7** it is possible to see the gold concentrations before (MLV) and after (LUV) extrusion and before and after (purified) ultrafiltration purification used to remove the non-encapsulated NCs in excess (outer medium). The initial gold value corresponds to that measured in the MLVs + NCs solution (73.75 mg/L). Following the extrusion process, there is a loss of 27%, and what remains undergoes a further loss of 44% due to ultrafiltration to purify. Considering the initial Au concentration (73.75mg/L) compared to that after extrusion and purification (30mg/L), the Au encapsulation yield was found to be 40%. But the trapped volume of extruded LUVs with a pore size of 100 nm and a typical concentration of 10 mg / mL is about 10% according to the literature[125,126]. Hence the Au encapsulation yield of 40% is much higher than the trapping efficiency of liposomes. This latter result suggests that NCs are not only trapped in the internal volume of liposomes, but are also embedded in the bilayer membrane, thus greatly increasing the Au trapping efficiency of liposomes.

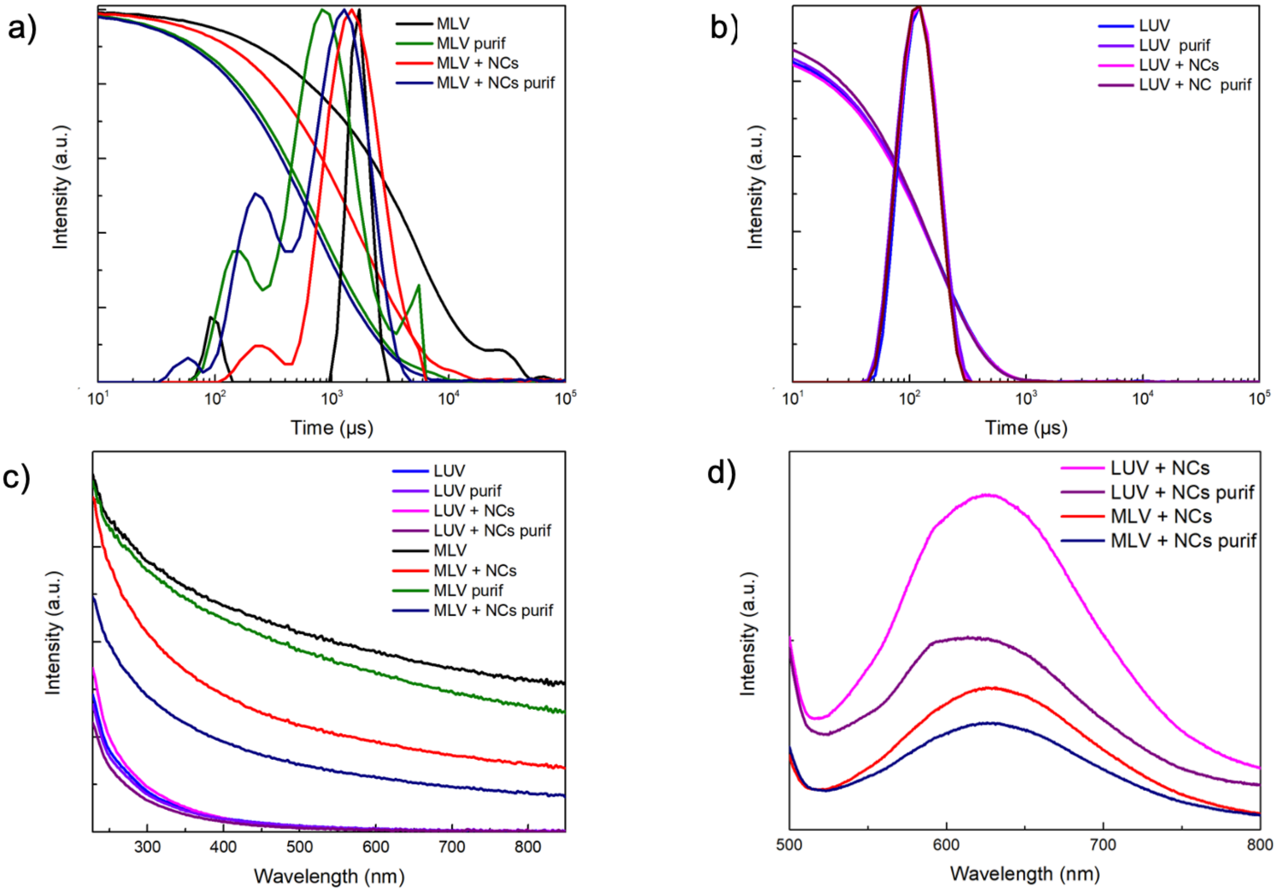

Figure 74. DLS intensity and correlogram of a) MLVs and b) LUVs with or without C_3E_6D Red NCs, before and after purification. c) Absorbance spectra and d) luminescence emission spectra (λ_{ex}=400 nm) of MLVs and LUVs with or without C_3E_6D Red NCs, before and after purification.

Furthermore, it is interesting to note that the MLVs and LUVs after purification have a similar concentration of Au (respectively 31.88 and 30 mg/L), indicating that the NCs are well encapsulated in the internal part of the liposomes, therefore both in the LUVs and in the MLVs the majority part of the NCs are found in the inner aqueous compartment; in fact, the only difference between the two types of vesicles is the extrusion process, which results in peeling the MLVs leaving only the central compartment encapsulated in one closed bilayer. Nevertheless, the gold encapsulation yield around 40% appears to be higher than what is expected from 100 nm diameter LUVs.

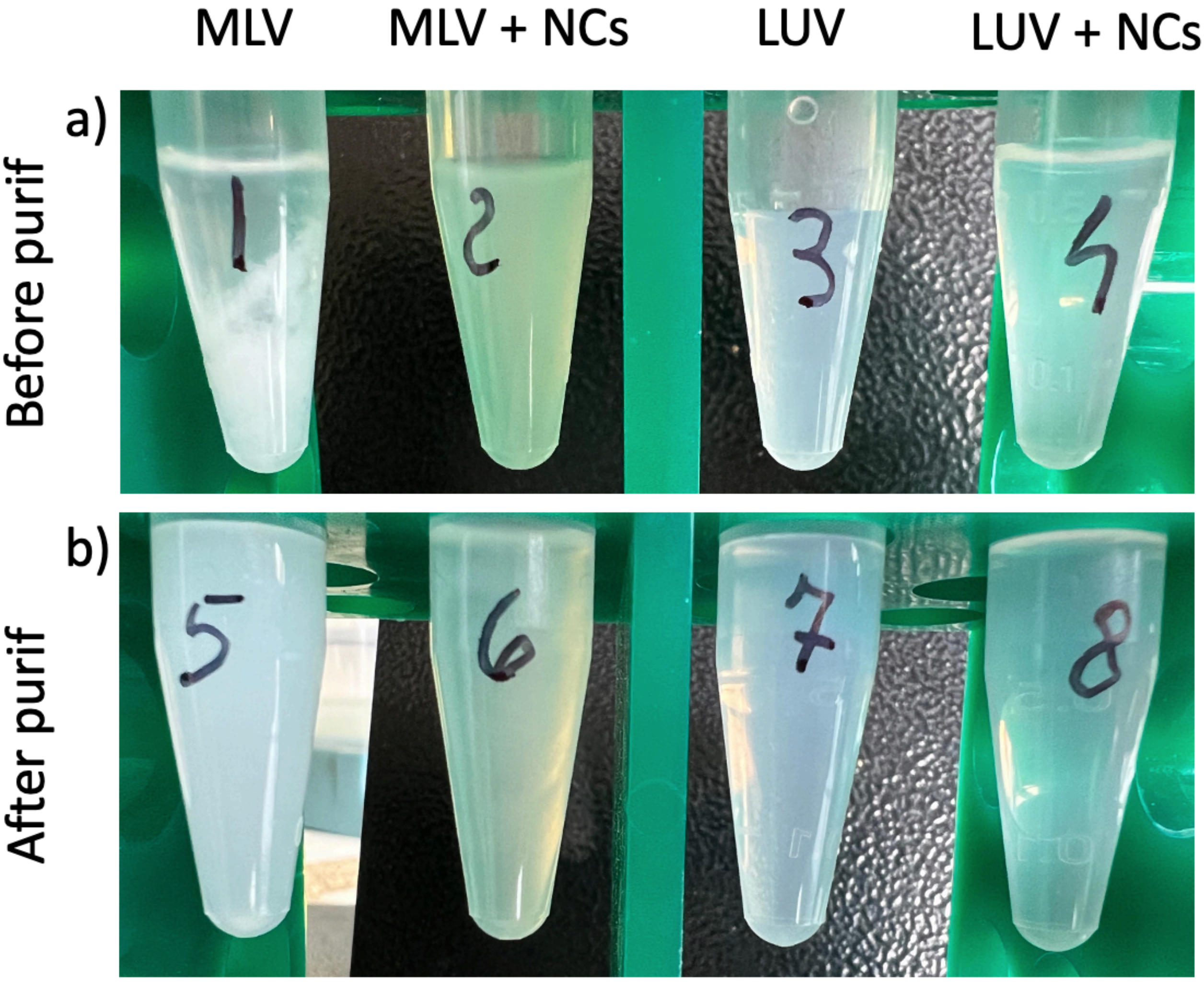

Figure 75. Images of synthetic vesicles suspensions with or without C_3E_6D Red NCs, a) before and b) after purification.

3.2.3 OPTICAL AND MORPHOLOGICAL CHARACTERISATION OF THE FLUORESCENT LIPOSOMES

To estimate more precisely the size of the vesicle population, the dimensions of the vesicles were analyzed before and after extrusion, and before and after purification by using Dynamic Light Scattering (DLS). In **Figure 74a** it is possible to note the correlogram and the DLS intensity curve of the MLVs before and after purification. In all cases there are large vesicles with dimensions of about 1 µm since they have not undergone the extrusion process. From the correlogram it is possible to note that the purification process, both in the presence of NCs and in their absence, leads to a reduction in the size of the vesicles by eliminating large aggregates. Furthermore, even before purification, the presence of NCs stabilizes the vesicles and does not allow the formation of multilamellar sheets that create precipitates after a few hours (**Figure 75**). **Figure 74b** instead shows the DLS measurement of MLVs after extrusion that form LUVs with very precise dimensions, peaking at 100 nm, both in the presence and absence of NCs. The result remains the same even after purification.

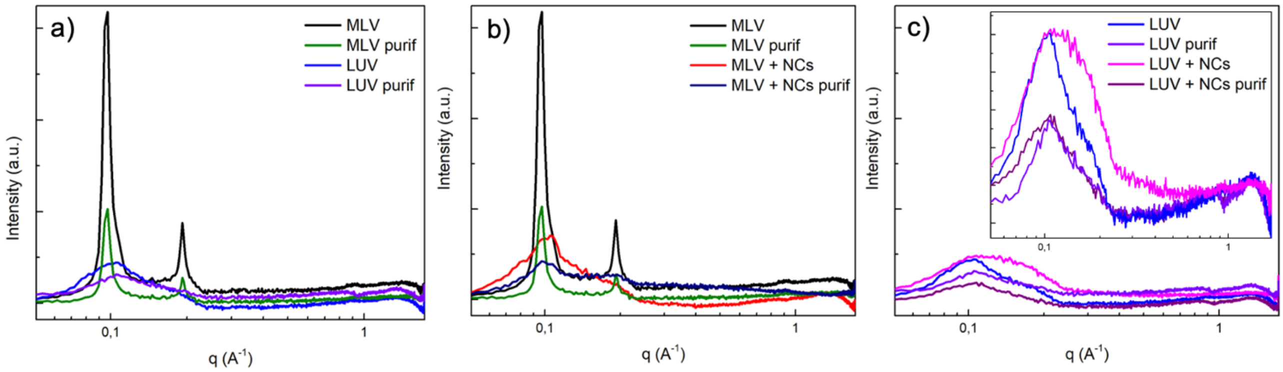

Figure 76. SAXS spectra comparison between a) MLVs and LUVs, b) MLVs with and without C_3E_6D Red NCs, c) LUVs with and without C_3E_6D Red NCs.

To better characterize the samples, a measurement of the UV-VIS absorbance was also carried out which evidence light scattering corresponding to the presence of nanometric objects that the incident light (**Figure 74**). This measurement also confirms the result obtained by the DLS in which the NCs stabilize the membranes of the MLVs and do not allow the formation of large aggregates as in the case of the MLVs alone. As expected, LUVs have a much lower and similar light scattering in all cases, showing a slightly higher level in the presence of an excess of NCs adding their scattering contribution to that of the vesicles.

To verify that the luminescence of the NCs did not undergo variations in intensity or emission wavelength following the encapsulation process, fluorescence studies were performed (**Figure 74d**). In the case of MLVs, despite having a higher NCs concentration because they have not undergone the extrusion process, there is a lower fluorescence intensity than in the case of LUVs. The highest fluorescence peak occurs in the case of LUVs in the presence of NCs before the purification process; the decrease of the fluorescence signal after purification confirms the elimination of the non-encapsulated NCs.

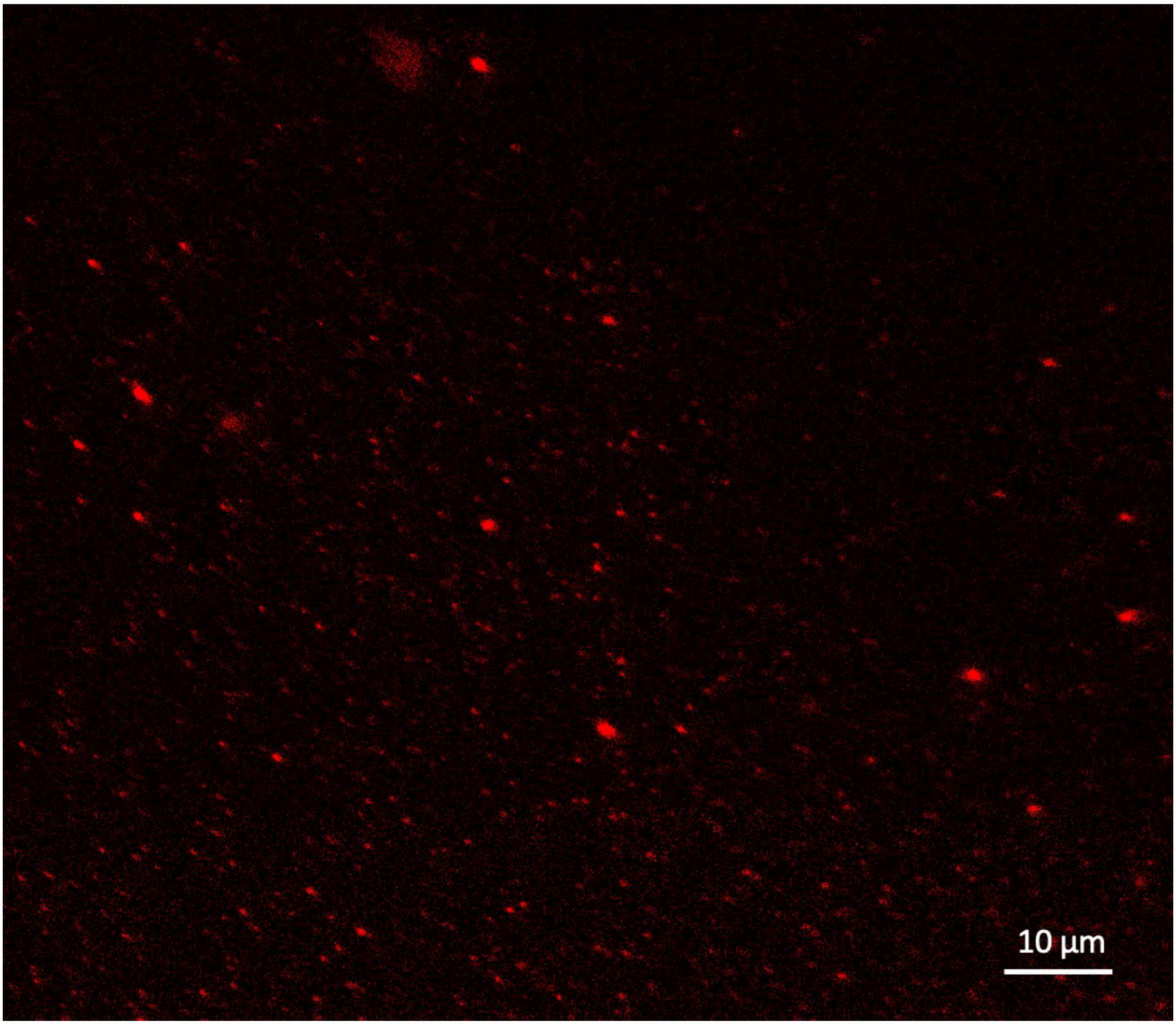

Figure 77. Confocal microscope images of C_3E_6D Red NCs encapsulated inside MLVs.

Angular X-Ray Spectroscopy (SAXS) measurements were performed to verify the presence of ordered lipid membranes within the sample and study the influence of NCs on this order (**Figure 76**). The MLVs have two very precise peaks (0.097 A $^{-1}$ = 6.4 nm and 0.192 A $^{-1}$= 3.2 nm) corresponding to the thickness of one lipid bilayer and the second order of the same signal and are not shifted in presence of the NCs. However, the intensity of these peaks is lowered by the presence of NCs which is attributed to a decreasing order. The presence of the NCs on the membrane surface and possibly between the lamellae, could induce a decrease in the multilamellar order (**Figure 76 a,b**)[124]. In the case of LUVs, the loss of the peak corresponding to the second order occurs as a result of the lowering of the main peak (**Figure 76c**). The main peak is lowered due to the decrease in the number of lipids due to the extrusion process which lowers the SAXS signal; moreover, the second order occurs rather in the case of multilamellar structures, which is no longer valid for LUVs which, following the extrusion, are unilamellar vesicles. In this case the presence of NCs does not decrease the peak, which instead widens to the right due to the presence of NCs before purification; this is probably due to the positioning of the NCs on the surface of the LUVs, which, being in excess, increase the thickness of the membrane.

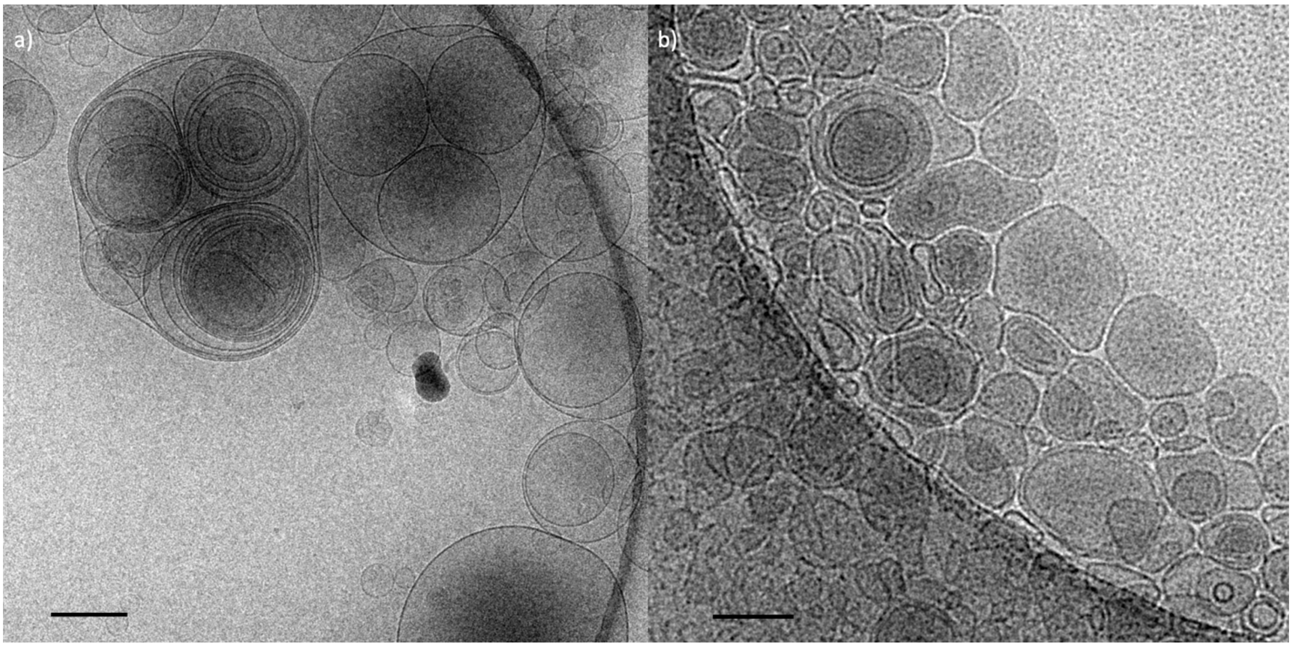

Figure 78. CryoTEM micrographs of DOPC a) MLVs and b) LUVs before purification without NCs. Scale bar 100 nm.

Since it is not possible to analyze MLVs and LUVs under the confocal microscope due to the size below the resolution limit (**Figure 77**), it was decided to analyze the samples using CryoTEM, the only technique that allows to see the vesicles closer to the original structure avoiding artifacts due to the sample freezing, and which allows to simultaneously detect the presence of NCs. However, these particles are so small that they fall within the resolution limit of the CryoTEM and consequently are only visible when they form small aggregates.

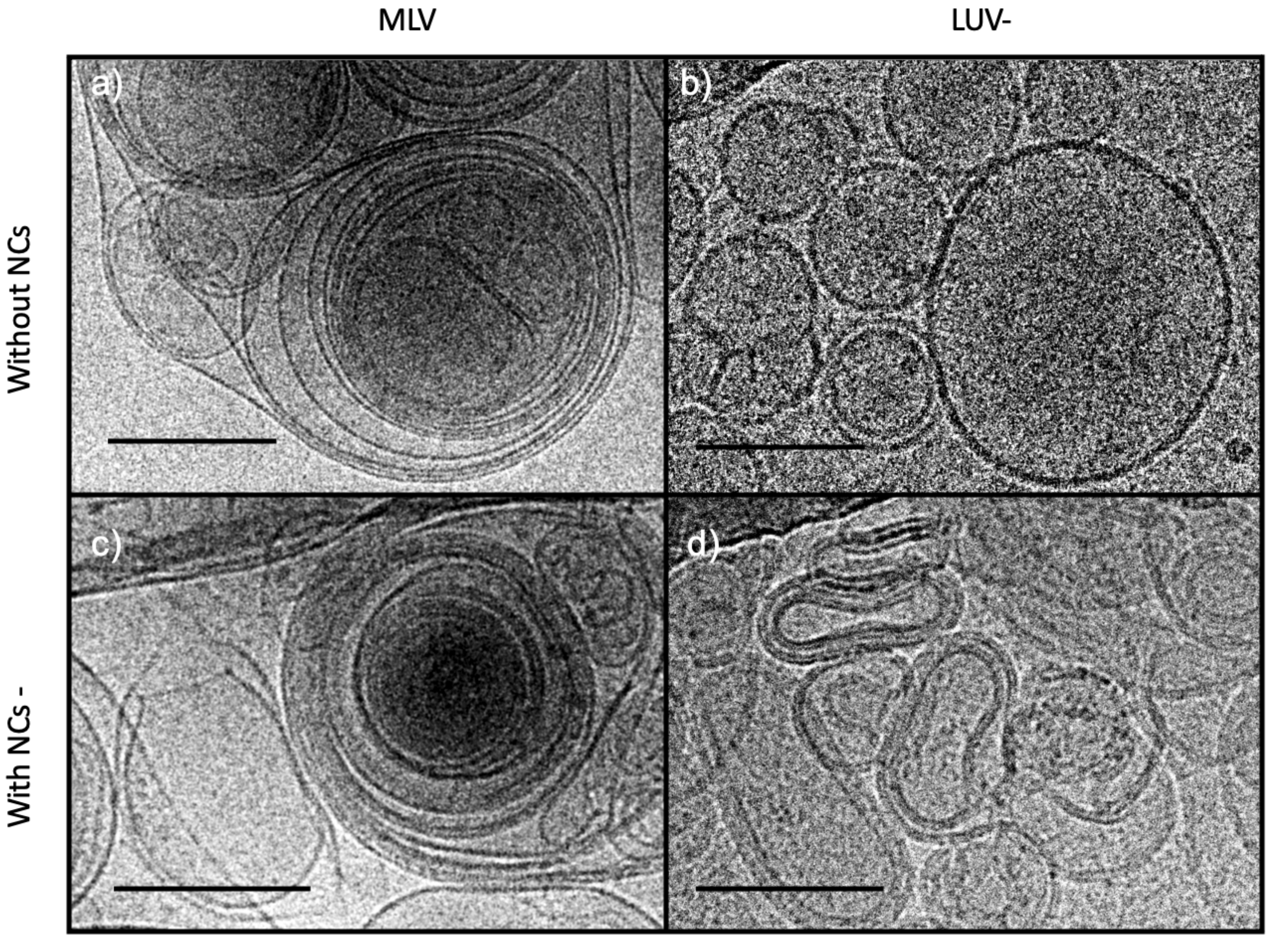

Figure 79. CryoTEM micrographs of DOPC a,c) MLVs and b,d) LUVs before purification a,b) without and c,d) with C_3E_6D Red NCs. Scale bar 100 nm.

Figure 78 shows the difference between MLVs and LUVs observed at CryoTEM: LUVs, as already appreciated by DLS measurements, have a size of about 100 nm quite monodisperse, unlike MLVs which have a much higher percentage of multilamellar vesicles of larger dimensions and polydisperse. CryoTEM images of MLVs and LUVs with or without NCs were compared in **Figure 79**.

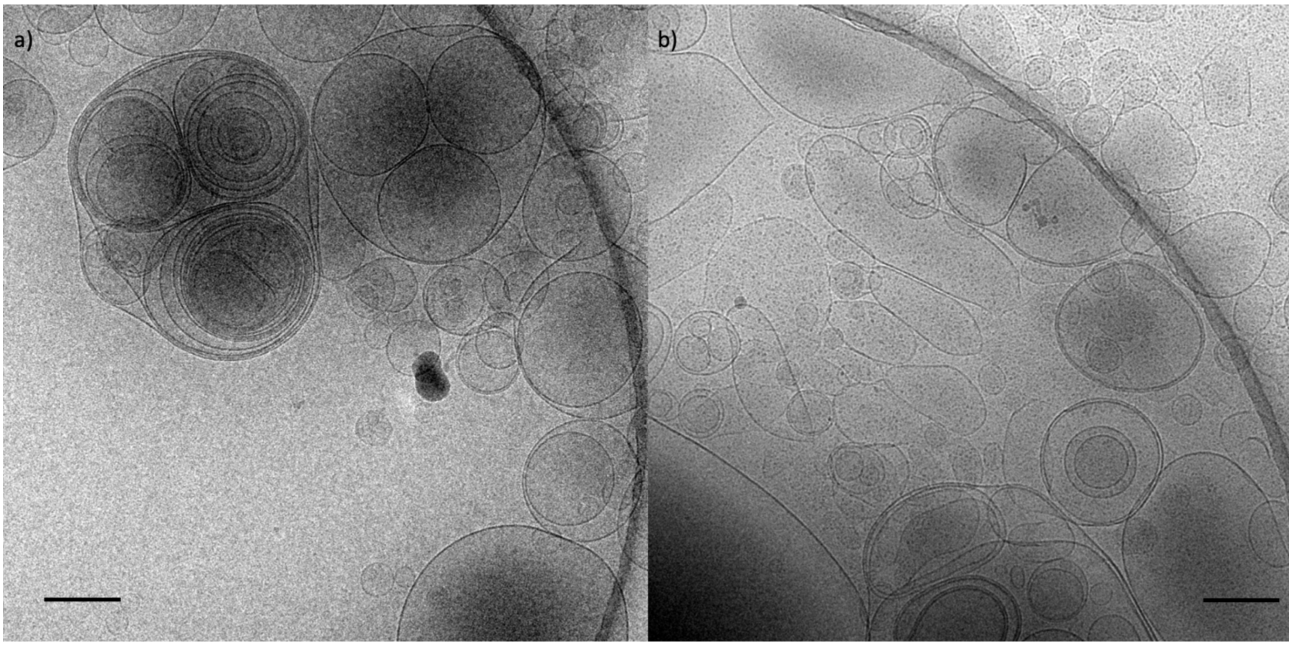

Figure 80. CryoTEM micrographs of DOPC MLVs before purification a) without and b) with C_3E_6D Red NCs. Scale bar 100 nm.

In the case of MLVs the presence of NCs is hardly visible on the membrane, perhaps due to a very dark color due to the presence of lipid multilayers; however, it is possible to notice in the background the presence of small black dots which could be small aggregates of NCs, not present in the control (**Figure 80**). In the case of LUVs , on the other hand, the NCs are more visible on the surface of the membrane, and it is possible to notice them also between the lamellae if the membrane is formed by several lipid bilayers (**Figure 81**). The image in **Figure 82** shows a CryoTEM overview of LUVs with and without NCs.

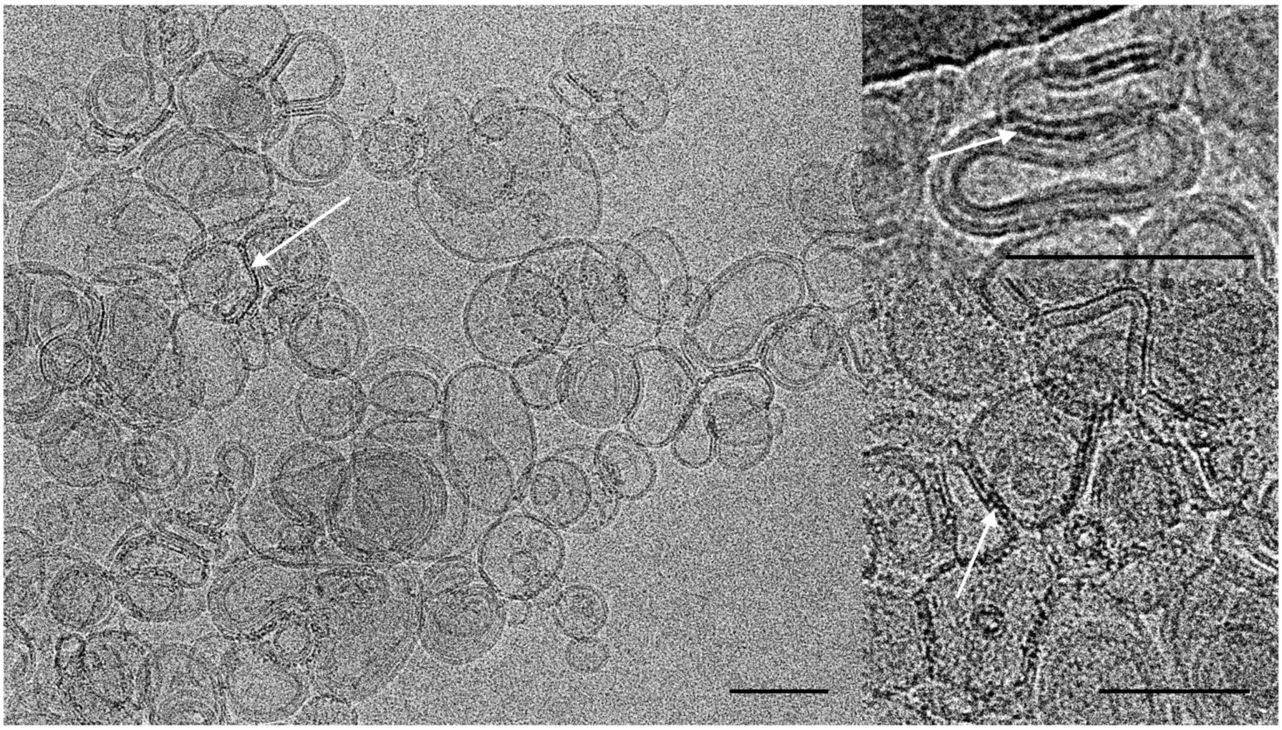

Figure 81. CryoTEM micrographs of DOPC LUVs before purification with C_3E_6D Red NCs. Scale bar 100 nm.

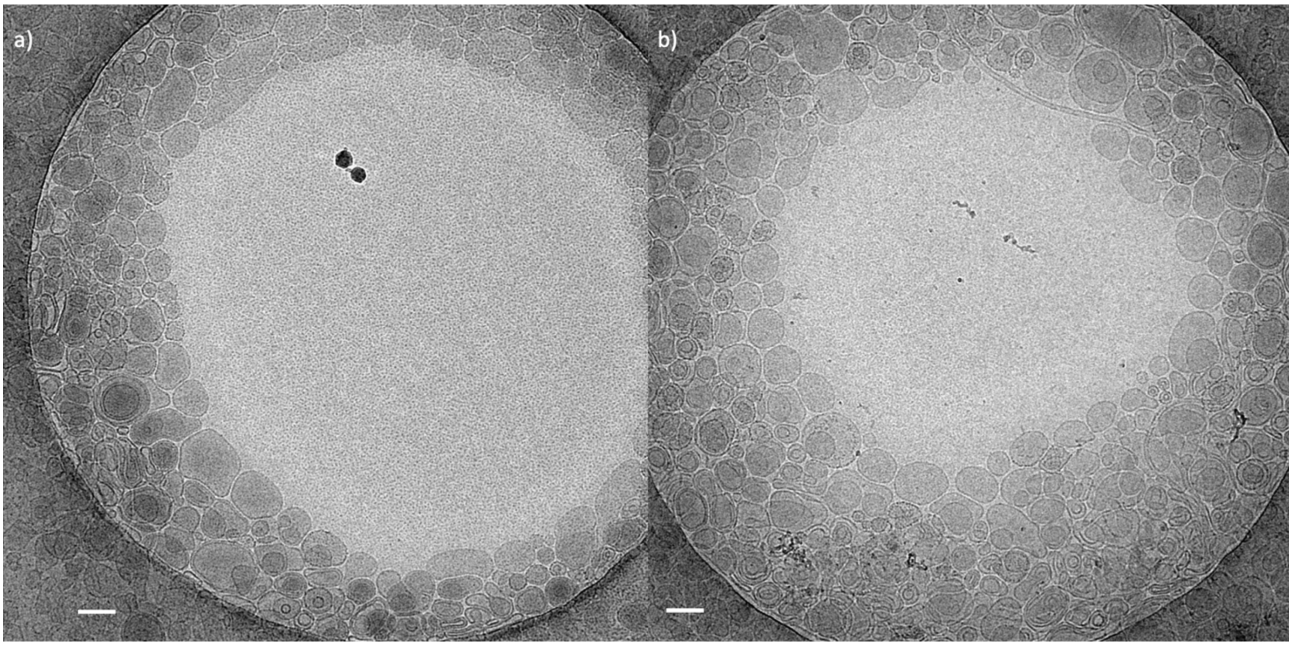

Figure 82. CryoTEM micrographs of DOPC LUVs before purification a) without and b) with C_3E_6D Red NCs. Scale bar 100 nm.

3.2.4 CONCLUSIONS AND PERSPECTIVES

Therefore, thanks to the complementary techniques used, it was possible to demonstrate the efficiency of the innovative encapsulation methods presented above; in fact, there is an encapsulation efficiency of 40% of Au NCs within LUVs. This result was possible to obtain through a careful optimization of the parameters and through the functionalization of the NCs with C_3E_6D which, by increasing the stability of the NCs, decreases the rupture of the membranes and the consequent leakage of NCs into the external liquid. Subsequently, the external part of the vesicles could also be functionalized in order to introduce specific recognition groups that can vehicle the NCs to target organism parts with a higher concentration.

3.2.5 EXPERIMENTAL SECTION

C_3E_6D Red NCs Synthesis[124]*.* All glassware used for these synthesis were cleaned in a bath of freshly prepared aqua regia (HCl:HNO_3, 3:1 by volume) and rinsed in water 10 times before using them. The NCs solution obtained could be stored at 4 ° C for months without significant change in their optical properties. A freshly prepared aqueous solution of glutathione denoted GSH (50 mM, 1,2 mL) were mixed with 16,8 mL of ultrapure water. The solution was heated in oil bath at 120°C and $HAuCl_4$ (20 mM, 2mL) and was rapidly added to it. The reaction was stopped after stirring for 3h. An aqueous suspension of orange-emitting GSH Au NCs was formed (2.6 µM). Then a freshly prepared aqueous solution of C_3E_6D (20 mM, 0.155 mL) was mixed with 1 mL of GSH Au NCs suspension. Afterwards, the mixture was incubated without stirring in dark at room temperature overnight to prepare the final C_3E_6D Red Au NCs.

C_3E_6D Blue NCs Synthesis. A freshly prepared aqueous solution of C3E6D (20 mM, 0.585 mL) was diluted with H_2O milliq to reach a final volume of 2.7 mL. After dipping the flask containing the solution in an oil bath at 120 ° C under stirring, a solution of HAuCl4 (20 mM, 0.3 mL) was quickly added to it. The reaction was stopped after 4 h. An aqueous solution of C3E6D Blue NCs was obtained which emit in the blue region.

C_3E_6D Blue or Red NCs Purification. C3E6D Blue NCs were purified by ultrafiltration (Amicon 3KDa) at 17000 g for 10 min. What remains inside the filter and does not pass the 3 KDa membrane will be the purified C3E6D Blue or Red NCs.

Giant unilamellar vesicles (GUVs) preparation[123]*.* A lipid solution was prepared dissolving DOPC or DOPC:DOTAP (95:5) molar lipidic mixture lipids in chloroform (10 mg / ml). 20 µL of this solution and 1.8 mL of paraffin oil are mixed and heated at 80°C for 30 min in a flask without cap. Then, the suspension is placed in a desiccator for 20 min in order to evaporate the chloroform and to obtain the final lipid organic solution. To prepare the GUV, 50 µL of sucrose (500 mM) are added to 400 µL of lipid solution vortexed for 40 s to form a water-in-oil (w/o) emulsion. Then, this emulsion is gently added on the top of a sucrose solution of high viscosity (200 µL, 500 mM in a second Eppendorf) without mixing. After waiting 10 minutes, the solution is centrifuged for 15 minutes at 18890 g The bottom was transferred into another Eppendorf, redispersed in 300 µl of glucose (500 mM) and centrifuged again at 18890 g for 5 minutes. After centrifugation, the bottom solution is taken up and the GUVs are ready to be stored in the refrigerator.

NCs inside Giant Unilamellar Vesicles (GUVs). A lipid solution was prepared by dissolving DOPC or a DOPC: DOTAP (95:5) lipidic mixture in chloroform (10 mg / ml). 20 µL of this solution and 1.8 mL of paraffin oil are mixed and heated at 80 ° C for 30 min in a flask without cap. Then, the solution is placed in a desiccator for 20 min in order to evaporate all the chloroform and to obtain the final lipid solution. To encapsulate NCs in GUV, 25 µL of sucrose solution (1 M) and 25 µL of NCs (2µM of particles concentration) solution are added to 400 µL of lipid solution vortexed for 40 s to form a water-in-oil (w/o) emulsion. Then, this emulsion is gently added on the top of a sucrose solution of high viscosity (200 µL, 500 mM in a second Eppendorf) without mixing. After an overnight incubation, the GUVs are formed in the bottom and are ready to be collected.

NCs inside Large Unilamellar Vesicles (LUVs). A lipid solution was prepared by dissolving DOPC or a DOPC: DOTAP (95:5) lipidic mixture in chloroform (10 mg / ml). 1 mL of this solution is placed inside a flask in the rotary evaporator at 50°C and 70 mbar at the maximum speed rotation for 30 minutes, so that the flask only touches the surface of the water. After that, a solution of C_3E_6D NCs (~ 2 µM, 500 µL) mixed with a glucose solution (500 mM, 500 µL) was added to the flask containing the phospholipids. The flask was immersed in liquid nitrogen for 30 seconds with rotatory movements, and then again in the water bath at 50°C. This operation must be repeated 5 times. Once the cycles are completed, a 0.1 µM filter is inserted into the extruder and washed with a glucose solution (250 mM). Then, the sample is added with a Pasteur pipette into the extruder at 10 mbar. Once the sample comes out of the extruder, it must be reinserted again 10 times. At the end of this procedure, the sample was purified by ultrafiltration (Amicon 30 kDa). Finally, the concentrations of Au and Phosphorus elements in the LUVs suspension were determined by using the Inductively Coupled Plasma Mass Spectroscopy (ICP-MS) technique. The disruption of the liposomes and the dissolution of the Au NC were realized by incubating the suspension of LUVs containing the Au NCs in aqua regia (1 HNO_3 : 3 HCl) for one night.

Small-Angle X-ray Scattering (SAXS) (in collaboration with Dr. Franck Artzner, Institut de Physique, University of Rennes 1). X-ray patterns were collected with a Mar345 Image-Plate detector

(Maresearch, Norderstedt, Germany) mounted on a rotating anode X-ray generator FR591 (Bruker, Courtaboeuf, France) operated at 50 kV and 50 mA. The sample to detector distance (422 mm) has been calibrated by using silver behenate. The X-ray patterns were therefore recorded for a range of reciprocal spacing $q = 4\pi \sin\theta/\lambda$ from is 0.04-1.2 Å^{-1} where θ is the diffraction angle. The experiments performed with the present set-up provide accurate measurements of distances between 150 Å and 5.2 Å. The acquisition time was 1 hour. Samples were loaded in thin Lindman glass capillaries (diameter 1 ± 0.1 mm and thickness 10 µm; GLAS, Muller, Berlin, Germany) sealed with paraffin. The lipid-NCs hybrid complexes were prepared by mixture of a micromolar concentration NCs solution (10 µL, 1.70 µM NCs concentration) and millimolar concentration SUV suspension (10 µL, 16 mM total phospholipid concentration) in the glass capillaries. All samples exhibited powder diffraction rings, and the scattering intensities as a function of the radial wave vector were determined by circular integration.

Dynamic Light Scattering (DLS). The measurements of the mean hydrodynamic diameters were performed at an angle of 90° using a Nanosizer ZEN3600 (Malvern Instruments, England) and collected at 25 °C, without dilution or filtration.

Inductively Coupled Plasma Mass Spectroscopy (ICP-MS) (with the assistance of Dr. Bertrand Lefeuvre, Institut des Sciences Chimiques, University of Rennes 1). To obtain a precise measurement, 3 solutions at different concentrations of NCs encapsulated in LUVs were prepared to be analyzed. To do this, divers volumes of the starting solution (65 μL, 125 μL, 250 μL) were dissolved in 500 μL aqua regia (1 HNO_3 : 3 HCl) heated for 1h at 50°C to dissolve better dissolve lipids and at left 4°C overnight. The next day H_2O was added to bring the volume of each sample to a total of 25 mL and the measurement was carried out. A sampling curve for Au and P from 0.2 to 2 ppm was prepared for the measurement.

Spectrofluorimetry. Photoluminescence measurements were performed on a Jasco FP-8300 spectrofluorometer. The measurements were performed at room temperature on liquid samples. The wavelength resolution of both the excitation and the emission slits was set to 5 nm, the response times was 0.5 s, the detector sensitivity was set to medium and the scan speed was 500 nm/min.

UV-visible Absorbance. The UV-visible Absorbance measurements were performed using a ThermoFisher Scientific NanoDrop by placing 2 µL of non-diluted sample over the pedestal.

Luminescence Lifetime measurements (in collaboration with Dr. Giorgia Franzo, Department of Physics and Astronomy, University of Catania). Luminescence measurements were performed by pumping with the 325 nm line of an HeCd laser. The pump power was 0.6 mW over a circular area with a 1 mm diameter and the laser beam was chopped through an acousto-optic modulator at a frequency of 55 Hz. The luminescence signal was analyzed by a single grating monochromator and detected by a photomultiplier tube. Luminescence lifetime measurements were performed by detecting the luminescence signal at 600 nm after pumping to steady state, switching off the laser beam and analyzing it with a photon counting multichannel scaler having the signal from the modulator as a trigger.

Light Optical Microscopy. The fluorescence optical microscopy observations were performed either under direct bright light and epifluorescence on an inverted microscope IX71 (Olympus, Japan) equipped with both a 20 x, 0.45 (NA) objectives (Olympus, Japan). NCs solutions were excited at 365 nm by a high vacuum mercury lamp (200 W). Images were acquired by a Photometrics CoolSNAP HQ2 camera equipped with a soft imaging system (Olympus, Japan).

Confocal Microscopy (with the assistance of Dr. Stephanie Dutertre and Dr. Xavier Pinson, MRic platform Photonics). Fluorescence confocal images were acquired using a LEICA SP8 confocal microscope equipped with a 63 × oil immersion objective (NA = 1.40). Excitation light was provided with a 405 nm laser diode.

Transmission Electron Microscopy (TEM) (with the assistance of Dr. Vincent Dorcet, THEMIS platform). Transmission Electron Microscopy analysis were carried out with with JEOL 2100 transmission electron microscope operated at 200 KV supplied with UltraScan 1000XP CCD Camera. For the sample preparation, 300 mesh carbon coated nickel grids were placed for 1 min on top of a 40 µL sample droplet and dried up with paper. Particle sizes and interparticle distances were determined from TEM micrographs using Fiji Software.

Cryo-Transmission Electron Microscopy (Cryo-TEM) (in collaboration with Dr. Aurélien Dupont, CNRS Inserm). Vitrification of vesicles was performed using an automatic plunge freezer (EM GP, Leica) under controlled humidity and temperature (Dubochet and McDowall, 1981). The samples were deposited to glow-discharged electron microscope grids followed by blotting and vitrification by rapid freezing into liquid ethane. Grids were transferred to a single-axis cryo-holder (model 626, Gatan) and were observed using a 200 kV electron microscope (Tecnai G^2 T20 Sphera, FEI) equipped with a 4k × 4k CCD camera (XF416, TVIPS). Micrographs were acquired under low electron doses using the camera in binning mode 1 and at a nominal magnification of 25,000x.

3.3 Extracellular Vesicles from Follicular Fluids: Characterisation and Nanoclusters Interaction

Exosomes are Extracellular Vesicles (EVs) with a diameter between 30 and 200 nm, secreted by cells in biological fluids. They contain different molecules, and carry signals through the content of microRNA, DNA, proteins and lipids. They play an important role in cell cross-talk and are involved in numerous physiological and pathological processes, such as tumorigenesis, inflammation and mechanisms that regulate immunity. More and more interest is aimed at studying their potential use in diagnosis (as biomarkers of diseases) and in therapy[127,128].

In recent years, exosomes have been considered as an important marker for early cancer detection. Cancer cells have been found to have mutations that increase endocytosis and exocytosis of exosomes compared to healthy cells. Therefore, greater quantities of exosomes will be found in the body fluids in the presence of a tumor in the organism. Furthermore, tumor exosomes are also richer in miRNA content[129], have a more irregular shape and have an overexpression of the transmembrane protein CD63[130,131].

Exosomes are produced by different types of cells and can be found in various body fluids. By identifying the content of the cell, which depends on the type of cell that produced them, it is possible to identify the origin of the exosomes and consequently the location of the tumor. Exosomes can play a fundamental role in diagnostics but also in therapy: they can be used as vectors to transport chemotherapy drugs and kill cancer cells[128].

To create minimally invasive sensors, studies on salivary exosomes are taking place, in order to be able to quantify them and possibly understand their origin, in order to localize the tumor. To understand its origin the simplest way is the recognition of proteins on the outer membrane. An example concerns the exosomes secreted by a melanoma that have recognition proteins (antigens) associated with the same tumor on the membrane[127].

Cancer is not the only pathology for which there is an overproduction of exosomes. Also in the case of Parkinson's disease, a greater secretion of exosomes in the saliva originating from the neuronal endings was found. These exosomes had an overexpression of the L1CAM[i] and phosphorylated α-

---

[ii] The L1CAM protein encoded by this gene L1CAM (L1 Cell Adhesion Molecule) is an axonal glycoprotein belonging to the immunoglobulin supergene family. This cell adhesion transmembrane protein plays an important role in nervous system development, including neuronal migration and differentiation.

synuclein proteins[ii] on the membrane, two proteins that could act as biomarkers for the production of salivary devices for the diagnosis of Parkinson's disease[133].

The content of the exosomes plays a fundamental role in the development of the tumor mass, both for its growth and for its reduction. Because of the presence of miRNAs inside, that are involved in the function of suppressing or masking the tumor, the exosomes play an important role by making the tumor cells invisible to the immune system[134].

To study such exosomes, it is necessary to be able to quantify them and analyze their genetic content. Different techniques (DLS, TEM, SEM, NTA) allow to characterize and obtain an estimation of the exosomes size. But the distinction between exosomes and generic extracellular vesicles is made only by size. New techniques using luminescent nanostructures could allow the selective detection of exosomes: the recognition of membrane proteins of exosomes (e.g. CD81, CD63, CD9), would allow a more accurate distinction between exosomes and vesicles. Furthermore, thanks to their high surface / volume ratio, nanostructures are excellent candidates for creating more sensitive sensors.

For this reason, below we have analyzed in detail the different populations of EVs present within the human follicular fluid (FF), both healthy and with pathologies. As a preliminary study, we have also explored the possibility of making these vesicles interact with AuNCs grafted with antiCD81 to allow selective targeting and bioimaging of exosomes according to the proteins present on the surface.

The ovarian follicle represents a reproductive unit consisting of an oocyte surrounded by many somatic cells composed of granular cumulus, mural granulosa and theca cells and follicular fluid (FF). The formation of FF is due to the infiltration of various plasma components by transudation. It provides nourishment to the oocyte and allows it to mature within the follicle[135,136]. The growth of follicles and the maturation of oocytes are linked by a dynamical exchange of signals between somatic and germ cells. Granulosa cells such as ovarian somatic cells can interact with each other or with the oocyte via intercellular communications and homeostatic phagocytosis[137]. Cross-talk between oocyte and granulosa cells occurs via gap junctions, but recently EVs have been identified in follicular fluid as a new mode of communication in the ovarian follicle[109]. EVs is the generic term

---

[ii] α-Synuclein (α-syn), especially its abnormal oligomeric and phosphorylated form, plays a critical role in the pathogenesis of Parkinson's disease (PD)[132].

for naturally released particles from the cell that are bounded by a lipid bilayer with no functional nucleus[138]. EVs isolated from FF have been shown to influence the expression of selected genes in cultured granulosa cells by regulating genes involved in follicular development, meiotic recovery and ovulation[139].

Isolation of EVs from FF for research is challenging; several methods are used, the most commonly used being Ultracentrifugation (UC) in the field[140]. The UC uses centrifugal force to separate and purify the EVs using a high centrifugal speed for sufficient time for the individual EVs to travel the length of the tube in a pellet. For small volumes different commercial EVs isolation kits are used with size exclusion columns or ultracentrifugation for small volumes while density gradients are used for large volume EVs isolations. The sequential use of two or more isolation methods significantly reduced the presence of lipoproteins and protein contaminants in the sample; however, a significant decrease in the number of EVs is achieved[141]. Exosomes are defined by their protein content, including the CD9, CD63 and CD81 tetraspanins. Flow cytometric detection of CD63 is an alternative approach to confirm EVs[141]. The presence of EVs by CD63-positive staining in ovarian follicular fluid was first identified in horses[142].

Recent studies have analyzed the morphology and size of the Small EVs of the FF (**Figure 83**)[69]. These vesicles, despite having a similar size, cannot be defined as exosomes if the surface proteins and ideally the contents are not analyzed, and for this reason they will be called Small EVs. We will use a similar approach but we will analyze the complete population of vesicles present in the FF, without focusing only on the Small EVs.

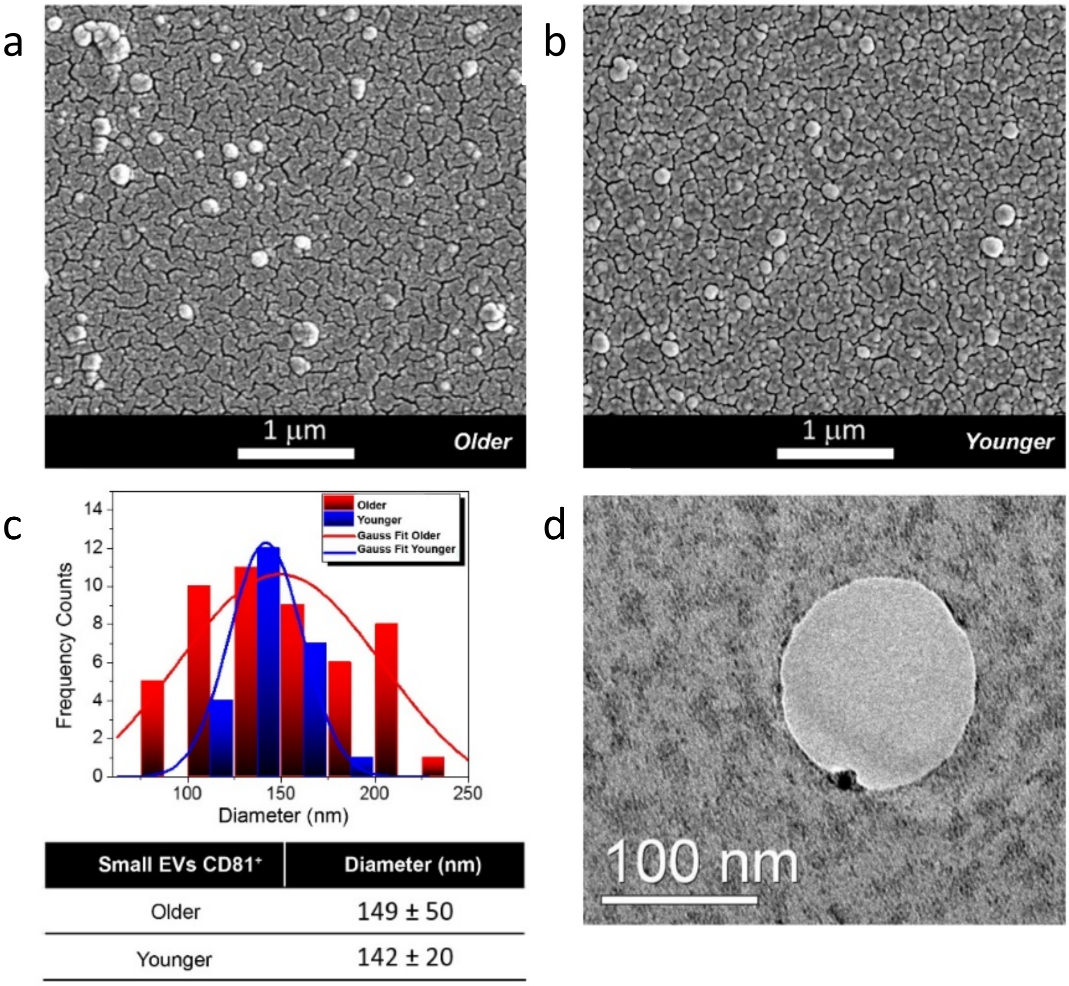

Small EVs CD81⁺	Diameter (nm)
Older	149 ± 50
Younger	142 ± 20

Figure 83. Morphological characterization of EVs from FF of older and younger women. (a,b) Scanning Electron Micrographs of EVs isolated from the FF of older (a) and younger women (b). (c) Diameter distribution of EVs from FFs of older and younger women. Gauss fit of the diameters measured on SEM microscopies for older women (red) and for younger women (blue). (d) TEM image of small Gold Nanoparticle (AuNP) functionalized with anti-CD81 antibody over a small FF-EV membrane.

3.3.1 SIZE SEPARATION

Since it was intended to label human fluid exosomes with fluorescent NCs for early diagnosis of various diseases, the idea was to focus on follicular fluid (FF) which has a large number of extracellular vesicles, as well as being of particular interest for in vitro fertilization (IVF) medical application.

FF constitutes the oocyte microenvironment which plays a key role in the optimal development of the female gamete. Its composition reflects the physiological state of the ovarian follicle. EVs isolated from FF are involved in various biological functions related to follicular growth, oocyte maturation and embryo development. However, knowledge on the morphology of FF-related EVs is limited, mainly due to their submicron size and inherent limitations in the methods applied for their characterization. For example, for the morphological characterization of EVs the NTA technique is often used which does not consider all vesicles below 50-100 nm (beyond the limit of detection of the technique) which for the most part are exosomes that are not quantified.

Different roles are assigned to FF-EVs as they are involved in intercellular communication within the ovarian follicle[143]. The FF provides a favorable environment for the normal development of an oocyte to be fertilized. FF-derived EVs are involved in the regulation of pathways that control follicular growth and hormonal response, as well as cytoplasmic maturation of oocytes and resumption of meiosis. Integration of culture media with EVs isolated from follicular fluid during oocyte maturation and early embryo development may partially modify developmental and metabolic genes[144]. These vesicles can mediate the transport of information from the follicular fluid to the oocyte showing a positive effect of CD63-EVs on the correct development of the bovine embryo[144]. FF-derived EVs can be absorbed by cultured granulosa cells and transfer bioactive material, highlighting cell-to-cell communication within the antral follicle[145,142].

There is a clinical interest to select the best oocytes for IVF through the quality of the follicular fluid evaluated by the extracellular vesicles (in collaboration with Prof. Célia Ravel in the Rennes University Hospital, Pontchaillou CHU Rennes, France).

In this view, we first explore the physico-chemical properties of the FF. Before working on the purified exosomes of this fluid, it was decided to analyze the morphology and the size of the entire population of extracellular vesicles starting from the FF. A purification and analysis methodology were therefore developed to separate the different families of vesicles present in the FF. In this work the different families of human FF EVs were then separated by the differential ultracentrifugation method[146]. Once the pellet was obtained and dispersed in PBS, it was analyzed the next day by DLS and NTA[147] to evaluate its size taking into account all the particles even those under 100 nm by means of DLS and to have an estimate of the number of EVs by means of NTA. Furthermore, the CryoTEM grids were frozen on the same day to be able to view them in the following days without changes. The CryoTEM technique allows a high resolution dimensional and morphological analysis, allowing the EVs to maintain the morphology as close as possible to the native one in biological liquids, minimizing artifacts. For the analysis, FFs from healthy subjects were used, but later the FFs from patients with pathologies will also be analyzed to compare them.

The aim of this study is to provide a complete description of FF EVs from healthy subjects. For this reason, due to the high polydispersity of EVs present in the FF, we did not focus on a single type of vesicles, which could be done using commercial isolation kits for EVs, but it was decided to analyze the sample in its integrality. In the work two ultracentrifugation techniques are compared, the direct one which would allow to have the entire population of EVs and the differential one which allows to separate the different families.

Vesicles are defined as round structures that have a lipid bilayer. The process of ultracentrifugation and freezing can induce physical forces that modify the structure of the EVs. However, the samples are frozen so quickly by CryoTEM that there is no osmotic stress. The oval or tubular shape found in the EVs of the analyzed samples reveals an excess of surface area of the lipid membrane or a loss of volume with an osmotic pressure higher outside than inside. It has been suggested that biological molecules, such as lipid rafts, cytoskeletal components, and/or membrane-shaping proteins, such as BAR domain proteins, could influence the shape of vesicles and oval tubules[148,149]. We choose the most common separation technique used, but ultracentrifugation can cause aggregation of EVs, which could lead to artifacts during analysis.

3.3.1.1 DIFFERENTIAL CENTRIFUGATION OF FOLLICULAR FLUIDS

Samples were taken from healthy subjects, subjected to a light centrifugation to remove cell debris, and frozen until use. Before being able to use them, therefore, the samples were thawed by placing them at room temperature and were ultracentrifuged according to the protocol in **Figure 84**.

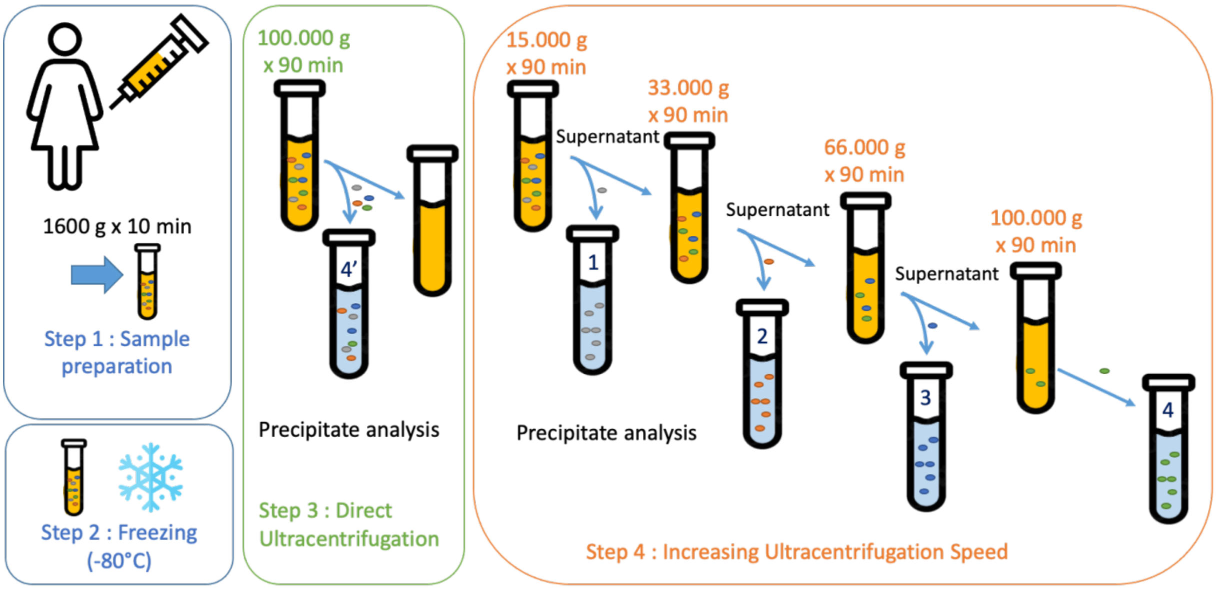

Figure 84: schematic view of the protocols to separate the different subclasses of EVs in FF.

For each condition (1-4 and 4'), the size distribution of the EVs was determined by various techniques characterization and compared considering the advantages and disadvantages of each technique to overcome the problem of high dimensional polydispersity and to have a complete description of the population of EVs. Since both NTA and DLS overestimate size by measuring the hydrodynamic radius of electric vehicles, the images were also analyzed using CryoTEM microscopy to achieve the most realistic size distribution possible, although the statistic is poorer than for DLS. To compare the number of EVs belonging to the different conditions via CryoTEM images, a similar number of photos were analyzed for each ultracentrifugation condition.

3.3.1.2 MORPHOLOGICAL CHARACTERIZATION OF EXTRACELLULAR VESICLES FAMILIES

All particles in the CryoTEM images were classified based on their morphology. The size of these particles varies from 5 to 700 nm. Each condition analyzed showed a population of small (30-100 nm) extracellular vesicles similar to exosomes and a population of large extracellular vesicles (> 100 nm) similar to microvesicles. Contrary to seminal plasma[150] myelinosoma (200-700 nm) were found in this experiment .

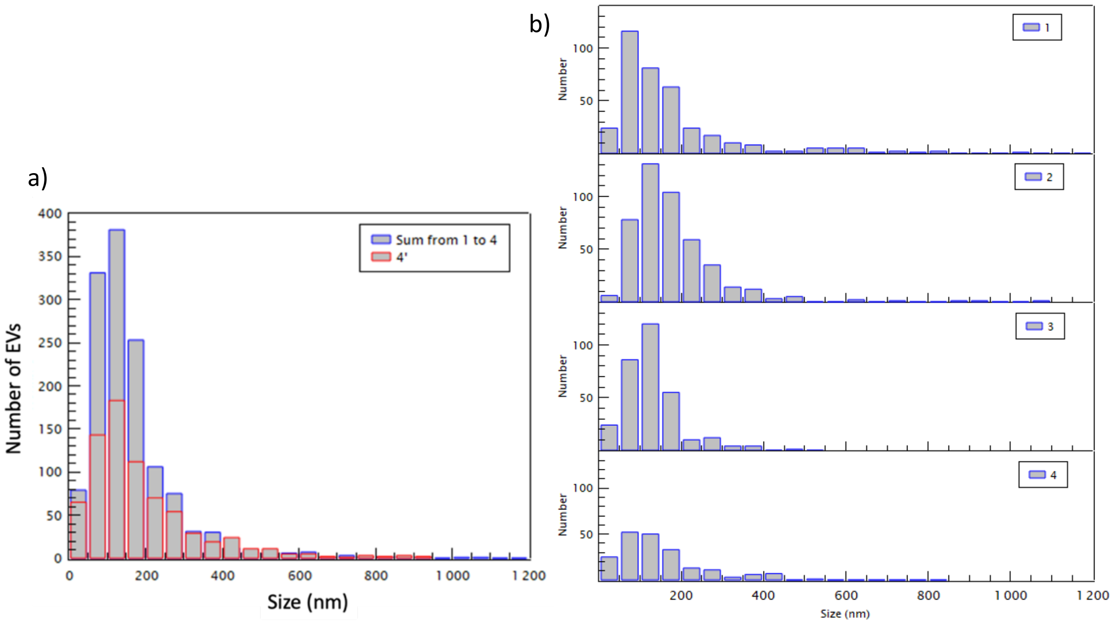

Figure 85 a) Size histograms of the EVs populations obtained from DLS by sequential centrifugation (sum of conditions 1 to 4, in blue) and by one-step ultracentrifugation (condition 4', in red). b) Size histograms of the EVs populations obtained from DLS by sequential centrifugation 1, 2, 3 and 4.

The size histograms, relating to the different conditions, obtained by measuring the vesicles from the CryoTEM images are shown in **Figure 85**. The distribution obtained from the sum of conditions 1 to 4 resulting from the differential ultracentrifugation was compared to the distribution obtained following the direct ultracentrifugation (**Figure 85a**).

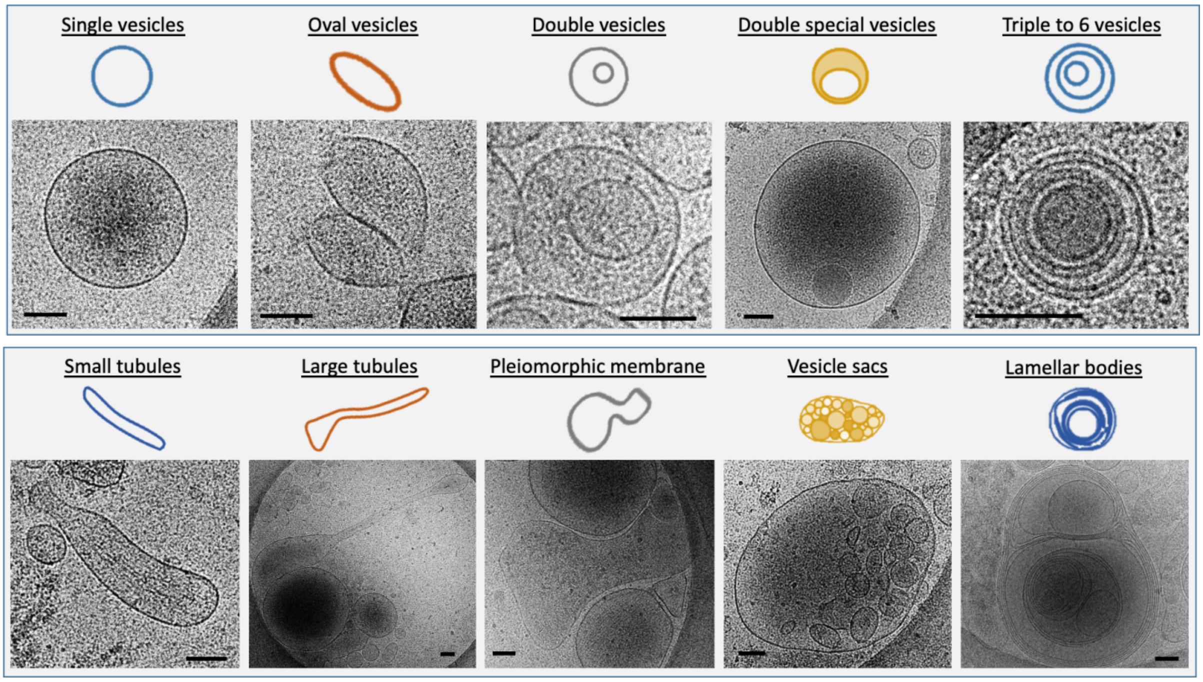

Figure 86. CryoTEM images of the 10 subcategories (according to Höög et Lötvall 2015) classification depending on their size and their morphology.

All structures of EVs found in the images were measured and divided into 10 subcategories according to the Höög et Lötvall classification[149] according to their size and morphology (**Figure 86**): the "single vesicles" have a double layer 5 nm thick and are the most common EVs ; the "oval vesicles" have a shape that resembles single vesicles but deformed; "Double vesicles" contain a smaller vesicle within a larger vesicle; "special double vesicles" have a larger diameter than double vesicles; "3 to 6 vesicles" consist of one large vesicle containing smaller vesicles; the "small and large tubules" have an aspect ratio greater than 5 and some of them contain filaments or appear to be folded; "pleomorphic membrane" structures include pear-shaped membrane compartments; "vesicular sacs" are several vesicles arranged within a larger membrane in which vesicles with double membrane layers have also been observed; "lamellar bodies" are large, complex, multi-layered membrane structures that have also been visualized in FF samples.

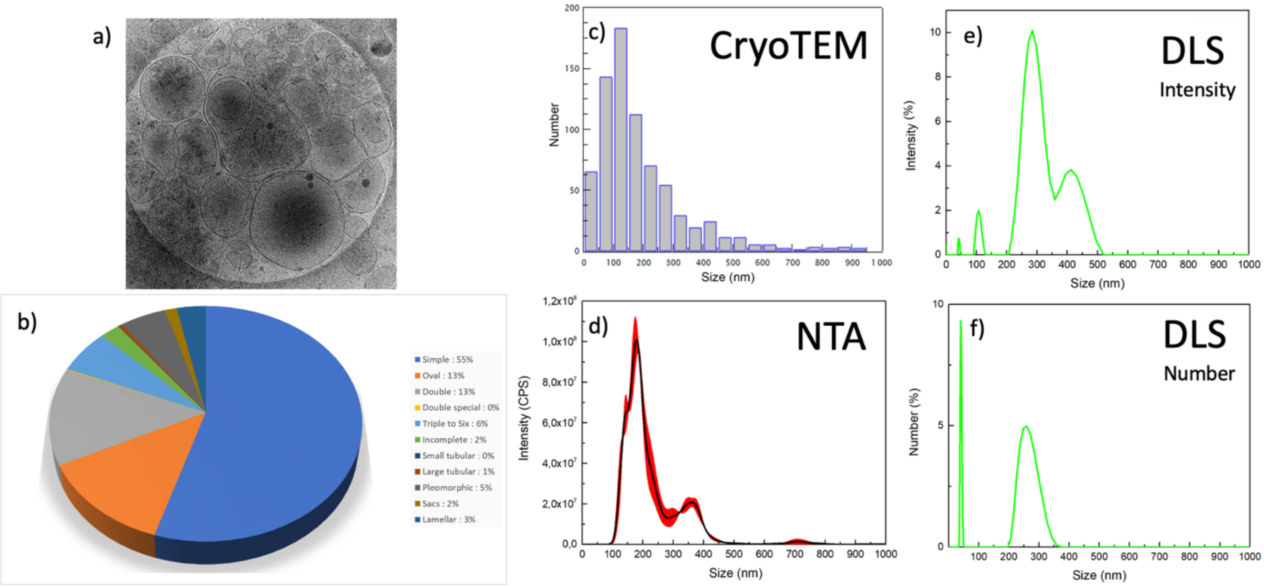

Figure 87. a) Example of Cryo TEM images used for b) morphological quantification pie chart and c) size distribution analysis of FF- EVs after high speed (100 000g) centrifugation without differential steps (condition 4'). d) NTA and DLS c) intensity and f) number of the same FF- EVs sample.

The EVs content of FF resembles that previously described for seminal plasma in men[149]. However, if three subtypes of EVs have been described in the male genital tract : microvesicles, myelinosomes and exosomes[151], we did not find any myelinosomes in our samples, but only microvesicles and exosomes. Obviously, this does not mean that there are none and further analyzes will be necessary before confirming the absence of these very particular structures in human FF. Our data show that, like other human fluids, follicular fluid contains spherical EVs approximately 200 nm in diameter, tubular EVs , with an average length close to 2 µm and large fragments, 1–8 µm in size as described[152]. FF also contained microvesicles ranging from 100 to 1000 nm, which are formed by budding from the plasma membrane and the exosomes having a diameter of 30-150 nm formed by the inward budding of the lumen (internal cavity) of the late endosome forming a multi- vesicular body (MVB), secreted by the fusion of MVB with the plasma membrane. A structure of particular interest is the vesicular sac as it hosts EVs of different morphologies within the same membrane. In addition, small particles 10-50 nm in size were also observed in the FF samples that were not surrounded by a lipid bilayer; they probably consisted of protein or lipoprotein complexes. Similar to a blood plasma, FF contained the compartments of the pleomorphic membrane and tubular structures[153].

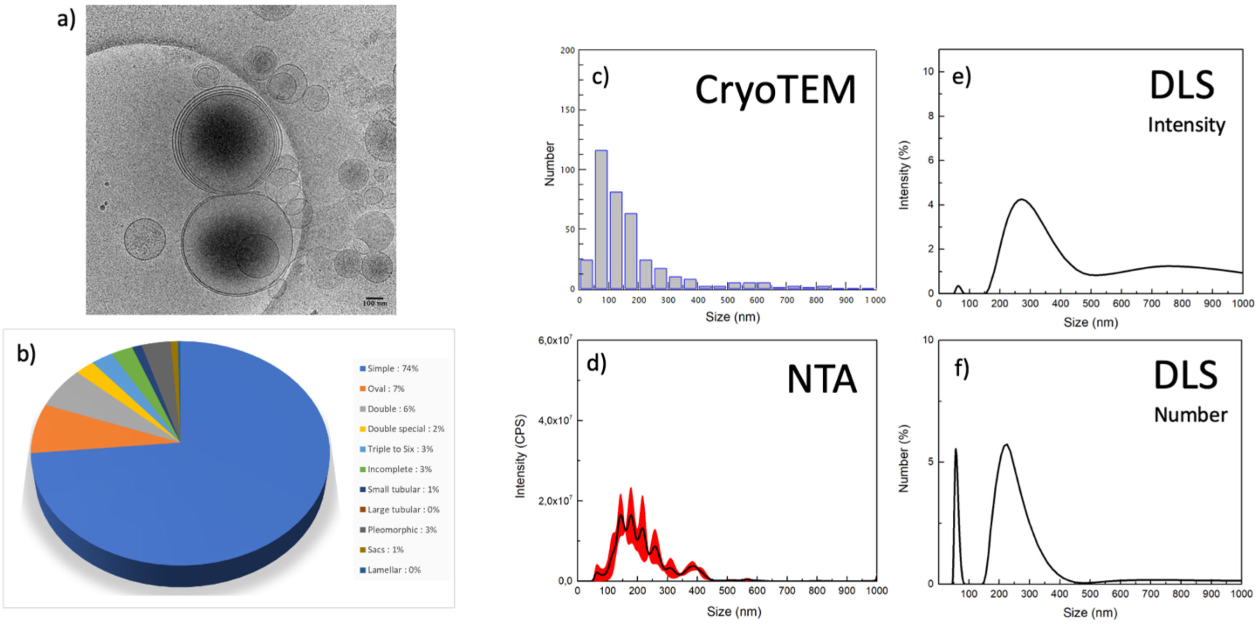

Figure 88. a) Example of Cryo TEM images used for b) morphological quantification pie chart and c) size distribution analysis of FF- EVs after low speed (15 000g) centrifugation (condition 1). d) NTA and DLS e) intensity and f) number of the same FF- EVs sample.

As shown in **Figure 87**, *condition 4'* gives a general idea of the size diversity of the complete population. The CryoTEM technique allows to specify the morphology of the IV subpopulations of different sizes. Samples were analyzed by NTA to evaluate EVs concentration and size distribution. Since the sample has a high polydispersity, it is difficult to detect EVs from NTA in the case of a hydrodynamic radius of less than 100 nm. Therefore, not all EVs with smaller radius were considered, underestimating the concentration of EVs. Consequently, the same sample was analyzed with DLS to also measure EVs with a diameter less than 100 nm and to improve statistics. This technique does not allow to quantify the number of particles per mL unlike the NTA, but it is able to estimate the ratio in number between the different families of EVs. Through the DLS intensity measurements, there is an overestimation of large EVs compared to small ones (the scattered intensity follows a law in D^6 where D is the diameter of the vesicle); for this reason, the size graph linked to the frequency in number of vesicles was also presented. This graph, generated by the machine through a mathematical calculation, enhances the contribution coming from small EVs that have a lower scattering signal.

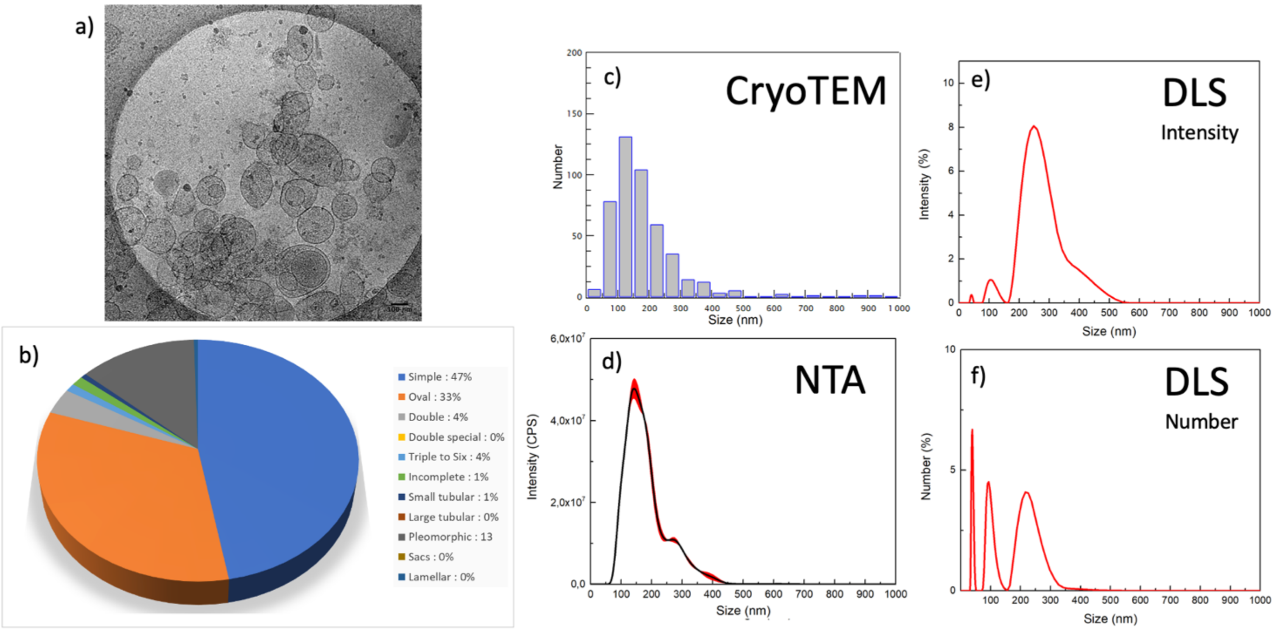

Figure 89. a) Example of Cryo TEM images used for b) morphological quantification pie chart and c) size distribution analysis of FF- EVs after mild speed (33 000g) centrifugation (condition 2). d) NTA and DLS e) intensity and f) number of the same FF- EVs sample.

In the case of *the 4 'condition* (1.11 x 10^{11} particles/mL), two major subpopulations of EVs are visible from NTA and DLS around 100-200 nm and around 300-400 nm. The appearance of larger EVs around 500-700 nm visible via NTA may also be noted. Finally, an abundant population of very small particles around 10-30 nm is systematically detected by DLS through the ratio (%) in number analysis (**Figure 87**); however, these particles were found not to be surrounded by a lipid bilayer, as observed in CryoTEM images; therefore, they are probably protein or lipoprotein complexes.

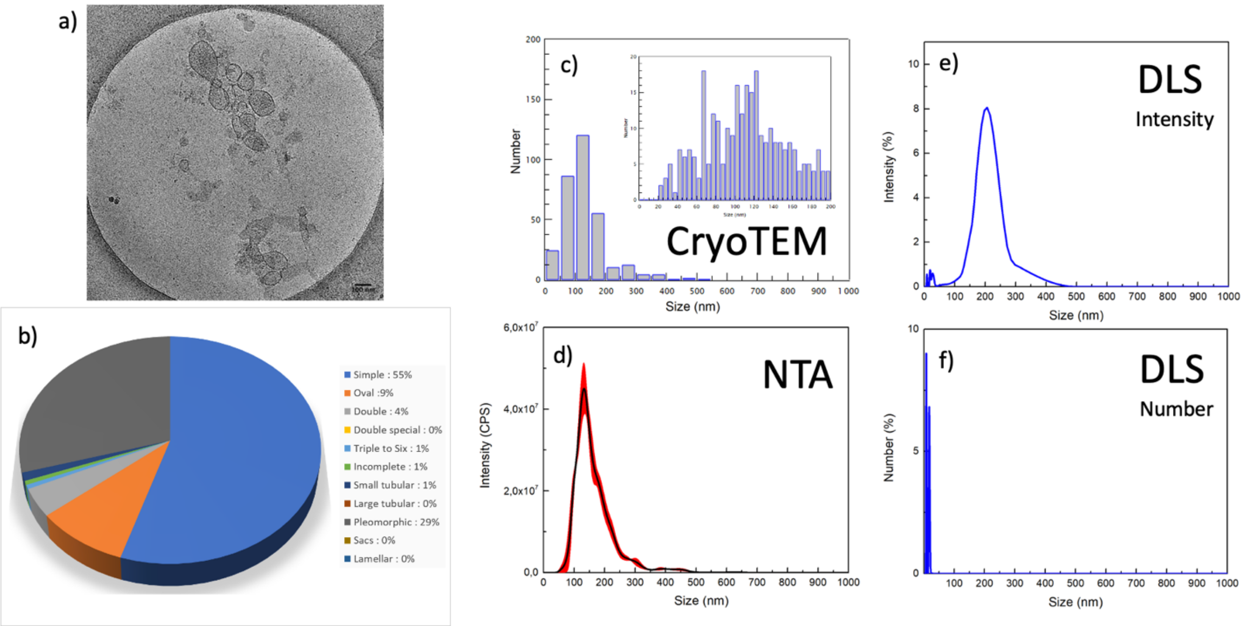

Figure 90. a) Example of Cryo TEM images used for b) morphological quantification pie chart and c) size distribution analysis of FF- EVs after mild speed (66 000g) centrifugation (condition 3). d) NTA and DLS e) intensity and f) number of the same FF- EVs sample.

Samples resulting from sequential centrifugation were analyzed using the same complementary techniques. As shown in **Figure 88**, the sample “*Condition 1”* (2.5 x 10^{10} particles/ml) is enriched with large EVs and large apoptotic bodies with dimensions greater than 200 nm, between 200 and 300 nm with some large aggregates of 500-700 nm and some small EVs of 50 nm. The sample “*Condition 2”* (6, 1 x 10^{10} particles/ml) has the highest concentration of EVs measured by NTA compared to the other conditions and the size distribution is between 50 and 300 nm, with no larger EVs (**Figure 89**). “*Conditions 3* and *4”* (respectively 4.2 x 10^{10} particles/mL and 3.1 x 10^{10} particles/mL) can be combined since they have a very similar population enriched in small EVs of similar size (less than 200 nm) (**Figure 90** and **Figure 91**). Through DLS, especially in conditions 3 and 4, the particles of about 10 nm without lipidic bilayer were found already in “condition 4'”, but here they represent most of the sample.

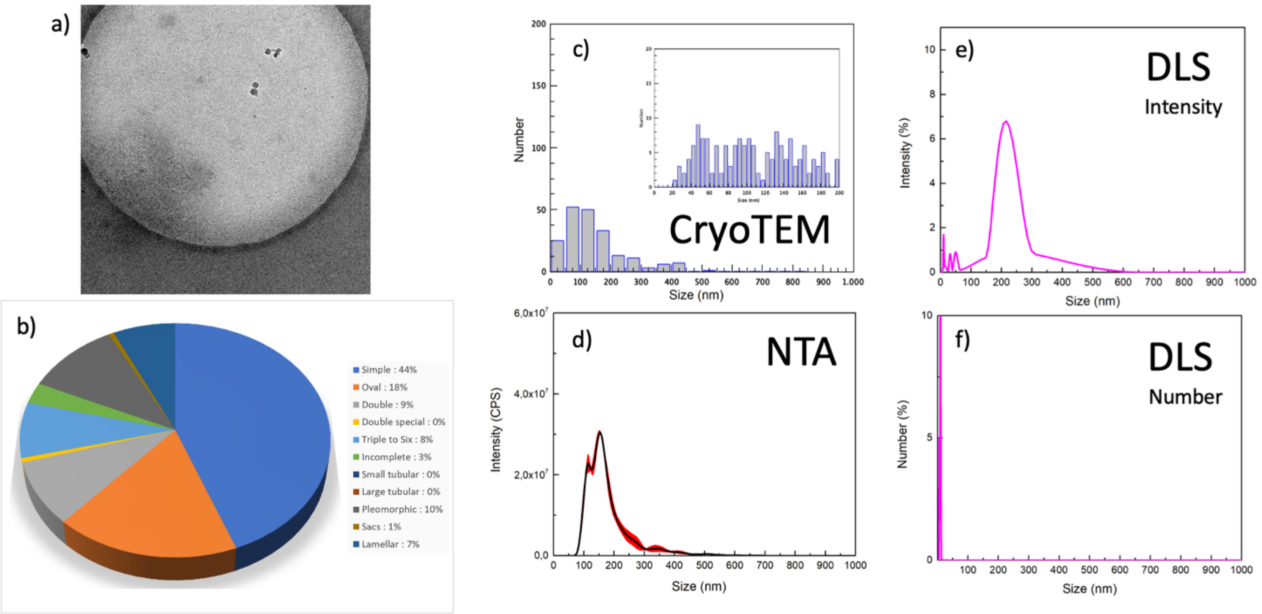

Figure 91. a) Example of Cryo TEM images used for b) morphological quantification pie chart m and c) size distribution analysis of FF- EVs after high speed (100 000g) centrifugation (condition 4). d) NTA and DLS e) intensity and f) number of the same FF- EVs sample.

Regarding the concentrations of EVs obtained by NTA, we observe that the sum of the concentrations of the four conditions from 1 to 4 i.e. (1.6 x 10^{11} particles/mL) is higher than that obtained by ultracentrifugation one-step *Condition 4'* (1,1 x 10^{11} particles/ml). This can be explained because the EVs population of the one-step ultracentrifugation, *condition 4 '*, does not correspond to the sum of the 4 conditions since the total time taken to perform the 4 centrifugations (300 min) is much greater than that used to do the *condition 4 '* (90 min); consequently, a part of the EVs in the case of direct ultracentrifugation remained in the supernatant. In addition, there was a significant decrease in particle sizes ranging from 50 nm to 400 nm after ultracentrifugation in one step (**Figure 85**). It is worth noting that large EVs (> 400 nm) and very small EVs (<100 nm) are not well quantified by NTA[146].

3.3.1.3 CONCLUSIONS AND PERSPECTIVES

Interestingly, the analysis of the CryoTEM images reveals that the EVs appear darker in the central part indicating the presence of an important load inside that could be attributed to various biological material including miRNAs or protein aggregates. From the literature, about 32 miRNAs found in FF-EVs have been described and are capable of regulating follicular development, meiotic resumption and ovulation[154]. Specific FF miRNA profiles have been associated with oocyte quality and embryo outcome[155]. The methods by which exosomes are purified can have a different functional impact on oocyte maturation and subsequent embryo development, showing EVs resulting from FF in vivo exert a positive impact on embryo development[156].

The inventory of FF-EVs is therefore important for the development of future experimental approaches and for interpreting previously published data on the role of EVs for human fertility. Further studies on the content of EVs -FF will open promising new applications in diagnosis and therapy. These include the discovery of non-invasive markers of various diseases such as specific miRNA contained in the EVs, the identification of new therapeutic targets and the development of innovative drug delivery systems[157]. This can open new perspectives for the optimization of assisted reproductive technologies by improving the maturation of oocytes in vitro in humans.

3.3.1.4 EXPERIMENTAL SECTION

Patients (in collaboration with Dr. Anne-Sophie Neyroud, CHU Rennes 1 hospital). FF samples were collected from 20 healthy normal-ovulating patients who had undergone intracytoplasmic sperm injection due to a male factor. Samples were provided by the GERMETHEQUE Biobank, dedicated to human fertility. Informed consent was obtained from each couple for the use of the follicular fluid sample that was obtained during oocyte retrieval for the ICSI treatment. Ethical approval (CP-GM n° 20210808) was also obtained for this study. Patients were stimulated with recombinant FSH. Ultrasound monitoring of the follicular development occurred from day 6 of ovarian stimulation until the day of oocyte retrieval. When at least 3 ovarian follicles had grown up to 18 mm in diameter, 10 000 IU human chorionic gonadotropin was administered and the follicles were aspirated 36 hours later. The patients' average age is 31.5 years, the average Antral Follicle Count is 21, and the average AMH (anti-Müllerian hormone) level is 3.4 ng / mL

Sample preparation (in collaboration with Dr. Grégory Moulin, CHU Rennes 1 hospital). FF was collected by transvaginal ultrasound-guided aspiration of follicles up to 18 mm in diameter. Fluid samples were centrifuged at 1300g for 10 minutes at 4°C to remove cells and the supernatant was stored at -196°C degrees. Samples were warmed to room temperature for 30 minutes before ultracentrifugation and analysis.

Ultracentrifugation (in collaboration with Dr. Grégory Moulin, CHU Rennes 1 hospital). FF sample went through multi-step differential ultra-centrifugations, using the supernatant from the previous condition. Condition 1: 15 000g for 90 min, condition 2 :33 000g for 90 min, condition 3: 67 000g for 90 min and condition 4:100 000g for 90 min. Each pellet was resuspended in 250 µL of PBS (Sodium chloride, 150 mM, and sodium phosphate, 150 mM, pH = 7,2). One direct ultracentrifugation at 100 000g for 90 min was performed (condition 4’). All steps were performed at 4°C.

Cryo-Transmission Electron Microscopy (Cryo-TEM) (in collaboration with Dr. Aurélien Dupont, CNRS Inserm). Vitrification of the samples was performed using an automatic plunge freezer (EM GP, Leica) under controlled humidity and temperature [158]. The samples were deposited to glow-discharged electron microscope grids followed by blotting and vitrification by rapid freezing into liquid ethane. Grids were transferred to a single-axis cryo-holder (model 626, Gatan) and were observed using a 200 kV electron microscope (Tecnai G2 T20 Sphera, FEI) equipped with a 4k × 4k CCD camera (TemCam-XF-416, TVIPS). Micrographs were acquired under low electron doses using the camera in binning mode 1 and at a nominal magnification of 25,000x.

Dynamic Light Scattering (DLS). Each sample (pellets re-suspended in 250 µL PBS buffer) was diluted 100 times with PBS just before measurement, to avoid structural modification linked to the dilution process. The measurements of the mean hydrodynamic diameters were performed at an angle of 173° using a Nanosizer ZEN3600 (Malvern Instruments, England) and collected at 25 °C.

Nanoparticle Tracking Analysis (NTA). Each pellet was resuspended in 250 µL of phosphate-buffered saline (PBS). For NTA, each sample was diluted just before measurement with PBS following the manufacturer's instructions. The initial dilution factor used was 10 in PBS for samples 1,2,3,4 and 100 for sample 4'. Samples (700 µL) were injected into the NanoSightLM10 unit (Malvern Instruments, Malvern, UK) with a 1 mL sterile syringe. Capturing and analyzing settings were manually set according to the protocol. Using the NanoSight LM10 instrument, vesicles were visualized by laser light scattering, and Brownian motion of these vesicles was captured on video. The number of tracks always exceeded 200, and three size distribution measurements were taken for each sample. Recorded videos were then analyzed with the software NanoSight NTA 3.1 software (Malvern, UK) which provided high-resolution particle size distribution profiles and concentration measurements of the vesicles in solution. EVs analysis was performed in 3 videos of 30 s each and temperature controlled of 25 °C.

3.3.2 PATHOLOGIES

The EVs can be important biomarkers for the diagnosis of these pathologies since the content of the EVs coming from the follicular fluid can influence the competence of the oocytes and therefore the reproductive capacity of women. Indeed, EVs can mediate the transport of information from the follicular fluid to the oocyte[159,160].The EVs can reveal the evidence of disease by their content and their physico-chemical properties (concentration, morphology, size…).

In the present work in collaboration with Prof Célia Ravel (CECOS, CHU Rennes France), it was decided to analyze the EVs contained within the follicular fluid belonging to sterile patients with pathologies called "PolyCystic Ovary Syndrome" (PCOS) and "Ovarian Failure" (OF) and to compare them to those contained in the healthy follicular fluid.

The ovarian reserve ensures the woman's fertility by releasing mature oocytes that can be fertilized. Anti-Müllerian hormone (AMH) expression is detected in granulosa cells of activated primordial follicles, but is absent in follicular stages following follicle-stimulating hormone (FSH) dependent selection. Therefore, AMH acts as a follicular gatekeeper ensuring that each small antral follicle (up to 8mm) produces little E2 before selecting the follicle that will undergo ovulation[161]. The level of this hormone is very useful for doctors to evaluate infertile patients, since a high level as well as a low level of this hormone leads to infertility. If infertile patients have greater follicular activity, and consequently a high AMH value, it is in the presence of "polycystic ovary syndrome" (PCOS). PCOS affects 5-20% of women of reproductive age worldwide[162]The clinical presentation of this syndrome is related to an excess of androgens and insulin resistance associated with the reproductive, metabolic and cardiovascular components[163]. Although PCOS amplifies the ovarian response to ovarian stimulation, it does not have a negative impact on the quality or competence of oocytes [164]. Elevated AMH values are the only truly universal finding in all PCOS patients; yet to date, paradoxically, they are not recognized as a diagnostic parameter for a diagnosis of PCOS[165]. On the contrary, if infertile patients have a lower follicular activity, and consequently a low AMH value, it is in the presence of the pathology called "ovarian insufficiency" (OF).The causes of the disease involve certain genetic diseases, autoimmune diseases, chemotherapy or environmental factors. Diagnosis is easy based on low AMH values in women under 40[166].

In this work the aim is to morphologically compare the EVs of the different pathologies with respect to the EVs of healthy patients, also measuring the number and size, as well as the amount of protein present in the FF of the different patients.

3.3.2.1 STORAGE TEMPERATURE EFFECTS ON EVS DIMENSIONS

For these analyzes, the samples were not ultracentrifuged, thus analyzing the entire vesicle population and decreasing artifacts due to excessive sample handling.

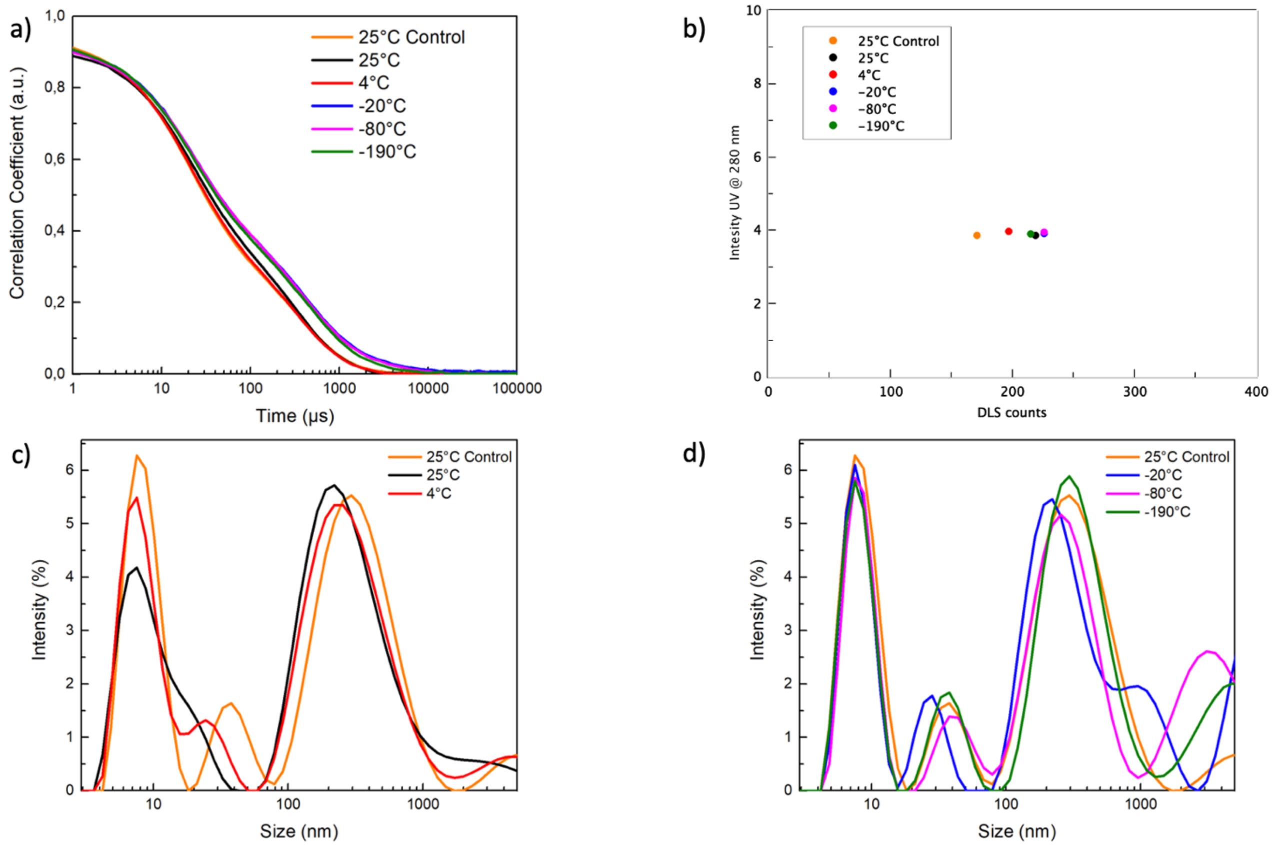

Figure 92. Dynamic Light Scattering (DLS) a) correlogram and c,d) Intensity of Extracellular Vesicles (EVs) stocked at different temperatures. b) Two-dimensional graph representing DLS counts in function of Absorbance at 280 nm of EVs stocked at different temperatures.

The influence of the storage temperature on the shape of the vesicles was studied to understand if it could vary the morphology of the EVs in their natural state. Through DLS, large aggregates (> 1 µm) appear, after thawing, in samples stored at -20 ° C, -80 ° C and -190 ° C; such aggregates are not present with storage temperatures of 25 ° C and 4°C (**Figure 92**).

Consequently, for all the samples analyzed in this study, it was decided to perform a low-speed centrifugation after thawing, in order to eliminate any aggregates formed as a result of the freezing process, which could distort the results obtained.

3.3.2.2 MORPHOLOGICAL COMPARISON BETWEEN HEALTHY AND PATHOLOGICAL EVS

In **Figure 93**, the DLS correlogram and intensity spectra analysis reveal the presence of families with different sizes in all samples analyzed. In particular, a greater polydispersity of size is revealed in FF-EVs of older patients compared to young patients in the case of control[167]and PCOS patients; however, this result is less evident for OF-FF as the difference between older and younger patients becomes less pronounced (**Figure 94**).

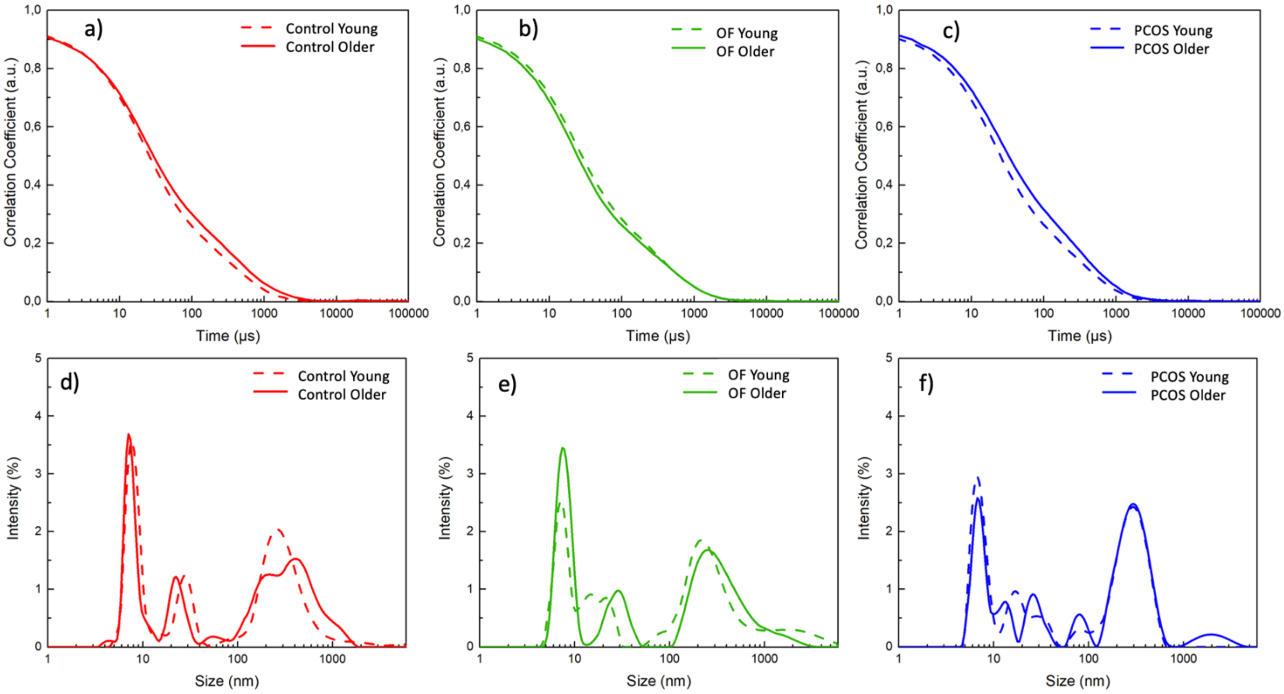

Figure 93. DLS a,b,c) correlogram and d,e,f) intensity spectra of a,d) Control, b,e) OF and c,f) PCOS (respectively red, green and blue line) young and older patients (respectively dash and solid line).

There are more peaks in the DLS intensity plot for the PCOS-FF group than for the control and OF-FF, therefore, there is greater polydispersity linked to different types of EVs within the sample, as well as larger EVs being present; this result is also confirmed in the CryoTEM images in which microtubules are predominant for the PCOS-FF samples (**Figure 97**, **Figure 100**).

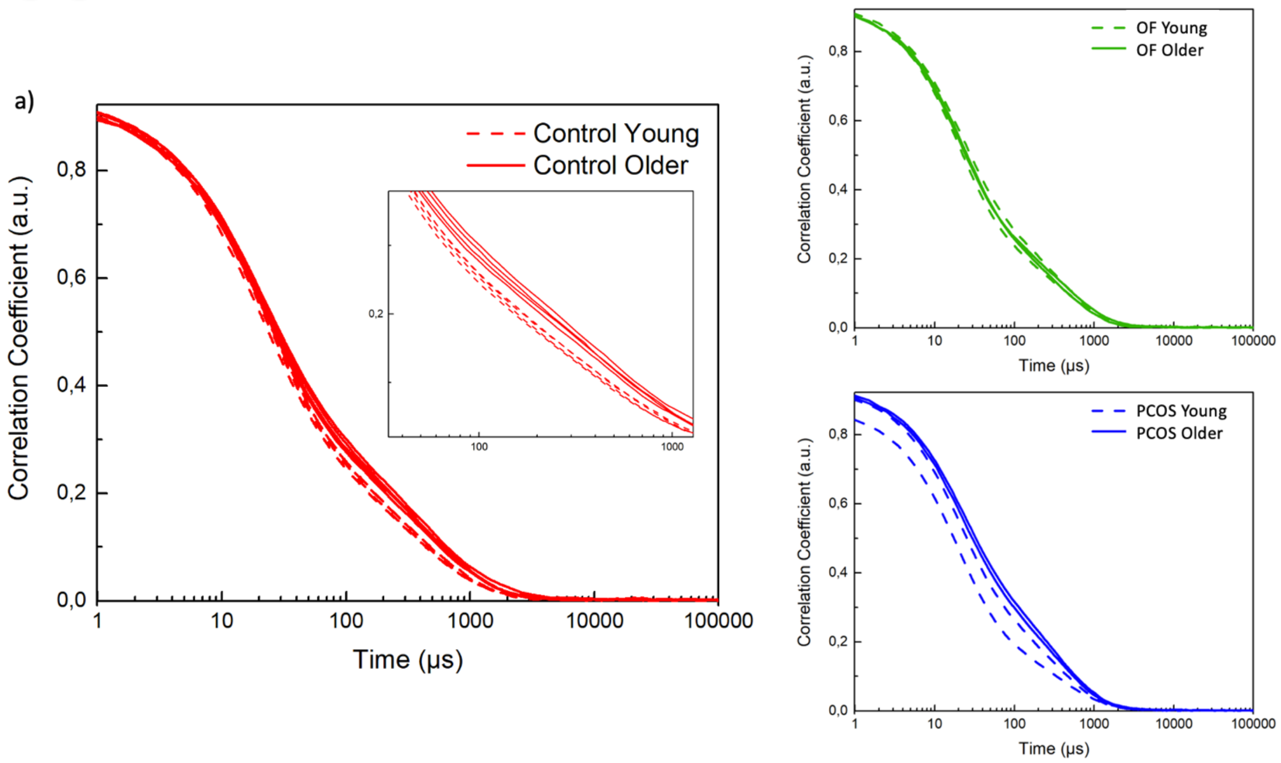

Figure 94. DLS correlogram of a) Control, (b) OF and c) PCOS (respectively red, green and blue line) of young and older patients (respectively dash and solid line).

To compare the pathologies, all the DLS intensity curves were reported together in **Figure 95**a. For the OF and PCOS groups, larger EVs are present, between 1000 and 4000 nm, almost not present in the control at all; such EVs, as we will show later, could be microtubules or deformed EVs with a greater aspect ratio, more present in pathological EVs. In the insert we wanted to focus on vesicles of about 100-700 nm which will represent all the rest of the morphologies. In the case of the OF group the average of the peaks is at 230 nm, for the SOPK group it is at 300 nm, while there are EVs with intermediate size for the control with average at 260 nm.

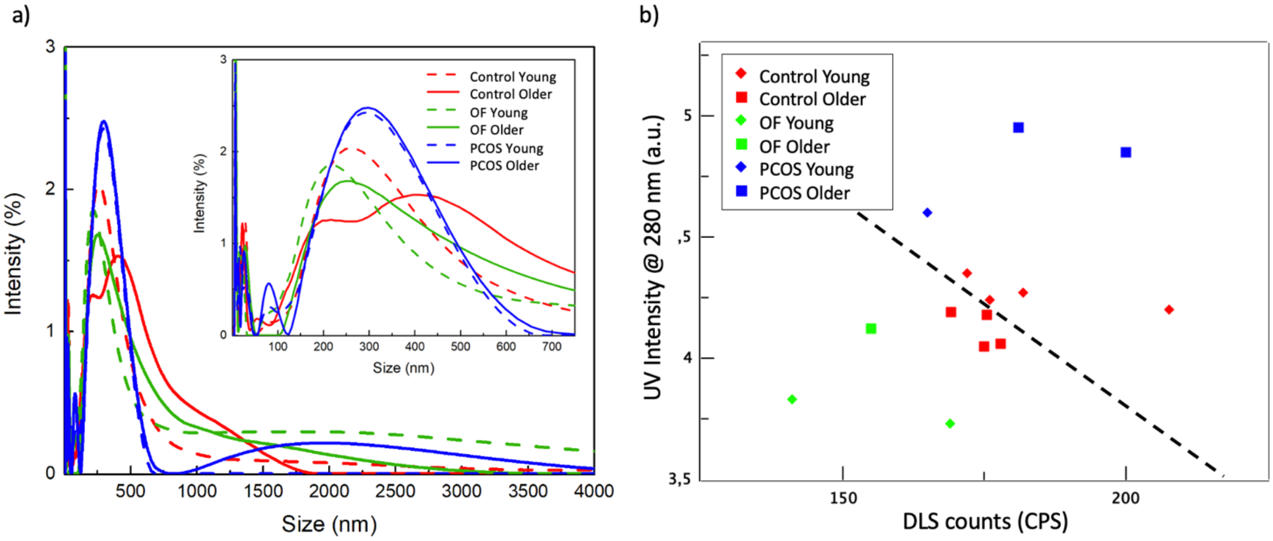

Figure 95. a) DLS Intensity of Control, OF and PCOS (respectively red, green and blue line) of young and older patients (respectively dash and solid line). b) Two-dimensional graph representing DLS counts in function of Absorbance at 280 nm of Control, OF and PCOS (respectively red, green and blue) of young and older patients (respectively rhombus and square).

Through the analysis presented in **Figure 95**b and **Figure 96**c, it is possible to note that the points relating to the different groups of patients are positioned in different areas of the two-dimensional graph (UV intensity at 280 nm versus DLS intensity). The absorption intensity at 280 nm reflects the light absorbed by the proteins and is related to the amount of protein, while the DLS count is related to the number of photons scattered by the vesicles, indirectly reflecting the concentration. However, a higher DLS count could also be affected by the presence of larger vesicles generating more scattered photons. Consequently, it is difficult to decorrelate the concentration from the size of the EVs. It should also be emphasized that the quantity of proteins, since the sample has not undergone ultracentrifugation, does not refer only to the proteins present inside the vesicles but also to those present outside, therefore to the entire content of proteins present in the FF.

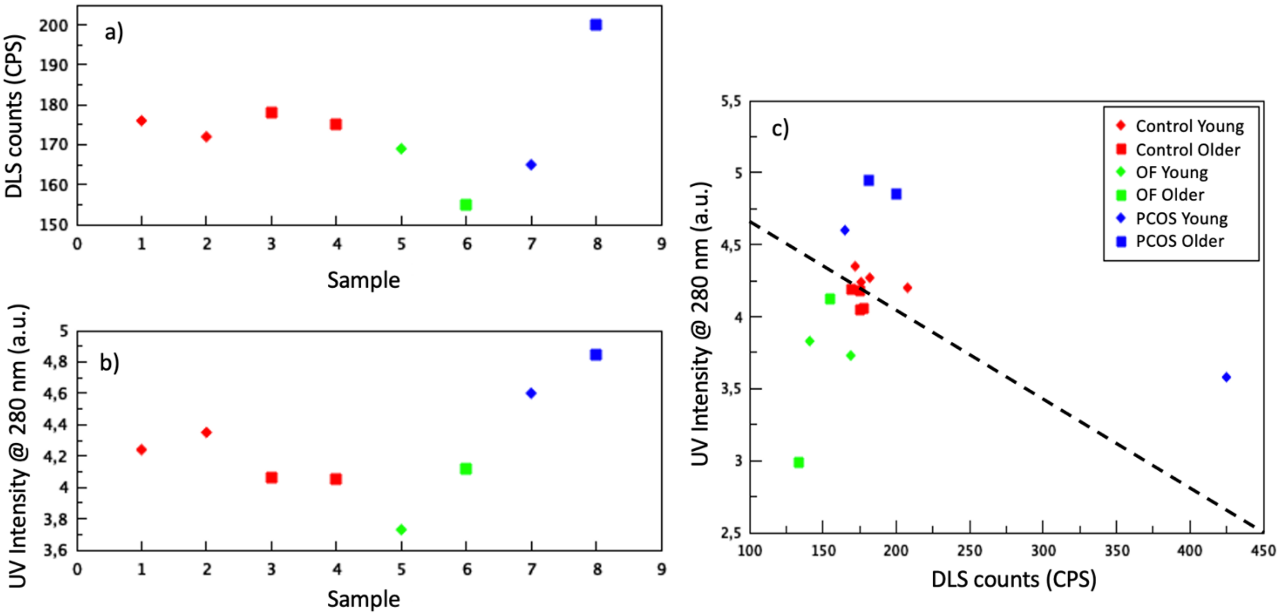

Figure 96. (a) DLS counts and (b) Absorbance at 280 nm of Control, OF and PCOS (respectively red, green and blue) young and older patients (respectively rhombus and square). (c) Two-dimensional graph representing DLS counts in function of Absorbance at 280 nm.

The EVs of the PCOS group are positioned in the upper right region of the graph, which means that there are more proteins and more or larger EVs than the control. This result agrees with the presence of larger particles present in the DLS Intensity graph (**Figure 95**a) and from the CryoTEM images (**Fig. 6** and **9**). Conversely, the points relating to the EVs belonging to the OF group are located in the lower left corner of the 2D graph, so the sample has fewer proteins and fewer or smaller EVs. Healthy juveniles appear to have more protein than older controls, but this is not the case with pathological samples; this causes the younger controls to be closer to the PCOS region while the older controls appear to be closer to the OF samples. The percentage reduction of simple vesicles in pathologies results in a greater polydispersion of pathological samples.

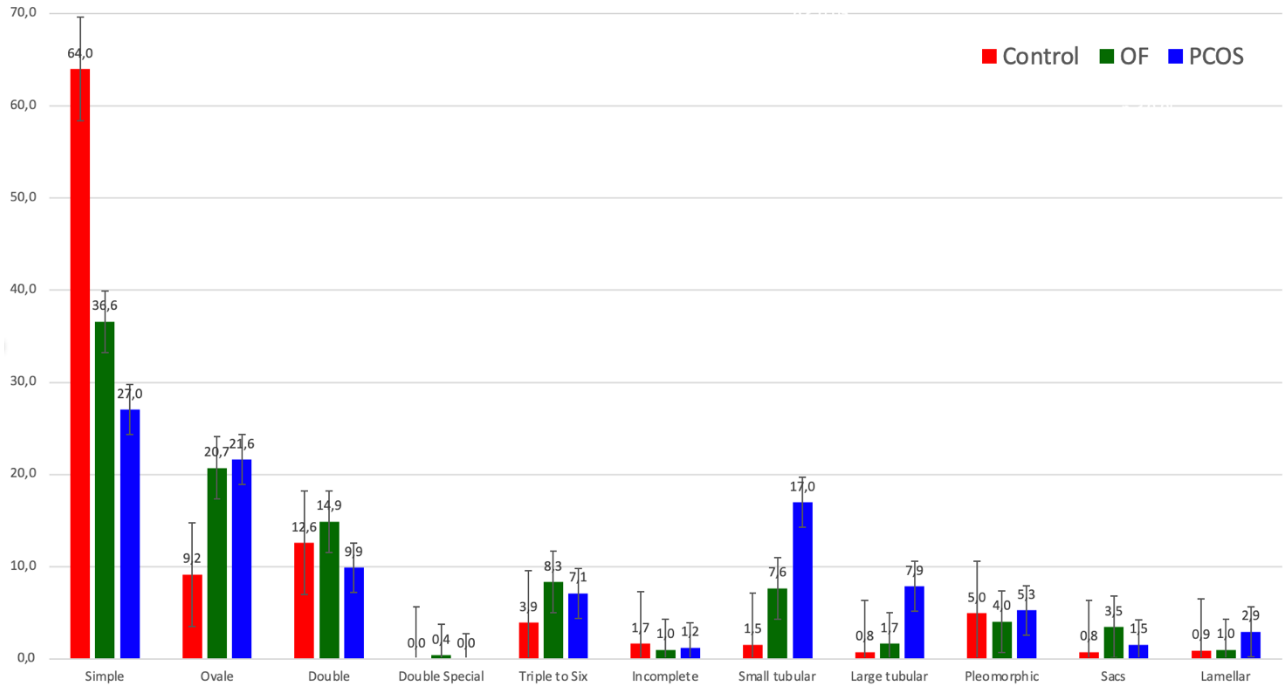

Figure 97. Histogram indicating the number of vesicles of different morphologies present in Control (blue), OF (orange) and PCOS (gray).

Figure 96 shows the entire group of analyzed samples, also including diverging points which however fall well within the zones defined for each pathology. The trend on the dimensions found in the DLS analyzes in **Figure 95**a seems to be confirmed also in the DLS counts of the graph in **Figure 95**b.

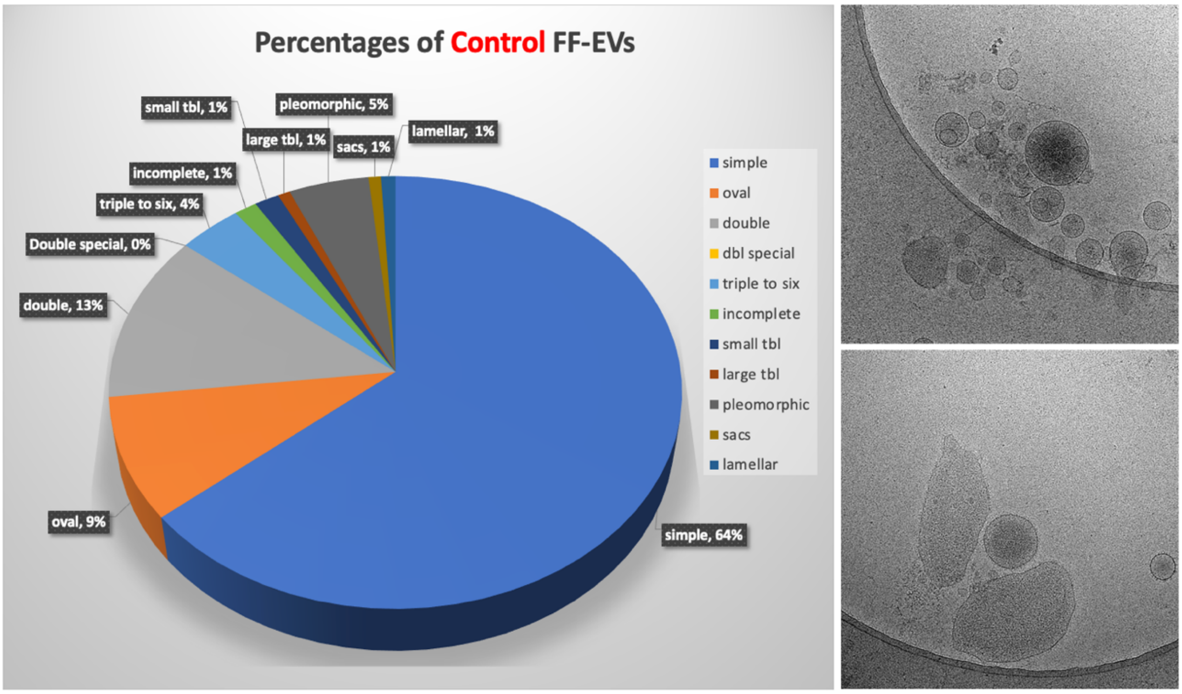

Figure 98. a) Morphological quantification pie histogram and b,c) CryoTEM micrograph of Control FF-EVs.

To visualize the FF-EVs morphologies belonging to each group, it was necessary to ultracentrifuge at 100 000g, in order to eliminate all the biological material external to the vesicles, having clearer Cryo TEM images, but above all to increase the concentration to allow bioimaging and counting. So, through the CryoTEM analyzes the EVs of the different FF groups were counted; they appear limited by a lipid membrane, as evidenced by the presence at their periphery of two dark lines about 4 nm apart, characteristic of the lipid bilayers[152]. Analyzing about 70 images per group, for the control there were 788 vesicles, less for the OF one (717) and even less for the PCOS one (657). This means that a higher DLS count for PCOS is not related to a higher concentration of EVs (being fewer EVs in the CryoTEM images) but to the presence of larger EVs (e.g. more tubular EVs and fewer simple EVs) (**Figure 97**).

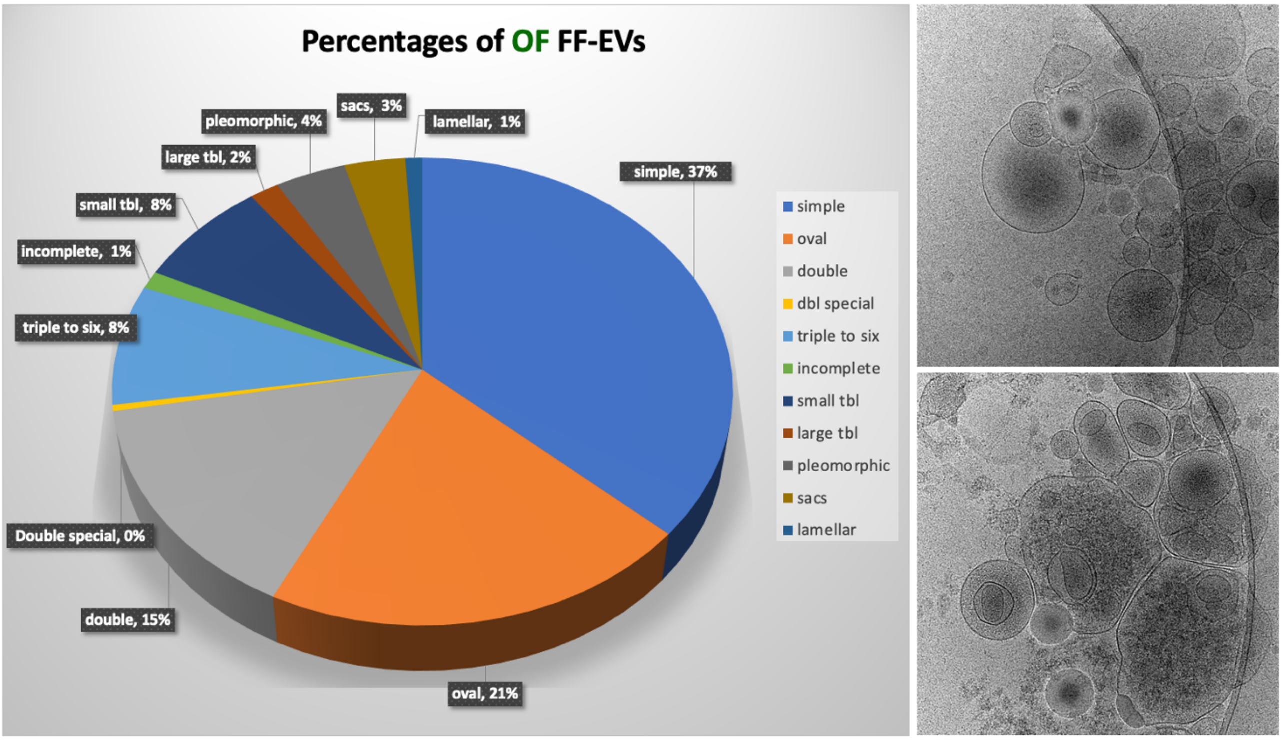

Figure 99. a) Morphological quantification pie histogram and b,c) CryoTEM micrograph of OF FF-EVs.

EVs presenting a circular shape (called "simple" EVs) constitute more than half of EVs in healthy FF (64%) while less than half in OF (37%) and PCOS (27%); in all cases, however, they represent most of the sample. It appears, therefore, that the pathological FF EVs are more deformed, in particular with the type of oval vesicles. Oval vesicles are higher in OF-FF or PCOS-FF (21%) than in healthy subjects (9%). In patients with PCOS, there is an elongation of the EVs detectable following the presence at CryoTEM of numerous tubules ("small tubular " + "large tubular " = 25 %), less present in the OF-FF (10%) and almost absent in the control (2%). Double vesicles containing a smaller vesicle within a larger vesicle are observed in all groups. Special double vesicles having a larger diameter and containing electron-dense material as a charge are seen only in the OF-FF group in this study. Three to 6 vesicles consist of 2 small vesicles blocked in a larger one and are observed in the three groups. In the FF samples of the three groups, pleomorphic membrane structures, vesicular sacs consisting of several vesicles arranged within a larger membrane and lamellar bodies were also visualized (**Figure 98**, **Figure 99**, **Figure 100**).

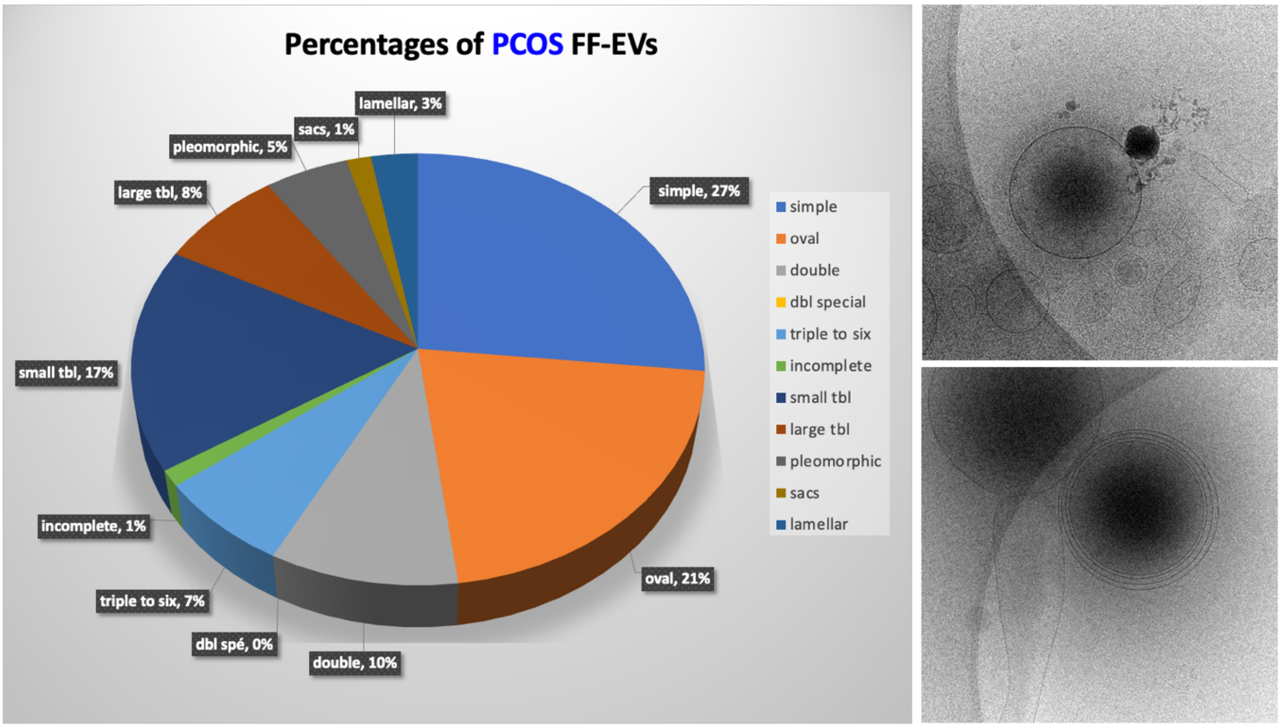

Figure 100. a) Morphological quantification pie histogram and b,c) CryoTEM micrograph of PCOS FF-EVs.

3.3.2.3 CONCLUSIONS AND PERSPECTIVES

In summary, in this work it is shown for the first time that the morphology of EVs is related to ovarian pathophysiology. It was revealed that PCOS-FF appears to have more proteins and fewer EVs but with larger sizes. In contrast, the OF-FF appears to contain fewer proteins, a slightly lower amount of EVs than the control but still comparable, with more oval and tubular EVs than the control but fewer than the PCOS-FF. In both pathological cases a greater polydispersity in morphology was found compared to the control. Furthermore, our study confirms a result already present in the literature[168]that older healthy patients have EVs with greater polydispersity than younger ones;

through this study we have also shown that this result is also valid in patients with PCOS pathology, but it is not always respected in OF patients.

The EVs play an essential role in intercellular communication between mural cells, granular cumulus cells and the oocyte and may constitute an innovative approach for the development of targeted infertility treatments[169,170]. For example, human umbilical cord mesenchymal stem cells (hucMSC) are widely applied in clinical settings as these cells exhibit good safety and low immunogenicity. EVs are the critical component regulating the activity of these cells which have great potential for the treatment of OF[171]. FF-EVs are enriched in proteins that may play a role in regulating follicle growth, oocyte energy metabolism, oocyte maturation, stress response and cell-to-cell communication. Furthermore, FF- EVs improve meiotic recovery of vitrified COCs and can be used as a tool to improve cryopreservation of gametes[172]. For all these reasons it becomes essential to analyze the microenvironment of oocytes, and in particular EVs, in order to identify new non-invasive biomarkers. In fact, by analyzing the content of the EVs, important information on the quality of the oocytes could be obtained.

3.3.2.4 EXPERIMENTAL SECTION

Patients (in collaboration with Dr. Anne-Sophie Neyroud, CHU Rennes 1 hospital). Samples were provided by the GERMETHEQUE Biobank, dedicated to human fertility. Informed consent was obtained from each couple for the use of the follicular fluid sample that was obtained during oocyte retrieval for the ICSI treatment. Ethical approval was also obtained for this study. Patients were stimulated with recombinant FSH. When at least 3 ovarian follicles had grown up to 18 mm in diameter, 10 000 IU human chorionic gonadotropin was administered, and the follicles were aspirated 36 hours later. FF samples were collected from 32 healthy normal-ovulating patients who had undergone intracytoplasmic sperm injection due to a male factor, 16 patient presenting an Ovarian Failure (OF) and 16 patients presenting PolyCystic Ovary Syndrome (PCOS). Normo-ovulating patients have an average age of 33.2 years; the antral follicle count (AFC) medium is 21.4; average AMH (anti-Mullerian hormone) level at 3.17 ng/mL. Ovarian Failure patients have an age of 31.1 years; average AFC is 10.9 and average AMH at 1.02 ng/mL. PCOS patients have an average age of 31.5 years old; average AFC is 46; average AMH at 5.72 ng/mL.

Sample preparation (in collaboration with Dr. Grégory Moulin, CHU Rennes 1 hospital). FF was collected by transvaginal ultrasound-guided aspiration of follicles up to 18 mm in diameter. Fluid samples were centrifuged at 1300g for 10 minutes at 4°C to remove cells and the supernatant was stored at -80°C degrees. Samples were warmed to room temperature before analysis.

Ultracentrifugation (in collaboration with Dr. Grégory Moulin, CHU Rennes 1 hospital and Solène Ducarre University of Rennes 1, France). FF sample went through two-steps differential ultra-centrifugations: the sample was ultracentrifuged at 20 000 g for 90 minutes, then the supernatant was again ultracentrifuged at 100 000 g for 90 minutes both at 4°C. Each pellet was resuspended in 250 µL of PBS (Sodium chloride, 150 mM, and sodium phosphate, 150 mM, pH = 7,2). To image the entire FF-EVs population at the CryoTEM, the two samples obtained from the two-steps differential ultra-centrifugations where pulled.

Cryo-Transmission Electron Microscopy (Cryo-TEM) (in collaboration with Dr. Aurélien Dupont, CNRS Inserm). We pooled 16 FF normo-ovulating patient samples, 8 OF-FF patient samples and 8 PCOS-FF patient samples. To increase the sample concentration for CryoTEM analysis, UltraCentrifugation was performed at 4°C 100.000 g x 90 min. Then, each pellet was re-suspended in 250 µL PBS buffer just before CryoTEM grids preparation. Vitrification of the samples was performed using an automatic plunge freezer (EM GP, Leica) under controlled humidity and temperature [158]. The samples were deposited to glow-discharged electron microscope grids followed by blotting and vitrification by rapid freezing into liquid ethane. Grids were transferred to a single-axis cryo-holder (model 626, Gatan) and were observed using a 200 kV electron microscope (Tecnai G2 T20 Sphera, FEI) equipped with a 4k × 4k CCD camera (TemCam-XF-416, TVIPS). Micrographs were acquired under low electron doses using the camera in binning mode 1 and at a nominal magnification of 25,000x. A total of 2162 vesicles contained within the images were measured and divided into 10 subcategories according Höög et Lötvall's classification (Höög et Lötvall 2015) depending on their size and their morphology. 63 images were analyzed with 717 EVs described in OF group, 74 images with 657 EVs in PCOS group and 78 images with 788 EVs analyzed in the control group.

Dynamic Light Scattering (DLS). DLS experiments were realized using pools of 4 patients with the same pathology to highlight the specific effects of each ovarian pathology. However, for each group, a subdivision according age divided in two groups (young<30 year old and older>30 year old). After thawing the samples, they were centrifuged at 800g for 20 minutes. The measurements of the mean hydrodynamic diameters were performed without diluting the sample at an angle of 173° using a Nanosizer ZEN3600 (Malvern Instruments, England) and collected at 25 °C.

UV-Vis Spectrometer. Absobance experiments were realized using pools of 4 patients with the same pathology to highlight the specific effects of each ovarian pathology. The absorption spectra were performed on a Thermo Scientific™ NanoDrop™ UV-Vis spectrometer by diluting the sample 10 times with PBS just before the measurements to avoid sample variation due to the dilution process.

3.3.3 MIRNA

In this article we analyzed the morphological and miRNA content differences in FF-EVs from patients with two different diseases (OF and PCOS) compared to healthy patients. To simplify the analyzes and have more accurate results, it was first decided to separate, by means of differential centrifugation, the population of EVs into two sub-populations: Big and Small EVs. To obtain the Big EVs the sample was ultracentrifuged at 20,000 g for 90 minutes at 4°C, then the supernatant was again ultracentrifuged at 100,000 g for 90 minutes at 4°C to obtain the Small EVs. In both cases the pellets were resuspended in 250 µL of PBS.

3.3.3.1 AGING EFFECT ON HEALTHY PATIENTS EVS

Initially, healthy (control) patients were analyzed to see the morphological differences between the Big and Small EVs (**Figure 101**) and between the Young and Older patient control (**Figure 102**). Only later, the morphological changes of the EVs coming from pathological patients were compared with the controls (**Figure 103**).

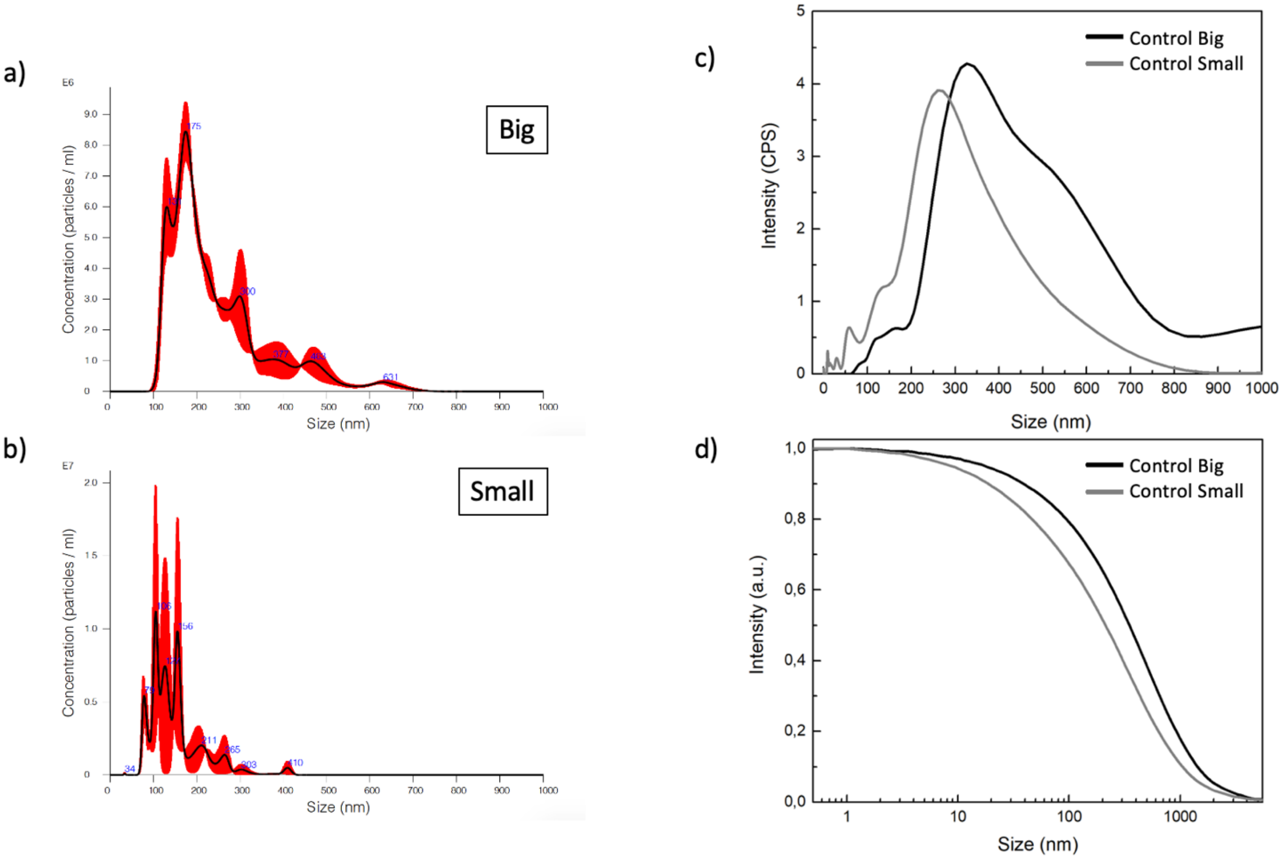

Figure 101. NTA spectra of a) Big and b) Small of Control FF-EVs. DLS c) intensity and d) correlogram spectra of (green line) Big and (back line) Small Control FF-EVs.

The two families of Control EVs (Big and Small) were morphologically analyzed in **Figure 101** by NTA and DLS. NTA measurements show larger vesicles above 300 nm for Big EVs (**Figure 101a**) not present in the case of Small EVs (**Figure 101b**). The result was also confirmed by DLS (**Figure 101 c,d**).

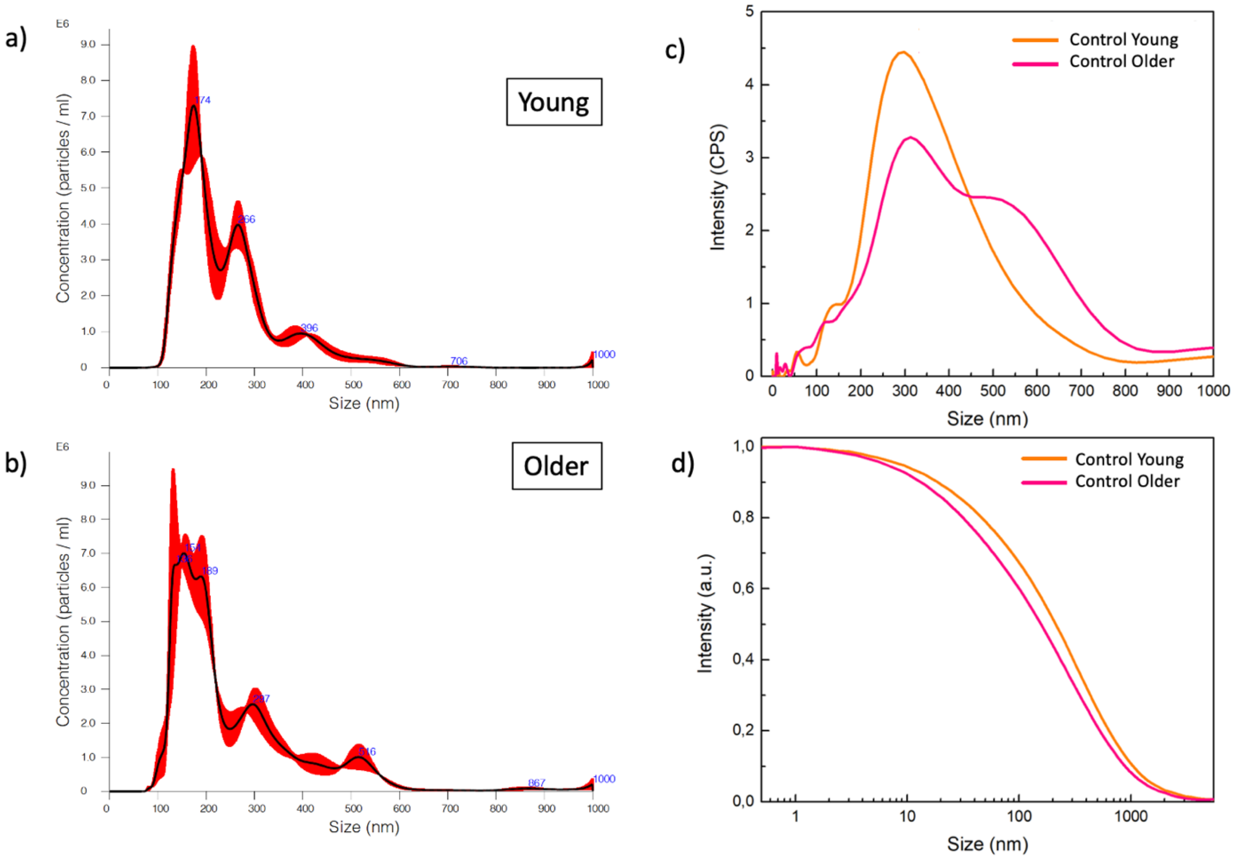

Figure 102. NTA spectra of a) Young and b) Older Control FF-EVs (Big + Small). DLS c) intensity and d) correlogram spectra of (pink line) Young and (green line) Older Control FF-EVs.

In **Figure 102** the difference between the Controls Young and Older EVs was studied. For the Control Older there is a greater polydispersity in size of the EVs compared to the Young Controls since the DLS peak at 300 nm (**Figure 102c**) is lowered and the presence of ever smaller EVs increases. The main average peak goes from 290 nm to 310 nm and a second peak appears at about 550 nm, only in the case of the Older Controls. This result agrees with the results obtained previously for a similar study in the literature[167].

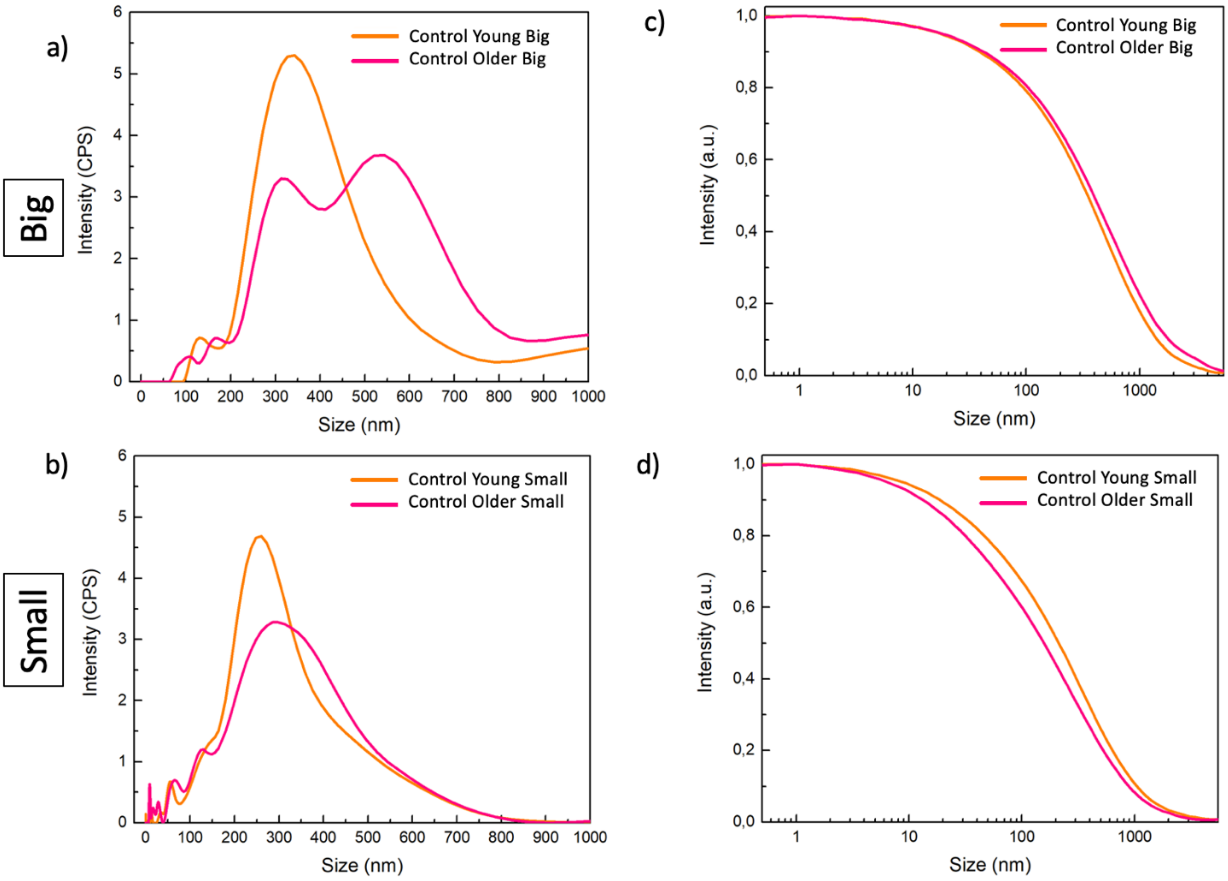

Figure 103. DLS a,b) intensity and c,d) correlogram spectra of a,c) Big and b,d) Small Control FF-EVs for (blue line) Young and (light green line) Older healthy patients.

These measurements are relative to the total sample, with both Small and Big EVs. To go into more detail, the Small and Big EVs have been presented separately in the graphs in **Figure 103**. For both families there is a similar effect with greater polydispersity and larger vesicles for Older patients, but the effect is more evident. on the Big EVs family (**Figure 103c**) as they undergo the most important morphological variation following the aging of patients.

3.3.3.2 Increase in polydispersity for pathologic EVs

After carefully studying the differences between the populations of EVs (Big and Small) present in healthy Controls and the morphological variations related to the Controls of different ages, it was decided to analyze the pathological patients in a similar way. Without considering the age factor and considering the complete population of EVs, it is possible to note an increase in polydispersity for both diseases (**Figure 104**).

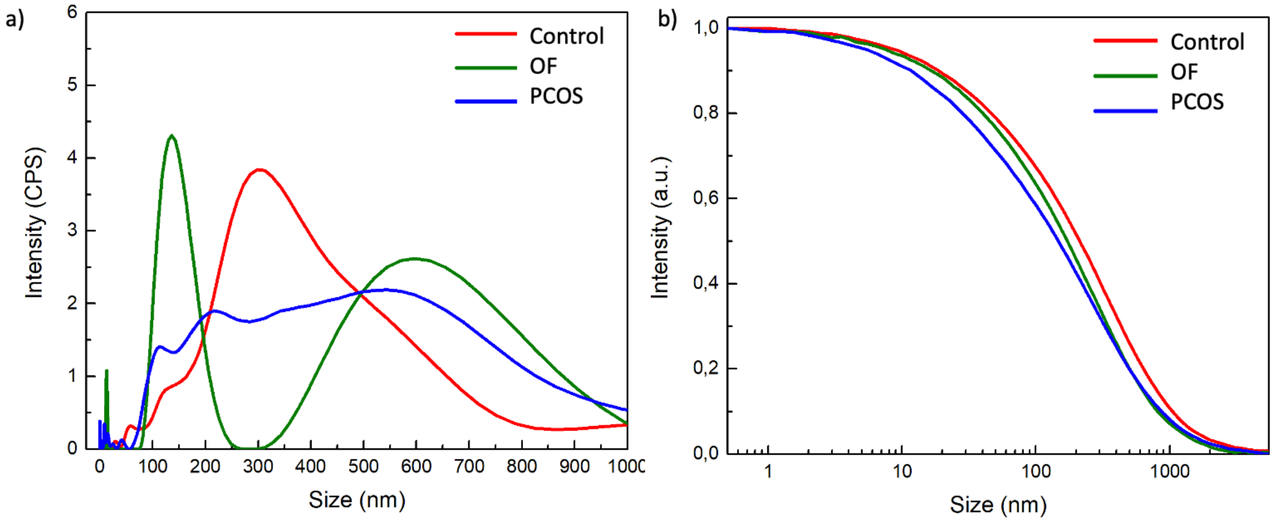

Figure 104. DLS a) intensity and b) correlogram spectra of (red line) Control, (green line) OF and (blue line) PCOS FF-EVs (Big + Small) of pulled Young and Older patients.

To go into more detail, **Figure 105** shows the morphological variations linked to diseases as a function of age and focusing only on the Big EVs in which the differences between the samples are more evident. In the DLS graphs (**Figure 105a**), it is possible to note that for younger patients there is a greater difference in the morphological distribution of EVs between the control and the pathologies: the precise and almost monodisperse peak of the Controls at about 350 nm (mainly related to simple vesicles, as seen above), in case of pathology it shifts to smaller and larger vesicles, forming more Small EVs and more microtubules.

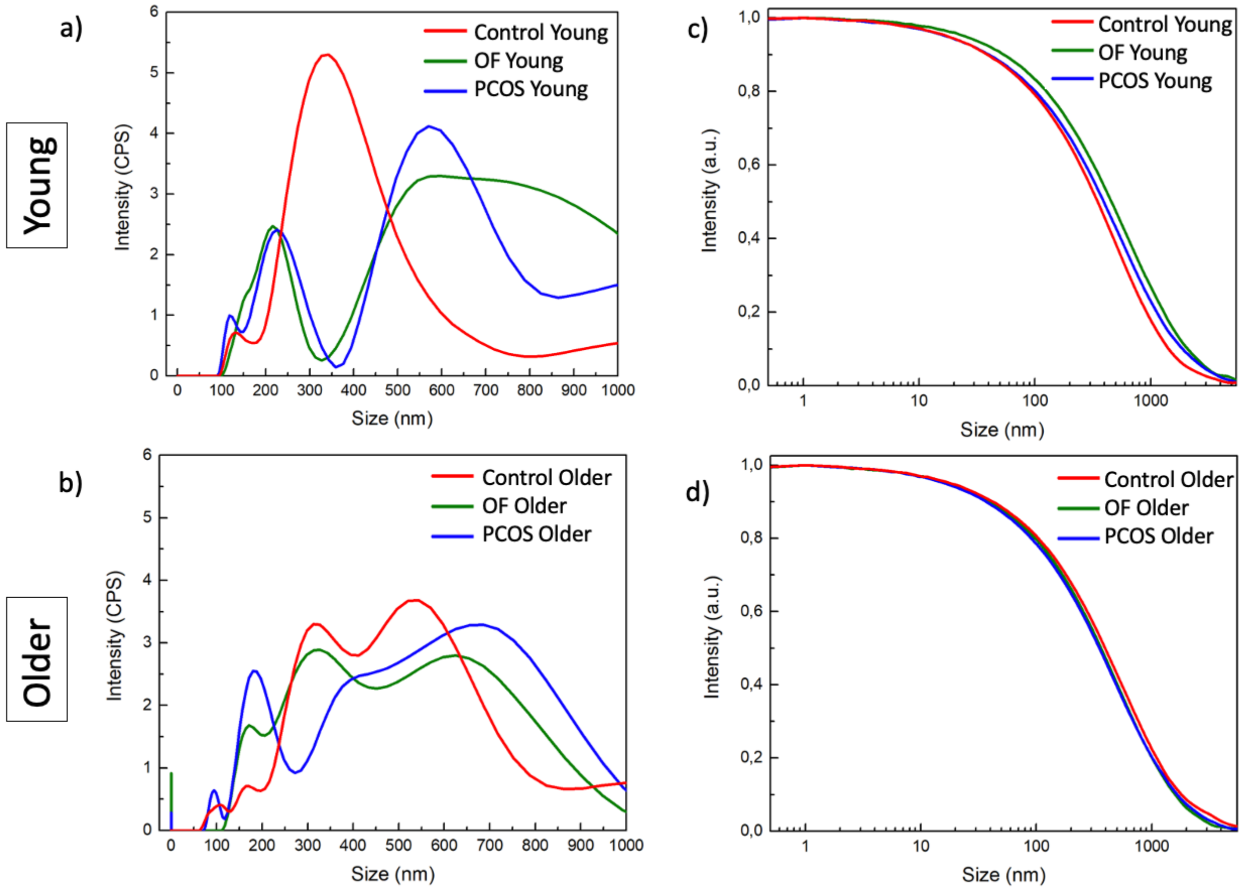

Figure 105. DLS a,b) intensity and c,d) correlogram spectra of a,c) Young and b,d) Older Big FF-EVs for (red line) Control, (green line) OF and (blue line) PCOS patients.

This increase in polydispersity of pathological patients compared to control is also visible in the case of Older patients (**Figure 105b**) but, since the Control EVs also increase in polydispersity with aging, the difference between pathological EVs and controls in the case of Older patients is less evident; in Young patients it is therefore easier to see the morphological differences between Control EVs and pathologic EVs.

3.3.3.3 Difference in miRNA content in healthy and pathological EVs

After analyzing the morphology, the content of the EVs was studied to correlate the presence of miRNA to the pathology. From the samples described above, which are the same as the CryoTEM images analyzed previously, the miRNAs and RNAs were extracted, analyzing their size distribution based on disease and age, studying the Big and Small EVs separately in collaboration with Dr C. Penno (ECOBIO, University of Rennes 1, France) and S. Ducarre (PhD student University of Rennes 1).

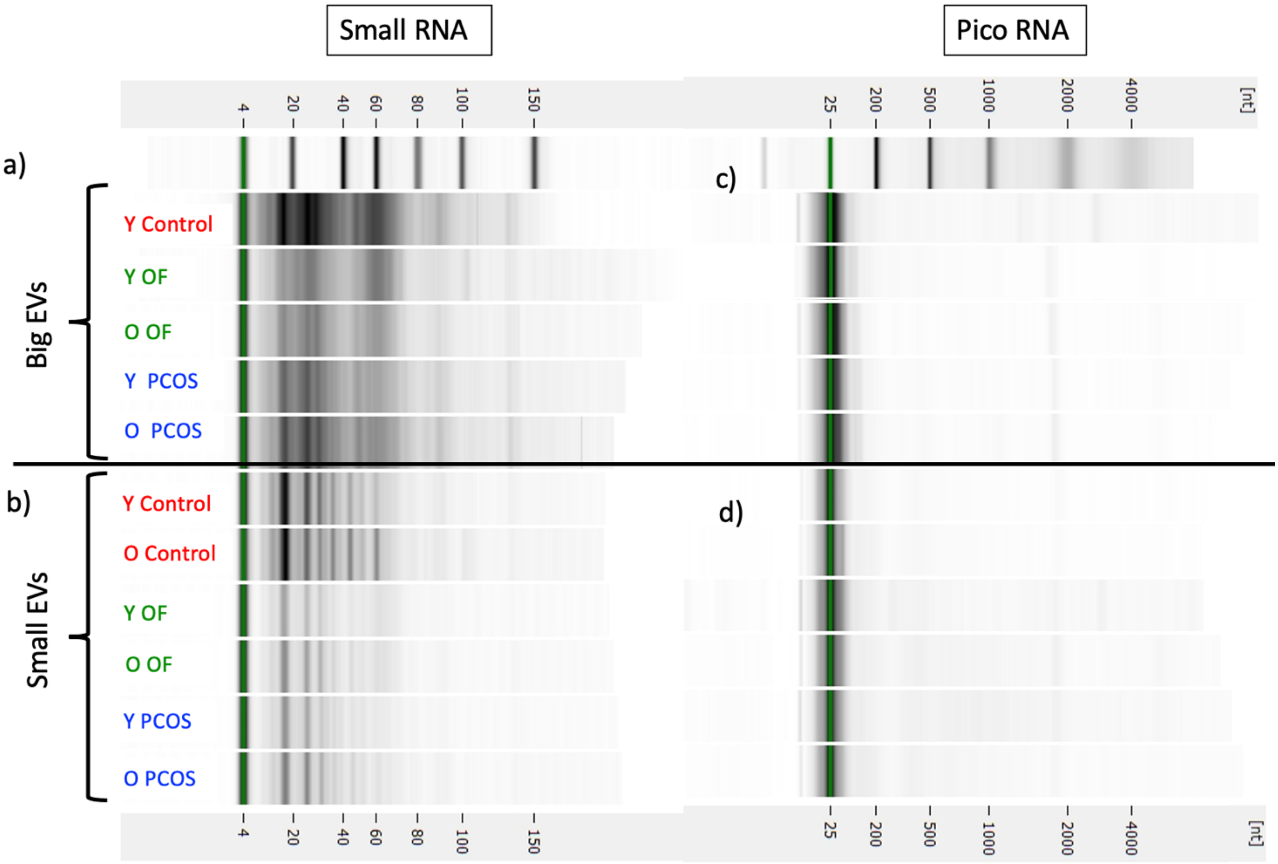

Figure 106. a,b) Small and c,d) Pico RNA analysis of a,c) Big and b,d) Small FF-EVs for (red) Control, (green) OF and (blue) PCOS (Y) Young and (O) Older patients.

In **Figure 106** it is possible to visualize the result, with the detail in number of nucleotides (named $[nt]$) for each peak in **Figure 107** and **Figure 108**.

It is possible to notice a greater presence of miRNA than RNA in the sample. In the case of Big EVs there are smoother peaks than in Small EVs, which have thinner peaks present in all samples. Furthermore, it appears that for all controls (Young or Older, Small or Big EVs), there is a greater intensity of the peaks, and consequently a higher concentration of miRNA within the EVs.

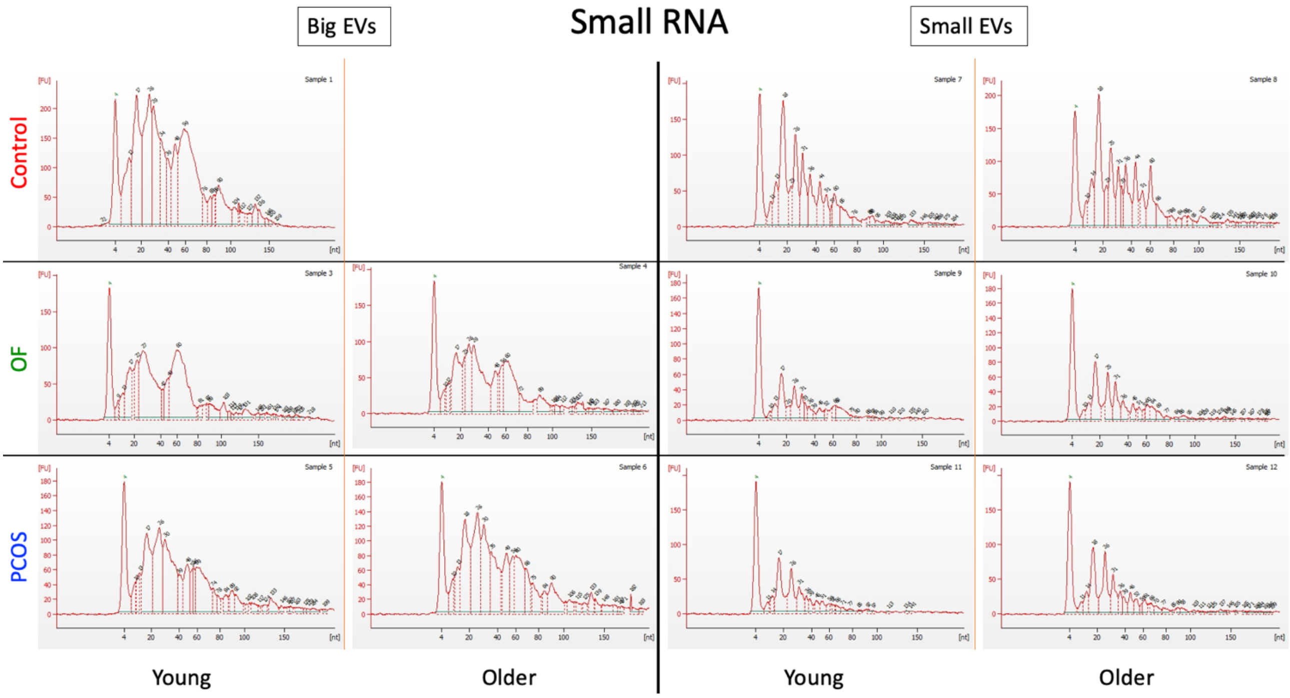

Figure 107. Small RNA analysis of (left) Big and (right) Small FF-EVs for (red) Control, (green) OF and (blue) PCOS Young and Older patients.

Furthermore, in the case of Big EVs, it appears that OF patients have a lower amount of miRNA than PCOS patients and in both cases lower than the control. In the case of Small EVs, on the other hand, it is possible to notice a slightly lower quantity of miRNA for Young patients, both in controls and in pathologies. In some cases, there are darker lines in a sample than in others, which will then be analyzed more carefully by correlating these dimensions in terms of number of nucleotides to a specific miRNA.

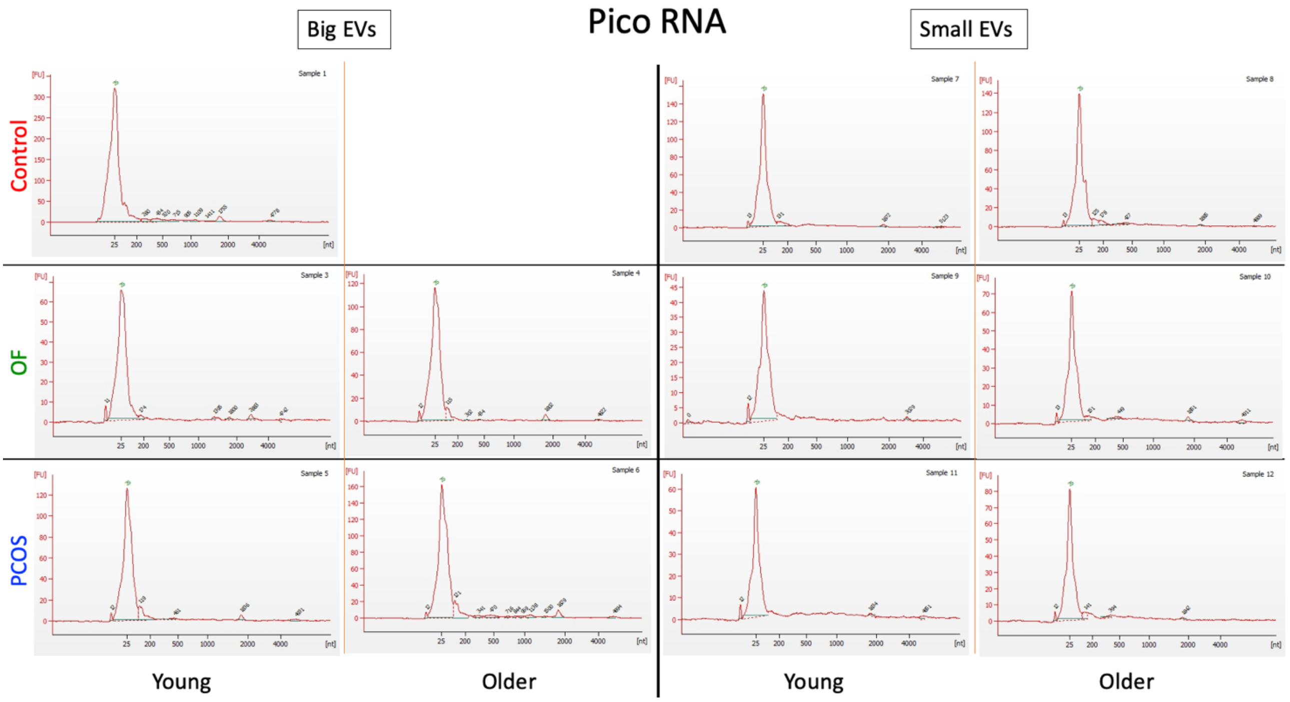

Figure 108. Small RNA analysis of (left) Big and (right) Small FF-EVs for (red) Control, (green) OF and (blue) PCOS Young and Older patients.

Through the quantitative analysis present in **Table 8**, which reports the concentration in RNA and miRNA for the Big and Small EVs, the considerations made previously on the differences between control and pathologies and between young and adult patients can be expressed quantitatively. Most small RNAs are represented by miRNAs in all samples (> 53%).

Big EVs have a greater quantity of Small RNA, however this value could be due to the greater number of EVs in the case of Big EVs (according to NTA and DLS measurements there are more EVs in the Big group than in the Small one). Despite this, the percentages of miRNA within the sample are higher in the case of Small EVs (~ 63%) than in Big EV (~ 77%), most likely because the Small EVs are enriched in exosomes known to be rich in miRNA.

In all controls there is a greater quantity of Small RNA than in the pathological samples for both pathologies and in all cases greater quantities are present for the Older samples ; this data coincides with the results obtained in the literature in which Older patients , following stress, secrete more small EVs [167]which, as mentioned before, are the EVs that contain more miRNA .

The amount of Small RNA and in particular of miRNA appears to be lower in OF patients than in PCOS patients, in both families of EVs. For the Big EVs of the Young Control there is a lower percentage of miRNA (53%) than the pathological samples (> 60%) but a quantity of Small RNA almost 400 times greater than the pathological samples; this result must be verified by repeating the experiment later. The same value is not obtained in the case of the controls in the Small EVs, in which the percentage of miRNA is comparable to that of the pathological subjects and the concentration is only doubled. The highest percentage of miRNA is obtained in the Young PCOS Small EVs, although the amount of miRNA is always greater in the Older PCOS.

Big EVs	**Pico RNA Concentration (µg/µL)**	**Small RNA Concentration (µg/µL)**	**miRNA Concentration (µg/µL)**	**Percentage miRNA over small RNA (%)**
Y Control	0.84	1117.06	597.31	53
Y OF	0.27	3.54	2.22	63
O OF	0.34	3.34	2.21	66
Y PCOS	0.53	3.91	2.67	68
O PCOS	0.82	4.48	3.01	67
Small EVs	**Pico RNA Concentration (µg/µL)**	**Small RNA Concentration (µg/µL)**	**miRNA Concentration (µg/µL)**	**Percentage miRNA over small RNA (%)**
Y Control	0.45	3.30	2.55	77
O Control	0.51	3.63	2.71	75
Y OF	0.19	1.19	0.91	76
O OF	0.49	1.54	1.18	76
Y PCOS	0.41	1.42	1.15	81
O PCOS	0.43	1.88	1.40	75

Table 8. Small and Pico RNA analysis quantitative results of Big and Small FF-EVs for (red) Control, (green) OF and (blue) PCOS (Y) Young and (O) Older patients.

3.3.3.4 CONCLUSIONS AND PERSPECTIVES

In conclusion, through the DLA and NTA analyzes it is possible to state that the signs of the pathologies on the morphology of the EVs are more evident in the case of the Big EVs group of Young patients.

As already demonstrated in the literature, even through our studies, Older patients show EVs with more polydisperse dimensions; moreover, it has been found that this result is valid not only for healthy patients but also for pathological ones.

Analyzing the content of the FF-EVs it was also found that in all the cases analyzed the quantity of pico RNA is always lower than that of the Small RNA. In particular, the quantity of Small RNA is always higher in controls than in pathological patients. Furthermore, for the Big EVs there are more Small RNAs for the PCOS group than for the OF group, while for the Small EVs there are more Small RNAs in the Older patients for all groups, indicating that more exosomes that have a high content of Small RNA [167] may be produced following aging. The next step of this work would be to identify the sequences of RNA associated to these samples.

3.3.3.5 EXPERIMENTAL SECTION

Patients (in collaboration with Dr. Anne-Sophie Neyroud, CHU Rennes 1 hospital). Samples were provided by the GERMETHEQUE Biobank, dedicated to human fertility. Informed consent was obtained from each couple for the use of the follicular fluid sample that was obtained during oocyte retrieval for the ICSI treatment. Ethical approval was also obtained for this study. Patients were stimulated with recombinant FSH. When at least 3 ovarian follicles had grown up to 18 mm in diameter, 10 000 IU human chorionic gonadotropin was administered and the follicles were aspirated 36 hours later. FF samples were collected from 16 healthy normal-ovulating patients who had undergone intracytoplasmic sperm injection due to a male factor, 8 patients presenting an Ovarian Failure (OF) and 8 patients presenting PolyCystic Ovary Syndrome (PCOS). Normo-ovulating patients have an average age of 33.2 years; the antral follicle count (AFC) medium is 21.4; average AMH (anti-Mullerian hormone) level at 3.17 ng/mL. Ovarian Failure patients have an age of 31.1 years; average AFC is 10.9 and average AMH at 1.02 ng/mL. PCOS patients have an average age of 31.5 years old; average AFC is 46; average AMH at 5.72 ng/mL.

Sample preparation (in collaboration with Dr. Grégory Moulin, CHU Rennes 1 hospital and Solène Ducarre University of Rennes 1, France). FF was collected by transvaginal ultrasound-guided aspiration of follicles up to 18 mm in diameter. Fluid samples were centrifuged at 1300g for 10 minutes at 4°C to remove cells and the supernatant was stored at -80°C degrees. Samples were warmed to room temperature and centrifuged at 800g for 20 minutes to remove large aggregates before analysis. After differential ultracentrifugation (20.000g for 90 min and 100.000g for 90 min at 4°C) to separate big EVs from small EVs, each pellet was resuspended in 250 µL of phosphate-buffered saline (PBS).

Dynamic Light Scattering (DLS). DLS experiments were realized using pools of 4 patients with the same pathology to highlight the specific effects of each ovarian pathology. The measurements of the mean hydrodynamic diameters were performed without diluting the sample at an angle of 173° using a Nanosizer ZEN3600 (Malvern Instruments, England) and collected at 25 °C.

Nanoparticle Tracking Analysis (NTA). For NTA, each sample was diluted just before measurement with PBS following the manufacturer's instructions. Samples were diluted 500 times in PBS just before the analysis. Samples (700 µL) were injected into the NanoSightLM10 unit (Malvern Instruments, Malvern, UK) with a 1 mL sterile syringe. Capturing and analyzing settings were manually set according to the protocol. Using the NanoSight LM10 instrument, vesicles were visualized by laser light scattering, and Brownian motion of these vesicles was captured on video. The number of tracks always exceeded 200, and three size distribution measurements were taken for each sample. Recorded videos were then analyzed with the software NanoSight NTA 3.1 software (Malvern, UK) which provided high-resolution particle size distribution profiles and concentration measurements of the vesicles in solution. EVs analysis was performed in 3 videos of 30 s each and temperature controlled of 25 °C.

miRNA extraction (in collaboration with Dr. Christophe Penno, ECOBIO, and Dr. Solène Ducarre, University of Rennes 1, France). Isolation of total RNA, including microRNAs, was performed with the miRNeasy Micro Kit 50 (Qiagen, reference 217084) following the Qiagen manufacturer's instructions for purifying total RNA, including small RNAs, with the following conditions. 100µl of purified vesicles, stored in 1X PBS at -80°C, was used as starting material and mix with 700µl of QIAzol in a 2ml BeadBug™ tube already prefilled with 0.1mm silica glass beads, acid washed (Sigma, reference Z763721). The tubes were agitated at 30 m s−1 for 1 min in a bead beating. The downstream steps of RNA isolation follow the Quick-Start Protocol described by Qiagen. The tubes were (1) then incubated at room temperature for 5 min, (2) 140µl chloroform was added, and were shaken vigorously for 15s and incubate at room temperature for 2 min, (3) centrifugate 12,000 x g for 15 min at 4°C. (4) The upper phase was transferred to a new RNase-free microtube, (5) and 1.5 volume of 100% ethanol was added and mixed well by pipetting. (6) 700µl of the mix was transferred into a RNeasy MinElute spin column, followed by centrifugation at max speed for 15s. This step was repeated with the remaining volume of step (5). Then, the column was then washed with (7) 700µl buffer RWT, followed by 500µl Buffer RPE, and by 500µl 80% with the recommended centrifugation speed and time between each wash. At the end, the RNA was eluted in 15µl RNase-free water. Aliquot of 4µl was transferred in an RNase-free microtube and use for RNA quality control. The remaining 10µl-volume was immediately stored at -80°C for the preparation of RNA NGS library.

miRNA analysis (in collaboration with Dr. Christophe Penno, ECOBIO, University of Rennes 1, France). 1µl of total RNA was analyzed on Agilent 2000 Bioanalyzer (Agilent Technologie) using an Agilent RNA 6000 Pico kit following the manufacturer's instructions. This kit allow allows a quantitative range from 50 to 5000 pg/µl with a qualitative range from 25nt to 6000nt.

3.3.4 ANTIBODY EXOSOMES LABELLING

The count of exosomes within a large population of EVs is very important for the early diagnosis of some diseases, including cancer. In particular, an increase in the amount of exosomes within the body fluids can allow the early diagnosis of diseases also through liquid biopsy[130,131]. The type of fluid in which the overexpression of exosomes is found and their content, especially in terms of miRNA, can also trace the place of origin of these exosomes and consequently localize the disease or for example understand where a solid tumor is located[1,128].

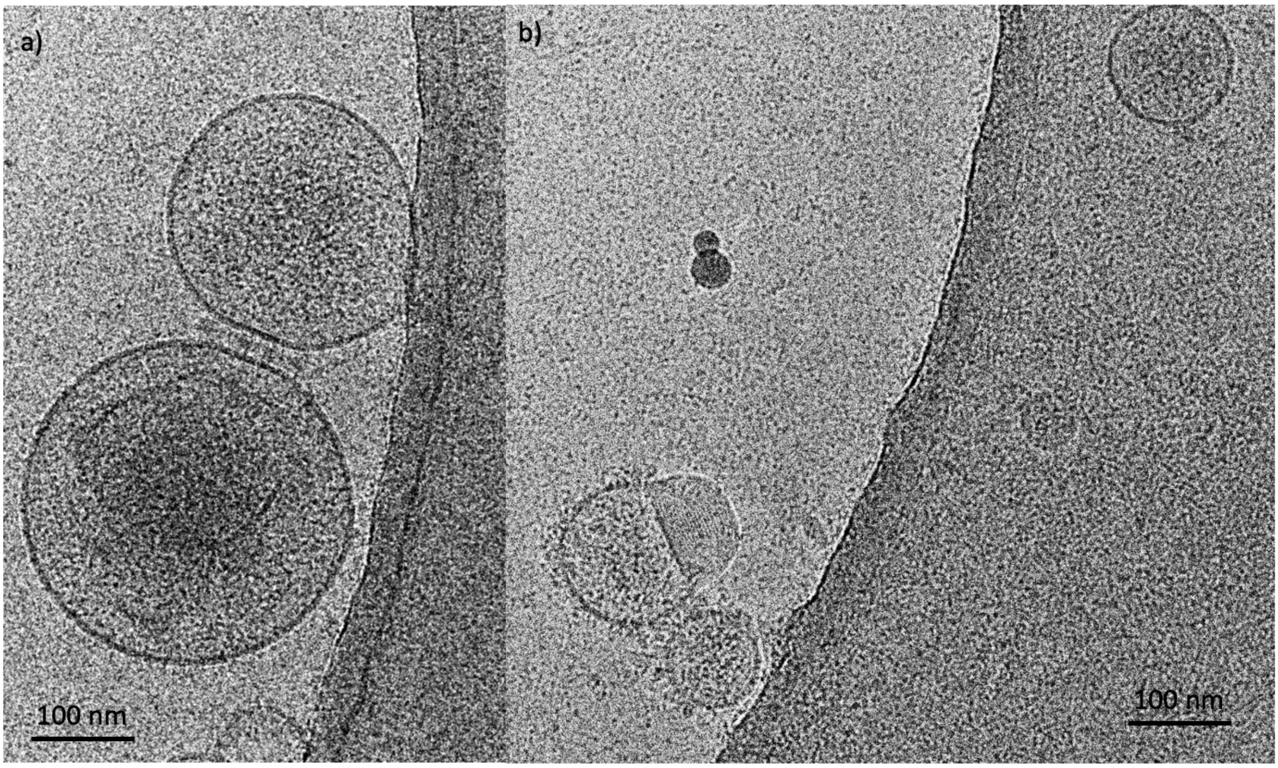

FIGURE 109. (a) Big and (b) small EVs present in the same sample incubated with AntiCD81 functionalized Red NCs.

For these reasons, after studying the large population of vesicles within the follicular fluid, it was intended to selectively label the exosomes, which until now have been distinguished from other vesicles only by their size (between 30 nm and 200 nm). But there are also vesicles with similar dimensions that are not exosomes since they do not contain genetic material and have a different genesis; for this reason, it is important to find a technique that can distinguish them from other EVs not only through their size but through membrane proteins. There are transmembrane proteins such as CD81, CD63, CD9 which are overexpressed in exosomes compared to other types of EVs. So, it was decided to put a protocol to functionalize the NCs or the lanthanide doped Y2O3 NPs with an anti-CD81 antibody in order to have a selective targeting of the exosomes. This objective is not simple since to mark such small vesicles, it is necessary to use nanoparticles of comparable or even smaller size. For this reason, it was decided to functionalize the NCs in the first place (d ≤ 2nm). Once the anti-CD81 antibody had been linked through the C3E6D carboxylic forceps forming a stable peptide bond, the NCs were incubated together with the EVs and analyzed at CryoTEM to visualize their position. As can be seen in **Figure 109** within the same sample there are larger smooth vesicles and smaller vesicles with small protuberances on the surface that are thought to be NCs. The difficulty of viewing the NCs at CryoTEM makes it difficult to interpret the result. Despite this, these images give hope that the marking has worked, since especially the small EVs are marked, which coincides with the concept that the exosomes are smaller than the rest of the EVs, and that particles with a diameter greater than 200 nm are not exosomes. and consequently, no surface markings are visible.

These represent only preliminary studies; in the future, in order to make the presence of exosomes within a solution easily quantifiable, the fluorescence properties of NCs could be used, removing NCs not bound to the vesicles through washing processes, for example by ultrafiltration. Once the sample has been purified from unbound NCs, it is possible to measure the fluorescence level of the sample and get an idea of the concentration of the exosomes by measuring the remaining fluorescence signal. Initially, a calibration curve could be made by incubating the same quantity of NCs with vesicles of known concentration and relating the fluorescence signal to this concentration.

To clearly visualize the NPs on the surface of the EVs, the Lanthanide doped Y2O3 NPs (d) could also be used, which being larger (d ~ 40 nm) are more visible to CryoTEM. Moreover, having a stable fluorescence even under electron beam (cathodoluminescence), it is possible to measure the quantity of the fluorescent labeled vesicles. Furthermore, by using probes with different emission wavelengths it will also be possible to proceed with multiple targeting, for example by measuring the coexistence of different proteins on the same vesicles, to assert with certainty that they are exosomes. Through this technique it is also possible to measure emission spectra punctually, and in the case of this type of NPs there is a fingerprint with emission peaks at a very precise wavelength, which would vary in case of overlapping of the fluorophores.

3.3.4.1 EXPERIMENTAL SECTION

Anti-CD81 NCs functionalisation. To functionalize the NCs with the CD81 antibody, 2 mL of 1 µM solution of C3E6D Red NCs were concentrated 10 times by ultrafiltration with Amicon 3KDa up to 200 µL of a 10 µM solution. From this solution 25 µL (256 nmol of peptide = 1eq) were taken and added to 69 µL (0.5 mg / mL) of anti-CD81 (1.28 nmol = 5 eq). The solutions of the coupling agents EDC and NHS were freshly prepared and 4.8 µL of EDC (1mg / mL) (25.6 nmol = 100 eq) and 5.6 µL of NHS (1mg / mL) (25.6 nmol = 100 eq) were added to the solution of NCs and antibody. Afterwards, we wrap everything in aluminum foil and mixed gently for 1h30.

3.4 NANOCLUSTERS TARGETING OF PANCREATIC TUMOR CELLS

Tumor-targeted fluorescence imaging is a fast, non-invasive method of tumor diagnosis and is used in practice for the localization of cancerous tissues as well as for image-guided therapy. Several fluorophores were used to visualize the tumor mass well, including up-conversion nanoparticles with rare earths[173], semiconductor quantum dots[174], carbon nanomaterials and noble metal [175,176,177,6]. Among them, small gold [179,180]. Through a post synthesis ligand exchange it is possible to functionalize the NCs to make them selective and have a specific tumor targeting[1,182,183].

The urokinase Plasminogen Activating Receptor (uPAR) is overexpressed in many types of cancer cells, particularly those of the prostate and breast[8]. The urokinase Plasminogen Activator (uPA) binds to this cellular receptor (uPAR) with high affinity and initiates signaling cascades implicated in pathological processes including tumor growth, metastasis and inflammation[184]. The structural analysis of the complex (uPA/uPAR) allows to identify a short sequence of 11 aminopeptides in the uPA protein called U_{11} that interacts with the uPAR receptor by means of an equilibrium dissociation constant Kd of 1.3-1.4 µM[185]. A U_{11} peptide-lipid amphiphile was processed as a biologically active ligand to induce specific receptor-mediated endocytosis (RME) and delivery of plasmid DNA to uPAR positive cells (DU145 cells)[185].

To design luminescent AuNCs with active targeting, we describe here an original "one- pot " synthesis based on an original short peptide named $C_3E_6U_{11}$ which is composed of three cysteines, a PEG and the functional group U_{11}.

The tricysteine has the role of anchoring to the NCs, since the thiol groups have a strong affinity for gold. The PEG serves as a spacer to increase the stability and luminescence of the NCs and limit their non-specific interactions. Finally, the functional group U_{11} allows the specific targeting of pancreatic tumor cells as well as internalization into cells through receptor-mediated endocytosis. In order to evaluate their ability for active targeting and bioimaging, the interaction of these $C_3E_6U_{11}$ NCs was studied in vitro with pancreatic tumor cell lines (PANC cells).

Within this original peptide ($C_3E_6U_{11}$), PEG plays a vital role as it prevents the binding of serum proteins in vivo which often leads to rapid elimination from the bloodstream. Furthermore, its flexibility allows to make the binding site of the 11 amino acid peptides accessible. The C_3E_6D peptide acts as a short intercalating PEG derivative and allows to optimize the surface concentration of the recognition peptide $C_3E_6U_{11}$ between 0 and 5% of the molar ratio[186]. Since it has been shown that the U_{11} peptide tends to form b-sheet structures when its concentration increases, resulting in steric masking of the surface presented to the receptor, it is necessary to find the suitable percentage of $C_3E_6U_{11}$ in order to have a high targeting efficiency but without the formation of b-sheets which could lead to the loss of the functional bond[185]. The aim is therefore to optimize the targeting efficiency and selectivity of the nanoclusters $C_3E_6U_{11}$ to specific human cells that overexpressed the uPAR [187]membrane receptor. Since the two derivatives C_3E_6D and $C_3E_6U_{11}$ possess the same gold anchoring group (tricysteine) and the same hydrophilic spacer (PEG), they are expected to have the same affinity for the surface of the gold, and that it is therefore easier to define the percentage of one with respect to the other on the surface of the NC.

3.4.1 SYNTHESIS OF FUNCTIONALIZED $C_3E_6U_{11}$ NCS

To prepare NCs functionalized with the U_{11} recognition peptide, two approaches were used: the first (**Figure 110a**) involves two steps (synthesis of GSH NCs and ligand exchange to functionalize with $C_3E_6U_{11}$) and generates NCs with a red emission at 620 nm ($C_3E_6U_{11}$ Red NCs); the second (**Figure 110b**) provides an innovative synthesis in a single step which allows to obtain NCs with blue emission at 480 nm already functionalized with the peptide U_{11} ($C_3E_6U_{11}$Blue NCs).

The synthesis process to produce Red and Blue NCs has already been described and detailed previously in the chapter X on the synthesis and characterization of NCs.

For the functionalization of the NCs with both methods, a $C_3E_6U_{11}/C_3E_6D$ mixture with different molar ratio was used.

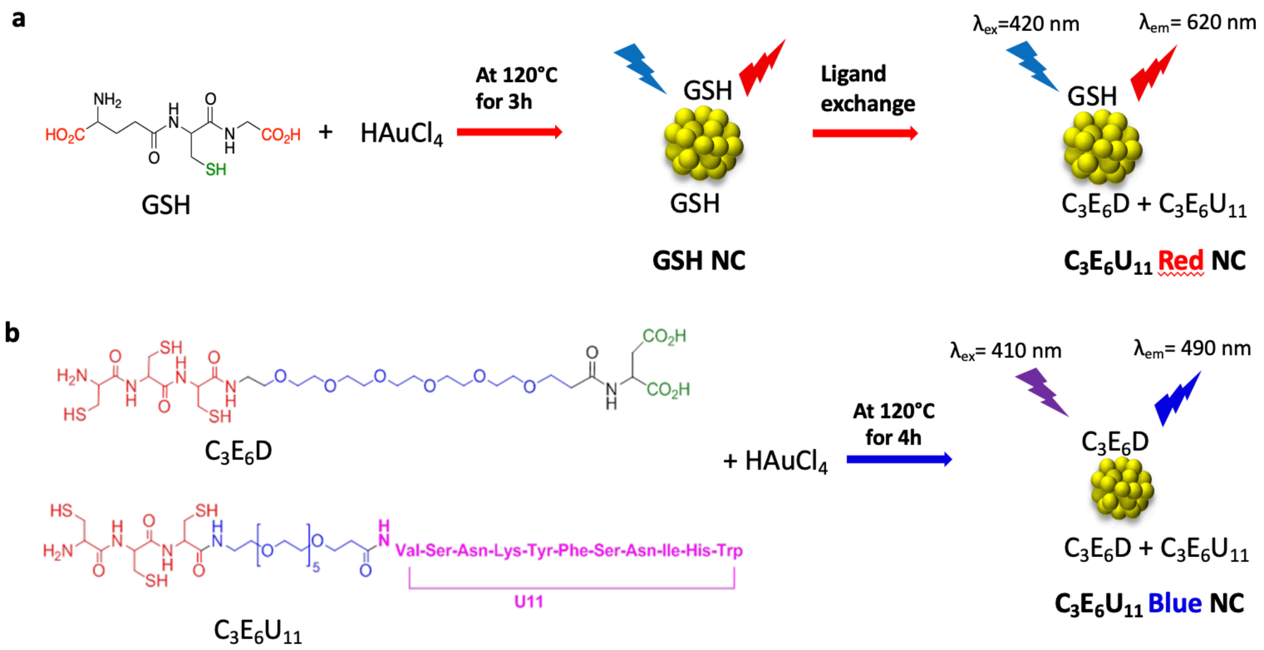

Figure 110. a) Schematic route of the $C_3E_6U_{11}$ red NCs in two steps including one first step of GSH induced Au NCs nucleation followed by a ligand exchange step at the surface. b) Schematic route of the $C_3E_6U_{11}$ blue NCs in a direct one-pot nucleation of the nanoclusters stabilized by a ($C_3E_6U_{11}$:C_3E_6D) mixture at the given molar ratio.

Our one-pot synthesis (**Figure 110b**) has several advantages over the classical synthesis (**Figure 110a**). First, the reaction time required to synthesize the Blue NCs is shorter, since the synthesis of GSH NCs involved 24 hours of reaction versus the 4 hours of one pot synthesis. Secondly, the functionalization step that requires an incubation night is avoided and therefore the total synthesis time is further extended, as well as having a more precise control of the surface ligands. Indeed, it avoids that a part of the GSH ligand used in the **Figure 110a** can remain on the surface after the ligand exchange. Furthermore, the synthesis costs decrease considerably since the use in large quantities of functionalizing ligands (quite expensive) is avoided, which must be present in large excess within the solution if we want to be sure that the exchange takes place successfully.

C_3E_6D ligand is strategic since, thanks to the two carboxylate groups, it is also possible to bind it to amino groups of antibodies or other recognition groups using known protocols of peptide coupling in the presence of EDC and NHS.

3.4.2 QUANTITY OF RECOGNITION SEGMENT OPTIMIZATION FOR LABELLING

The $C_3E_6U_{11}$: C_3E_6D ratio, which defines the surface concentration of U_{11}, was evaluated to optimize targeting efficiency and selectivity. In this perspective, the cell biolabeling efficiency was initially verified by means of red emission quantum dots (QD $_{605nm}$) functionalized with different percentages of $C_3E_6U_{11}$ (from 0% to 5%) compared to C_3E_6D (**Figure 111**). The QDs were first incubated for one hour in the presence of uPAR positive pancreatic tumor cells (PANC1 cells) and then, through several washes, the unbound QDs were removed.

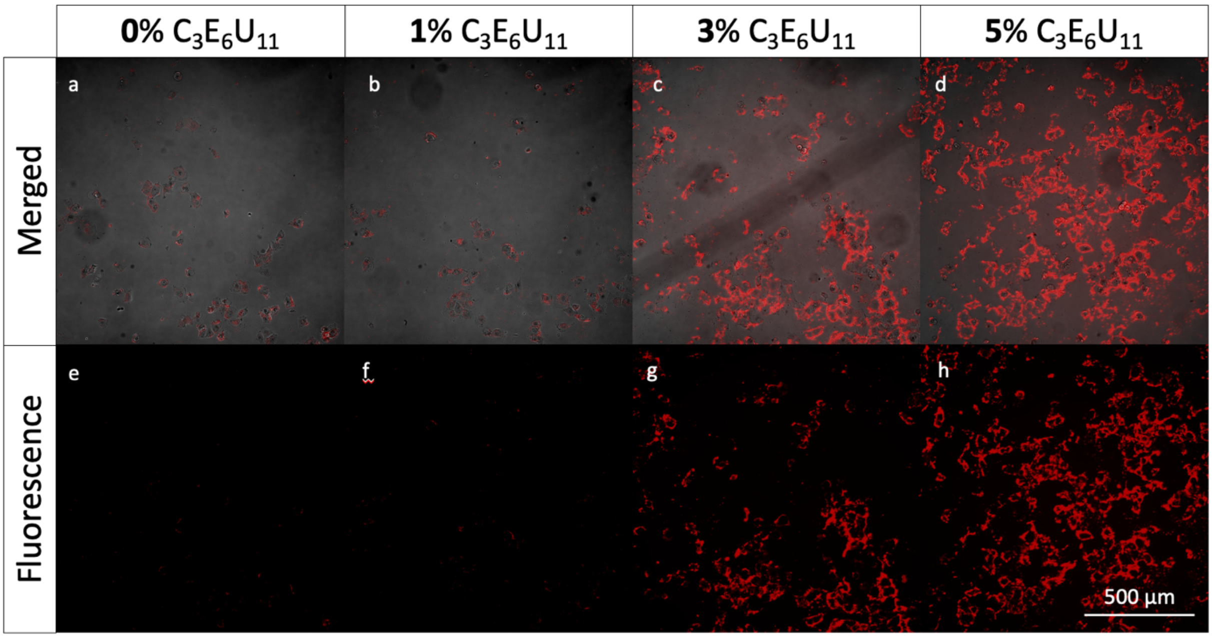

Figure 111. Light optical microscopy images showing selective fluorescence labeling of the uPAR positive tumoral pancreatic cells (PANC cells) incubated with the 0% (a,e) 1% (b,f) 3% (c,g) and 5 % (d,h) $C_3E_6U_{11}$ QDs observed by phase contrast imaging and by fluorescence (excitation wavelength at 555 nm).

The cells were imaged by light optical microscopy in the case of different molar $C_3E_6U_{11}$: C_3E_6D ratio of 0%, 1%, 3% and 5% on the surface of the QD. The results indicate an efficient targeting of the cells which increases as the molar percentage of U_{11} increases, showing the targeting efficacy of this peptide and the precision with which, it is possible to obtain nanoparticles with different percentages of U_{11} on the surface.

A similar experiment was also conducted with C_3E_6D Blue and Red NCs with different molar ratio of $C_3E_6U_{11}$. The C_3E_6D Blue NCs were purified by ultrafiltration with Amicon 3KDa to remove the excess of free ligand (using the technique described in the chapter relating to the synthesis and characterization of these NCs).

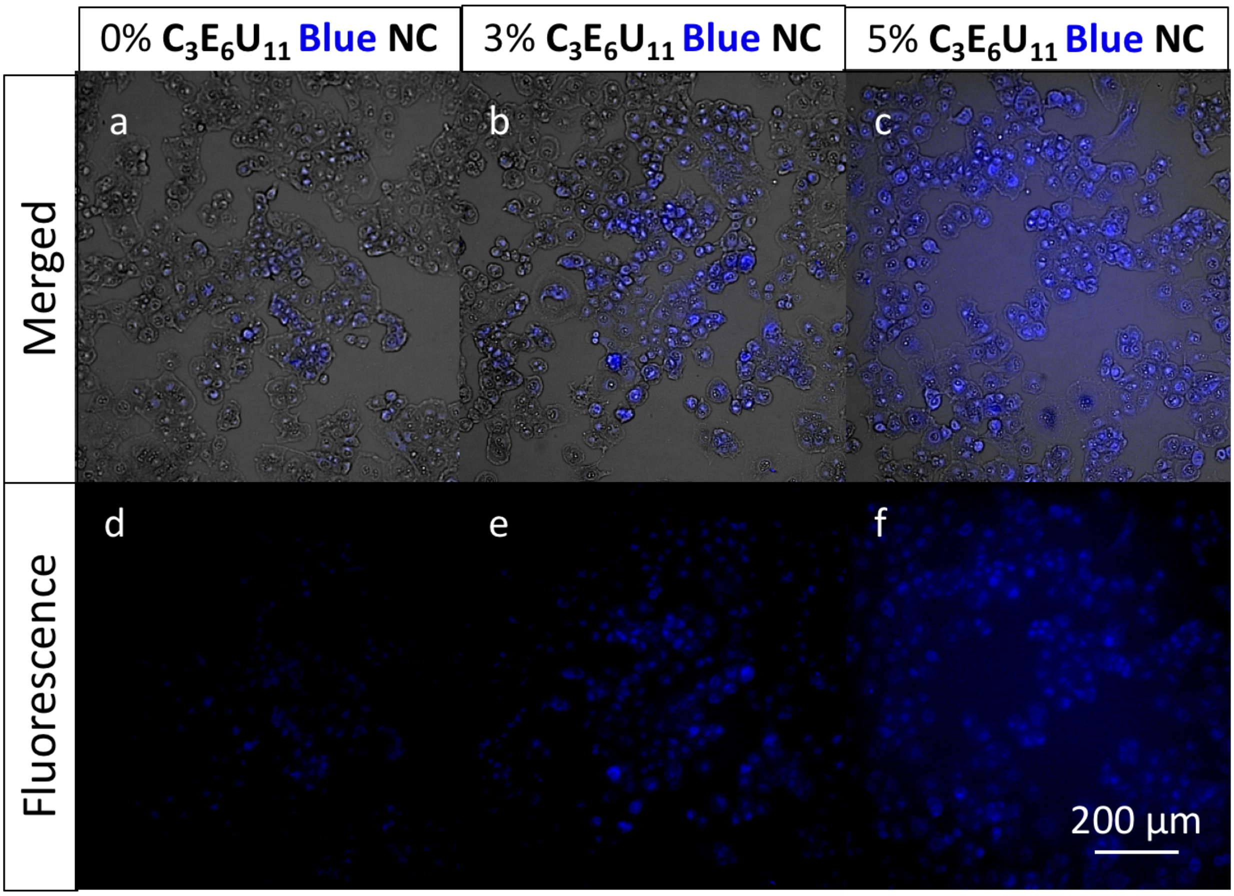

Figure 112. Light optical microscopy images showing selective fluorescence labeling of the uPAR positive tumoral pancreatic cells (PANC cells) incubated with heated ligand C_3E_6D + 0% (a,d) 3% (b,e) and 5 % (c,f) $C_3E_6U_{11}$ observed by phase contrast imaging and by fluorescence (excitation wavelength at 390 nm).

Then it was decided to test not only the purified NCs retained inside the filter, but also the ligand itself in excess that exceeds the pores of the membrane. This ligand heated following the synthesis was found to be also fluorescent, although it was not so at the beginning; therefore, to test the localization and effective marking of NCs on tumor cells, it is essential to also test the localization of the fluorescent ligand. For this reason, the fluorescent ligand with different percentages of $C_3E_6U_{11}$was also visualized under the optical fluorescence microscope (**Figure 112**). As in the case of QDs, also in this case there is an increase in the labeling with the increase in the percentage of U_{11}, indicating the ability of $C_3E_6U_{11}$ NCs to mark tumor cells. The fluorescence distribution of the QDs seems, however, to differ from that of the simple heated ligand, being rather at the periphery of the cell. This indicates that, unlike the fluorescent ligand, for which there is a localization of the fluorescence inside the cell, the QDs are unable to overcome the cellular barrier.

3.4.3 FUNCTIONALIZED NANOCLUSTERS POSITIONING INSIDE THE CELLS

To visualize the exact position in the cell of the fluorescence of the ligand and of the NCs, the observation was performed with a confocal light microscope. This time, in addition to the heated ligand, the C_3E_6D + 5% $C_3E_6U_{11}$ were also incubated as well as $C_3E_6U_{11}$ Red and Blue NCs (for simplicity the latter are named 5% $C_3E_6U_{11}$NCs).

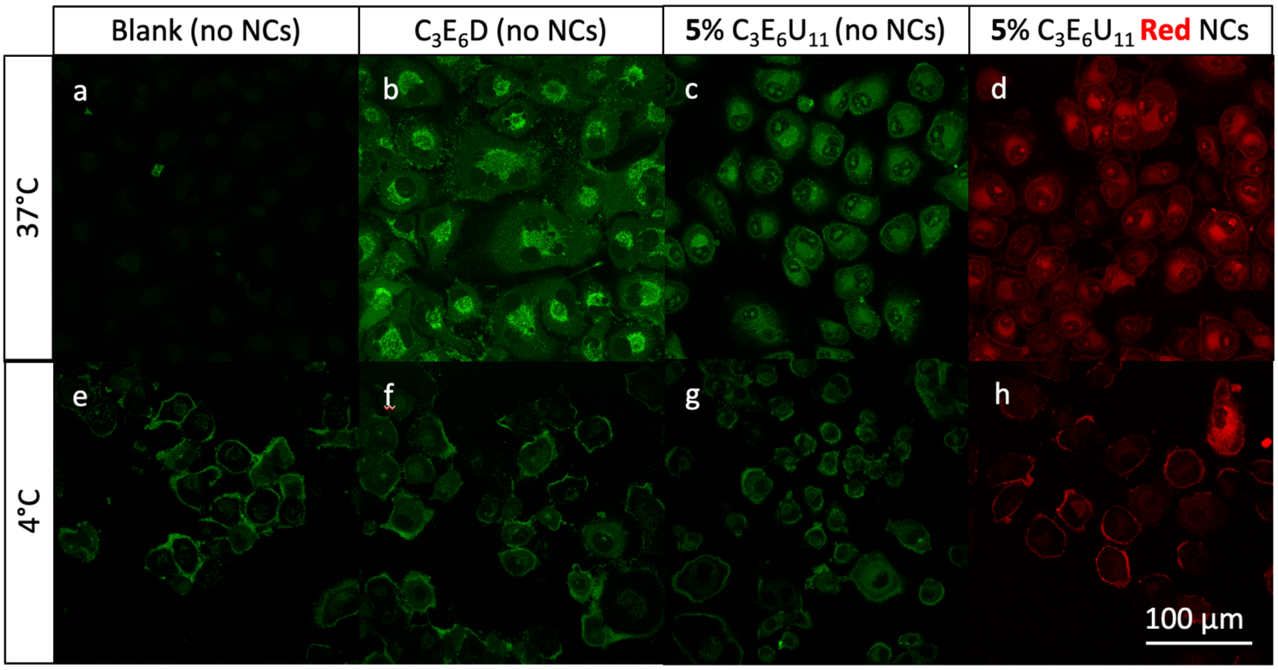

Figure 113. Confocal microscope images of the uPAR positive tumoral pancreatic cells (PANC cells) incubated at (a-d) 37°C and (e-h) 4°C, (a,e) without ligands or NCs, (b,f) with heated C_3E_6D, (c,g) with heated C_3E_6D + 5 % $C_3E_6U_{11}$ and (d,h) C_3E_6D + 5 % $C_3E_6U_{11}$ Red NCs excited at 405 nm.

A first result of this incubation is presented in **Figure 113**, in which the incubation of the Red NCs was compared with that of the simple heated ligand with and without $C_3E_6U_{11}$. The images obtained show that, in all cases with incubation at 37°C, there is an internalization inside the cell, both for the Red NCs and for the heated ligands. The most notable difference is however the presence of fluorescence inside the nucleus which always and only occurs in the presence of $C_3E_6U_{11}$. In fact, the ligand 5% $C_3E_6U_{11}$alone it already manages to penetrate right into the nucleus, and the same goes for the Red NCs that present this ligand on the surface, indicating that thanks to it they are also able to overcome the nuclear barrier. However, the presence of $C_3E_6U_{11}$ is not a sufficient condition for the nucleus to be marked, since, in the case of QDs, the $C_3E_6U_{11}$, while leading to an excellent membrane marking, did not allow even to overcome the cellular barrier. In **Figure 113d** it is evident that not only the NCs are internalized in the cell, but they manage to penetrate to the nucleus, overcoming the nuclear barrier, which is difficult to overcome for most of the existing fluorophores.

The control of cells labeled with C_3E_6D in the absence of U_{11} (**Figure 113b**) however shows an internalization of the ligand, which seems to accumulate in the endoplasmic reticulum, but no fluorescence is found inside the nucleus, nor there is a specific marking of the membrane. On the contrary, cells labeled with 5% $C_3E_6U_{11}$ show a localization very similar to that of $C_3E_6U_{11}$ NCs indicating that the NCs are positioned inside the nucleus thanks to the role of $C_3E_6U_{11}$. It is important to underline that for the 5% $C_3E_6U_{11}$ Red NCs, the ligand is not fluorescent since it has not undergone any heat treatment as opposed to the 5% $C_3E_6U_{11}$ Blue NCs in which the ligand was also present during the synthesis of NCs at 120°C. Consequently, the red fluorescence in **Figure 113d** derives solely from the intrinsic fluorescence of the NCs. It seems, therefore, that the presence of U_{11} generates a receptor-mediated internalization that allows the $C_3E_6U_{11}$ to reach the nucleus where, in addition to the membrane, there are also uPAR receptors, dragging with it also the NCs to which they are related.

To elucidate the mechanism of internalization and understand if the transport of the NCs actually takes place via an active transport due to endocytosis or by passive diffusion, the cells were incubated at 4°C with the same fluorescent ligands and NCs used previously (**Figure 113 e-h**); the endocytosis of exogenous substances, including nanoparticles, is in fact an energy-dependent cellular process, which is consequently blocked at low temperatures[188]. It is interesting to note that both in the case of ligands and in that of Red NCs there is an almost complete inhibition of the internalization process, and they seem to accumulate rather on the surface, demonstrating that the main mechanism of internalization is in no case diffusion. Even if a small number of ligands or NCs still manage to enter the cell, they never reach the nucleus at 4°C. Since both in the presence or not of $C_3E_6U_{11}$ the internalization is rather attributed to a endocytosis process, the different localization of the fluorescence at 37°C between **Figure 113b** and **Figure 113c** suggests that it is a simple endocytosis in the absence of $C_3E_6U_{11}$ and receptor-mediated endocytosis in the presence of $C_3E_6U_{11}$.

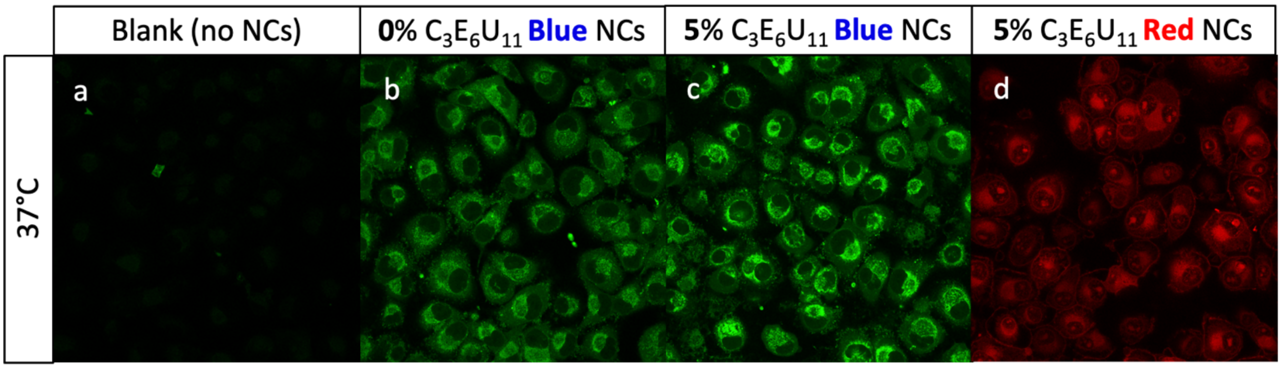

Figure 114. Confocal microscope images of the uPAR positive tumoral pancreatic cells (PANC cells) incubated at 37°C, (a) without NCs, (b) with C_3E_6D Blue NCs, (c) with C_3E_6D + 5 % $C_3E_6U_{11}$ Blue and (d) Red NCs excited at 405 nm.

The incubation experiment at 37 ° C was also conducted for the 5% $C_3E_6U_{11}$ Blue NCs and the results were compared to those obtained with the 5% $C_3E_6U_{11}$Red NCs in **Figure 114**. Also in the case of the 5% $C_3E_6U_{11}$ Blue NCs there is an internalization inside the cell but, despite the presence of $C_3E_6U_{11}$ it is highlighted by a stronger labelling for the 5% $C_3E_6U_{11}$NCs, this time there is no fluorescence inside the nucleus.

3.4.4 CONCLUSIONS AND PERSPECTIVES

It is difficult to interpretate the different behavior of red and blue 5% $C_3E_6U_{11}$NCs regarding the efficiency of the nucleus labelling. It is not possible to exclude an alteration of the C_3E_6D peptide following heating to 120°C in the case of blue 5% $C_3E_6U_{11}$NCs which, in addition to generating fluorescence properties, varies the structure of the peptide that forms agglomerates around the NC, increasing its hydrodynamic radius. As demonstrated in the chapter on the synthesis and characterization of Blue NCs, the phenomenon is not very evident immediately after the synthesis and the agglomerations around the NCs increase in size with the passing of the months. They are less stable against aggregation than the red NCs. This could cause the particle to increase in size considerably, and the large size could be one of the reasons that does not allow the NCs to be internalized in the nucleus. A similar explanation could also be plausible in the case of QDs which being larger than NCs, despite functionalization with $C_3E_6U_{11}$, cannot even cross the cell wall.

Subsequently, it was realized that the main problem came from the purchased batch of C_3E_6D, since by changing the supplier in subsequent syntheses the excess peptide that exceeded the 3 KDa membrane was found to have almost zero fluorescence, visible only to the spectrofluorimeter and with low intensities. This peptide was also less toxic for subsequent experiments with zebrafish and at TEM we obtain NCs with uniform distribution without the presence of agglomerates of NCs surrounded by organic matter, as in the case of the old C_3E_6D.

Furthermore, to completely eliminate problems due to possible degradation of the C_3E_6D, the synthesis temperature could be lowered to 70°C by extending the times to 24 hours, as in the case of the classical synthesis of GSH NCs mentioned above[189]; furthermore, the NCs could be used immediately after synthesis in order to avoid possible phenomena generated by the aging of the sample.

These preliminary experiments demonstrate the great potential of gold NCs, which are distinguished from organic fluorophores for a more stable fluorescence and from QDs for low toxicity and for being able to overcome not only the cellular barrier, but also the nuclear barrier. This opens the way to broad possibilities for the application of NCs as multivalent probes for tumor theragnostic and other pathologies.

3.4.5 EXPERIMENTAL SECTION

Nanoclusters synthesis. All glassware used for these synthesis was cleaned in a bath of freshly prepared aqua regia ($HCl:HNO_3$, 3:1 by volume) and rinsed 10 times in water before using them. The NCs solution obtained could be stored at 4°C for months with negligible changes in their optical properties.

Red NCs synthesis. A freshly prepared aqueous solution of GSH (50 mM, 1,2 mL) were mixed with 16,8 mL of ultrapure water. After dipping the flask containing the solution in an oil bath at 120°C under stirring, a solution of $HAuCl_4$ (20 mM, 2mL) was quickly added to it. The reaction was stopped after 3h. An aqueous solution of orange-emitting GSH Au NCs was formed (≈ 3 µM in number of NCs).

Blue NCs C_3E_6D + 0, 3, 5 % U_{11} synthesis. A freshly prepared aqueous solution of C_3E_6D (20 mM, 0.585 mL) was mixed with 0mL, 0.35 mL, 0.975 mL of a U11 solution (1 mM) to obtain C_3E_6D NCs functionalized with 0%, 3%, 5% respectively of U_{11} compared to C_3E_6D; H_2O was added to the solution to reach a final volume of 2.7 mL. After dipping the flask containing the solution in an oil bath at 120 ° C under stirring, a solution of HAuCl4 (20 mM, 0.3 mL) was quickly added to it. The reaction was stopped after 4 h. An aqueous solution of C_3E_6D/U_{11} NCs was obtained which emit in the blue region. For purification 1.85 mL of C_3E_6D/U_{11} NCs were centrifuged through centrifuge filters (3 KDa) at 4,500 g For 10 minutes. Thereafter, 3 mL of HBSS without red phenol buffer was added and the NCs were re-centrifuged at 4,500 g for 20 minutes. What remains inside the filter and does not pass the 3 KDa membrane will be the purified C_3E_6D/U_{11} NCs.

Red NCs + 4 % U_{11} ligand exchange. The GSH NCs solution obtained after the synthesis (20mL) was lyophilized and then 300µL of H2O was added to the powders. To obtain U_{11} functionalized NCs, a ligand exchange was performed by incubating the GSH NCs (37 µL) overnight in presence of a solution of C_3E_6D (20 mM, 237 µL) and U_{11} (1mM, 295 µL). The excess binder was removed by centrifugal filtration using Amicon 3 KDa and centrifuging for 3 min at 7,379 g for 4 times, and adding 100 µL of HBSS each time, reaching a final volume of 300 µL (about 20 µM in number of NCs).

QD + 0,1,3,5% U_{11} ligand exchange. Initially, peptide solutions of C_3E_6D + X% U11 (X = 0,1,3,5) were prepared. To do this, 0µL, 5µL, 15 µL, 25 µL of U_{11} (1mM) were added respectively to a solution of C3E6D (50 µL, 10 mM). To prepare the functionalized QDs, 800 µL of MeOH were added to 200 µL of QD in decane (1 µM). The solution was then centrifuged at 7,379 g for 6 minutes to precipitate the QDs. Once the supernatant was removed, the precipitate was dried at 80 mbar for 10 minutes. After drying, 800 µL of $CHCl_3$ were added followed by mixing by vortexing. To functionalize QDs with different percentages of U_{11}, 10 µL of the previously prepared peptide solutions were added to 100 µL of the QD solution in $CHCl_3$, obtaining a total of 4 samples with different percentages of U_{11}. To make the QDs stable in water, 10 µL of TMAOH was added followed by vortexing. Once the supernatant has been removed, the precipitate is dried at 80 mbar for 20 minutes. Then H_2O is added to reach a final volume of 50 µL for each sample (0.5 µM in number of QDs). For the purification process, the final solutions of 50 µL of QD functionalized in H2O were placed inside centrifugal filters (Amicon 3 KDa) together with 300 µL of H_2O and centrifuged at 14,462 g for 40 minutes. The volume was adapted to the initial 50 µL in order to maintain the concentration at 0.5 µM. For the pancreatic cells labelling, the solution was diluted 25 times with HBSS without red phenol in order to have a QDs concentration of 0.02 µM.

NCs incubation protocol in PANC1 cells (Cell culture prepared by Dr.Hélène Solhi, ImPACcell platform). For the labelling of pancreatic tumor cells with Au NCs, we used a plaque 8 wells (0.2 - 0.5 µL) glass base with 10,000 cells for each well. At the beginning we washed each well 2 times with 500µL of HBSS without phenol red. Then the wells are emptied and 100 µL of the NCs solution (~ 3 µM) or QDs solution (0.02 µM) are quickly added. After an incubation of 1h30 at 37 °C with CO_2 or 4°C without CO_2, the wells are washed 3 times with 500 µL of HBSS without phenol red and imaged with a LEICA SP8 confocal microscope.

Spectrofluorimetry. Photoluminescence measurements were performed on a Jasco FP-8300 spectrofluorometer. The measurements were performed at room temperature on liquid samples. The wavelength resolution of both the excitation and the emission slits was set to 5 nm, the response times was 1 s, the detector sensitivity was set to medium and the scan speed was 500 nm/min.

Transmission Electron Microscopy (TEM) (with the assistance of Dr. Vincent Dorcet, THEMIS platform). Transmission Electron Microscopy analysis were carried out with with JEOL 2100 transmission electron microscope operated at 200 KV supplied with UltraScan 1000XP CCD Camera. For the sample preparation, 300 mesh carbon coated nickel grids were placed for 1 min on top of a 40 µL sample droplet and dried up with paper. Particle sizes and interparticle distances were determined from TEM micrographs using Fiji Software.

UV-visible Absorbance. The UV-visible Absorbance measurements were performed using a ThermoFisher Scientific NanoDrop by placing 2 µL of non-diluted sample over the pedestal.

Absolute Quantum Yield. The absolute quantum yields were measured using a C9920–03 Hamamatsu system by exciting the samples at 410 nm.

Confocal Microscopy (with the assistance of Dr. Stephanie Dutertre and Dr. Xavier Pinson, MRic platform Photonics). Fluorescence confocal images were acquired using a LEICA SP8 confocal microscope equipped with a 63 × oil immersion objective (NA = 1.40). Excitation light was provided with a 405 nm laser diode.

Luminescence Lifetime (with the assistance of Dr. Gregory Taupier, CAPHTER platform). Lifetime measurements were realized using a picosecond laser diode (Jobin Yvon deltadiode, 375 nm) and a Hamamatsu C10910-25 streak camera mounted with a slow single sweep unit.

Luminescence Excitation and Emission 2D maps. Photoluminescence maps were realized using a Horiba spectrofluorometer (Duetta).

Optical Microscopy. Optical miscopy images were acquired using a Zeiss observer Z1 equipped with Filter Set 49 (Hoechst), used to detect the Blue NCs luminescence, and Filter Set 45 (Texas Red) to detect the Red NCs luminescence.

3.5 BIOCOMPATIBILITY STUDY OF NANOCLUSTERS WITH ZEBRAFISH

The Zebrafish (Danio rerio) is a robust and excellent animal model for in vivo imaging[190]and biocompatibility assessments of nanomaterials[191], due to its high optical transparency, similarity to mammals such as mice, rats and humans, as well as its very simple maintenance. These intriguing features of zebrafish can offer direct detection of anomalies or malformations[192].

3.5.1 NANOCLUSTERS INCUBATION WITH ZEBRAFISH EGGS

To evaluate biocompatibility in living organisms from the animal kingdom, NCs with different surface functionalization were incubated in the presence of Zebrafish in two different developmental states: embryo eggs and free-swimming larvae (**Figure 115a**). At the embryonic stage the Zebrafish are protected by a protective membrane called chorion , which presents pores with a diameter of 3 KDa[190]; subsequently the embryos leave the chorion and pass to the free- swimming stage larvae in which they can move freely in space but cannot yet feed from the outside, eating the nourishment present in the yolk sac[190,191].

Incubating C_3E_6D Red NCs at concentrations of about 1.5 µM does not result in embryo mortality for long incubation times (more than 6 hours). The images in **Figure 115** are taken after 2 hours of incubation in presence of the NCs (1.5 µM), without washing the NCs, in order to observe them at different times. Some embryos begin to die after 24 hours of incubation, but still alive embryos remain even after 3 days of incubation with NCs.

A higher mortality was found with the only heated (fluorescent) C_3E_6D ligand since, unlike the Red NCs, it manages to pass the chorion (**Figure 115c**). This happens because the heated C_3E_6D ligand comes from the purification waste of the C_3E_6D Blue NCs (bottom solution) (see chapter on NCs synthesis and characterization), and therefore has a size less than 3KDa which allows it to pass through the pores of the chorion. The Red NCs, on the other hand, having dimensions greater than 3KDa, are unable to overcome the chorion and accumulate on its surface (**Figure 115b**). It is important to remember that the C_3E_6D found on the surface of Red NCs is not fluorescent, as it has not undergone heating processes, in addition, the free C_3E_6D excess was eliminated during the purification process.

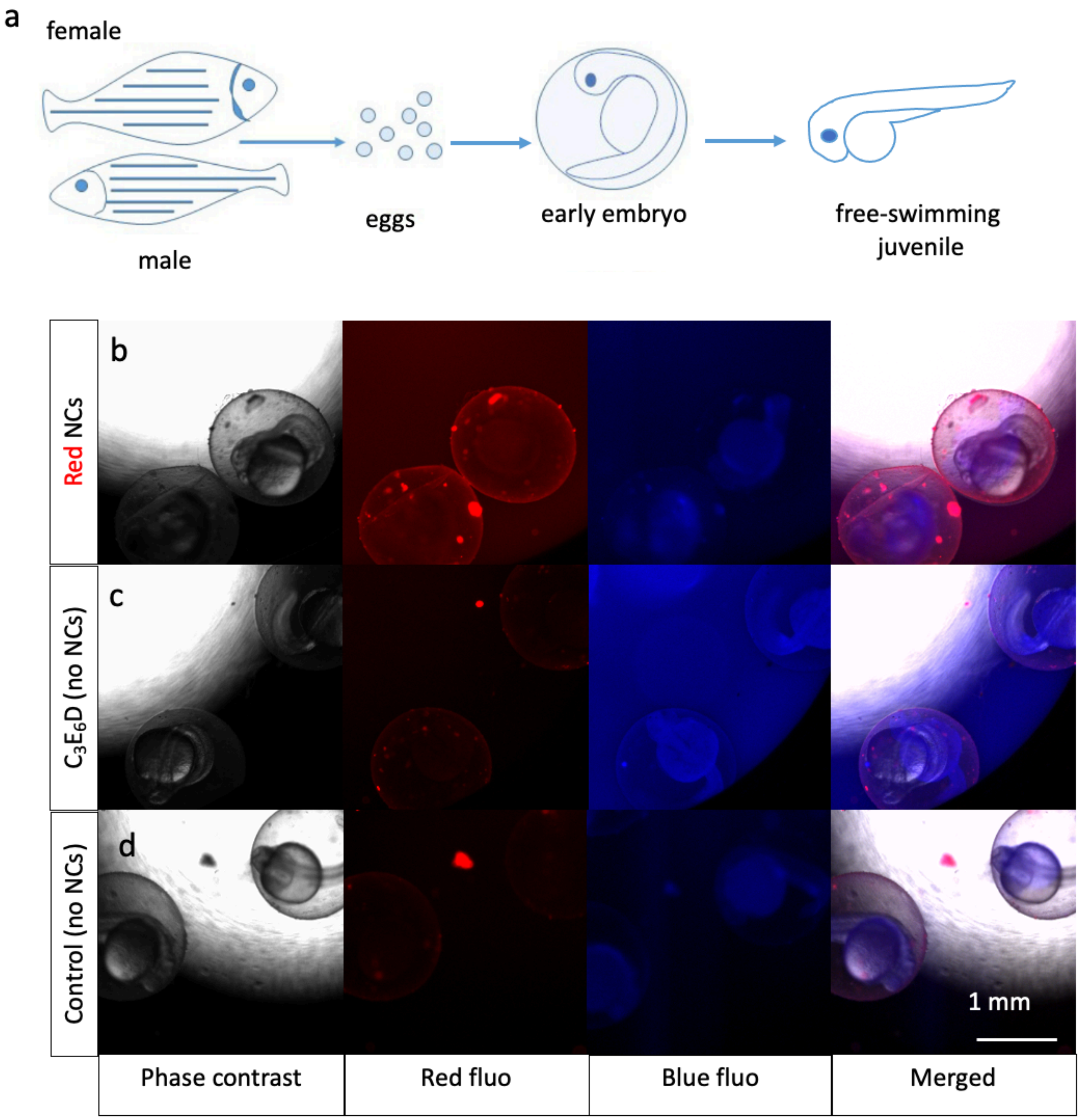

Figure 115. (a) Scheme of zebrafish development stages from eggs to free-swimming larvae. (b,c,d) Light optical microscopy images of Zebrafish embryos incubated with (a) C_3E_6D Red NCs, (b) heated C_3E_6D without NCs and (d) control without NCs observed by phase contrast imaging and by fluorescence excited at 405 nm.

3.5.2 NANOCLUSTERS INCUBATION WITH ZEBRAFISH EMBRYO

A further experiment was conducted by incubating fluorescent C_3E_6D and C_3E_6D Red NCs in the presence of Zebrafish free-swimming larvae (**Figure 116**). In this experiment, the chorion is no longer present, therefore, by removing the protective barrier, the fish are exposed more directly to the ligand and NCs. As shown in **Figure 116a**, the C_3E_6D Red NCs cannot penetrate inside the Zebrafish and this result is the same regardless of the incubation time and concentration of the NCs in the solution; The incubation can last up to 3 days without having toxic or death effects. Carrying out the same experiment in the presence of the fluorescent C_3E_6D, the result is completely different. As shown in **Figure 116 b,c,d** , the fluorescent C_3E_6D seems to penetrate the head initially and then move to the rest of the body. Since the free-swimming larvae cannot feed from the outside yet, a possible route for internalization inside the head could be through the gills. All fish in which the fluorescent C_3E_6D is observed inside the body, die after a maximum of one hour. By decreasing the concentration of the fluorescent C_3E_6D solution, no fluorescence inside the body is observed and the zebrafish remain alive even after days of incubation.

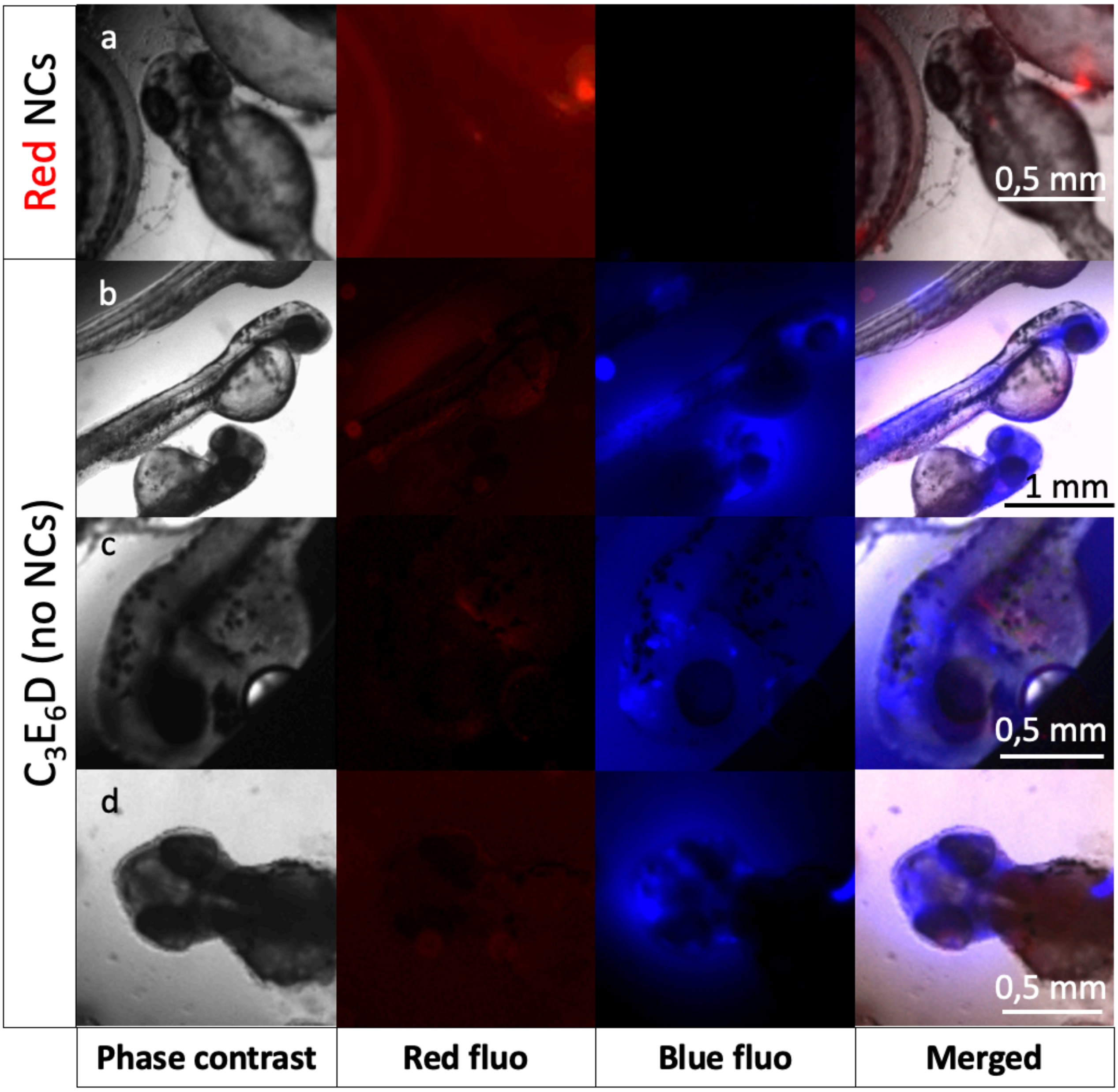

Figure 116. Light optical microscopy images of Zebrafish free-swimming larvae incubated with (a) C_3E_6D Red NCs and (b,c,d) heated C_3E_6D without NCs observed by phase contrast imaging and by fluorescence excited at 385 nm for the blue and at 555 nm for the red after 30 mn incubation.

3.5.3 CONCLUSIONS AND PERSPECTIVES

These studies suggest that it is necessary to well purify the NCs to avoid toxic effects due to the excess ligand, since in all cases of non-purified NCs, there were higher mortality effects in zebrafish. Another strategy would be to synthesize NCs at lower temperatures to avoid alterations of the peptide.

The solution containing Blue NCs purified from excess ligand (upper solution) (see chapter on NCs synthesis and characterization) has not yet been tested in presence of Zebrafish; consequentially further studies are needed to evaluate the influence of Blue NCs on zebrafish at different stages of development, and via different internalization pathways, such as microinjection or, in adult zebrafish, via ingestion. In this way, being transparent fish, it will be possible to follow their biodistribution in luminescence, as well as to study their toxicity.

3.5.4 EXPERIMENTAL SECTION

Incubation of zebrafish eggs with NCs (Zebrafish eggs provided by Dr. Marie Madeleine Gueguen, ImPACcell platform). Initially, using an optical microscope, the eggs still alive were chosen, distinguishable from the inside of a yellow color. In each well, 3 eggs selected in this way were inserted together with 80 µL of marine solution and 80 µL of a 3 µM Red NCs solution (in number of NCs). To test also a different concentration other wells were filled with 133 µL of marine solution and 27 µL of the solution of a 3 µM NCs solution. We immediately moved to the fluorescence light microscope to follow the evolution of egg growth and the influence of NCs. Eggs were observed daily for the next 3 days.

Incubation of Zebrafish embryos with NCs (Zebrafish embryos provided by Dr. Marie Madeleine Gueguen, ImPACcell platform). In each well, 5 selected Zebrafish embryos already released from the chorion were inserted together with 187 µL of marine solution and 63 µL of a 3 µM Red NCs solution (in number of NCs). To test also a different concentration other wells were filled with 208 µL of marine solution and 42 µL of 3 µM NCs solution. We immediately underwent a fluorescence light microscope to follow the evolution of the influence of NCs on Zebrafish embryos. Embryos were observed daily for the next 3 days.

4 CONCLUSIONS

During my PhD work we synthesize, fully characterize and functionalize two types of luminescent nanoparticles that can be used as probes for biological applications: lanthanide doped Y_2O_3 NPs and gold NCs.

One of the objectives set during my PhD was the targeting of exosomes and, given their small size, it was initially thought to use NCs for this purpose, given the high biocompatibility and ultra-small size. Consequently, we have focused on these very promising nanoparticles, but in the future similar studies could also be carried out for lanthanide doped Y_2O_3 NPs, known to be excellent probes for cathodoluminescence imaging, a technique that cannot be used on NCs due to their luminescence which is extinguished under electron beam.

After studying the interaction of NCs with synthetic vesicles (liposomes) through strong electrostatic interaction, the high biocompatibility of NCs with biological membranes was noted since, in the case in which the NCs do not saturate the surface, there is no rupture of the membranes and not even the thickness is changed since they are positioned between the polar heads of the membrane phospholipids. Furthermore, both Blue and Red NCs have been efficiently encapsulated within synthetic liposomes of different sizes (SUVs, LUVs and GUVs) using innovative protocols with a high encapsulation yield (about 40%).

Before moving on to exosomes labeling by NCs, the entire population of extracellular (EVs) vesicles present within the follicular fluid of healthy and pathological patients was analyzed. In addition to implementing a method for the separation and study of the different families of EVs within the FF of healthy subjects. Correlations were found between the morphology of the EVs and the presence of pathologies such as OF (Ovarian Failure) and PECOS (Polycystic ovary syndrome). More precisely, the EVs coming from subjects with pathologies seem to be more polydisperse in size than the control and with more deformed shapes due to the high presence of oval vesicles and microtubules. Furthermore, the Small RNA content of the EVs and the number of proteins within the entire FF was analyzed by always comparing healthy and pathological FF: the EVs of the controls seem to contain more Small RNA than the pathological EVs while, considering the FF as a whole, there seem to be more proteins than the control in the case of the PCOS EVs and less in the case of the OF EVs. Subsequently, the EVs were incubated with the NCs functionalized with antiCD81, obtaining CryoTEM images that give encouraging results on the possible labeling of the Small EVs membranes by the NCs, although further tests are necessary.

Subsequently, to study the interaction between NCs and cells, more complex systems than vesicles, the NCs were functionalized with a recognition peptide called $C_3E_6U_{11}$ capable of selectively binding to the membrane receptor uPar overexpressed by pancreatic cancer cells (PANC1). The results of this interaction show that functionalized NCs can efficiently label the cell membrane and penetrate not only inside the cell but also inside the nucleus. The presence of NCs inside the nucleus was found only in the presence of the $C_3E_6U_{11}$ peptide; this result, together with studies conducted at 4°C to block the mechanisms of endocytosis, lead to the conclusion that NCs are most likely internalized through the mechanism of receptor-mediated endocytosis. It has also been found that the QDs, although presenting the same surface functionalization, are not only never found inside the nucleus, but they are also unable to overcome the cell membrane, positioning themselves only on the external part.

Finally, it was decided to test the NCs on entire living organisms of the animal world (Zebrafish). Studies with Zebrafish larvae did not lead to any internalization in fish in the case of the red NCs, consequently further studies on more adult fish able to feed from the external environment, or micro-injection experiments are needed to evaluate their actual toxicity.

Ultimately, through the one pot synthesis shown above, it is possible to synthesize functionalized NCs in a few steps and with a green synthesis, in order to have a luminescent probe for biosensing and bioimaging. In addition, these NCs are attractive candidates for drug delivery and to enhance the effects of radiotherapy thanks to the high Z number of gold. For these reasons and for their high biocompatibility, NCs could represent a multivalent luminescent platform for theragnostic applications in biology and medicine.

5 LIST OF PUBLICATIONS

- European Patent : Methods for the synthesis of bioactivated metal nanocluster and their medical application.
  EP3 967 330 A1
  Date of publication: 16.03.2022
- Luminescent Gold Nanoclusters Interacting with Synthetic and Biological Vesicles.
  Regina M. Chiechio et al. The Journal of Physical Chemistry Letters – 2022
- Encapsulation of Luminescent Gold Nanoclusters into Synthetic Vesicles
  Regina M. Chiechio et al. Nanomaterials – 2022
- Diversity of Extracellular Vesicles in Human Follicular Fluid: Morphological Analysis and Quantification.
  AS. Neyroud, Regina M. Chiechio et al. Int. J. Mol. Sci – 2022
- Extra-cellular vesicles of the male genital tract: new actors in male fertility?
  AS. Neyroud, Regina M. Chiechio et al. Basic Clin. Androl.– 2021
- Active U11 Peptide Luminescent Gold Nanoclusters for Tumor Cell targeting.
  Regina M. Chiechio et al. ACS Applied Nano Materials – Submitted.
- Er:Y2O3 and Nd: Y2O3 Nanoparticles: Synthesis, Pegylation, Characterization and Study of their Luminescence Properties.
  Regina M. Chiechio et al. Chemosensors – Submitted.
- Follicular Fluid related Extracellular Vesicles in Ovarian Diseases: Morphological Analysis and Quantification
  Regina M. Chiechio et al. – in course of editing.
- Follicular Fluid related Extracellular Vesicles in Ovarian Diseases: miRNA Analysis
  Regina M. Chiechio et al. – in course of editing.

6 ANNEXES

6.1 LIGANDS CHEMICAL STRUCTURE

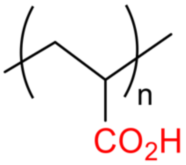

Figure 117. Chemical structure of PAAc.

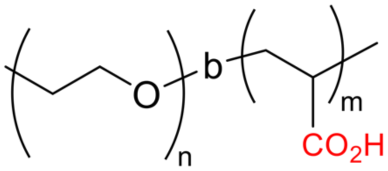

Figure 118. Chemical structure of PEG-b-PAAc.

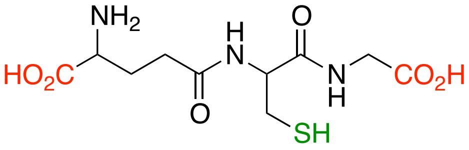

Figure 119. Chemical structure of GSH.

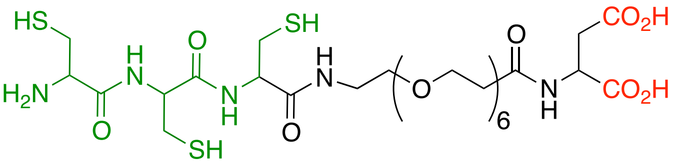

Figure 120. Chemical structure of C_3E_6D.

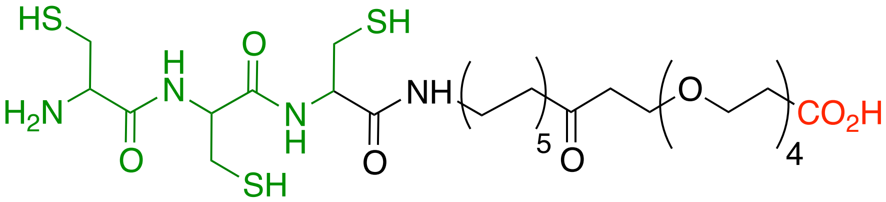

Figure 121. Chemical structure of C_5PEG_4.

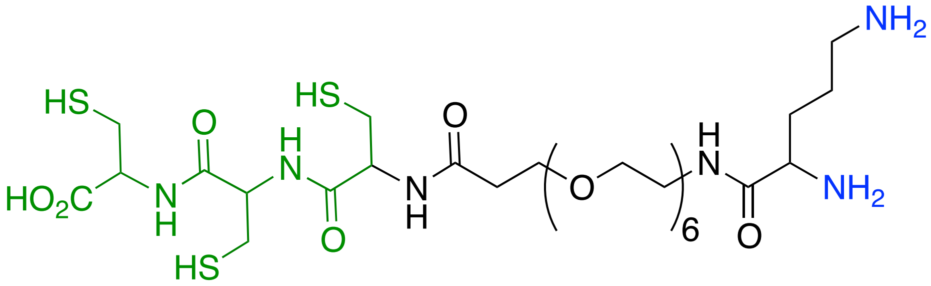

Figure 122. Chemical structure of K5-C-NH2.

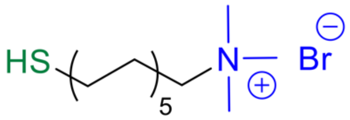

Figure 123. Chemical structure of MUTAB.

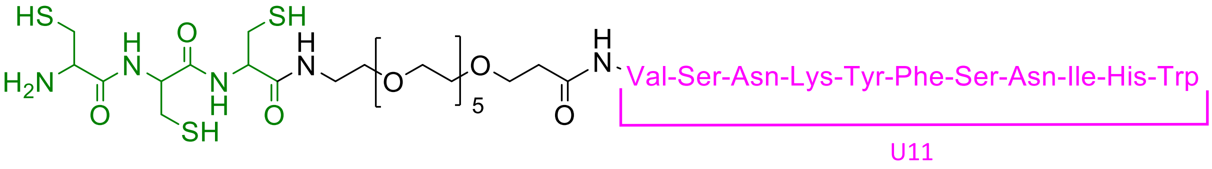

Figure 124. Chemical structure of $C_3E_6U_{11}$.

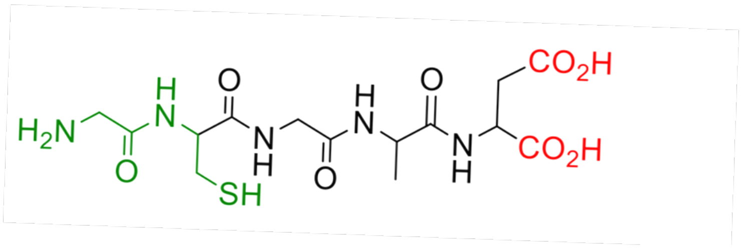

Figure 125. Chemical structure of peptide “C Short”.

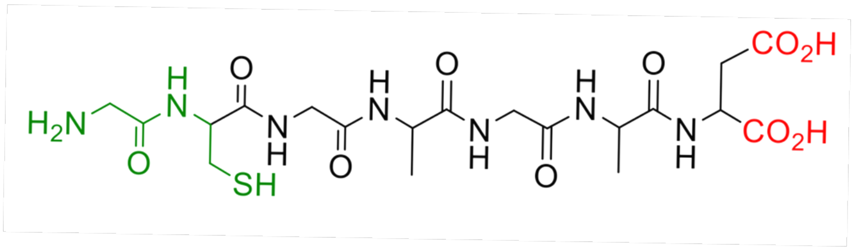

Figure 126. Chemical structure of peptide “C Long”.

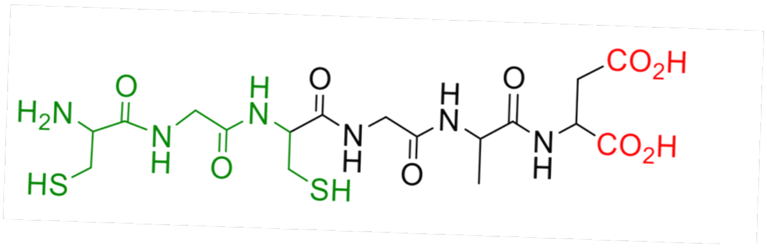

Figure 127. Chemical structure of peptide “CC Short”.

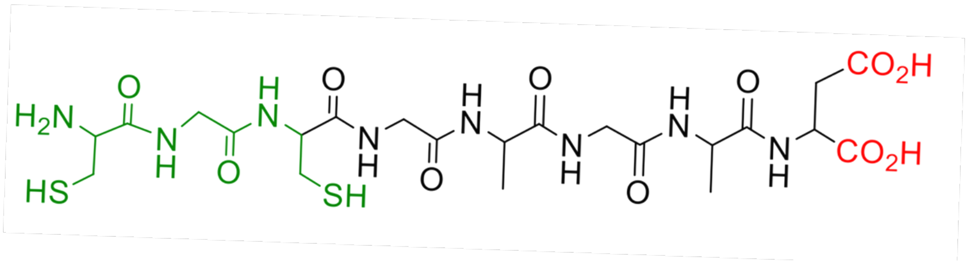

Figure 128. Chemical structure of peptide “CC Long”.

6.2 PREPARATION OF PHOSPHOLIPIDIC VESICLES

Lipids are molecules composed of a hydrophobic part, mainly consisting of carbon chains, and a hydrophilic polar head. The molecules that have both a hydrophilic and hydrophobic part are called amphiphilic, and this characteristic generates self-assembly in aqueous solution. Depending on the structure of the polar head or the properties of the chains (fluidity and volume), lipids assemble into various forms: spherical, cylindrical, double planar micelles, floating vesicles, etc. In particular, the vesicles, also called liposomes (**Figure 129a**), are lipid bilayers with the shape of a sphere suspended in an aqueous solution.

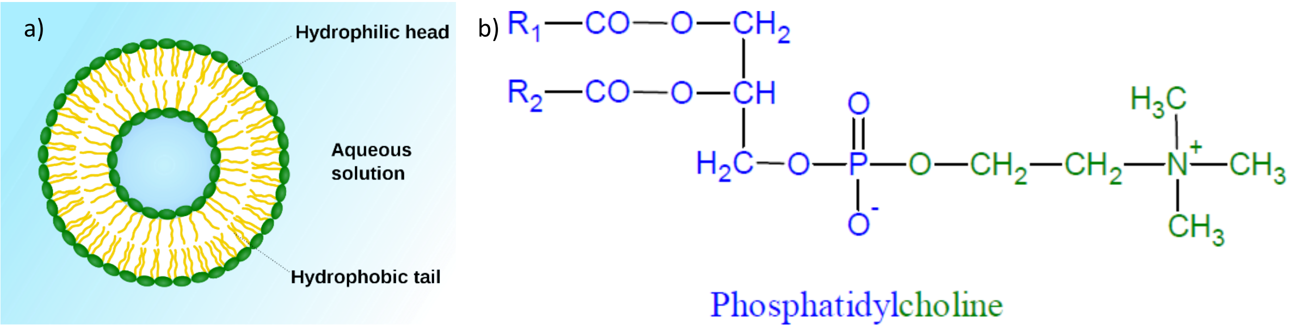

Figure 129. a) Diagram of a lipid vesicle and b) structure of phosphatidylcholine.

These bilayers are found in the biological cell of which they make up the membrane, together with proteins. Therefore, vesicles are simplified membrane models and are useful for studying possible interactions between particles and cells.

For the formation of the synthetic vesicles (liposomes) present in this work, phosphatidylcholine (PC) lipids were used (**Figure 129b**) and different types of vesicles were produced to verify the impact of NCs on artificial membranes of different sizes (**Figure 130**).

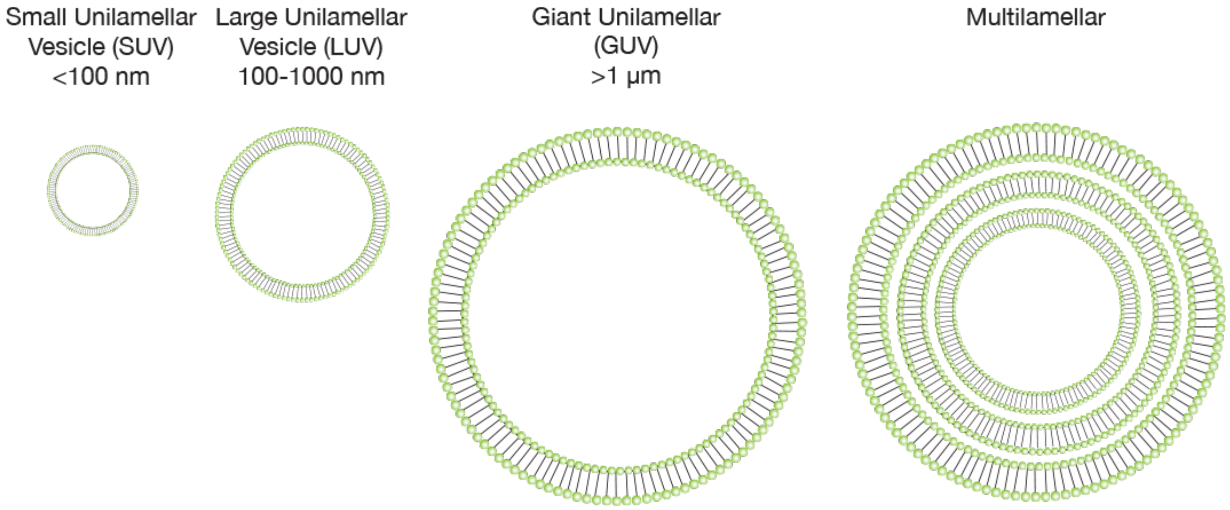

Figure 130. Dimensions different type of phospholipidic vesicles (SUVs, LUVs, and GUVs).

6.2.1 PROTOCOL SUVS SYNTHESIS (SMALL UNILAMELLAR VESICLES)

The lipid solution is initially produced using 20 mg of DMPC lipids and 1.74 mg of DMTAP lipids which are dissolved in 2 mL of dichloromethane. This solution is introduced into a 50 mL flask with a sufficiently large opening to be able to introduce the sonicator later. By means of a rotary evaporator (Buchi Heating Bath) the dichloromethane is evaporated (40°C, 500mbar) and subsequently an aqueous solution of sucrose (2mL, 50mM) is added to reach a total lipid concentration of 10mg/mL.

The solution obtained is sonicated using an ultrasonic titanium probe (Misonix Incorporated) set at full power for 30 minutes. The solution is then collected from the flask and placed in Eppendorf to centrifuge it at 7500 rcf (Relative Centrifugal Force or G-force) for 10 minutes. At the bottom of the Eppendorf, a small black precipitate corresponding to the titanium small pieces of the sonicator appears. The supernatant containing the SUVs is ready to be used or stored in the fridge for future use.

6.2.2 PROTOCOL LUVS SYNTHESIS (LARGE UNILAMELLAR VESICLES)

Initially, the (1:9 mol %) lipid mixture is produced using DOPC (1mL at 10 mg/mL dichloromethane) and DOTAP (98.5µL, 10 mg/mL dichloromethane). The lipid solutions thus produced are placed in a 50 mL flask which is placed in a rotary evaporator (Büchi Heating Bath) to evaporate the dichloromethane (40°C, 500mbar). In this way a lipid film is formed on the vial walls.

Then an aqueous solution of sucrose (1.2mL, 50mM) is added. The obtained mixture is subjected to 7-10 freezing/thawing cycles through the passage between the 40°C bath of the evaporator and the liquid nitrogen. This step allows to detach the lipid film from the wall of the vial and results in the formation of MLV (MultiLamellar Vesicles). To generate the LUVs, the solution must then undergo 10 extrusion cycles at 15 mbar, conducted through a Thermobarrel extruder Extruder Lipex Membrane apparatus. In this way the MLVs are forced to pass through a 0.1 µm filter (Millipore membrane) under pressure, and in this way each passage will allow to eliminate the outer layers of the MLVs and reduce them in size.

6.2.3 Protocol GUVs synthesis (Giant Unilamellar Vesicles)

The GUV training protocol follows a procedure described in the literature (**Figure 131**)[123].

Preparation of solutions.

Initially 3 solutions are prepared:

1. inner solution (500 mM sucrose);
2. bottom solution (500mM glucose);
3. lipidic solution.

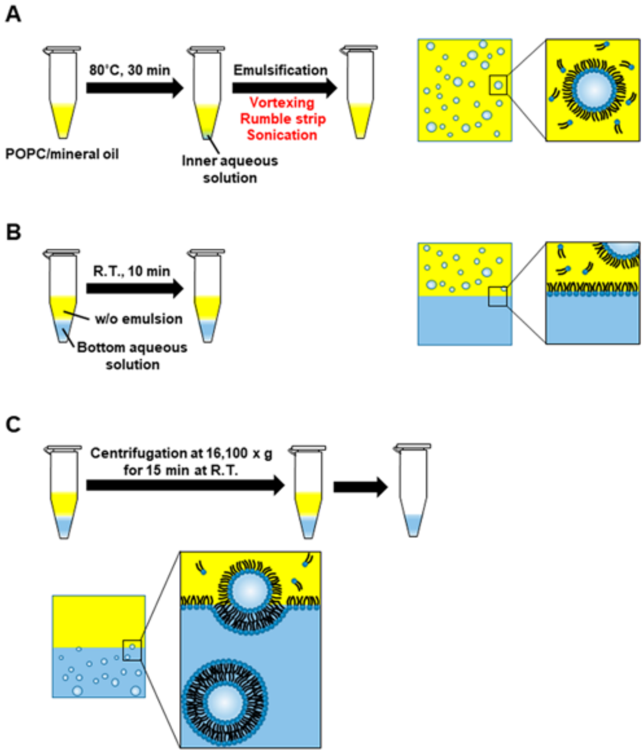

Figure 131. Scheme for GUVs production protocol.

The lipid solution (3) was prepared using zwitterionic 100 %DOPC lipid or a mixture of DOPC and 5 mol % DOTAP positive lipid. In both cases the lipids are dissolved in the chloroform to give a final concentration of 10 mg/mL. Then 20 µL of the lipid solution in chloroform is then added to 1800 µL of paraffin oil in a 5 mL flask, and the solution is heated to 80 ° C for 30 min without a lid. In this way the chloroform evaporates and causes a solution of lipids to be created in the oil. To make sure that all the chloroform has evaporated, the solutions are placed inside a desiccator for 20 min. The lipid solution (3) is ready.

GUV Preparation:

50 µL of (1) + 400 µL of (3) are placed in an Eppendorf and vortexed for 40 s to form a water-in-oil emulsion (w/o). In a second Eppendorf 200 µL of (2) are introduced onto which the newly formed emulsion is gently added. Wait 10 minutes and proceed to centrifuge the solutions for 15 minutes at 16000 rcf. Once the centrifuge is finished, the stock is transferred to another eppendorf, redispersed in 300 µL of solution (2) and further centrifuged at 16000 rcf for 5 minutes. At the end of the centrifuge, the bottom is removed again, and the GUVs are ready to be stored in the fridge.

To encapsulate NCs the procedure is slightly different. The 50 µL of inner solution will be represented by 25 µL of sucrose solution (1M) + 25 µL of NCs solution. It is also important that for encapsulations the GUVs are not subjected to centrifugation, since by presenting NCs inside, the centrifuge leads to the rupture of the vesicles. The passage of the centrifuge is therefore replaced by an incubation during the night, which allows the GUVs to form, settle on the bottom and be collected the next day.

6.3 POST SYNTHESIS TECHNIQUES

6.3.1 SIZE EXCLUSION CHROMATOGRAPHY

The columns (NAP) was used in the laboratory as a post synthesis technique to remove excess ligand. These columns use the principle of gel filtration chromatography. This principle is based on the separation of particles based on their shape and size. In this technique the stationary phase is composed of a hydrated material containing pores that can only be crossed with molecules having certain dimensions. Molecules that are too large will not be able to enter the pores and consequently will be excluded from the volume of liquid retained inside; they will quickly cross the column and exit first.

Filtration procedure via NAP:

- Initially it is necessary to equilibrate the column with the solvent of the solution to be filtered (in our case water). To do this, open the cap positioned on the column, wait for all the liquid contained inside to have dropped and proceed to refill it with distilled water. The water is expected to go down and this step is repeated 3 times.
- When all the water has gone down, the solution to be filtered is inserted, and all the volume inserted is expected to be absorbed by the gel.
- Following the quantities indicated in the instructions (which vary according to the type of column and the amount of solution to be filtered), a precise amount of water is added to allow the solution trapped in the gel to descend and be withdrawn.

6.3.2 ULTRAFILTRATION

The centrifuge (**Figure 132a**) is an apparatus used to accelerate the separation between bodies having different densities using centrifugal force.

In the case of the purification of the solutions, the centrifuge allows to expel a part of the water of the sample together with the excess of ligands, since the dimensions of the ligands are smaller than those of the pores. On the contrary, the NCs, having larger dimensions, remain within the solution.

Filtration procedure via Amicon:

- insert 0.5 mL of solution into the Amicon Ultracel 3K (**Figure 132b**);
- centrifuge at 10,000 rpm for 3 minutes;
- add water to the Amicon until the volume of 0.5 mL is reached again and repeat the centrifuge;

- repeat the operation 4 times.

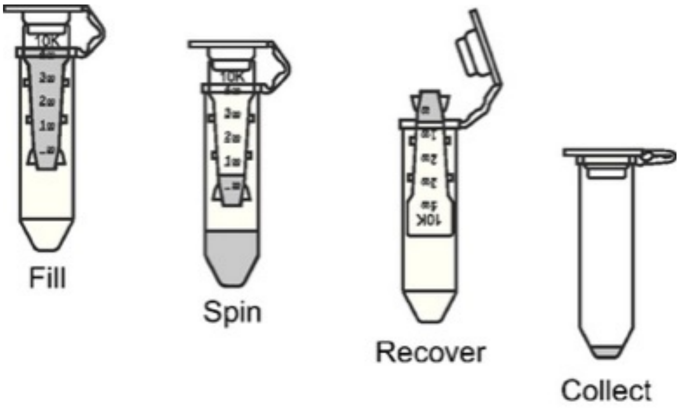

Figure 132. Procedure for using filters Amicons Ultracel.

6.3.3 FREEZE-DRYING

The freeze dryer is the tool used to remove the water from the solutions and, through the sublimation process, to obtain a product in powder.

Basically, a freeze dryer is composed of:

- a support system in which it is possible to position the solutions, and capable of supporting high vacuum values;
- a chiller capable of lowering the temperature down to -45°C;
- a vacuum pump, capable of developing a vacuum of at least 0.01 mbar;
- freeze-drying, in fact, exploits the low temperature and the vacuum to sublimate the frozen water.

Freeze-drying procedure:

- the flask with the solution inside is immersed in liquid nitrogen until completely frozen.
- taking care not to touch the flask to prevent it from thawing, attach the flask to one arm of the freeze dryer.
- wait for about 24 hours to be sure all the water is sublimated.
- remove the flask and store the powder produced in the fridge.

6.4 CHARACTERIZATION TECHNIQUES

6.4.1 UV -VIS SPECTROSCOPY

The UV-visible spectroscopy or UV-visible spectroscopy is a spectroscopic technique in which photons at various wavelengths that are collected after passing through the sample: in this way a spectrum of transmitted photons is obtained which allows to trace to the spectrum of photons absorbed with the help of a reference sample. The spectrum is often presented as the absorbance as a function of wavelength.

The substrates analyzed in our case are in solution and measurements were made using the Nanodrop This instrument shows significant advantages over a traditional UV-VIS spectrometer:

- it is possible to use very small quantities as 2 of solution are enough µL;
- sample dilution is not necessary as it is able to measure high absorbance intensities;
- a container is not needed;
- the measurement is very fast and allows to measure the absorbance of various solutions in a row while maintaining the same reference spectrum measured initially;
- it is very accurate (± 1nm) and wavelengths range from 190nm to 750nm.

With this instrument, however, it is only possible to measure samples in aqueous solutions.

6.4.2 FLUORIMETRY

Fluorescence is a spectroscopy technique that allows you to analyze the fluorescence of a sample, in our case of a solution. A beam of photons at a precise wavelength will excite the electrons of the sample, which when de-energized will emit photons at different wavelengths.

The emission spectra are obtained by measuring the number of fluorescence photons emitted at the various wavelengths while the photoexcitation spectra are obtained by exciting at various wavelengths but collecting the photons emitted only at a precise wavelength.

The fluorometer used is the Fluorolog-3TM model (FL3-22, Horiba Jobin Yvon, Japan), based on fluororenceTM software. The source is a 450W xenon lamp, the intensity is collected at 90 ° to the source (right angle mode).

It is possible to vary the width of the slits both in excitation and in emission (from 1 to 5 nm). For the processed samples the slit width was set at 5 nm and the solutions were excited at 365 nm in most cases.

6.4.3 ELECTROPHORESE

Electrophoresis makes it possible to differentiate charged species, and in particular proteins, after their displacement in an electric field.

The electrophoresis technique is based on the displacement of charged species (positively or negatively) under the effect of an electric field. Due to their characteristics (charge, size and shape), the species will have different migration rates, so they will separate from each other. Positive species migrate towards the cathode (-) and negative ones towards the anode (+).

Sample preparation:

5 µL of water + 10 µL of NC + 2 µL of glycerol (30%).

Gel preparation:

- dissolve 0.5 g of agarose in 100 mL of buffer (0.5%), in our case a borate buffer (10 mM, pH = 8, I = 10mM).
- heat the solution at 95 ° for about 15min, until the agarose is completely dissolved in the buffer.
- for 15 µL of solution into a mold topped with a comb to create the wells.
- leave to cool for 15 minutes at room temperature and another 15 minutes in the fridge, in this way the gel will be cross-linked and usable
- place the gel in the apparatus and immerse it with 350 ml of buffer.

Migration:

Gel electrophoresis migrations are performed on a XLUltra ™ V-2 Gel (Labnet International, USA).

A volume of 15 µL of sample is placed in each well. The migration time is variable but is generally a minimum of 20 minutes with a constant voltage of 50 V (distance between electrodes: 15 cm).

Reading:

After migration, the gel is extracted and observed in an imager ImageQuant 350 (GE Healtcare, USA) with UV or white light excitation. The IQuant Capture 350 software enables the acquisition and processing of the resulting images.

6.4.4 DYNAMIC LIGHT SCATTERING (DLS)

The Dynamic Light Scattering is a spectroscopic analysis technique that allows to know the size of particles in solution from about 1 to 500 nm in diameter.

Since the particles are smaller than the wavelength of the laser hitting them, the light undergoes an elastic (Rayleigh) diffusion.

The intensity of the light scattered by the particles is collected over time at a precise angle (typically 90°) (**Figure 133**). Particles in a liquid undergo Brownian motion due to thermal agitation, therefore, the distance between the particles changes constantly.

This causes constructive or destructive interference from scattered light and the total measured intensity contains information on the speed of movement of the particles, which is related to their size (**Figure 134**).

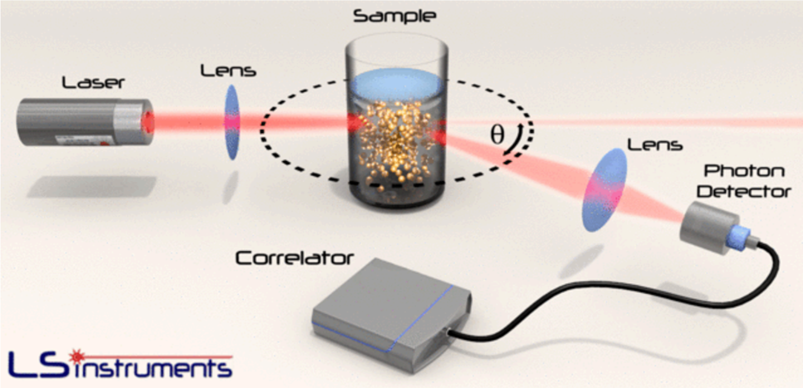

Figure 133. Operational scheme of DLS.

This technique is sensitive to the diffuse intensity of all components of the sample; it is therefore a global measure that allows to characterize the monodispersity of a sample.

The counter- ions adsorbed on their surface also contribute to the diffusion of the particles: the technique therefore allows to measure the "hydrodynamic diameter".

The hydrodynamic diameter (**Figure 135**) of a particle in solution includes the physical diameter of the particle and several layers of hydration. Two layers are distinguished in contact with the particle: the Stern layer where the counter - ions adsorb to the surface and a diffuse layer in which the counter- ions are more concentrated than in solution.

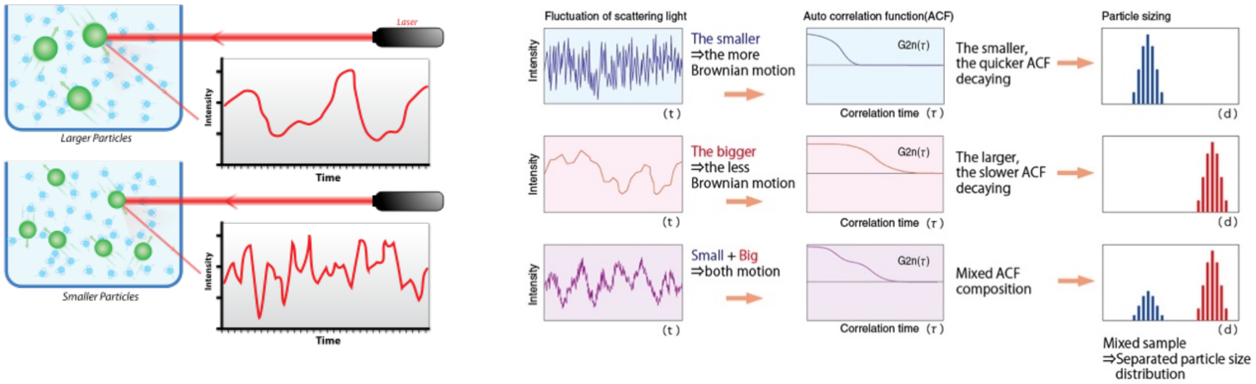

Figure 134. Method used to find particles size by starting from the speed of their Brownian movement in solution.

With the same device (**Figure 133**) For it is also possible to make a Zetametry measurement, ie to measure the average surface charge of the nanoparticles through their electrophoretic mobility. The results are complementary to the migrations obtained in electrophoresis.

6.4.5 ZETAMETRY

The Zetametry allows to measure the Zeta potential of a particle immersed in a solution, that is its average surface charge.

Under the effect of the electric field created by two electrodes (+) and (-), these particles will migrate in one direction or another, according to the principle of electrophoresis.

To measure this potential, laser Doppler electrophoresis is used: an electric field is applied to a solution to make the contained particles move at a speed related to their zeta potential. This velocity is measured using a patented laser interferometry method called M3-PALS (Phase Analysis Light Scattering). Through this technology it is possible to calculate the electrophoretic mobility and from it the distribution of the Zeta potential.

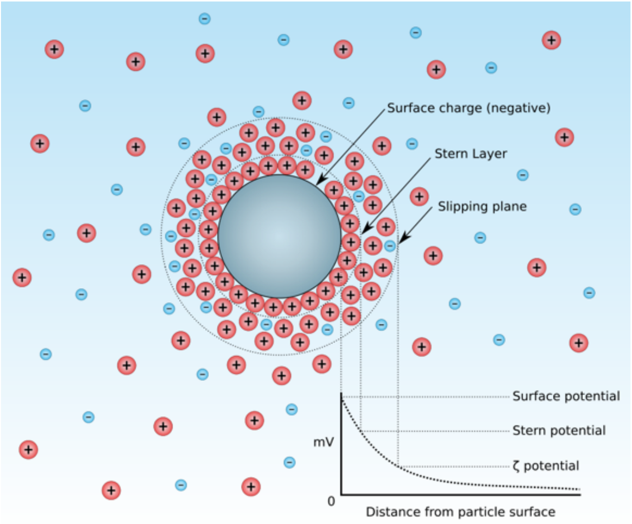

Figure 135. Hydrodynamic diameter and zeta potential.

6.4.6 OPTICAL MICROSCOPE

The microscope we use is a confocal phase contrast microscope, which can also be used for fluorescence microscopy.

When such a microscope is used in the phase contrast mode, it transforms the differences in refractive index into difference in contrast. However, this technique can only be used with thin samples

Since it is a confocal microscope, it allows a cross-sectional image to be formed without being disturbed by light outside the focal plane; it is thus possible to have a clear image of the objects in three dimensions.

To allow its use also in fluorescence mode, it is equipped with 3 lasers that allow to excite the sample with fluorescent properties with three different wavelengths.

6.4.7 TRANSMISSION ELECTRON MICROSCOPY (TEM)

The Transmission Electron Microscopy is a microscopy technique in which an electron beam passes through a very thin sample. The interaction effects between the electrons and the sample give rise to an image.

The technique consists in placing a sufficiently thin sample under an electron beam and, through a system of magnetic lenses, projecting the electronic image of the sample on a phosphorescent screen which transforms it into an optical image. For crystalline samples, another way to use is to visualize the sample diffraction pattern (HR-TEM).

Its theoretical resolution, linked to the wavelength of the electrons, can reach 0.08 nanometers, but it is very limited by the aberrations due to magnetic lenses.

Measurements are carried out at ultra-high vacuum (10^{-6} mbar to 10^{-10} mbar).

This microscope has different imaging modalities, those used during the stage are the following:

- Picture mode

The electron beam interacts with the sample based on the thickness, density or chemical nature of the sample, which leads to the formation of a contrast image in the image plane.

- Diffraction mode

This mode uses the wave behavior of electrons. When the ray passes through a crystallographic sample, it gives rise to the phenomenon of diffraction. The beam is diffracted and then recombined on the image plane thanks to the magnetic lenses and gives us information on the crystallinity of the sample.

- HR-TEM

High-resolution transmission electron microscopy (HRTEM) is a transmission electron microscope (TEM) imaging modality that enables direct imaging of the atomic structure of the sample. HRTEM is a powerful tool for studying the properties of materials on the atomic scale.

The contrast of an HRTEM image derives from the interference in the image plane of the electronic wave with itself, which following the interaction with the sample is modified in phase and intensity. Each imaging electron independently interacts with the sample. The wave of an electron can be approximated as a plane wave incident on the surface of the sample. As it enters the sample, it is attracted to the positive atomic potentials of the atomic nuclei and the atomic columns of the crystallographic lattice. The interaction between the electron wave and the columns of atoms leads to Bragg diffraction.

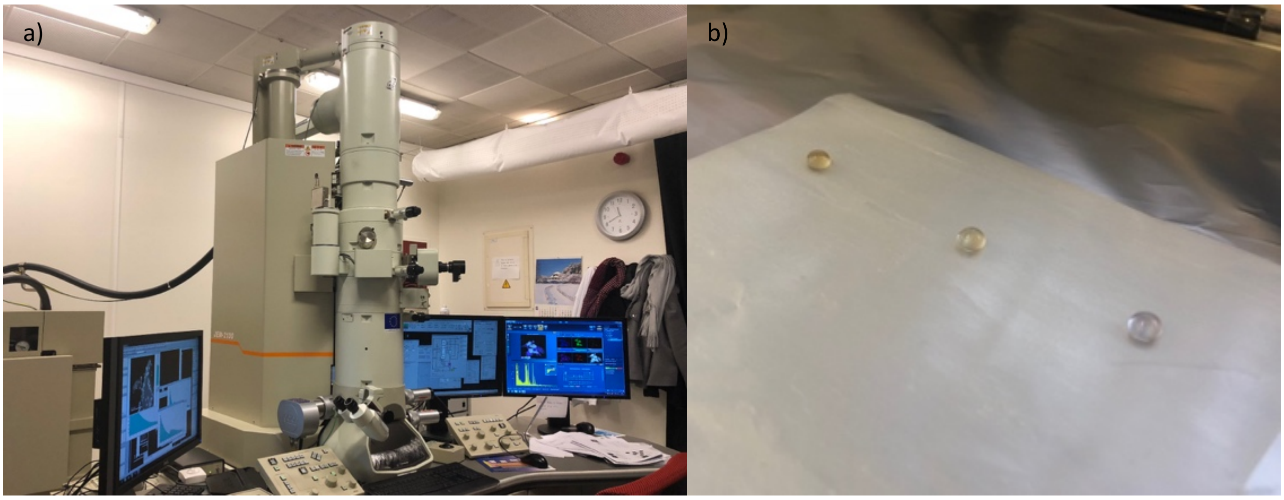

Figure 136. a) TEM microscope at the University of Rennes 1 and b) drop of solutions to prepare TEM grids.

It is important to realize that the recorded image is NOT a direct representation of the crystallographic structure of the samples. For example, the representation of a column of atoms does not indicate that the position of the atoms that compose it is exactly that shown in the image. Our samples were taken from a TEM (JEM 1400 JEOL, 120 k V) equipped with an ORIUS 1000 camera, at the University of Rennes 1 (**Figure 136a**) (TEM platform Mric-UMS 3480-Biosit-University of Rennes1).

The images were taken in the HR-TEM mode to allow the imaging of objects of the order of a few nanometers, and to be able to verify their crystallinity.

Having to analyze solutions, the samples were deposited and left to dry on suitable copper grids according to the following procedure:

- arrange an aluminum foil with a parafilm sheet on top;
- place a drop of 40 µl for each sample on the parafilm (**Figure 136b**);
- place a grid on each drop, taking care to put the functional part of the grid in contact with the sample, and wait 3 minutes;
- pick up the grid with tweezers and absorb excess product with a paper towel before putting the grid back into the case;
- allow the sample to dry for about 24 hours before looking at it under the microscope.

6.4.8 SMALL-ANGLE X-RAY SCATTERING (SAXS)

Small-angle X-ray scattering (**Figure 137a**) is an experimental technique for studying the structural properties of materials on a scale from 1 to 100 nm.

The method is accurate, non-destructive and usually requires only a minimum of sample preparation.

This technique is based on the elastic interaction of photons with electronic clouds.

The wavelengths of X-rays are between 10^{-8} and 10^{-12} meters, which is of the same order of magnitude as the interatomic distances, giving rise to the phenomenon of diffraction.

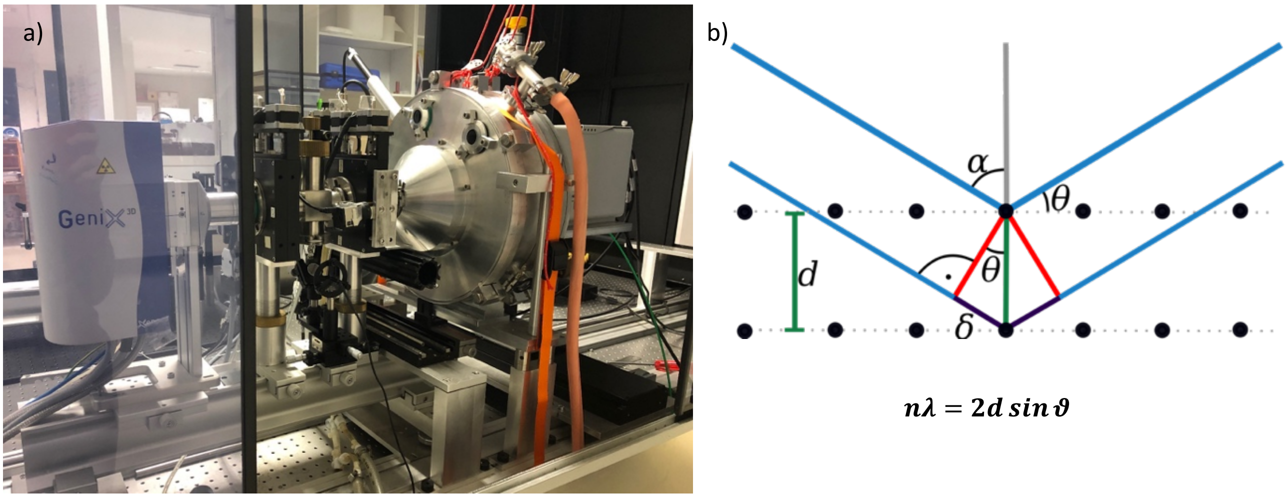

Figure 137. a) saxs at the University of Rennes 1. b) bragg's law**.**

Bragg's law (**Figure 137b**) indicates that the constructive interference of the reflected rays is obtained at the diffraction angle (Θ) only if the path difference between the reflected beams is an integer (n) of the wavelength (λ) of the incident beam, and this happens only at a certain distance

(d) between the crystalline planes. Therefore, by sending an X-ray beam at the same wavelength, each angle corresponds to a precise distance.

Having to detect small distances (of the order of ångströms), the diffraction angles must also be small (of the order of one hundredth of a degree), hence the name of the technique.

6.4.9 MASS SPECTROSCOPY (ICP-MS)

Mass spectrometry is an analysis technique capable of identifying the molecules of interest by measuring their mass and characterizing their chemical structure. Its principle lies in the separation in the gas phase of the charged molecules (ions) based on their mass / charge ratio (m / z).

Inductively coupled plasma mass spectrometry, denoted by ICP- MS (Inductively Coupled Plasma Mass Spectrometry), is a technique based on the use of mass spectrometry combined with inductively coupled plasma. It is a very sensitive technique and capable of determining different substances present in concentrations of up to about one part per billion (ppb). It exploits the use of an ICP plasma torch to produce the ionization and a mass spectrometer for the separation and detection of the produced ions. With the ICP-MS it is also possible to perform isotope analysis.

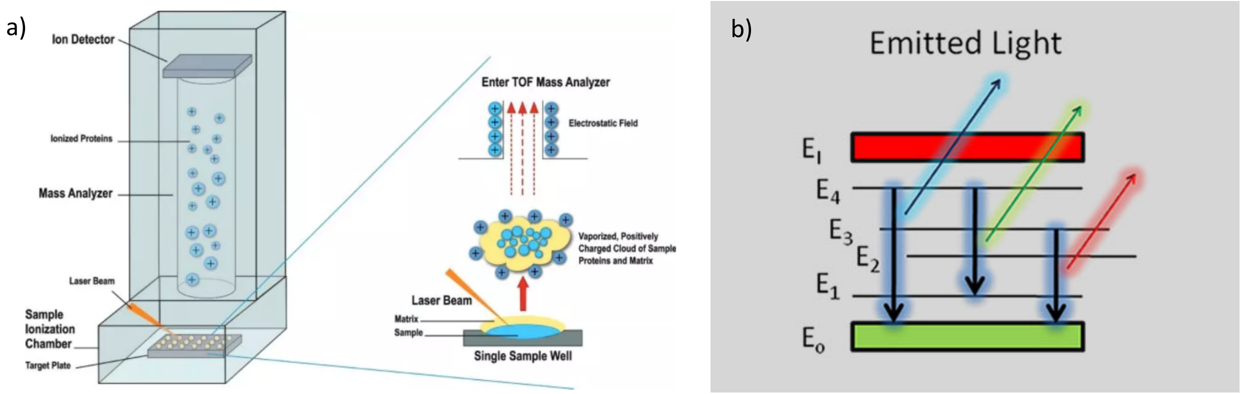

Figure 138. a) ICP-MS structure. b) Radiative de-excitation scheme.

6.4.10 FOURIER TRANSFORM INFRARED SPECTROSCOPY (FTIR)

Fourier Transform Infrared Spectroscopy (FTIR) is a highly effective spectroscopic technique for studying and understanding surface chemistry and chemistry in various types of materials. It is carried out using an interferometer, which allows the scanning of all the frequencies present in the IR radiation generated by the source. Scanning is possible thanks to a moving mirror which, when moving, introduces a difference in the optical path, which causes constructive or destructive interference with the ray reflected from a fixed mirror (**Figure 139a**). In this way an interferogram is obtained which shows the intensity of the signal as a function of time; through the Fourier transform of the interferogram we obtain the infrared spectrum, that is the intensity as a function of the frequency.

Therefore, information on the structure of a molecule can be readily obtained via the molecular vibrational spectrum. FT-IR has a much better signal / noise ratio than traditional infrared spectroscopy, thus ensuring higher performance, as well as significantly reduced analysis times.

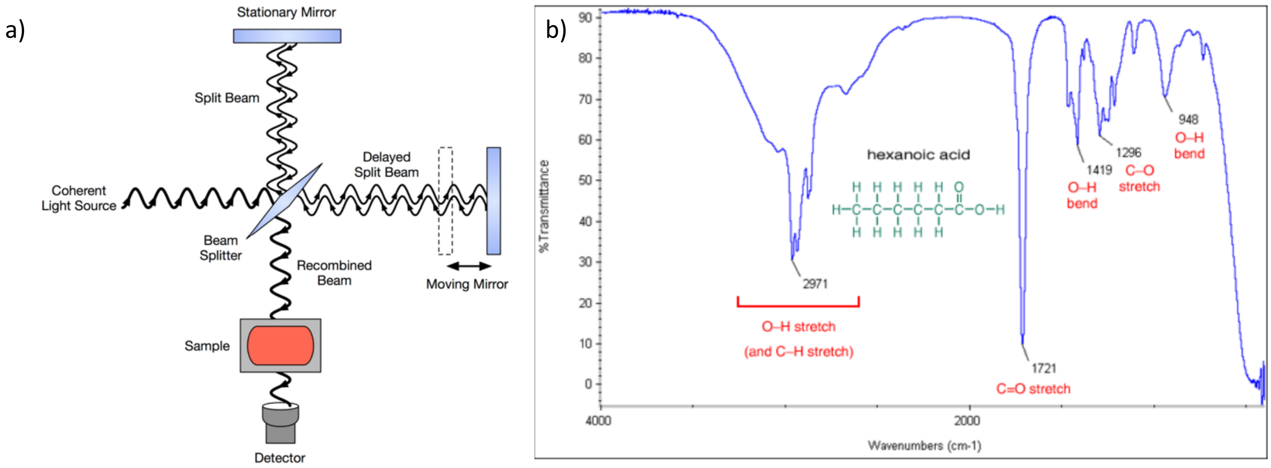

Figure 139. FT-IR a) apparatus scheme and b) example of spectrum.

When exposed to infrared radiation, the sample molecules selectively absorb radiation of specific wavelengths and pass from the ground state to the excited state, varying the dipole moment. The number of peaks is related to the vibrational freedom number of the molecule. In a typical infrared spectrum, we have the wave number on the abscissa and the transmittance on the ordinate (**Figure 139b**). Vibrations can be of two types: stretching of the chemical bond (stretching) and deformation of the bond angle (bending).

In the IR spectrum it is possible to distinguish mainly two zones: the functional group zone, which extends from 3800 to 1300 cm-1 which includes the stretching and bending bands of the functional groups (e.g. NH, OH, CH, C = C bonds , C = O, etc.), and the fingerprint area , from 1300 to 650 cm-1, which owes its name to the presence of characteristic bands of each molecule because they originate from vibrations of the entire molecular skeleton (**Figure 140**).

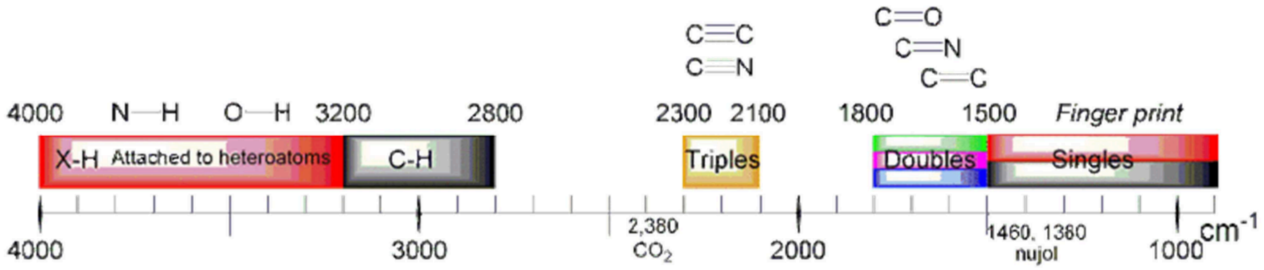

Figure 140. Zones of absorbance IR spectrum.

6.4.11 FLUORESCENCE MACROSCOPE

The fluorescence Macroscope is a fluorescence light microscope that resembles a binocular microscope but has a single light path instead of the double light paths of the latter, generating an identical image in both eyepieces. This microscope is optimized for imaging relatively large samples, a few centimeters and, having a large fixed working distance (independent of magnification) between the underside of the objective lens and the subject, handling of the samples and / or the introduction of supplementary lighting becomes simplified. A further advantage of the macroscope is that, during the "z stack" acquisition, there is no parallax error (apparent lateral displacement of the sample).

6.4.12 TRANSMISSION ELECTRON CRYOMICROSCOPY (CRYOTEM)

Transmission Electron CryoMicroscopy (CryoTEM) is a type of transmission electron microscopy (TEM) in which the sample is studied at cryogenic temperatures (usually liquid nitrogen temperatures) (**Figure 142a**).

For biological samples, the structure is preserved by inclusion in a vitreous ice environment. To do this, an aqueous solution of the sample is applied to a TEM microscopy grid and frozen by immersing it in liquid ethane (**Figure 141**).

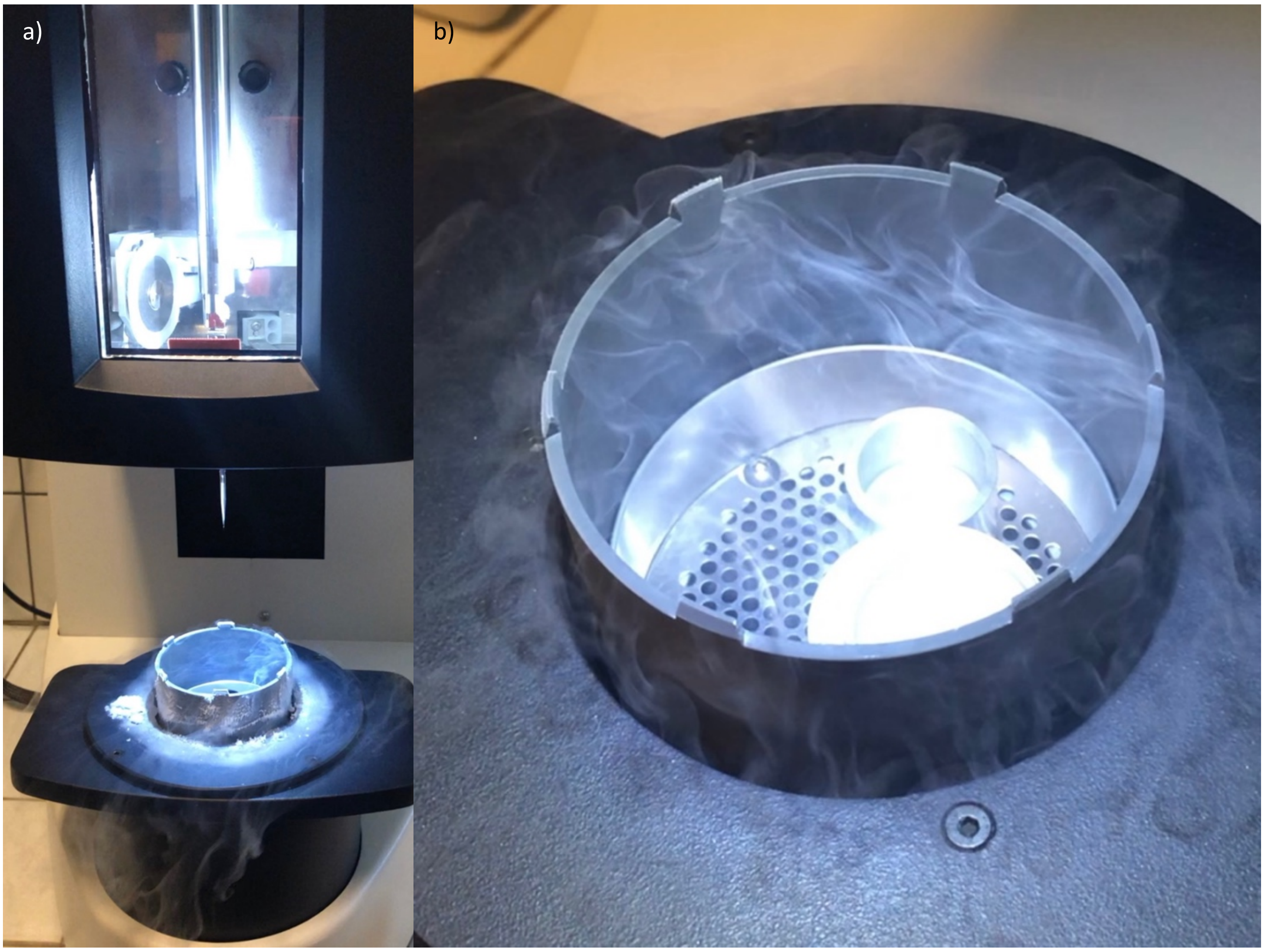

Figure 141. a) Photo of the machinery used for freezing the grids for the CryoTEM. b) Detail of the well containing liquid ethane.

The usefulness of transmission electron cryomicroscopy derives from the possibility of observing the samples in their native state, without manipulating the sample and procedures that introduce artifacts. Thanks to advances in detector technology and more powerful software imaging algorithms, it has been possible to use this technique to determine macromolecular structures at near atomic resolution. Some examples of the macromolecules displayed include viruses, ribosomes, mitochondria, ion channels, and enzyme complexes. An application of CryoTEM is cryo-electronic tomography (cryo-ET), in which it is possible to create a 3D reconstruction of the sample starting from inclined 2D images.

By keeping the samples at liquid nitrogen temperature or lower, they can be introduced into the high vacuum of the electron microscope column through a sample holder with liquid nitrogen inside which allows the grid to be kept frozen (**Figure 142b**). Since most biological samples are extremely sensitive to radiation generated by the electron beam, low voltage and low beam doses must be used; in this the low temperature of cryomicroscopy serves precisely to protect the samples from damage due to the beam.

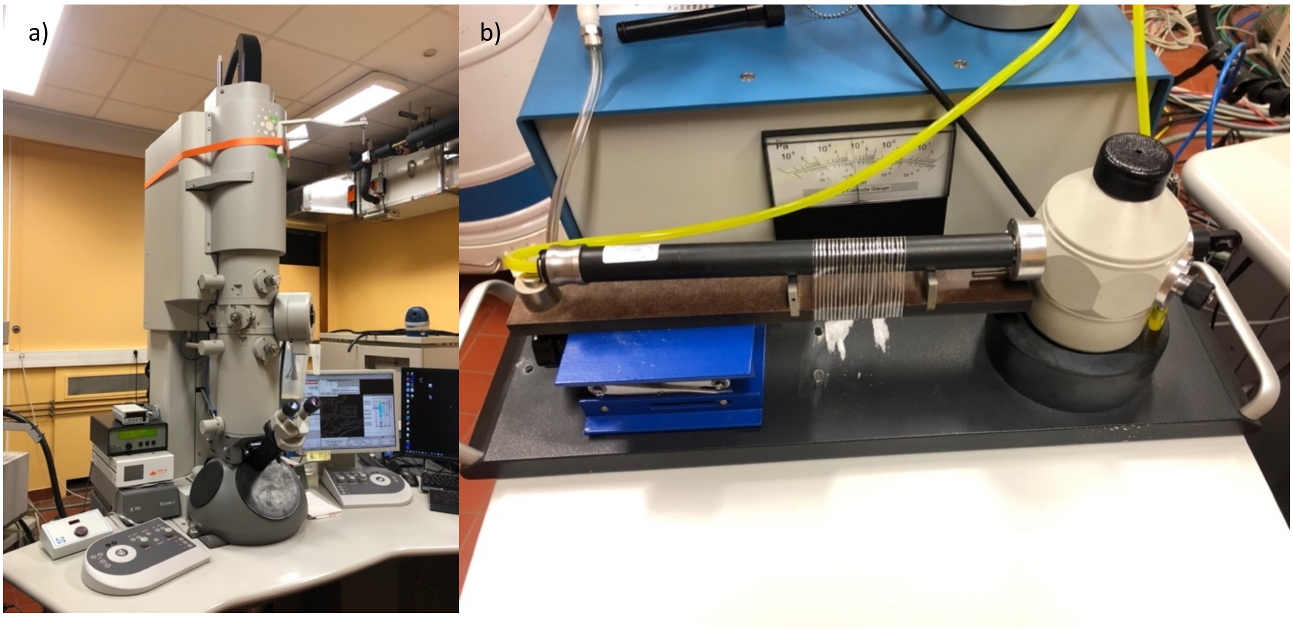

Figure 142. a) photo of the CryoTEM and b) of its sample holder.

6.4.13 Energy Dispersive X-ray Analysis (EDX)

The term Energy Dispersive X-ray Analysis refers to the study of the characteristic X-rays emitted by a sample, whose atoms are excited by the electron beam of the microscope (TEM or SEM) in which the energy dispersion spectrometer is integrated. The electron beam that hits the sample promotes the ionization of the electrons belonging to the innermost orbitals of the atom, and, from the consequent relaxation, X-rays are emitted, characteristic of the elements that make up the sample (**Figure 143**).

The wavelength of the X-rays emitted by the sample allows to determine the elemental composition of the analyzed material. This technique, by measuring the number of counts as a function of the energy of the detected photon, also provides information on the ratios (in weight or number of atoms) between the different elements present in the sample.

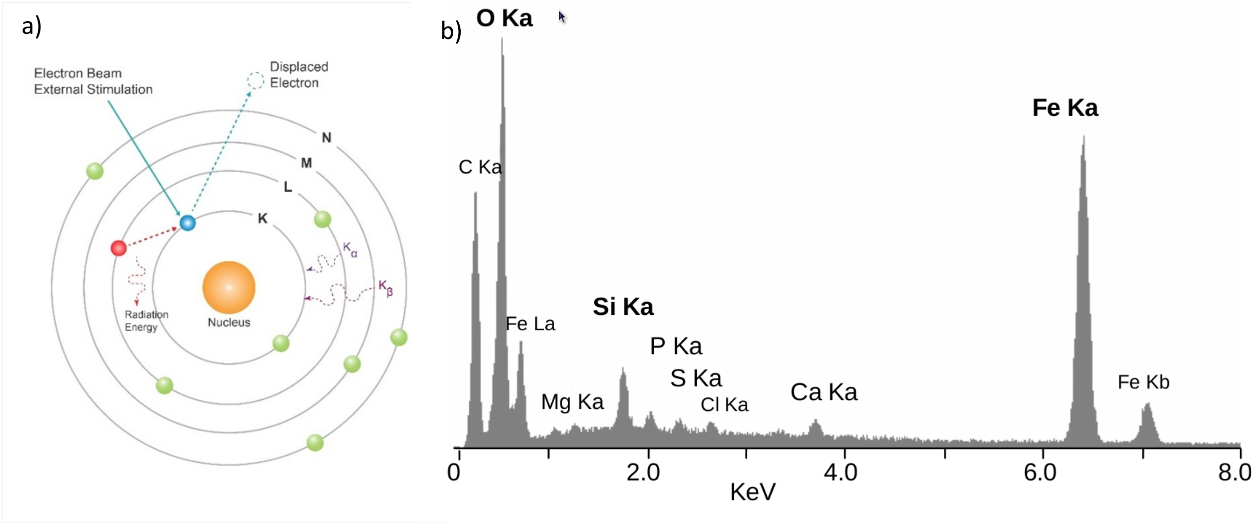

Figure 143. a) Scheme of interaction between electron beam and sample. b) EDX example specrtum.

This technique has numerous advantages: it allows both point measurements and production of elemental distribution maps, is non-destructive for samples that are stable under an electron beam, and covers all elements except light ones (cannot detect elements lighter than Na), as for low Z values the emission of Auger electrons is favored , a competitive process to fluorescence X.

6.4.14 RUTHERFORD BACK SCATTERING (RBS)

Rutherford Back Scattering (RBS) is a quantitative and non-destructive technique that is used to determine the structure and composition of materials by measuring the backscattering of a beam of high-energy ions (generally He^+ ions, with energy of the order of MeV) affecting a sample. When the beam hits the sample, the majority of the ions remain in the material, while a small fraction (1 out of 10^5 - 10^6) is back scattered by ion-nucleus collisions; this "collision" is actually an exchange of energy that occurs due to the Coulomb forces between the nuclei of the He^+ ion and the target in close proximity to each other. The surface interaction, according to classical physics, can be represented as an elastic collision.

backscattered ion, i.e. the position of the peak, depends both on the loss of energy caused by crossing the medium (before and after the collision) and on the collision between the nucleus of the ion and that of the target. In addition to the energy, it is also important to evaluate the intensity of the peaks which is linked to the number of backscatter events. The number of backscatter events related to a given element depends both on the concentration of the element itself and on the actual size of its core. The probability of a material causing a collision is called the dispersion cross section.

An RBS tool generally includes three essential components:

- A source of ions or, less commonly, protons.
- A high-energy linear particle accelerator.
- A detector capable of measuring the energies of retro scattered ions over a certain range of angles.

These basic components are accompanied by a rotation system in the (high vacuum) sample chamber, useful for recording the backscattered beam at different angles, a preamplifier, an amplifier, and a multichannel analyzer (MCA) (**Figure 144**)

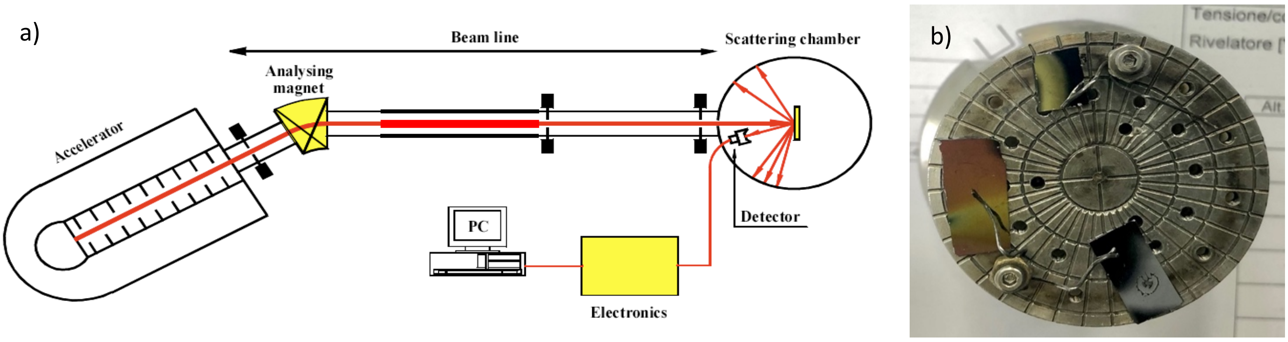

Figure 144. a) Scheme of an RBS system and b) its sample holder.

6.4.15 NANOPARTICLE TRACKING ANALYSIS (NTA)

Nanoparticle Tracking Analysis is one of the few methods to visualize and measure the dimensions and concentrations of suspended nanoparticles in the range of 10 to 1000 nm, based on the analysis of Brownian motion. To do this, the technique is equipped with an optical microscope (**Figure 145**) which, despite the particles being below the resolution limit of the microscope, is able to detect the light scattered by the particles, forming bright spots with Brownian movement in the image.

The particles appear in the microscope chamber as bright spots that move more or less quickly depending on their size. The NTA software, following the movement of the nanoparticles, can calculate the diffusion coefficient of hundreds of particles simultaneously and their hydro-dynamic radius using the Stokes-Einstein equation.

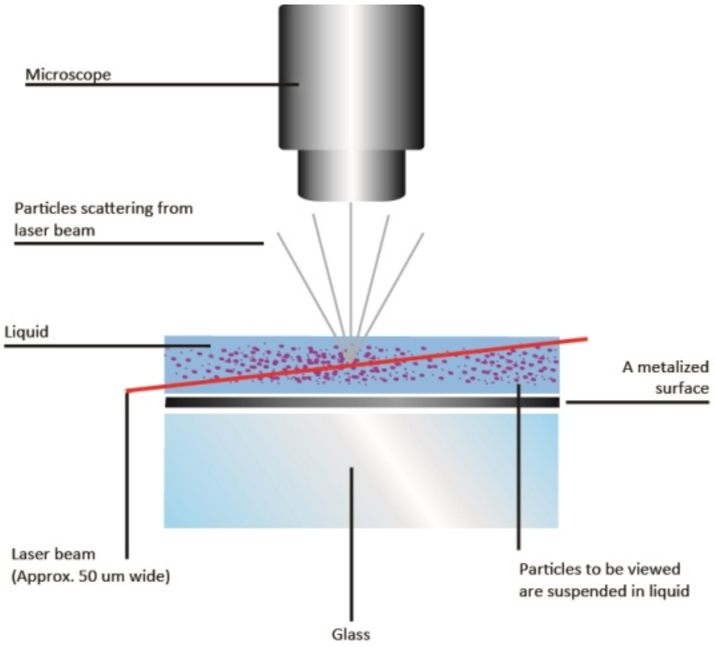

Figure 145. Schematic configuration of an NTA system.

6.4.16 RAMAN SPECTROSCOPY

Raman spectroscopy is an analysis technique widely used in the study of materials and is based on the phenomenon of diffusion of a monochromatic electromagnetic radiation by the analyzed sample.

When light interacts with molecules, most of the photons are scattered maintaining the same energy as the incident photons, according to the phenomenon of elastic scattering or ***Rayleigh scattering***. Nonetheless, a very small amount of these photons, after scattering, have a different frequency from that of the incident photon (***inelastic scattering***). This process is due to the excitation of a molecule following the interaction with the incident photon, with consequent de-excitation, falling back into a vibrational energy level different from the initial one, and thus producing a photon with a different energy. The difference between the energy of the incident photon and the energy of the scattered photon is called the **Raman shift** (or Raman shift).

The emission of the photon can occur in two distinct ways:

1) if the energy of the scattered photon is less than that of the incident photon, the phenomenon is called the **Stokes scattering**;
2) if the energy of the scattered photon is greater than that of the incident photon, the phenomenon is called **anti-Stokes scattering**.

The three types of issue are represented in (**Figure 146**)

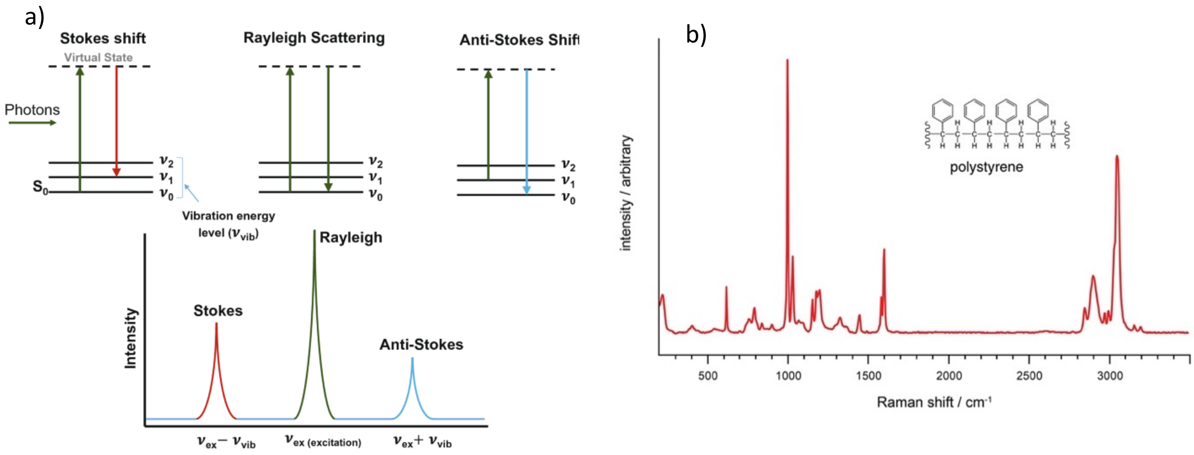

Figure 146. a) Explanation of the different Raman signals and their positioning in the graph. b) Example of RAMAN graph of polystyrene.

Raman spectroscopy is a technique that also allows the detection of vibrational modes characteristic of the crystal lattice, which originate from collective movements of the molecules in the unit cell and which produce dynamic deformations of the lattice itself. These modes are called lattice vibrations or lattice phonons, the frequencies of which fall in the spectral zone 10-150 cm $^{-1}$. The phonons, probing the intermolecular interactions, are therefore also sensitive to small differences in the packaging of the crystalline solid (astellucci, 1999).

6.4.17 Scanning Electron Microscope (SEM)

The scanning electron microscope is used for observing the surface of samples. The electrons generated by a source are focused on the surface of the sample thanks to electromagnetic lenses and an objective lens. The electrons interact with the sample generating different types of signals (mostly electrons and X-rays) which are collected by the detectors and reprocessed to produce the image of the surface (**Figure 147**).

The main signals produced by the beam on the sample are the following:

- Backscattered electrons (BSE) that arise from an elastic interaction between the electrons of the beam and the nuclei of the atoms making up the sample. They allow to obtain a compositional image, in which the gray scale is a function of the composition of the sample. The darker areas, in fact, will correspond to lighter elements, the lighter ones to elements with a higher atomic weight (which return more signal).

- Secondary electrons (SE) that arise from an inelastic interaction between the beam and the atoms of the sample. In this case there is therefore a loss of part of the energy, so that the secondary electrons have significantly lower energy than the backscattered ones. For this reason, only the SEs close to the surface (in the range of a few tens of nm) can emerge from the sample and reach the detector. The image obtained does not return compositional information but has more surface details and in general has a more three-dimensional appearance.
- X-rays that have a characteristic energy dependent on the element that emits them. For this reason, they allow to identify the chemical nature of the sample, both from a qualitative and semi-quantitative point of view, through the EDX analysis coupled to the SEM.

This technique, as for TEM, requires high vacuum and conductive samples to prevent the electrons of the beam from accumulating on the surface of the sample, making observation impossible. Non-conductive samples can however be observed by SEM by making metal coatings on them or by observing the sample for a very short time and at low voltages, to avoid the accumulation of charge and overheating of the sample.

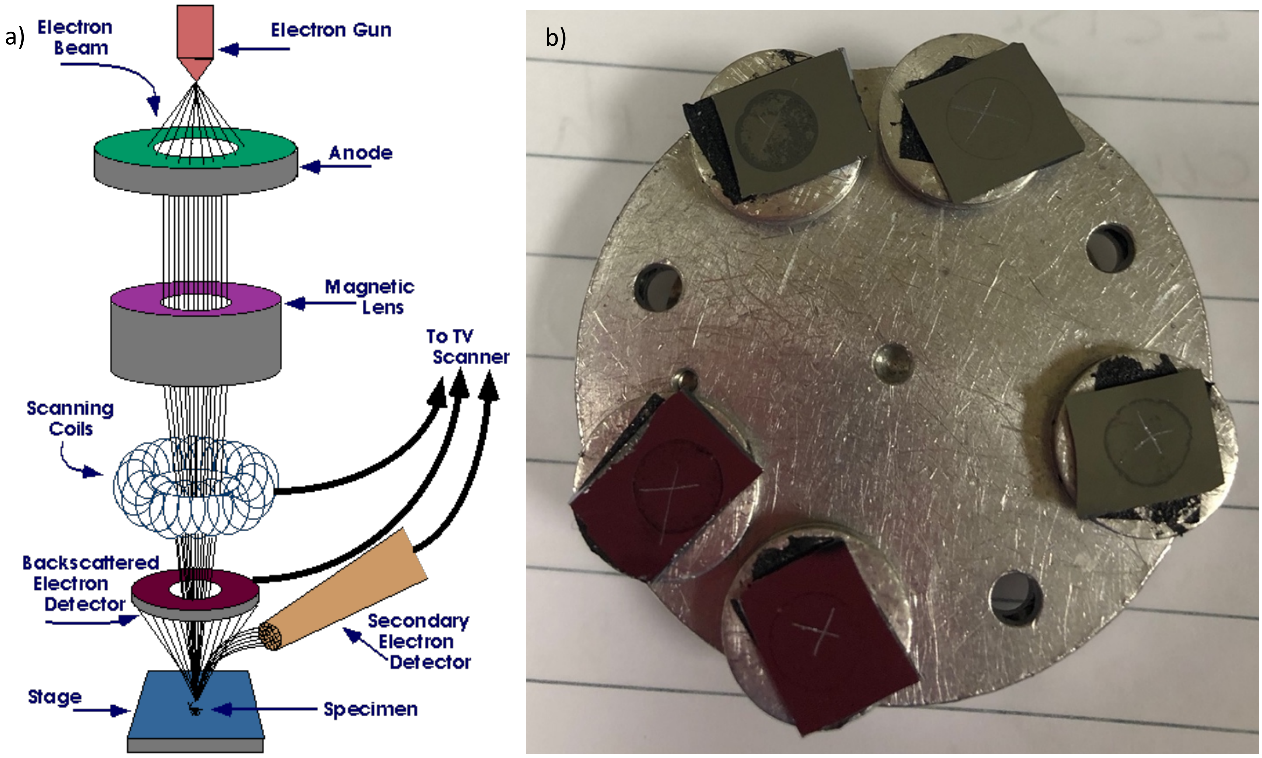

Figure 147. a) Scheme of an SEM microscope and b) its sample holder.

7 REFERENCES

(1) DaCosta, M. V.; Doughan, S.; Han, Y.; Krull, U. J. Lanthanide Upconversion Nanoparticles and Applications in Bioassays and Bioimaging: A Review. *Anal. Chim. Acta* **2014**, *832*, 1–33. https://doi.org/10.1016/j.aca.2014.04.030.

(2) Fukushima, S.; Furukawa, T.; Niioka, H.; Ichimiya, M.; Sannomiya, T.; Tanaka, N.; Onoshima, D.; Yukawa, H.; Baba, Y.; Ashida, M.; Miyake, J.; Araki, T.; Hashimoto, M. Correlative Near-Infrared Light and Cathodoluminescence Microscopy Using Y2O3:Ln, Yb (Ln = Tm, Er) Nanophosphors for Multiscale, Multicolour Bioimaging. *Sci. Rep.* **2016**, *6* (1). https://doi.org/10.1038/srep25950.

(3) Niioka, H.; Furukawa, T.; Ichimiya, M.; Ashida, M.; Araki, T.; Hashimoto, M. Multicolor Cathodoluminescence Microscopy for Biological Imaging with Nanophosphors. *Appl. Phys. Express* **2011**, *4* (11), 112402. https://doi.org/10.1143/APEX.4.112402.

(4) Zheng, J.; Zhou, C.; Yu, M.; Liu, J. Different Sized Luminescent Gold Nanoparticles. *Nanoscale* **2012**, *4* (14), 4073. https://doi.org/10.1039/c2nr31192e.

(5) Zhang, Y.; Zhang, C.; Xu, C.; Wang, X.; Liu, C.; Waterhouse, G. I. N.; Wang, Y.; Yin, H. Ultrasmall Au Nanoclusters for Biomedical and Biosensing Applications: A Mini-Review. *Talanta* **2019**, *200*, 432–442. https://doi.org/10.1016/j.talanta.2019.03.068.

(6) Zheng, Y.; Lai, L.; Liu, W.; Jiang, H.; Wang, X. Recent Advances in Biomedical Applications of Fluorescent Gold Nanoclusters. *Adv. Colloid Interface Sci.* **2017**, *242*, 1–16. https://doi.org/10.1016/j.cis.2017.02.005.

(7) Zhang, X.-D.; Wu, D.; Shen, X.; Liu, P.-X.; Fan, F.-Y.; Fan, S.-J. In Vivo Renal Clearance, Biodistribution, Toxicity of Gold Nanoclusters. *Biomaterials* **2012**, *33* (18), 4628–4638. https://doi.org/10.1016/j.biomaterials.2012.03.020.

(8) Cantero, D.; Friess, H.; Deflorin, J.; Zimmermann, A.; Bründler, M.-A.; Riesle, E.; Korc, M.; Büchler, M. Enhanced Expression of Urokinase Plasminogen Activator and Its Receptor in Pancreatic Carcinoma. *Br. J. Cancer* **1997**, *75* (3), 388–395. https://doi.org/10.1038/bjc.1997.63.

(9) Hirai, M.; Minematsu, H.; Kondo, N.; Oie, K.; Igarashi, K.; Yamazaki, N. Accumulation of Liposome with Sialyl Lewis X to Inflammation and Tumor Region: Application to in Vivo Bio-Imaging. *Biochem. Biophys. Res. Commun.* **2007**, *353* (3), 553–558. https://doi.org/10.1016/j.bbrc.2006.12.060.

(10) Benesch, J.; Hungerford, G.; Suhling, K.; Tregidgo, C.; Mano, J. F.; Reis, R. L. Fluorescence Probe Techniques to Monitor Protein Adsorption-Induced Conformation Changes on Biodegradable Polymers. *J. Colloid Interface Sci.* **2007**, *312* (2), 193–200. https://doi.org/10.1016/j.jcis.2007.03.016.

(11) Venkatachalam, N.; Hemmer, E.; Yamano, T.; Hyodo, H.; Kishimoto, H.; Soga, K. Synthesis and Toxicity Assay of Ceramic Nanophosphors for Bioimaging with Near-Infrared Excitation. *Prog. Cryst. Growth Charact. Mater.* **2012**, *58* (2–3), 121–134. https://doi.org/10.1016/j.pcrysgrow.2012.02.002.

(12) Choy, G.; Choyke, P.; Libutti, S. K. Current Advances in Molecular Imaging: Noninvasive in Vivo Bioluminescent and Fluorescent Optical Imaging in Cancer Research. *Mol. Imaging* **2003**, *2* (4), 15353500200303142. https://doi.org/10.1162/15353500200303142.

(13) Kogure, T.; Karasawa, S.; Araki, T.; Saito, K.; Kinjo, M.; Miyawaki, A. A Fluorescent Variant of a Protein from the Stony Coral Montipora Facilitates Dual-Color Single-Laser Fluorescence Cross-Correlation Spectroscopy. *Nat. Biotechnol.* **2006**, *24* (5), 577–581. https://doi.org/10.1038/nbt1207.

(14) Kuningas, K.; Ukonaho, T.; Päkkilä, H.; Rantanen, T.; Rosenberg, J.; Lövgren, T.; Soukka, T. Upconversion Fluorescence Resonance Energy Transfer in a Homogeneous Immunoassay for Estradiol. *Anal. Chem.* **2006**, *78* (13), 4690–4696. https://doi.org/10.1021/ac0603983.

(15) Morgan, C. G.; Dad, S.; Mitchell, A. C. Present Status of, and Future Prospects for, Upconverting Phosphors in Proximity-Based Bioassay. *J. Alloys Compd.* **2008**, *451* (1–2), 526–529. https://doi.org/10.1016/j.jallcom.2007.04.124.

(16) Prasad, P. Emerging Opportunities at the Interface of Photonics, Nanotechnology and Biotechnology. *Mol. Cryst. Liq. Cryst.* **2004**, *415* (1), 1–7. https://doi.org/10.1080/15421400490482943.

(17) Hampl, J.; Hall, M.; Mufti, N. A.; Yao, Y. M.; MacQueen, D. B.; Wright, W. H.; Cooper, D. E. Upconverting Phosphor Reporters in Immunochromatographic Assays. *Anal. Biochem.* **2001**, *288* (2), 176–187. https://doi.org/10.1006/abio.2000.4902.

(18) Niedbala, R. S.; Feindt, H.; Kardos, K.; Vail, T.; Burton, J.; Bielska, B.; Li, S.; Milunic, D.; Bourdelle, P.; Vallejo, R. Detection of Analytes by Immunoassay Using Up-Converting Phosphor Technology. *Anal. Biochem.* **2001**, *293* (1), 22–30. https://doi.org/10.1006/abio.2001.5105.

(19) Matsuura, D.; Ikeuchi, T.; Soga, K. Upconversion Luminescence of Colloidal Solution of Y2O3 Nano-Particles Doped with Trivalent Rare-Earth Ions. *J. Lumin.* **2008**, *128* (8), 1267–1270. https://doi.org/10.1016/j.jlumin.2007.12.024.

(20) Konishi, T.; Shimizu, M.; Kameyama, Y.; Soga, K. Fabrication of Upconversion Emissive LaOCl Phosphors Doped with Rare-Earth Ions for Bioimaging Probes. *J. Mater. Sci. Mater. Electron.* **2007**, *18* (S1), 183–186. https://doi.org/10.1007/s10854-007-9185-9.

(21) Wang, L.; Yan, R.; Huo, Z.; Wang, L.; Zeng, J.; Bao, J.; Wang, X.; Peng, Q.; Li, Y. Fluorescence Resonant Energy Transfer Biosensor Based on Upconversion-Luminescent Nanoparticles. *Angew. Chem. Int. Ed.* **2005**, *44* (37), 6054–6057. https://doi.org/10.1002/anie.200501907.

(22) Morgan, C. G.; Mitchell, A. C. Prospects for Applications of Lanthanide-Based Upconverting Surfaces to Bioassay and Detection. *Biosens. Bioelectron.* **2007**, *22* (8), 1769–1775. https://doi.org/10.1016/j.bios.2006.08.024.

(23) Jackson, B. R.; Liu, X.; McCandlish, E. F.; Riman, R. E. Self-Assembly of Monolayer-Thick Alumina Particle−Epoxy Composite Films. *Langmuir* **2007**, *23* (23), 11399–11403. https://doi.org/10.1021/la070138w.

(24) Fukushima, S.; Furukawa, T.; Niioka, H.; Ichimiya, M.; Sannomiya, T.; Tanaka, N.; Onoshima, D.; Yukawa, H.; Baba, Y.; Ashida, M.; Miyake, J.; Araki, T.; Hashimoto, M. Correlative Near-Infrared Light and Cathodoluminescence Microscopy Using Y2O3:Ln, Yb (Ln = Tm, Er) Nanophosphors for Multiscale, Multicolour Bioimaging. *Sci. Rep.* **2016**, *6* (1). https://doi.org/10.1038/srep25950.

(25) Bogdan, N.; Vetrone, F.; Ozin, G. A.; Capobianco, J. A. Synthesis of Ligand-Free Colloidally Stable Water Dispersible Brightly Luminescent Lanthanide-Doped Upconverting Nanoparticles. *Nano Lett.* **2011**, *11* (2), 835–840. https://doi.org/10.1021/nl1041929.

(26) Suk, J. S.; Xu, Q.; Kim, N.; Hanes, J.; Ensign, L. M. PEGylation as a Strategy for Improving Nanoparticle-Based Drug and Gene Delivery. *Adv. Drug Deliv. Rev.* **2016**, *99*, 28–51. https://doi.org/10.1016/j.addr.2015.09.012.

(27) Partikel, K.; Korte, R.; Stein, N. C.; Mulac, D.; Herrmann, F. C.; Humpf, H.-U.; Langer, K. Effect of Nanoparticle Size and PEGylation on the Protein Corona of PLGA Nanoparticles. *Eur. J. Pharm. Biopharm.* **2019**, *141*, 70–80. https://doi.org/10.1016/j.ejpb.2019.05.006.

(28) Medvedev, V. A.; Mamonova, D. V.; Kolesnikov, I. E.; Khokhlova, A. R.; Mikhailov, M. D.; Manshina, A. A. Synthesis and Luminescence Properties of YVO4: Nd3+, Er3+ and Tm3+ Nanoparticles. *Inorg. Chem. Commun.* **2020**, *118*, 107990. https://doi.org/10.1016/j.inoche.2020.107990.

(29) Chen, X.; Ma, E.; Liu, G. Energy Levels and Optical Spectroscopy of Er $^{3+}$ in Gd $_2$ O $_3$ Nanocrystals. *J. Phys. Chem. C* **2007**, *111* (28), 10404–10411. https://doi.org/10.1021/jp072980g.

(30) Zhou, B.; Shi, B.; Jin, D.; Liu, X. Controlling Upconversion Nanocrystals for Emerging Applications. *Nat. Nanotechnol.* **2015**, *10* (11), 924–936. https://doi.org/10.1038/nnano.2015.251.

(31) Pacio, A.; Santiago, A. C.; Portillo, M. C.; Díaz, A. R.; Galicia, C. A.; Pacio, M.; Moreno, O. P. Visible Upconversion of Erbium Oxide and Their Correlation with Crystalline Defects. *Optik* **2021**, *240*, 166912. https://doi.org/10.1016/j.ijleo.2021.166912.

(32) Sukul, P. P.; Kumar, K. Near-Infrared (808 and 980 Nm) Excited Photoluminescence Study in Nd-Doped Y_2O_3 Phosphor for Bio-Imaging. *Methods Appl. Fluoresc.* **2016**, *4* (4), 044005. https://doi.org/10.1088/2050-6120/4/4/044005.

(33) Liu, Q.; Sun, Y.; Yang, T.; Feng, W.; Li, C.; Li, F. Sub-10 Nm Hexagonal Lanthanide-Doped $NaLuF_4$ Upconversion Nanocrystals for Sensitive Bioimaging in Vivo. *J. Am. Chem. Soc.* **2011**, *133* (43), 17122–17125. https://doi.org/10.1021/ja207078s.

(34) Zhao, L.; Peng, J.; Huang, Q.; Li, C.; Chen, M.; Sun, Y.; Lin, Q.; Zhu, L.; Li, F. Near-Infrared Photoregulated Drug Release in Living Tumor Tissue via Yolk-Shell Upconversion Nanocages. *Adv. Funct. Mater.* **2014**, *24* (3), 363–371. https://doi.org/10.1002/adfm.201302133.

(35) Deng, R.; Xie, X.; Vendrell, M.; Chang, Y.-T.; Liu, X. Intracellular Glutathione Detection Using MnO_2-Nanosheet-Modified Upconversion Nanoparticles. *J. Am. Chem. Soc.* **2011**, *133* (50), 20168–20171. https://doi.org/10.1021/ja2100774.

(36) Khnayzer, R. S.; Blumhoff, J.; Harrington, J. A.; Haefele, A.; Deng, F.; Castellano, F. N. Upconversion-Powered Photoelectrochemistry. *Chem Commun* **2012**, *48* (2), 209–211. https://doi.org/10.1039/C1CC16015J.

(37) Li, Y.; Chen, Q.; Pan, X.; Lu, W.; Zhang, J. Development and Challenge of Fluorescent Probes for Bioimaging Applications: From Visualization to Diagnosis. *Top. Curr. Chem.* **2022**, *380* (4), 22. https://doi.org/10.1007/s41061-022-00376-8.

(38) Zhang, J.; Campbell, R. E.; Ting, A. Y.; Tsien, R. Y. Creating New Fluorescent Probes for Cell Biology. *Nat. Rev. Mol. Cell Biol.* **2002**, *3* (12), 906–918. https://doi.org/10.1038/nrm976.

(39) Jaiswal, J. K.; Mattoussi, H.; Mauro, J. M.; Simon, S. M. Long-Term Multiple Color Imaging of Live Cells Using Quantum Dot Bioconjugates. *Nat. Biotechnol.* **2003**, *21* (1), 47–51. https://doi.org/10.1038/nbt767.

(40) Chen, G.; Qiu, H.; Prasad, P. N.; Chen, X. Upconversion Nanoparticles: Design, Nanochemistry, and Applications in Theranostics. *Chem. Rev.* **2014**, *114* (10), 5161–5214. https://doi.org/10.1021/cr400425h.

(41) Chen, Y.; Xue, L.; Zhu, Q.; Feng, Y.; Wu, M. Recent Advances in Second Near-Infrared Region (NIR-II) Fluorophores and Biomedical Applications. *Front. Chem.* **2021**, *9*, 750404. https://doi.org/10.3389/fchem.2021.750404.

(42) Chen, G.; Ohulchanskyy, T. Y.; Kumar, R.; Ågren, H.; Prasad, P. N. Ultrasmall Monodisperse $NaYF_4$:Yb^{3+}/Tm^{3+} Nanocrystals with Enhanced Near-Infrared to Near-Infrared Upconversion Photoluminescence. *ACS Nano* **2010**, *4* (6), 3163–3168. https://doi.org/10.1021/nn100457j.

(43) Harrison, V. S. R.; Carney, C. E.; MacRenaris, K. W.; Waters, E. A.; Meade, T. J. Multimeric Near IR–MR Contrast Agent for Multimodal *In Vivo* Imaging. *J. Am. Chem. Soc.* **2015**, *137* (28), 9108–9116. https://doi.org/10.1021/jacs.5b04509.

(44) Thi Kim Dung, D.; Umezawa, M.; Nigoghossian, K.; Yeroslavsky, G.; Okubo, K.; Kamimura, M.; Yamaguchi, M.; Fujii, H.; Soga, K. Development of Molecular Imaging Probe for Dual NIR/MR Imaging. *J. Photopolym. Sci. Technol.* **2020**, *33* (1), 117–122. https://doi.org/10.2494/photopolymer.33.117.

(45) Yang, Z.; Sharma, A.; Qi, J.; Peng, X.; Lee, D. Y.; Hu, R.; Lin, D.; Qu, J.; Kim, J. S. Super-Resolution Fluorescent

Materials: An Insight into Design and Bioimaging Applications. *Chem. Soc. Rev.* **2016**, *45* (17), 4651–4667. https://doi.org/10.1039/C5CS00875A.

(46) Liu, J.; Chen, C.; Ji, S.; Liu, Q.; Ding, D.; Zhao, D.; Liu, B. Long Wavelength Excitable Near-Infrared Fluorescent Nanoparticles with Aggregation-Induced Emission Characteristics for Image-Guided Tumor Resection. *Chem. Sci.* **2017**, *8* (4), 2782–2789. https://doi.org/10.1039/C6SC04384D.

(47) Chen, Z.; Chen, H.; Hu, H.; Yu, M.; Li, F.; Zhang, Q.; Zhou, Z.; Yi, T.; Huang, C. Versatile Synthesis Strategy for Carboxylic Acid−functionalized Upconverting Nanophosphors as Biological Labels. *J. Am. Chem. Soc.* **2008**, *130* (10), 3023–3029. https://doi.org/10.1021/ja076151k.

(48) Yang, Y.; Sun, Y.; Cao, T.; Peng, J.; Liu, Y.; Wu, Y.; Feng, W.; Zhang, Y.; Li, F. Hydrothermal Synthesis of NaLuF4:153Sm,Yb,Tm Nanoparticles and Their Application in Dual-Modality Upconversion Luminescence and SPECT Bioimaging. *Biomaterials* **2013**, *34* (3), 774–783. https://doi.org/10.1016/j.biomaterials.2012.10.022.

(49) Furukawa, T.; Niioka, H.; Ichimiya, M.; Nagata, T.; Ashida, M.; Araki, T.; Hashimoto, M. High-Resolution Microscopy for Biological Specimens via Cathodoluminescence of Eu- and Zn-Doped Y_2O_3nanophosphors. *Opt. Express* **2013**, *21* (22), 25655. https://doi.org/10.1364/OE.21.025655.

(50) Van Hest, J. J. H. A.; Agronskaia, A. V.; Fokkema, J.; Montanarella, F.; Gregorio Puig, A.; De Mello Donega, C.; Meijerink, A.; Blab, G. A.; Gerritsen, H. C. Towards Robust and Versatile Single Nanoparticle Fiducial Markers for Correlative Light and Electron Microscopy: ROBUST SINGLE NANOPARTICLE FIDUCIAL MARKERS. *J. Microsc.* **2019**, *274* (1), 13–22. https://doi.org/10.1111/jmi.12778.

(51) Vinogradov, S. V.; Bronich, T. K.; Kabanov, A. V. Nanosized Cationic Hydrogels for Drug Delivery: Preparation, Properties and Interactions with Cells. *Adv. Drug Deliv. Rev.* **2002**, *54* (1), 135–147. https://doi.org/10.1016/S0169-409X(01)00245-9.

(52) Gref, R.; Lück, M.; Quellec, P.; Marchand, M.; Dellacherie, E.; Harnisch, S.; Blunk, T.; Müller, R. H. ‘Stealth’ Corona-Core Nanoparticles Surface Modified by Polyethylene Glycol (PEG): Influences of the Corona (PEG Chain Length and Surface Density) and of the Core Composition on Phagocytic Uptake and Plasma Protein Adsorption. *Colloids Surf. B Biointerfaces* **2000**, *18* (3–4), 301–313. https://doi.org/10.1016/S0927-7765(99)00156-3.

(53) Gustafson, H. H.; Holt-Casper, D.; Grainger, D. W.; Ghandehari, H. Nanoparticle Uptake: The Phagocyte Problem. *Nano Today* **2015**, *10* (4), 487–510. https://doi.org/10.1016/j.nantod.2015.06.006.

(54) Bar-Ilan, O.; Albrecht, R. M.; Fako, V. E.; Furgeson, D. Y. Toxicity Assessments of Multisized Gold and Silver Nanoparticles in Zebrafish Embryos. *Small* **2009**, *5* (16), 1897–1910. https://doi.org/10.1002/smll.200801716.

(55) Meng, H.; Chen, Z.; Xing, G.; Yuan, H.; Chen, C.; Zhao, F.; Zhang, C.; Zhao, Y. Ultrahigh Reactivity Provokes Nanotoxicity: Explanation of Oral Toxicity of Nano-Copper Particles. *Toxicol. Lett.* **2007**, *175* (1–3), 102–110. https://doi.org/10.1016/j.toxlet.2007.09.015.

(56) Hoshino, A.; Fujioka, K.; Oku, T.; Suga, M.; Sasaki, Y. F.; Ohta, T.; Yasuhara, M.; Suzuki, K.; Yamamoto, K. Physicochemical Properties and Cellular Toxicity of Nanocrystal Quantum Dots Depend on Their Surface Modification. *Nano Lett.* **2004**, *4* (11), 2163–2169. https://doi.org/10.1021/nl048715d.

(57) Waters, K. M.; Masiello, L. M.; Zangar, R. C.; Tarasevich, B. J.; Karin, N. J.; Quesenberry, R. D.; Bandyopadhyay, S.; Teeguarden, J. G.; Pounds, J. G.; Thrall, B. D. Macrophage Responses to Silica Nanoparticles Are Highly Conserved Across Particle Sizes. *Toxicol. Sci.* **2009**, *107* (2), 553–569. https://doi.org/10.1093/toxsci/kfn250.

(58) Singh, N.; Manshian, B.; Jenkins, G. J. S.; Griffiths, S. M.; Williams, P. M.; Maffeis, T. G. G.; Wright, C. J.; Doak, S. H. NanoGenotoxicology: The DNA Damaging Potential of Engineered Nanomaterials. *Biomaterials* **2009**, *30* (23–24), 3891–3914. https://doi.org/10.1016/j.biomaterials.2009.04.009.

(59) Oberdörster, G.; Maynard, A.; Donaldson, K.; Castranova, V.; Fitzpatrick, J.; Ausman, K.; Carter, J.; Karn, B.; Kreyling, W.; Lai, D.; Olin, S.; Monteiro-Riviere, N.; Warheit, D.; Yang, H.; A report from the ILSI Research Foundation/Risk Science Institute Nanomaterial Toxicity Screening Working Group. Principles for Characterizing the Potential Human Health Effects from Exposure to Nanomaterials: Elements of a Screening Strategy. *Part. Fibre Toxicol.* **2005**, *2* (1), 8. https://doi.org/10.1186/1743-8977-2-8.

(60) Lai, D. Y. Toward Toxicity Testing of Nanomaterials in the 21st Century: A Paradigm for Moving Forward. *WIREs Nanomedicine Nanobiotechnology* **2012**, *4* (1), 1–15. https://doi.org/10.1002/wnan.162.

(61) DaCosta, M. V.; Doughan, S.; Han, Y.; Krull, U. J. Lanthanide Upconversion Nanoparticles and Applications in Bioassays and Bioimaging: A Review. *Anal. Chim. Acta* **2014**, *832*, 1–33. https://doi.org/10.1016/j.aca.2014.04.030.

(62) Wang, N.; Fuh, J. Y. H.; Dheen, S. T.; Senthil Kumar, A. Synthesis Methods of Functionalized Nanoparticles: A Review. *Bio-Des. Manuf.* **2021**, *4* (2), 379–404. https://doi.org/10.1007/s42242-020-00106-3.

(63) Esposito, S. “Traditional” Sol-Gel Chemistry as a Powerful Tool for the Preparation of Supported Metal and Metal Oxide Catalysts. *Materials* **2019**, *12* (4), 668. https://doi.org/10.3390/ma12040668.

(64) Bogdal, D.; Prociak, A.; Michalowski, S. Synthesis of Polymer Nanocomposites Under Microwave Irradiation. *Curr. Org. Chem.* **2011**, *15* (2), 178–188. https://doi.org/10.2174/138527211793979835.

(65) Wang, F.; Banerjee, D.; Liu, Y.; Chen, X.; Liu, X. Upconversion Nanoparticles in Biological Labeling, Imaging, and Therapy. *The Analyst* **2010**, *135* (8), 1839. https://doi.org/10.1039/c0an00144a.

(66) van Niel, G.; D’Angelo, G.; Raposo, G. Shedding Light on the Cell Biology of Extracellular Vesicles. *Nat. Rev. Mol. Cell Biol.* **2018**, *19* (4), 213–228. https://doi.org/10.1038/nrm.2017.125.

(67) Stella, M.; Falzone, L.; Caponnetto, A.; Gattuso, G.; Barbagallo, C.; Battaglia, R.; Mirabella, F.; Broggi, G.; Altieri, R.; Certo, F.; Caltabiano, R.; Barbagallo, G. M. V.; Musumeci, P.; Ragusa, M.; Pietro, C. D.; Libra, M.; Purrello, M.; Barbagallo, D. Serum Extracellular Vesicle-Derived CircHIPK3 and CircSMARCA5 Are Two Novel Diagnostic Biomarkers for Glioblastoma Multiforme. *Pharmaceuticals* **2021**, *14* (7), 618. https://doi.org/10.3390/ph14070618.

(68) Ebrahimkhani, S.; Vafaee, F.; Hallal, S.; Wei, H.; Lee, M. Y. T.; Young, P. E.; Satgunaseelan, L.; Beadnall, H.; Barnett, M. H.; Shivalingam, B.; Suter, C. M.; Buckland, M. E.; Kaufman, K. L. Deep Sequencing of Circulating Exosomal MicroRNA Allows Non-Invasive Glioblastoma Diagnosis. *Npj Precis. Oncol.* **2018**, *2* (1), 28. https://doi.org/10.1038/s41698-018-0071-0.

(69) Battaglia, R.; Musumeci, P.; Ragusa, M.; Barbagallo, D.; Scalia, M.; Zimbone, M.; Lo Faro, J. M.; Borzì, P.; Scollo, P.; Purrello, M.; Vento, E. M.; Di Pietro, C. Ovarian Aging Increases Small Extracellular Vesicle CD81+ Release in Human Follicular Fluid and Influences MiRNA Profiles. *Aging* **2020**, *12* (12), 12324–12341. https://doi.org/10.18632/aging.103441.

(70) Brannon-Peppas, L.; Blanchette, J. O. Nanoparticle and Targeted Systems for Cancer Therapy. *Adv. Drug Deliv. Rev.* **2012**, *64*, 206–212. https://doi.org/10.1016/j.addr.2012.09.033.

(71) Cho, K.; Wang, X.; Nie, S.; Chen, Z.; Shin, D. M. Therapeutic Nanoparticles for Drug Delivery in Cancer. *Clin. Cancer Res.* **2008**, *14* (5), 1310–1316. https://doi.org/10.1158/1078-0432.CCR-07-1441.

(72) Zhang, X.-D.; Luo, Z.; Chen, J.; Song, S.; Yuan, X.; Shen, X.; Wang, H.; Sun, Y.; Gao, K.; Zhang, L.; Fan, S.; Leong, D. T.; Guo, M.; Xie, J. Ultrasmall Glutathione-Protected Gold Nanoclusters as Next Generation Radiotherapy Sensitizers with High Tumor Uptake and High Renal Clearance. *Sci. Rep.* **2015**, *5* (1). https://doi.org/10.1038/srep08669.

(73) Liang, G.; Jin, X.; Zhang, S.; Xing, D. RGD Peptide-Modified Fluorescent Gold Nanoclusters as Highly Efficient Tumor-Targeted Radiotherapy Sensitizers. *Biomaterials* **2017**, *144*, 95–104. https://doi.org/10.1016/j.biomaterials.2017.08.017.

(74) Avvakumova, S.; Galbiati, E.; Pandolfi, L.; Mazzucchelli, S.; Cassani, M.; Gori, A.; Longhi, R.; Prosperi, D. Development of U11-Functionalized Gold Nanoparticles for Selective Targeting of Urokinase Plasminogen Activator Receptor-Positive Breast Cancer Cells. *Bioconjug. Chem.* **2014**, *25* (8), 1381–1386. https://doi.org/10.1021/bc500202b.

(75) Aldeek, F.; Muhammed, M. A. H.; Palui, G.; Zhan, N.; Mattoussi, H. Growth of Highly Fluorescent Polyethylene Glycol- and Zwitterion-Functionalized Gold Nanoclusters. *ACS Nano* **2013**, *7* (3), 2509–2521. https://doi.org/10.1021/nn305856t.

(76) Wu, Z.; Suhan, J.; Jin, R. One-Pot Synthesis of Atomically Monodisperse, Thiol-Functionalized Au $_{25}$ Nanoclusters. *J Mater Chem* **2009**, *19* (5), 622–626. https://doi.org/10.1039/B815983A.

(77) Luo, Z.; Yuan, X.; Yu, Y.; Zhang, Q.; Leong, D. T.; Lee, J. Y.; Xie, J. From Aggregation-Induced Emission of Au(I)–Thiolate Complexes to Ultrabright Au(0)@Au(I)–Thiolate Core–Shell Nanoclusters. *J. Am. Chem. Soc.* **2012**, *134* (40), 16662–16670. https://doi.org/10.1021/ja306199p.

(78) Yuan, Q.; Wang, Y.; Zhao, L.; Liu, R.; Gao, F.; Gao, L.; Gao, X. Peptide Protected Gold Clusters: Chemical Synthesis and Biomedical Applications. *Nanoscale* **2016**, *8* (24), 12095–12104. https://doi.org/10.1039/C6NR02750D.

(79) Wu, Z.; Jin, R. On the Ligand's Role in the Fluorescence of Gold Nanoclusters. *Nano Lett.* **2010**, *10* (7), 2568–2573. https://doi.org/10.1021/nl101225f.

(80) Pyo, K.; Thanthirige, V. D.; Kwak, K.; Pandurangan, P.; Ramakrishna, G.; Lee, D. Ultrabright Luminescence from Gold Nanoclusters: Rigidifying the Au(I)–Thiolate Shell. *J. Am. Chem. Soc.* **2015**, *137* (25), 8244–8250. https://doi.org/10.1021/jacs.5b04210.

(81) Kawasaki, H.; Hamaguchi, K.; Osaka, I.; Arakawa, R. Ph-Dependent Synthesis of Pepsin-Mediated Gold Nanoclusters with Blue Green and Red Fluorescent Emission. *Adv. Funct. Mater.* **2011**, *21* (18), 3508–3515. https://doi.org/10.1002/adfm.201100886.

(82) Nasaruddin, R. R.; Chen, T.; Yan, N.; Xie, J. Roles of Thiolate Ligands in the Synthesis, Properties and Catalytic Application of Gold Nanoclusters. *Coord. Chem. Rev.* **2018**, *368*, 60–79. https://doi.org/10.1016/j.ccr.2018.04.016.

(83) Riveros, A.; Dadlani, K.; Salas, E.; Caballero, L.; Melo, F.; Kogan, M. J. Gold Nanoparticle-Membrane Interactions: Implications in Biomedicine. *J. Biomater. Tissue Eng.* **2013**, *3* (1), 4–21. https://doi.org/10.1166/jbt.2013.1067.

(84) Sot, J.; Mendanha-Neto, S. A.; Busto, J. V.; García-Arribas, A. B.; Li, S.; Burgess, S. W.; Shaw, W. A.; Gil-Carton, D.; Goñi, F. M.; Alonso, A. The Interaction of Lipid-Liganded Gold Clusters (Aurora ^{TM}) with Lipid Bilayers. *Chem. Phys. Lipids* **2019**, *218*, 40–46. https://doi.org/10.1016/j.chemphyslip.2018.11.007.

(85) Venkatachalam, N.; Saito, Y.; Soga, K. Synthesis of Er3+ Doped Y2O3 Nanophosphors. *J. Am. Ceram. Soc.* **2009**, *92* (5), 1006–1010. https://doi.org/10.1111/j.1551-2916.2009.02986.x.

(86) Venkatachalam, N.; Hemmer, E.; Yamano, T.; Hyodo, H.; Kishimoto, H.; Soga, K. Synthesis and Toxicity Assay of Ceramic Nanophosphors for Bioimaging with Near-Infrared Excitation. *Prog. Cryst. Growth Charact. Mater.* **2012**, *58* (2–3), 121–134. https://doi.org/10.1016/j.pcrysgrow.2012.02.002.

(87) Jiang, X.; Wu, W.; Li, Y.; Guo, X.; Wang, N.; Song, Q.; Wang, X.; Han, Y.; Wang, L. Hydrothermal Method for Y2O3:Eu3+ Uniform Nanophosphors with Different Templates. *Mod. Phys. Lett. B* **2019**, *33* (20), 1950227. https://doi.org/10.1142/S0217984919502270.

(88) Sanchez, L. M.; Martin, D. A.; Alvarez, V. A.; Gonzalez, J. S. Polyacrylic Acid-Coated Iron Oxide Magnetic Nanoparticles: The Polymer Molecular Weight Influence. *Colloids Surf. Physicochem. Eng. Asp.* **2018**, *543*, 28–37. https://doi.org/10.1016/j.colsurfa.2018.01.050.

(89) Panáček, A.; Prucek, R.; Hrbáč, J.; Nevečná, T.; Šteffková, J.; Zbořil, R.; Kvítek, L. Polyacrylate-Assisted Size

Control of Silver Nanoparticles and Their Catalytic Activity. *Chem. Mater.* **2014**, *26* (3), 1332–1339. https://doi.org/10.1021/cm400635z.

(90) Hanafy, N. A. N.; De Giorgi, M. L.; Nobile, C.; Rinaldi, R.; Leporatti, S. Control of Colloidal CaCO3 Suspension by Using Biodegradable Polymers during Fabrication. *Beni-Suef Univ. J. Basic Appl. Sci.* **2015**, *4* (1), 60–70. https://doi.org/10.1016/j.bjbas.2015.02.009.

(91) Alrowaili, Z. A.; Taha, T. A.; El-Nasser, K. S.; Donya, H. Significant Enhanced Optical Parameters of PVA-Y2O3 Polymer Nanocomposite Films. *J. Inorg. Organomet. Polym. Mater.* **2021**, *31* (7), 3101–3110. https://doi.org/10.1007/s10904-021-01995-2.

(92) Wang, L.; Wang, N.; Wang, S.; Liang, D.; Cai, X.; Wang, D.; Han, Y.; Jia, G. Preparation of Lanthanide Ions-Doped BiPO $_4$ Nanoparticles and Fe $^{3+}$ Ions Assay. *J. Nanosci. Nanotechnol.* **2018**, *18* (6), 4000–4005. https://doi.org/10.1166/jnn.2018.15038.

(93) Zimbone, M.; Musumeci, P.; Contino, A.; Maccarrone, G.; Calcagno, L. DNA-Triggered Asymmetric ZnO Nanoparticles. *Colloids Surf. Physicochem. Eng. Asp.* **2016**, *489*, 336–342. https://doi.org/10.1016/j.colsurfa.2015.10.058.

(94) Osipov, V. V.; Solomonov, V. I.; Spirina, A. V.; Vovkotrub, E. G.; Strekalovskii, V. N. Raman Scattering and Luminescence of Yttria Nanopowders and Ceramics. *Opt. Spectrosc.* **2014**, *116* (6), 946–955. https://doi.org/10.1134/S0030400X14040225.

(95) Laricchiuta, G.; Vandervorst, W.; Vickridge, I.; Mayer, M.; Meersschaut, J. Rutherford Backscattering Spectrometry Analysis of InGaAs Nanostructures. *J. Vac. Sci. Technol. A* **2019**, *37* (2), 020601. https://doi.org/10.1116/1.5079520.

(96) Kamimura, M.; Miyamoto, D.; Saito, Y.; Soga, K.; Nagasaki, Y. Design of Poly(Ethylene Glycol)/Streptavidin Coimmobilized Upconversion Nanophosphors and Their Application to Fluorescence Biolabeling. *Langmuir* **2008**, *24* (16), 8864–8870. https://doi.org/10.1021/la801056c.

(97) Campajola, L.; Di Capua, F. Applications of Accelerators and Radiation Sources in the Field of Space Research and Industry. In *Applications of Radiation Chemistry in the Fields of Industry, Biotechnology and Environment*; Venturi, M., D'Angelantonio, M., Eds.; Topics in Current Chemistry Collections; Springer International Publishing: Cham, 2017; pp 269–297. https://doi.org/10.1007/978-3-319-54145-7_10.

(98) Liu, J.; Duchesne, P. N.; Yu, M.; Jiang, X.; Ning, X.; Vinluan, R. D.; Zhang, P.; Zheng, J. Luminescent Gold Nanoparticles with Size-Independent Emission. *Angew. Chem. Int. Ed.* **2016**, *55* (31), 8894–8898. https://doi.org/10.1002/anie.201602795.

(99) Piñeiro, Y.; Rivas, J.; López-Quintela, M. A. The Emergence of Quantum Confinement in Atomic Quantum Clusters. In *Colloidal Foundations of Nanoscience*; Elsevier, 2014; pp 81–105. https://doi.org/10.1016/B978-0-444-59541-6.00004-7.

(100) Huang, Y.; Fuksman, L.; Zheng, J. Luminescence Mechanisms of Ultrasmall Gold Nanoparticles. *Dalton Trans.* **2018**, *47* (18), 6267–6273. https://doi.org/10.1039/C8DT00420J.

(101) Porret, E.; Sancey, L.; Martín-Serrano, A.; Montañez, M. I.; Seeman, R.; Yahia-Ammar, A.; Okuno, H.; Gomez, F.; Ariza, A.; Hildebrandt, N.; Fleury, J.-B.; Coll, J.-L.; Le Guével, X. Hydrophobicity of Gold Nanoclusters Influences Their Interactions with Biological Barriers. *Chem. Mater.* **2017**, *29* (17), 7497–7506. https://doi.org/10.1021/acs.chemmater.7b02497.

(102) Chatterjee, A.; Purkayastha, P. The Impact of Lipid Head-Groups in GUVs on Electron Transfer by Surface-Adsorbed Fluorescent Gold Nanoclusters. *Mater. Adv.* **2021**, *2* (4), 1343–1350. https://doi.org/10.1039/D0MA00930J.

(103) Porret, E.; Fleury, J.-B.; Sancey, L.; Pezet, M.; Coll, J.-L.; Le Guével, X. Augmented Interaction of Multivalent Arginine Coated Gold Nanoclusters with Lipid Membranes and Cells. *RSC Adv.* **2020**, *10* (11), 6436–6443. https://doi.org/10.1039/C9RA10047D.

(104) Porret, E.; Le Guével, X.; Coll, J.-L. Gold Nanoclusters for Biomedical Applications: Toward *in Vivo* Studies. *J. Mater. Chem. B* **2020**, *8* (11), 2216–2232. https://doi.org/10.1039/C9TB02767J.

(105) Kauscher, U.; Penders, J.; Nagelkerke, A.; Holme, M. N.; Nele, V.; Massi, L.; Gopal, S.; Whittaker, T. E.; Stevens, M. M. Gold Nanocluster Extracellular Vesicle Supraparticles: Self- Assembled Nanostructures for Three-Dimensional Uptake Visualization. **2020**, 12.

(106) Dif, A.; Henry, E.; Artzner, F.; Baudy-Floc'h, M.; Schmutz, M.; Dahan, M.; Marchi-Artzner, V. Interaction between Water-Soluble Peptidic CdSe/ZnS Nanocrystals and Membranes: Formation of Hybrid Vesicles and Condensed Lamellar Phases. *J. Am. Chem. Soc.* **2008**, *130* (26), 8289–8296. https://doi.org/10.1021/ja711378g.

(107) Bizien, T.; Ameline, J.-C.; Yager, K. G.; Marchi, V.; Artzner, F. Self-Organization of Quantum Rods Induced by Lipid Membrane Corrugations. *Langmuir* **2015**, *31* (44), 12148–12154. https://doi.org/10.1021/acs.langmuir.5b03335.

(108) Contini, C.; Hindley, J. W.; Macdonald, T. J.; Barritt, J. D.; Ces, O.; Quirke, N. Size Dependency of Gold Nanoparticles Interacting with Model Membranes. *Commun. Chem.* **2020**, *3* (130), 1–12. https://doi.org/10.1038/s42004-020-00377-y.

(109) Hung, W.-T.; Navakanitworakul, R.; Khan, T.; Zhang, P.; Davis, J. S.; McGinnis, L. K.; Christenson, L. K. Stage-Specific Follicular Extracellular Vesicle Uptake and Regulation of Bovine Granulosa Cell Proliferation†. *Biol. Reprod.* **2017**, *97* (4), 644–655. https://doi.org/10.1093/biolre/iox106.

(110) Yefimova, M. G.; Béré, E.; Cantereau-Becq, A.; Meunier-Balandre, A.-C.; Merceron, B.; Burel, A.; Merienne, K.; Ravel, C.; Becq, F.; Bourmeyster, N. Myelinosome Organelles in the Retina of R6/1 Huntington Disease (HD) Mice: Ubiquitous Distribution and Possible Role in Disease Spreading. *Int. J. Mol. Sci.* **2021**, *22* (23), 12771. https://doi.org/10.3390/ijms222312771.

(111) Bourmeyster, N. Myelinosome-Driven Secretion: Non-Catabolic Management of Misfolded Proteins - Lessons from the Sertoli Cells. *J. Rare Dis. Res. Treat.* **2017**, *2* (2), 24–27. https://doi.org/10.29245/2572-9411/2017/2.1085.

(112) Yefimova, M. G.; Béré, E.; Cantereau-Becq, A.; Harnois, T.; Meunier, A.-C.; Messaddeq, N.; Becq, F.; Trottier, Y.; Bourmeyster, N. Myelinosomes Act as Natural Secretory Organelles in Sertoli Cells to Prevent Accumulation of Aggregate-Prone Mutant Huntingtin and CFTR. *Hum. Mol. Genet.* **2016**, *25* (19), 4170–4185. https://doi.org/10.1093/hmg/ddw251.

(113) Beach, A.; Zhang, H.-G.; Ratajczak, M. Z.; Kakar, S. S. Exosomes: An Overview of Biogenesis, Composition and Role in Ovarian Cancer. *J. Ovarian Res.* **2014**, *7* (1), 14. https://doi.org/10.1186/1757-2215-7-14.

(114) Bai, Y.; Lu, Y.; Wang, K.; Cheng, Z.; Qu, Y.; Qiu, S.; Zhou, L.; Wu, Z.; Liu, H.; Zhao, J.; Mao, H. Rapid Isolation and Multiplexed Detection of Exosome Tumor Markers Via Queued Beads Combined with Quantum Dots in a Microarray. *Nano-Micro Lett.* **2019**, *11* (1). https://doi.org/10.1007/s40820-019-0285-x.

(115) Cheng, J.; Nonaka, T.; Wong, D. Salivary Exosomes as Nanocarriers for Cancer Biomarker Delivery. *Materials* **2019**, *12* (4), 654. https://doi.org/10.3390/ma12040654.

(116) Neyroud, A.-S.; Chiechio, R.; Yefimova, M.; Lo Faro, M. J.; Dejucq-Rainsford, N.; Jaillard, S.; Even-Hernandez, P.; Marchi, V.; Ravel, C. Extra-Cellular Vesicles of the Male Genital Tract: New Actors in Male Fertility? *Basic Clin. Androl.* **2021**, *31* (1), 25. https://doi.org/10.1186/s12610-021-00141-9.

(117) Gurunatha, K. L.; Fournier, A. C.; Urvoas, A.; Valerio-Lepiniec, M.; Marchi, V.; Minard, P.; Dujardin, E. Nanoparticles Self-Assembly Driven by High Affinity Repeat Protein Pairing. *ACS Nano* **2016**, *10* (3), 3176–3185.

https://doi.org/10.1021/acsnano.5b04531.

(118) Oh, E.; Huston, A. L.; Shabaev, A.; Efros, A.; Currie, M.; Susumu, K.; Bussmann, K.; Goswami, R.; Fatemi, F. K.; Medintz, I. L. Energy Transfer Sensitization of Luminescent Gold Nanoclusters: More than Just the Classical Förster Mechanism. *Sci. Rep.* **2016**, *6* (1), 35538. https://doi.org/10.1038/srep35538.

(119) Fernandez, M.; Urvoas, A.; Even-Hernandez, P.; Burel, A.; Artzner, F.; Bouceba, T.; Minard, P.; Dujardin, E. Hybrid Gold Nanoparticles-Quantum Dots Self- Assembled Nanostructures Driven by Complementary Artificial Proteins. 17.

(120) Hamon, C.; Postic, M.; Mazari, E.; Bizien, T.; Dupuis, C.; Even-Hernandez, P.; Jimenez, A.; Courbin, L.; Gosse, C.; Artzner, F.; Marchi-Artzner, V. Three-Dimensional Self-Assembling of Gold Nanorods with Controlled Macroscopic Shape and Local Smectic B Order. *ACS Nano* **2012**, *6* (5), 4137–4146. https://doi.org/10.1021/nn3006027.

(121) Stamplecoskie, K. G.; Chen, Y.-S.; Kamat, P. V. Excited-State Behavior of Luminescent Glutathione-Protected Gold Clusters. *J. Phys. Chem. C* **2014**, *118* (2), 1370–1376. https://doi.org/10.1021/jp410856h.

(122) Oh, E.; Fatemi, F. K.; Currie, M.; Delehanty, J. B.; Pons, T.; Fragola, A.; Lévêque-Fort, S.; Goswami, R.; Susumu, K.; Huston, A. L.; Medintz, I. L. PEGylated Luminescent Gold Nanoclusters: Synthesis, Characterization, Bioconjugation, and Application to One- and Two-Photon Cellular Imaging. *Part. Part. Syst. Charact.* **2013**, *30* (5), 453–466. https://doi.org/10.1002/ppsc.201200140.

(123) Matsushita-Ishiodori, Y.; Hanczyc, M. M.; Wang, A.; Szostak, J. W.; Yomo, T. Using Imaging Flow Cytometry to Quantify and Optimize Giant Vesicle Production by Water-in-Oil Emulsion Transfer Methods. *Langmuir* **2019**, *35* (6), 2375–2382. https://doi.org/10.1021/acs.langmuir.8b03635.

(124) Chiechio, R. M.; Ducarre, S.; Moulin, G.; Dupont, A.; Marets, C.; Even-Hernandez, P.; Artzner, F.; Musumeci, P.; Franzò, G.; Ravel, C.; LoFaro, M. J.; Marchi, V. Luminescent Gold Nanoclusters Interacting with Synthetic and Biological Vesicles. *J. Phys. Chem. Lett.* **2022**, *13* (30), 6935–6943. https://doi.org/10.1021/acs.jpclett.2c01071.

(125) Mayer, L. D.; Hope, M. J.; Cullis, P. R. Vesicles of Variable Sizes Produced by a Rapid Extrusion Procedure. *Biochim. Biophys. Acta BBA - Biomembr.* **1986**, *858* (1), 161–168. https://doi.org/10.1016/0005-2736(86)90302-0.

(126) *Interaction, Lipid Exchange, and Effect of Vesicle Size in Systems of Oppositely Charged Vesicles - The Journal of Physical Chemistry (ACS Publications)*. https://pubs.acs.org/doi/10.1021/jp960327f (accessed 2019-03-26).

(127) Kahlert, C.; Kalluri, R. Exosomes in Tumor Microenvironment Influence Cancer Progression and Metastasis. *J. Mol. Med.* **2013**, *91* (4), 431–437. https://doi.org/10.1007/s00109-013-1020-6.

(128) Li, X.; Wang, X. The Emerging Roles and Therapeutic Potential of Exosomes in Epithelial Ovarian Cancer. *Mol. Cancer* **2017**, *16* (1). https://doi.org/10.1186/s12943-017-0659-y.

(129) Milane, L.; Singh, A.; Mattheolabakis, G.; Suresh, M.; Amiji, M. M. Exosome Mediated Communication within the Tumor Microenvironment. *J. Controlled Release* **2015**, *219*, 278–294. https://doi.org/10.1016/j.jconrel.2015.06.029.

(130) Cheng, J.; Nonaka, T.; Wong, D. Salivary Exosomes as Nanocarriers for Cancer Biomarker Delivery. *Materials* **2019**, *12* (4), 654. https://doi.org/10.3390/ma12040654.

(131) Chiabotto; Gai; Deregibus; Camussi. Salivary Extracellular Vesicle-Associated ExRNA as Cancer Biomarker. *Cancers* **2019**, *11* (7), 891. https://doi.org/10.3390/cancers11070891.

(132) Zheng, H.; Xie, Z.; Zhang, X.; Mao, J.; Wang, M.; Wei, S.; Fu, Y.; Zheng, H.; He, Y.; Chen, H.; Xu, Y. Investigation of α-Synuclein Species in Plasma Exosomes and the Oligomeric and Phosphorylated α-Synuclein as Potential Peripheral Biomarker of Parkinson's Disease. *Neuroscience* **2021**, *469*, 79–90. https://doi.org/10.1016/j.neuroscience.2021.06.033.

(133) Rani, K.; Mukherjee, R.; Singh, E.; Kumar, S.; Sharma, V.; Vishwakarma, P.; Bharti, P. S.; Nikolajeff, F.; Dinda, A. K.; Goyal, V.; Kumar, S. Neuronal Exosomes in Saliva of Parkinson's Disease Patients: A Pilot Study. *Parkinsonism Relat. Disord.* **2019**, *67*, 21–23. https://doi.org/10.1016/j.parkreldis.2019.09.008.

(134) Falcone, G.; Felsani, A.; D'Agnano, I. Signaling by Exosomal MicroRNAs in Cancer. *J. Exp. Clin. Cancer Res.* **2015**, *34* (1). https://doi.org/10.1186/s13046-015-0148-3.

(135) Sun, S.; Pimentel, C.; Yefimova, M.; Jaillard, S.; Ravel, C. [Neo-oogenesis in the adult ovary: What do we know? *Gynecol. Obstet. Fertil. Senol.* **2019**, *47* (5), 478–483. https://doi.org/10.1016/j.gofs.2019.02.011.

(136) Sun, S.; Pimentel, C.; Yefimova, M.; Jaillard, S.; Ravel, C. [Neo-oogenesis in the adult ovary: What do we know?]. *Gynecol. Obstet. Fertil. Senol.* **2019**, *47* (5), 478–483. https://doi.org/10.1016/j.gofs.2019.02.011.

(137) Yefimova, M.; Bere, E.; Neyroud, A. S.; Jegou, B.; Bourmeyster, N.; Ravel, C. Myelinosome-like Vesicles in Human Seminal Plasma: A Cryo-Electron Microscopy Study. *Cryobiology* **2020**, *92*, 15–20. https://doi.org/10.1016/j.cryobiol.2019.09.009.

(138) Théry, C.; Witwer, K. W.; Aikawa, E.; Alcaraz, M. J.; Anderson, J. D.; Andriantsitohaina, R.; Antoniou, A.; Arab, T.; Archer, F.; Atkin-Smith, G. K.; Ayre, D. C.; Bach, J.-M.; Bachurski, D.; Baharvand, H.; Balaj, L.; Baldacchino, S.; Bauer, N. N.; Baxter, A. A.; Bebawy, M.; Beckham, C.; Bedina Zavec, A.; Benmoussa, A.; Berardi, A. C.; Bergese, P.; Bielska, E.; Blenkiron, C.; Bobis-Wozowicz, S.; Boilard, E.; Boireau, W.; Bongiovanni, A.; Borràs, F. E.; Bosch, S.; Boulanger, C. M.; Breakefield, X.; Breglio, A. M.; Brennan, M. Á.; Brigstock, D. R.; Brisson, A.; Broekman, M. L.; Bromberg, J. F.; Bryl-Górecka, P.; Buch, S.; Buck, A. H.; Burger, D.; Busatto, S.; Buschmann, D.; Bussolati, B.; Buzás, E. I.; Byrd, J. B.; Camussi, G.; Carter, D. R.; Caruso, S.; Chamley, L. W.; Chang, Y.-T.; Chen, C.; Chen, S.; Cheng, L.; Chin, A. R.; Clayton, A.; Clerici, S. P.; Cocks, A.; Cocucci, E.; Coffey, R. J.; Cordeiro-da-Silva, A.; Couch, Y.; Coumans, F. A.; Coyle, B.; Crescitelli, R.; Criado, M. F.; D'Souza-Schorey, C.; Das, S.; Datta Chaudhuri, A.; de Candia, P.; De Santana, E. F.; De Wever, O.; del Portillo, H. A.; Demaret, T.; Deville, S.; Devitt, A.; Dhondt, B.; Di Vizio, D.; Dieterich, L. C.; Dolo, V.; Dominguez Rubio, A. P.; Dominici, M.; Dourado, M. R.; Driedonks, T. A.; Duarte, F. V.; Duncan, H. M.; Eichenberger, R. M.; Ekström, K.; EL Andaloussi, S.; Elie-Caille, C.; Erdbrügger, U.; Falcón-Pérez, J. M.; Fatima, F.; Fish, J. E.; Flores-Bellver, M.; Försönits, A.; Frelet-Barrand, A.; Fricke, F.; Fuhrmann, G.; Gabrielsson, S.; Gámez-Valero, A.; Gardiner, C.; Gärtner, K.; Gaudin, R.; Gho, Y. S.; Giebel, B.; Gilbert, C.; Gimona, M.; Giusti, I.; Goberdhan, D. C.; Görgens, A.; Gorski, S. M.; Greening, D. W.; Gross, J. C.; Gualerzi, A.; Gupta, G. N.; Gustafson, D.; Handberg, A.; Haraszti, R. A.; Harrison, P.; Hegyesi, H.; Hendrix, A.; Hill, A. F.; Hochberg, F. H.; Hoffmann, K. F.; Holder, B.; Holthofer, H.; Hosseinkhani, B.; Hu, G.; Huang, Y.; Huber, V.; Hunt, S.; Ibrahim, A. G.-E.; Ikezu, T.; Inal, J. M.; Isin, M.; Ivanova, A.; Jackson, H. K.; Jacobsen, S.; Jay, S. M.; Jayachandran, M.; Jenster, G.; Jiang, L.; Johnson, S. M.; Jones, J. C.; Jong, A.; Jovanovic-Talisman, T.; Jung, S.; Kalluri, R.; Kano, S.; Kaur, S.; Kawamura, Y.; Keller, E. T.; Khamari, D.; Khomyakova, E.; Khvorova, A.; Kierulf, P.; Kim, K. P.; Kislinger, T.; Klingeborn, M.; Klinke, D. J.; Kornek, M.; Kosanović, M. M.; Kovács, Á. F.; Krämer-Albers, E.-M.; Krasemann, S.; Krause, M.; Kurochkin, I. V.; Kusuma, G. D.; Kuypers, S.; Laitinen, S.; Langevin, S. M.; Languino, L. R.; Lannigan, J.; Lässer, C.; Laurent, L. C.; Lavieu, G.; Lázaro-Ibáñez, E.; Le Lay, S.; Lee, M.-S.; Lee, Y. X. F.; Lemos, D. S.; Lenassi, M.; Leszczynska, A.; Li, I. T.; Liao, K.; Libregts, S. F.; Ligeti, E.; Lim, R.; Lim, S. K.; Linē, A.; Linnemannstöns, K.; Llorente, A.; Lombard, C. A.; Lorenowicz, M. J.; Lörincz, Á. M.; Lötvall, J.; Lovett, J.; Lowry, M. C.; Loyer, X.; Lu, Q.; Lukomska, B.; Lunavat, T. R.; Maas, S. L.; Malhi, H.; Marcilla, A.; Mariani, J.; Mariscal, J.; Martens-Uzunova, E. S.; Martin-Jaular, L.; Martinez, M. C.; Martins, V. R.; Mathieu, M.; Mathivanan, S.; Maugeri, M.; McGinnis, L. K.; McVey, M. J.; Meckes, D. G.; Meehan, K. L.; Mertens, I.; Minciacchi, V. R.; Möller, A.; Møller Jørgensen, M.; Morales-Kastresana, A.; Morhayim, J.; Mullier, F.; Muraca, M.; Musante, L.; Mussack, V.; Muth, D. C.; Myburgh, K. H.; Najrana, T.; Nawaz, M.; Nazarenko, I.; Nejsum, P.; Neri, C.; Neri, T.; Nieuwland, R.; Nimrichter, L.; Nolan, J. P.; Nolte-'t Hoen, E. N.; Noren Hooten, N.; O'Driscoll, L.; O'Grady, T.; O'Loghlen, A.; Ochiya, T.; Olivier, M.; Ortiz, A.; Ortiz, L. A.; Osteikoetxea, X.; Østergaard, O.; Ostrowski, M.; Park, J.; Pegtel, D. M.; Peinado, H.; Perut, F.; Pfaffl, M. W.; Phinney, D. G.; Pieters, B. C.; Pink, R. C.; Pisetsky, D. S.; Pogge von Strandmann, E.; Polakovicova, I.; Poon, I. K.; Powell, B. H.; Prada, I.; Pulliam, L.; Quesenberry, P.; Radeghieri, A.; Raffai, R. L.; Raimondo, S.; Rak, J.; Ramirez, M. I.; Raposo, G.; Rayyan, M. S.; Regev-Rudzki, N.; Ricklefs, F. L.; Robbins, P. D.; Roberts, D. D.; Rodrigues, S. C.; Rohde, E.; Rome, S.; Rouschop, K. M.; Rughetti, A.; Russell, A. E.; Saá, P.; Sahoo, S.; Salas-Huenuleo, E.; Sánchez, C.; Saugstad, J. A.; Saul, M. J.; Schiffelers, R. M.; Schneider, R.; Schøyen, T. H.; Scott, A.; Shahaj, E.; Sharma, S.; Shatnyeva,

O.; Shekari, F.; Shelke, G. V.; Shetty, A. K.; Shiba, K.; Siljander, P. R.-M.; Silva, A. M.; Skowronek, A.; Snyder, O. L.; Soares, R. P.; Sódar, B. W.; Soekmadji, C.; Sotillo, J.; Stahl, P. D.; Stoorvogel, W.; Stott, S. L.; Strasser, E. F.; Swift, S.; Tahara, H.; Tewari, M.; Timms, K.; Tiwari, S.; Tixeira, R.; Tkach, M.; Toh, W. S.; Tomasini, R.; Torrecilhas, A. C.; Tosar, J. P.; Toxavidis, V.; Urbanelli, L.; Vader, P.; van Balkom, B. W.; van der Grein, S. G.; Van Deun, J.; van Herwijnen, M. J.; Van Keuren-Jensen, K.; van Niel, G.; van Royen, M. E.; van Wijnen, A. J.; Vasconcelos, M. H.; Vechetti, I. J.; Veit, T. D.; Vella, L. J.; Velot, É.; Verweij, F. J.; Vestad, B.; Viñas, J. L.; Visnovitz, T.; Vukman, K. V.; Wahlgren, J.; Watson, D. C.; Wauben, M. H.; Weaver, A.; Webber, J. P.; Weber, V.; Wehman, A. M.; Weiss, D. J.; Welsh, J. A.; Wendt, S.; Wheelock, A. M.; Wiener, Z.; Witte, L.; Wolfram, J.; Xagorari, A.; Xander, P.; Xu, J.; Yan, X.; Yáñez-Mó, M.; Yin, H.; Yuana, Y.; Zappulli, V.; Zarubova, J.; Žėkas, V.; Zhang, J.; Zhao, Z.; Zheng, L.; Zheutlin, A. R.; Zickler, A. M.; Zimmermann, P.; Zivkovic, A. M.; Zocco, D.; Zuba-Surma, E. K. Minimal Information for Studies of Extracellular Vesicles 2018 (MISEV2018): A Position Statement of the International Society for Extracellular Vesicles and Update of the MISEV2014 Guidelines. *J. Extracell. Vesicles* **2018**, *7* (1), 1535750. https://doi.org/10.1080/20013078.2018.1535750.

(139) Silveira, J. C. da; Andrade, G. M.; Collado, M. del; Sampaio, R. V.; Sangalli, J. R.; Silva, L. A.; Pinaffi, F. V. L.; Jardim, I. B.; Cesar, M. C.; Nogueira, M. F. G.; Cesar, A. S. M.; Coutinho, L. L.; Pereira, R. W.; Perecin, F.; Meirelles, F. V. Supplementation with Small-Extracellular Vesicles from Ovarian Follicular Fluid during in Vitro Production Modulates Bovine Embryo Development. *PLOS ONE* **2017**, *12* (6), e0179451. https://doi.org/10.1371/journal.pone.0179451.

(140) Gardiner, C.; Vizio, D. D.; Sahoo, S.; Théry, C.; Witwer, K. W.; Wauben, M.; Hill, A. F. Techniques Used for the Isolation and Characterization of Extracellular Vesicles: Results of a Worldwide Survey. *J. Extracell. Vesicles* **2016**, *5* (1), 32945. https://doi.org/10.3402/jev.v5.32945.

(141) Brennan, K.; Martin, K.; FitzGerald, S. P.; O'Sullivan, J.; Wu, Y.; Blanco, A.; Richardson, C.; Mc Gee, M. M. A Comparison of Methods for the Isolation and Separation of Extracellular Vesicles from Protein and Lipid Particles in Human Serum. *Sci. Rep.* **2020**, *10* (1), 1039. https://doi.org/10.1038/s41598-020-57497-7.

(142) da Silveira, J. C.; Veeramachaneni, D. N. R.; Winger, Q. A.; Carnevale, E. M.; Bouma, G. J. Cell-Secreted Vesicles in Equine Ovarian Follicular Fluid Contain MiRNAs and Proteins: A Possible New Form of Cell Communication within the Ovarian Follicle. *Biol. Reprod.* **2012**, *86* (3), 71. https://doi.org/10.1095/biolreprod.111.093252.

(143) Hung, W.-T.; Hong, X.; Christenson, L. K.; McGinnis, L. K. Extracellular Vesicles from Bovine Follicular Fluid Support Cumulus Expansion1. *Biol. Reprod.* **2015**, *93* (5). https://doi.org/10.1095/biolreprod.115.132977.

(144) da Silveira, J. C.; Andrade, G. M.; del Collado, M.; Sampaio, R. V.; Sangalli, J. R.; Silva, L. A.; Pinaffi, F. V. L.; Jardim, I. B.; Cesar, M. C.; Nogueira, M. F. G.; Cesar, A. S. M.; Coutinho, L. L.; Pereira, R. W.; Perecin, F.; Meirelles, F. V. Supplementation with Small-Extracellular Vesicles from Ovarian Follicular Fluid during in Vitro Production Modulates Bovine Embryo Development. *PLOS ONE* **2017**, *12* (6), e0179451. https://doi.org/10.1371/journal.pone.0179451.

(145) Sohel, M. M. H.; Hoelker, M.; Noferesti, S. S.; Salilew-Wondim, D.; Tholen, E.; Looft, C.; Rings, F.; Uddin, M. J.; Spencer, T. E.; Schellander, K.; Tesfaye, D. Exosomal and Non-Exosomal Transport of Extra-Cellular MicroRNAs in Follicular Fluid: Implications for Bovine Oocyte Developmental Competence. *PloS One* **2013**, *8* (11), e78505. https://doi.org/10.1371/journal.pone.0078505.

(146) Théry, C.; Witwer, K. W.; Aikawa, E.; Alcaraz, M. J.; Anderson, J. D.; Andriantsitohaina, R.; Antoniou, A.; Arab, T.; Archer, F.; Atkin-Smith, G. K.; Ayre, D. C.; Bach, J.-M.; Bachurski, D.; Baharvand, H.; Balaj, L.; Baldacchino, S.; Bauer, N. N.; Baxter, A. A.; Bebawy, M.; Beckham, C.; Bedina Zavec, A.; Benmoussa, A.; Berardi, A. C.; Bergese, P.; Bielska, E.; Blenkiron, C.; Bobis-Wozowicz, S.; Boilard, E.; Boireau, W.; Bongiovanni, A.; Borràs, F. E.; Bosch, S.; Boulanger, C. M.; Breakefield, X.; Breglio, A. M.; Brennan, M. Á.; Brigstock, D. R.; Brisson, A.; Broekman, M. L.; Bromberg, J. F.; Bryl-Górecka, P.; Buch, S.; Buck, A. H.; Burger, D.; Busatto, S.; Buschmann, D.; Bussolati, B.; Buzás, E. I.; Byrd, J. B.; Camussi, G.; Carter, D. R.; Caruso, S.; Chamley, L. W.; Chang, Y.-T.; Chen, C.; Chen, S.; Cheng, L.; Chin, A. R.; Clayton, A.; Clerici, S. P.; Cocks, A.; Cocucci, E.; Coffey, R. J.; Cordeiro-da-Silva, A.; Couch, Y.; Coumans, F. A.; Coyle, B.; Crescitelli, R.; Criado, M. F.; D'Souza-Schorey, C.; Das, S.; Datta Chaudhuri, A.; de Candia, P.; De Santana Junior, E. F.; De Wever, O.; del Portillo, H. A.; Demaret, T.; Deville, S.; Devitt, A.; Dhondt, B.; Di Vizio, D.; Dieterich, L. C.; Dolo, V.; Dominguez Rubio, A. P.;

Dominici, M.; Dourado, M. R.; Driedonks, T. A.; Duarte, F. V.; Duncan, H. M.; Eichenberger, R. M.; Ekström, K.; EL Andaloussi, S.; Elie-Caille, C.; Erdbrügger, U.; Falcón-Pérez, J. M.; Fatima, F.; Fish, J. E.; Flores-Bellver, M.; Försönits, A.; Frelet-Barrand, A.; Fricke, F.; Fuhrmann, G.; Gabrielsson, S.; Gámez-Valero, A.; Gardiner, C.; Gärtner, K.; Gaudin, R.; Gho, Y. S.; Giebel, B.; Gilbert, C.; Gimona, M.; Giusti, I.; Goberdhan, D. C.; Görgens, A.; Gorski, S. M.; Greening, D. W.; Gross, J. C.; Gualerzi, A.; Gupta, G. N.; Gustafson, D.; Handberg, A.; Haraszti, R. A.; Harrison, P.; Hegyesi, H.; Hendrix, A.; Hill, A. F.; Hochberg, F. H.; Hoffmann, K. F.; Holder, B.; Holthofer, H.; Hosseinkhani, B.; Hu, G.; Huang, Y.; Huber, V.; Hunt, S.; Ibrahim, A. G.-E.; Ikezu, T.; Inal, J. M.; Isin, M.; Ivanova, A.; Jackson, H. K.; Jacobsen, S.; Jay, S. M.; Jayachandran, M.; Jenster, G.; Jiang, L.; Johnson, S. M.; Jones, J. C.; Jong, A.; Jovanovic-Talisman, T.; Jung, S.; Kalluri, R.; Kano, S.; Kaur, S.; Kawamura, Y.; Keller, E. T.; Khamari, D.; Khomyakova, E.; Khvorova, A.; Kierulf, P.; Kim, K. P.; Kislinger, T.; Klingeborn, M.; Klinke II, D. J.; Kornek, M.; Kosanović, M. M.; Kovács, Á. F.; Krämer-Albers, E.-M.; Krasemann, S.; Krause, M.; Kurochkin, I. V.; Kusuma, G. D.; Kuypers, S.; Laitinen, S.; Langevin, S. M.; Languino, L. R.; Lannigan, J.; Lässer, C.; Laurent, L. C.; Lavieu, G.; Lázaro-Ibáñez, E.; Le Lay, S.; Lee, M.-S.; Lee, Y. X. F.; Lemos, D. S.; Lenassi, M.; Leszczynska, A.; Li, I. T.; Liao, K.; Libregts, S. F.; Ligeti, E.; Lim, R.; Lim, S. K.; Linē, A.; Linnemannstöns, K.; Llorente, A.; Lombard, C. A.; Lorenowicz, M. J.; Lörincz, Á. M.; Lötvall, J.; Lovett, J.; Lowry, M. C.; Loyer, X.; Lu, Q.; Lukomska, B.; Lunavat, T. R.; Maas, S. L.; Malhi, H.; Marcilla, A.; Mariani, J.; Mariscal, J.; Martens-Uzunova, E. S.; Martin-Jaular, L.; Martinez, M. C.; Martins, V. R.; Mathieu, M.; Mathivanan, S.; Maugeri, M.; McGinnis, L. K.; McVey, M. J.; Meckes Jr, D. G.; Meehan, K. L.; Mertens, I.; Minciacchi, V. R.; Möller, A.; Møller Jørgensen, M.; Morales-Kastresana, A.; Morhayim, J.; Mullier, F.; Muraca, M.; Musante, L.; Mussack, V.; Muth, D. C.; Myburgh, K. H.; Najrana, T.; Nawaz, M.; Nazarenko, I.; Nejsum, P.; Neri, C.; Neri, T.; Nieuwland, R.; Nimrichter, L.; Nolan, J. P.; Nolte-'t Hoen, E. N.; Noren Hooten, N.; O'Driscoll, L.; O'Grady, T.; O'Loghlen, A.; Ochiya, T.; Olivier, M.; Ortiz, A.; Ortiz, L. A.; Osteikoetxea, X.; Østergaard, O.; Ostrowski, M.; Park, J.; Pegtel, D. M.; Peinado, H.; Perut, F.; Pfaffl, M. W.; Phinney, D. G.; Pieters, B. C.; Pink, R. C.; Pisetsky, D. S.; Pogge von Strandmann, E.; Polakovicova, I.; Poon, I. K.; Powell, B. H.; Prada, I.; Pulliam, L.; Quesenberry, P.; Radeghieri, A.; Raffai, R. L.; Raimondo, S.; Rak, J.; Ramirez, M. I.; Raposo, G.; Rayyan, M. S.; Regev-Rudzki, N.; Ricklefs, F. L.; Robbins, P. D.; Roberts, D. D.; Rodrigues, S. C.; Rohde, E.; Rome, S.; Rouschop, K. M.; Rughetti, A.; Russell, A. E.; Saá, P.; Sahoo, S.; Salas-Huenuleo, E.; Sánchez, C.; Saugstad, J. A.; Saul, M. J.; Schiffelers, R. M.; Schneider, R.; Schøyen, T. H.; Scott, A.; Shahaj, E.; Sharma, S.; Shatnyeva, O.; Shekari, F.; Shelke, G. V.; Shetty, A. K.; Shiba, K.; Siljander, P. R.-M.; Silva, A. M.; Skowronek, A.; Snyder II, O. L.; Soares, R. P.; Sódar, B. W.; Soekmadji, C.; Sotillo, J.; Stahl, P. D.; Stoorvogel, W.; Stott, S. L.; Strasser, E. F.; Swift, S.; Tahara, H.; Tewari, M.; Timms, K.; Tiwari, S.; Tixeira, R.; Tkach, M.; Toh, W. S.; Tomasini, R.; Torrecilhas, A. C.; Tosar, J. P.; Toxavidis, V.; Urbanelli, L.; Vader, P.; van Balkom, B. W.; van der Grein, S. G.; Van Deun, J.; van Herwijnen, M. J.; Van Keuren-Jensen, K.; van Niel, G.; van Royen, M. E.; van Wijnen, A. J.; Vasconcelos, M. H.; Vechetti Jr, I. J.; Veit, T. D.; Vella, L. J.; Velot, É.; Verweij, F. J.; Vestad, B.; Viñas, J. L.; Visnovitz, T.; Vukman, K. V.; Wahlgren, J.; Watson, D. C.; Wauben, M. H.; Weaver, A.; Webber, J. P.; Weber, V.; Wehman, A. M.; Weiss, D. J.; Welsh, J. A.; Wendt, S.; Wheelock, A. M.; Wiener, Z.; Witte, L.; Wolfram, J.; Xagorari, A.; Xander, P.; Xu, J.; Yan, X.; Yáñez-Mó, M.; Yin, H.; Yuana, Y.; Zappulli, V.; Zarubova, J.; Žėkas, V.; Zhang, J.; Zhao, Z.; Zheng, L.; Zheutlin, A. R.; Zickler, A. M.; Zimmermann, P.; Zivkovic, A. M.; Zocco, D.; Zuba-Surma, E. K. Minimal Information for Studies of Extracellular Vesicles 2018 (MISEV2018): A Position Statement of the International Society for Extracellular Vesicles and Update of the MISEV2014 Guidelines. *J. Extracell. Vesicles* **2018**, *7* (1), 1535750. https://doi.org/10.1080/20013078.2018.1535750.

(147) Silva, A. K. A.; Morille, M.; Piffoux, M.; Arumugam, S.; Mauduit, P.; Larghero, J.; Bianchi, A.; Aubertin, K.; Blanc-Brude, O.; Noël, D.; Velot, E.; Ravel, C.; Elie-Caille, C.; Sebbagh, A.; Boulanger, C.; Wilhelm, C.; Rahmi, G.; Raymond-Letron, I.; Cherukula, K.; Montier, T.; Martinaud, C.; Bach, J.-M.; Favre-Bulle, O.; Spadavecchia, J.; Jorgensen, C.; Menasché, P.; Aussel, C.; Chopineau, J.; Mosser, M.; Ullah, M.; Sailliet, N.; Luciani, N.; Mathieu, N.; Rautou, P.-E.; Brouard, S.; Boireau, W.; Jauliac, S.; Dedier, M.; Trouvin, J.-H.; Gazeau, F.; Trouillas, M.; Peltzer, J.; Monsel, A.; Banzet, S. Development of Extracellular Vesicle-Based Medicinal Products: A Position Paper of the Group "Extracellular Vesicle TranslatiOn to ClinicaL PerspectiVEs - EVOLVE France." *Adv. Drug Deliv. Rev.* **2021**, *179*, 114001. https://doi.org/10.1016/j.addr.2021.114001.

(148) Diaz-Rohrer, B.; Levental, K. R.; Levental, I. Rafting through Traffic: Membrane Domains in Cellular Logistics. *Biochim. Biophys. Acta BBA - Biomembr.* **2014**, *1838* (12), 3003–3013. https://doi.org/10.1016/j.bbamem.2014.07.029.

(149) Höög, J. L.; Lötvall, J. Diversity of Extracellular Vesicles in Human Ejaculates Revealed by Cryo-Electron

Microscopy. *J. Extracell. Vesicles* **2015**, *4* (1), 28680. https://doi.org/10.3402/jev.v4.28680.

(150) Yefimova, M.; Bere, E.; Neyroud, A. S.; Jegou, B.; Bourmeyster, N.; Ravel, C. Myelinosome-like Vesicles in Human Seminal Plasma: A Cryo-Electron Microscopy Study. *Cryobiology* **2020**, *92*, 15–20. https://doi.org/10.1016/j.cryobiol.2019.09.009.

(151) Neyroud, A.-S.; Chiechio, R.; Yefimova, M.; Lo Faro, M. J.; Dejucq-Rainsford, N.; Jaillard, S.; Even-Hernandez, P.; Marchi, V.; Ravel, C. Extra-Cellular Vesicles of the Male Genital Tract: New Actors in Male Fertility? *Basic Clin. Androl.* **2021**, *31* (1), 25. https://doi.org/10.1186/s12610-021-00141-9.

(152) Arraud, N.; Linares, R.; Tan, S.; Gounou, C.; Pasquet, J.-M.; Mornet, S.; Brisson, A. R. Extracellular Vesicles from Blood Plasma: Determination of Their Morphology, Size, Phenotype and Concentration. *J. Thromb. Haemost.* **2014**, *12* (5), 614–627. https://doi.org/10.1111/jth.12554.

(153) Arraud, N.; Linares, R.; Tan, S.; Gounou, C.; Pasquet, J.-M.; Mornet, S.; Brisson, A. R. Extracellular Vesicles from Blood Plasma: Determination of Their Morphology, Size, Phenotype and Concentration. *J. Thromb. Haemost.* **2014**, *12* (5), 614–627. https://doi.org/10.1111/jth.12554.

(154) Santonocito, M.; Vento, M.; Guglielmino, M. R.; Battaglia, R.; Wahlgren, J.; Ragusa, M.; Barbagallo, D.; Borzì, P.; Rizzari, S.; Maugeri, M.; Scollo, P.; Tatone, C.; Valadi, H.; Purrello, M.; Di Pietro, C. Molecular Characterization of Exosomes and Their MicroRNA Cargo in Human Follicular Fluid: Bioinformatic Analysis Reveals That Exosomal MicroRNAs Control Pathways Involved in Follicular Maturation. *Fertil. Steril.* **2014**, *102* (6), 1751-1761.e1. https://doi.org/10.1016/j.fertnstert.2014.08.005.

(155) Qasemi, M.; Amidi, F. Extracellular MicroRNA Profiling in Human Follicular Fluid: New Biomarkers in Female Reproductive Potential. *J. Assist. Reprod. Genet.* **2020**, *37* (8), 1769–1780. https://doi.org/10.1007/s10815-020-01860-0.

(156) Asaadi, A.; Dolatabad, N. A.; Atashi, H.; Raes, A.; Van Damme, P.; Hoelker, M.; Hendrix, A.; Pascottini, O. B.; Van Soom, A.; Kafi, M.; Pavani, K. C. Extracellular Vesicles from Follicular and Ampullary Fluid Isolated by Density Gradient Ultracentrifugation Improve Bovine Embryo Development and Quality. *Int. J. Mol. Sci.* **2021**, *22* (2), 578. https://doi.org/10.3390/ijms22020578.

(157) Barile, L.; Vassalli, G. Exosomes: Therapy Delivery Tools and Biomarkers of Diseases. *Pharmacol. Ther.* **2017**, *174*, 63–78. https://doi.org/10.1016/j.pharmthera.2017.02.020.

(158) Dubochet, J.; Adrian, M.; Chang, J. J.; Homo, J. C.; Lepault, J.; McDowall, A. W.; Schultz, P. Cryo-Electron Microscopy of Vitrified Specimens. *Q. Rev. Biophys.* **1988**, *21* (2), 129–228. https://doi.org/10.1017/s0033583500004297.

(159) da Silveira, J. C.; Andrade, G. M.; Del Collado, M.; Sampaio, R. V.; Sangalli, J. R.; Silva, L. A.; Pinaffi, F. V. L.; Jardim, I. B.; Cesar, M. C.; Nogueira, M. F. G.; Cesar, A. S. M.; Coutinho, L. L.; Pereira, R. W.; Perecin, F.; Meirelles, F. V. Supplementation with Small-Extracellular Vesicles from Ovarian Follicular Fluid during in Vitro Production Modulates Bovine Embryo Development. *PloS One* **2017**, *12* (6), e0179451. https://doi.org/10.1371/journal.pone.0179451.

(160) Macaulay, A. D.; Gilbert, I.; Caballero, J.; Barreto, R.; Fournier, E.; Tossou, P.; Sirard, M.-A.; Clarke, H. J.; Khandjian, É. W.; Richard, F. J.; Hyttel, P.; Robert, C. The Gametic Synapse: RNA Transfer to the Bovine Oocyte. *Biol. Reprod.* **2014**, *91* (4), 90. https://doi.org/10.1095/biolreprod.114.119867.

(161) Bertho, S.; Neyroud, A. S.; Brun, T.; Jaillard, S.; Bonnet, F.; Ravel, C. Anti-Müllerian Hormone: A Function beyond the Müllerian Structures. *Morphologie* **2021**, S1286011521002514. https://doi.org/10.1016/j.morpho.2021.11.002.

(162) Azziz, R.; Carmina, E.; Chen, Z.; Dunaif, A.; Laven, J. S. E.; Legro, R. S.; Lizneva, D.; Natterson-Horowtiz, B.; Teede, H. J.; Yildiz, B. O. Polycystic Ovary Syndrome. *Nat. Rev. Dis. Primer* **2016**, *2* (1), 16057.

https://doi.org/10.1038/nrdp.2016.57.

(163) Ehrmann, D. A. Polycystic Ovary Syndrome. *N. Engl. J. Med.* **2005**, 14.

(164) Sigala, J.; Sifer, C.; Dewailly, D.; Robin, G.; Bruyneel, A.; Ramdane, N.; Lefebvre-Khalil, V.; Mitchell, V.; Decanter, C. Is Polycystic Ovarian Morphology Related to a Poor Oocyte Quality after Controlled Ovarian Hyperstimulation for Intracytoplasmic Sperm Injection? Results from a Prospective, Comparative Study. *Fertil. Steril.* **2015**, *103* (1), 112–118. https://doi.org/10.1016/j.fertnstert.2014.09.040.

(165) Gleicher, N.; Darmon, S.; Patrizio, P.; Barad, D. H. Reconsidering the Polycystic Ovary Syndrome (PCOS). *Biomedicines* **2022**, *10* (7), 1505. https://doi.org/10.3390/biomedicines10071505.

(166) Ravel, C.; Kazdar, N.; Leveque, J. Fertilité et insuffisance ovarienne : de nouveaux traitements en perspective ? *Gynécologie Obstétrique Fertil.* **2016**, *44* (1), 56–62. https://doi.org/10.1016/j.gyobfe.2015.10.008.

(167) Battaglia, R.; Musumeci, P.; Ragusa, M.; Barbagallo, D.; Scalia, M.; Zimbone, M.; Lo Faro, J. M.; Borzì, P.; Scollo, P.; Purrello, M.; Vento, E. M.; Di Pietro, C. Ovarian Aging Increases Small Extracellular Vesicle CD81+ Release in Human Follicular Fluid and Influences MiRNA Profiles. *Aging* **2020**, *12* (12), 12324–12341. https://doi.org/10.18632/aging.103441.

(168) Battaglia, R.; Palini, S.; Vento, M. E.; La Ferlita, A.; Lo Faro, M. J.; Caroppo, E.; Borzì, P.; Falzone, L.; Barbagallo, D.; Ragusa, M.; Scalia, M.; D'Amato, G.; Scollo, P.; Musumeci, P.; Purrello, M.; Gravotta, E.; Di Pietro, C. Identification of Extracellular Vesicles and Characterization of MiRNA Expression Profiles in Human Blastocoel Fluid. *Sci. Rep.* **2019**, *9* (1). https://doi.org/10.1038/s41598-018-36452-7.

(169) Yang, Z.; Du, X.; Wang, C.; Zhang, J.; Liu, C.; Li, Y.; Jiang, H. Therapeutic Effects of Human Umbilical Cord Mesenchymal Stem Cell-Derived Microvesicles on Premature Ovarian Insufficiency in Mice. *Stem Cell Res. Ther.* **2019**, *10* (1), 250. https://doi.org/10.1186/s13287-019-1327-5.

(170) Sun, B.; Ma, Y.; Wang, F.; Hu, L.; Sun, Y. MiR-644-5p Carried by Bone Mesenchymal Stem Cell-Derived Exosomes Targets Regulation of P53 to Inhibit Ovarian Granulosa Cell Apoptosis. *Stem Cell Res. Ther.* **2019**, *10* (1), 360. https://doi.org/10.1186/s13287-019-1442-3.

(171) Cai, J.-H.; Sun, Y.-T.; Bao, S. HucMSCs-Exosomes Containing MiR-21 Promoted Estrogen Production in Ovarian Granulosa Cells via LATS1-Mediated Phosphorylation of LOXL2 and YAP. *Gen. Comp. Endocrinol.* **2022**, *321–322*, 114015. https://doi.org/10.1016/j.ygcen.2022.114015.

(172) de Almeida Monteiro Melo Ferraz, M.; Fujihara, M.; Nagashima, J. B.; Noonan, M. J.; Inoue-Murayama, M.; Songsasen, N. Follicular Extracellular Vesicles Enhance Meiotic Resumption of Domestic Cat Vitrified Oocytes. *Sci. Rep.* **2020**, *10* (1), 8619. https://doi.org/10.1038/s41598-020-65497-w.

(173) Zhang, T.; Wang, Z.; Xiang, H.; Xu, X.; Zou, J.; Lu, C. Biocompatible Superparamagnetic Europium-Doped Iron Oxide Nanoparticle Clusters as Multifunctional Nanoprobes for Multimodal *In Vivo* Imaging. *ACS Appl. Mater. Interfaces* **2021**, *13* (29), 33850–33861. https://doi.org/10.1021/acsami.1c07739.

(174) Wegner, K. D.; Hildebrandt, N. Quantum Dots: Bright and Versatile in Vitro and in Vivo Fluorescence Imaging Biosensors. *Chem. Soc. Rev.* **2015**, *44* (14), 4792–4834. https://doi.org/10.1039/C4CS00532E.

(175) Zhang, L.; Wang, E. Metal Nanoclusters: New Fluorescent Probes for Sensors and Bioimaging. *Nano Today* **2014**, *9* (1), 132–157. https://doi.org/10.1016/j.nantod.2014.02.010.

(176) *Metal nanoclusters: New fluorescent probes for sensors and bioimaging - ScienceDirect*. https://www.sciencedirect.com/science/article/pii/S1748013214000267 (accessed 2019-01-07).

(177) Cantelli, A.; Battistelli, G.; Guidetti, G.; Manzi, J.; Di Giosia, M.; Montalti, M. Luminescent Gold Nanoclusters as

Biocompatible Probes for Optical Imaging and Theranostics. *Dyes Pigments* **2016**, *135*, 64–79. https://doi.org/10.1016/j.dyepig.2016.06.019.

(178) Shaikh, S.; Rehman, F. ur; Du, T.; Jiang, H.; Yin, L.; Wang, X.; Chai, R. Real-Time Multimodal Bioimaging of Cancer Cells and Exosomes through Biosynthesized Iridium and Iron Nanoclusters. *ACS Appl. Mater. Interfaces* **2018**, *10* (31), 26056–26063. https://doi.org/10.1021/acsami.8b08975.

(179) Nonappa. Luminescent Gold Nanoclusters for Bioimaging Applications. *Beilstein J. Nanotechnol.* **2020**, *11* (1), 533–546. https://doi.org/10.3762/bjnano.11.42.

(180) Hong, Y.; Che, S.; Hui, B.; Yang, Y.; Wang, X.; Zhang, X.; Qiang, Y.; Ma, H. Lung Cancer Therapy Using Doxorubicin and Curcumin Combination: Targeted Prodrug Based, PH Sensitive Nanomedicine. *Biomed. Pharmacother.* **2019**, *112*, 108614. https://doi.org/10.1016/j.biopha.2019.108614.

(181) Liang, G.; Jin, X.; Zhang, S.; Xing, D. RGD Peptide-Modified Fluorescent Gold Nanoclusters as Highly Efficient Tumor-Targeted Radiotherapy Sensitizers. *Biomaterials* **2017**, *144*, 95–104. https://doi.org/10.1016/j.biomaterials.2017.08.017.

(182) Desplancq, D.; Groysbeck, N.; Chiper, M.; Weiss, E.; Frisch, B.; Strub, J.-M.; Cianferani, S.; Zafeiratos, S.; Moeglin, E.; Holy, X.; Favier, A. L.; De Carlo, S.; Schultz, P.; Spehner, D.; Zuber, G. Cytosolic Diffusion and Peptide-Assisted Nuclear Shuttling of Peptide-Substituted Circa 102 Gold Atom Nanoclusters in Living Cells. *ACS Appl. Nano Mater.* **2018**, *1* (8), 4236–4246. https://doi.org/10.1021/acsanm.8b00988.

(183) Vankayala, R.; Kuo, C.-L.; Nuthalapati, K.; Chiang, C.-S.; Hwang, K. C. Nucleus-Targeting Gold Nanoclusters for Simultaneous In Vivo Fluorescence Imaging, Gene Delivery, and NIR-Light Activated Photodynamic Therapy. *Adv. Funct. Mater.* **2015**, *25* (37), 5934–5945. https://doi.org/10.1002/adfm.201502650.

(184) *Structure of Human Urokinase Plasminogen Activator in Complex with Its Receptor*. http://www.science.org/doi/10.1126/science.1121143 (accessed 2022-04-14). https://doi.org/10.1126/science.1121143.

(185) Wang, M.; Löwik, D. W. P. M.; Miller, A. D.; Thanou, M. Targeting the Urokinase Plasminogen Activator Receptor with Synthetic Self-Assembly Nanoparticles. *Bioconjug. Chem.* **2009**, *20* (1), 32–40. https://doi.org/10.1021/bc8001908.

(186) Wang, M.; Miller, A. D.; Thanou, M. Effect of Surface Charge and Ligand Organization on the Specific Cell-Uptake of UPAR-Targeted Nanoparticles. *J. Drug Target.* **2013**, *21* (7), 684–692. https://doi.org/10.3109/1061186X.2013.805336.

(187) Avvakumova, S.; Galbiati, E.; Pandolfi, L.; Mazzucchelli, S.; Cassani, M.; Gori, A.; Longhi, R.; Prosperi, D. Development of U11-Functionalized Gold Nanoparticles for Selective Targeting of Urokinase Plasminogen Activator Receptor-Positive Breast Cancer Cells. *Bioconjug. Chem.* **2014**, *25* (8), 1381–1386. https://doi.org/10.1021/bc500202b.

(188) Park, J. H.; Oh, N. Endocytosis and Exocytosis of Nanoparticles in Mammalian Cells. *Int. J. Nanomedicine* **2014**, 51. https://doi.org/10.2147/IJN.S26592.

(189) Luo, Z.; Yuan, X.; Yu, Y.; Zhang, Q.; Leong, D. T.; Lee, J. Y.; Xie, J. From Aggregation-Induced Emission of Au(I)–Thiolate Complexes to Ultrabright Au(0)@Au(I)–Thiolate Core–Shell Nanoclusters. *J. Am. Chem. Soc.* **2012**, *134* (40), 16662–16670. https://doi.org/10.1021/ja306199p.

(190) Braunbeck, T.; Kais, B.; Lammer, E.; Otte, J.; Schneider, K.; Stengel, D.; Strecker, R. The Fish Embryo Test (FET): Origin, Applications, and Future. *Environ. Sci. Pollut. Res.* **2015**, *22* (21), 16247–16261. https://doi.org/10.1007/s11356-014-3814-7.

(191) Haque, E.; Ward, A. Zebrafish as a Model to Evaluate Nanoparticle Toxicity. *Nanomaterials* **2018**, *8* (7), 561. https://doi.org/10.3390/nano8070561.

(192) Kim, K.-T.; Zaikova, T.; Hutchison, J. E.; Tanguay, R. L. Gold Nanoparticles Disrupt Zebrafish Eye Development and Pigmentation. *Toxicol. Sci. Off. J. Soc. Toxicol.* **2013**, *133* (2), 275–288. https://doi.org/10.1093/toxsci/kft081.

8 ACKNOWLEDGMENTS

This PhD course was very formative for me and allowed me to live a complete research experience, straddling two states, in a period in which travel was not facilitated. Despite the complications due to the period, thanks to the help of my tutors Dr. Valerie Marchi, Dr. Maria J. Lo Faro and Prof. Paolo Musumeci and cotutor Prof. Pascale Even-Hernandez, I was able to fully experience the opportunities offered by the PhD by working in various laboratories, collaborating with many research groups, departments, universities and research institutions, learning the importance of transversal scientific communication.

For the collaborations within the University of Catania I thank Dr. Giorgia Franzo and Prof. Riccardo Reitano from the Department of Physics and Astronomy; Prof. Giuseppe Maccarrone, Prof. Annalinda Contino and Dr. Ester Plumari of the Department of Chemical Sciences; Prof. Cinzia Di Pietro, Dr. Rosalia Battaglia and Dr. Angela Caponnetto of the Department of Biomedical and Biotechnological Sciences. I also thank all the members of Dr. Sabrina Carroccio's team of the CNR-IPCB of Catania for welcoming me into their team and making me feel welcome.

For the collaborations within the University of Rennes 1 I thank Dr. Christophe Penno and Prof. Abdelhak El Amrani of Laboratoire ECOBIO; Dr. Franck Artzner and Dr. Cristelle Mériadec of the Institut de Physique; Dr. Ludovic Favereau and Prof. Jean-Pierre Bazureau of the Institut des Sciences Chimiques; Dr. Aurélien Dupont and Dr. Claire Heichette of CNRS Inserm. For external collaborations I thank Dr. Olivier Mignen of the University of Brest; Dr. Célia Ravel, Dr. Grégory Moulin and Dr. Anne-Sophie Neyroud of the CHU Rennes 1 hospital.

This path has allowed me to use autonomously expensive and difficult to access machinery, learning a lot also from a technical point of view. For that I have to thank Dr. Vincent Dorcet of the THEMIS platform; Dr. Rémy Le Guevel, Dr.Hélène Solhi and Dr. Marie Madeleine Gueguen of the ImPACcell platform ; Dr. Gregory Taupier and Dr.Yann Molard of the CAPHTER platform; Dr. Stephanie Dutertre and Dr. Xavier Pinson of the MRic platform Photonics and CNR-IMM for the laboratories made available within the University of Catania.

A special thanks goes to all my colleagues, undergraduates, doctoral students and post docs with whom I shared this growth experience. Thanks Dr. Solène Ducarre, Dr. Raffaello Paolini and Dr. Imane Dalouzi for cheering up my final year of PhD, I'm sorry I didn't have you with me from the start. I thank Dr. Federica Pappalardo and Dr. Maria Laura Amoruso for accompanying and helping me in the experiments I conducted in Catania, I hope I have transmitted to you at least part of my passion and that your path will take you higher and higher.

I also thank all my family, my boyfriend and my friends, both French and Italian, for having cheered my path and for having been close to me at all times regardless of my mood.

Thank you.